

**STUDY OF SINGLE-SCREW EXTRUDERS
FOR CONTINUOUS FEEDING OF CANOLA PASTE FOR
SUPERCRITICAL FLUID EXTRACTION**

by

FANGZHI WANG

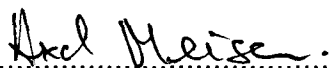
M.Sc., Tianjin University, 1983

**A THESIS SUBMITTED IN PARTIAL FULFILLMENT OF
THE REQUIREMENTS FOR THE DEGREE OF
DOCTOR OF PHILOSOPHY**

in

**THE FACULTY OF GRADUATE STUDIES
Department of Chemical Engineering**

**We accept this thesis as conforming
to the required standard**


.....


.....


.....

**THE UNIVERSITY OF BRITISH COLUMBIA
June 1993**

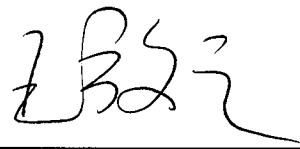
© FANGZHI WANG, 1993

ABSTRACT

The suitability of using a single-screw extruder to feed Canola seeds continuously into a supercritical fluid extractor was studied. The experiments were conducted with a custom-built extruder (0.44m long, 36.75 mm ID barrel) fitted with a screw having a single flight 4.9 mm high and 3 mm wide. The clearance between the top of the flight and the inside of the barrel was 0.0254 mm. Three screws with flight angles of 5.98° , 7.97° and 9.94° were used. The extruder screw was driven by two variable speed hydraulic motors operating typically at 66.5, 88.5 and 100.5 rpm. The extruder discharge port was fitted with a variable-size opening. The pressures and temperatures along the extruder barrel were measured by means of Iron-Constantan thermocouples (at 6 equispaced locations) and pressure transducers (at 4 locations), respectively. The discharge rate was determined gravimetrically.

A computer program of a three-velocity model was developed to simulate the extruder performance. The model was verified by comparison with experimental results obtained with Newtonian fluids in the viscosity range of 130 Pa·s. The agreement is satisfactory. The effects of operating parameters (like screw rotational speed) and geometric parameters (like flight angle) on the discharge rate and discharge pressure have been thoroughly investigated. The slip between the Canola paste and metal surface has been considered in the model, which plays a very important role in predicting the extruder performance. Although the Canola paste has a limited yield stress which may cause some plug flow in the screw channel, it was found that the flow behavior index n , which is 0.5 for the present concentration Canola pastes, has a stronger effect on the velocity profile

In presenting this thesis in partial fulfillment of the requirements for an advanced degree at The University of British Columbia, I agree that the Library shall make it freely available for reference and study. I further agree that permission for extensive copying of this thesis for scholarly purposes may be granted by the Head of the Department or by his or her representatives. It is understood that copying or publication of this thesis for financial gain shall not be allowed without my written permission.

(Signature) _____

Department of Chemical Engineering

The University of British Columbia
2216 Main Mall
Vancouver, B. C.
Canada
V6T 1Z4

Date: March 1993



National Library
of Canada

Bibliothèque nationale
du Canada

Acquisitions and
Bibliographic Services Branch

Direction des acquisitions et
des services bibliographiques

395 Wellington Street
Ottawa, Ontario
K1A 0N4

395, rue Wellington
Ottawa (Ontario)
K1A 0N4

Your file Votre référence

Our file Notre référence

The author has granted an irrevocable non-exclusive licence allowing the National Library of Canada to reproduce, loan, distribute or sell copies of his/her thesis by any means and in any form or format, making this thesis available to interested persons.

L'auteur a accordé une licence irrévocable et non exclusive permettant à la Bibliothèque nationale du Canada de reproduire, prêter, distribuer ou vendre des copies de sa thèse de quelque manière et sous quelque forme que ce soit pour mettre des exemplaires de cette thèse à la disposition des personnes intéressées.

The author retains ownership of the copyright in his/her thesis. Neither the thesis nor substantial extracts from it may be printed or otherwise reproduced without his/her permission.

L'auteur conserve la propriété du droit d'auteur qui protège sa thèse. Ni la thèse ni des extraits substantiels de celle-ci ne doivent être imprimés ou autrement reproduits sans son autorisation.

ISBN 0-315-85484-7

Canada

than the yield stress. Thus ignoring the yield stress did not likely introduce significant errors in the predictions. The reliability of the three-velocity model is satisfactory in predicting the output variables.

Experiments using pre-crushed Canola seeds showed that average discharge pressures ranging from 10 to 30 MPa could be achieved at flow rates varying from approximately 9.5 to 1.7 kg/hr. The average pressure along the screw was found to increase almost linearly and the pressure, at any point on the extruder barrel, varied sinusoidally around the mean. The amplitude of the pressure variations were typically 6% to 9% of the average pressure. If desired, higher discharge pressures can be achieved by lengthening the extruder and varying the screw-barrel geometries.

The apparent viscosity of Canola paste was determined at temperatures 288 to 323K, concentrations 35.3% to 95.7% (g solid/g liquid) and shear rates 0.15 to 225 s⁻¹. A modified power law equation was developed to express the apparent viscosity as a function of temperature, concentration and shear rate. The equation was found to be satisfactory in simulating the extruder performance.

The extruder discharges proved to be well suited for extraction with supercritical carbon dioxide since the discharge pressure of the extruder fell within the range of optimal operation of supercritical carbon dioxide extraction. The extrusion helped to rupture the Canola cell walls and thereby released the oil, thus improved the efficiency of extraction of Canola oil with supercritical carbon dioxide.

TABLE OF CONTENTS

	Page
ABSTRACT	ii
LIST OF FIGURES.....	vii
LIST OF TABLES.....	xviii
ACKNOWLEDGMENTS	xx
CHAPTER 1. INTRODUCTION	1
1.1 Introduction.....	1
1.2 Background	1
1.2.1 Supercritical Fluid Extraction.....	1
1.2.2 Canola Oil Processing.....	3
1.2.3 Principal Problems Associated with Supercritical Fluid Extraction of Solids	4
1.2.3.1 Solubility	4
1.2.3.2 Continuous Feeding of Solids.....	5
1.2.3.3 Solvent-Solute and Solvent-Solid Separation.....	8
1.2.3.4 Discharge of Extracted Solids.....	8
1.2.4 Principal Advantages of Screw Feeders.....	9
1.3 Thesis Objectives	9
CHAPTER 2. LITERATURE REVIEW	11
2.1 Introduction.....	11
2.2 History of Screw Extruders	11
2.3 Modeling of Screw Extrusion.....	13
2.3.1 Feed Section	13
2.3.2 Transition Section.....	15
2.3.3 Metering Section.....	16
2.4 Rheological Properties of Concentrated Fluid Biomaterials.....	29
CHAPTER 3. MATHEMATICAL MODEL FOR A SINGLE-SCREW EX- TRUDER	33
3.1 Mathematical Model of the Fully Developed Flow in a Single- screw Extruder	33
3.1.1 Flow Equations and Boundary Conditions.....	33
3.1.2 Dimensionless Equations and Boundary Conditions.....	41
3.1.3 Transverse Flow Equations	43

3.2 Discretization of Flow Equations and Boundary Conditions.....	46
3.3 Computer Program Flow Chart.....	55
CHAPTER 4. EXPERIMENTAL EQUIPMENT AND PROCEDURES	58
4.1 Introduction.....	58
4.2 Rheological Equipment	58
4.2.1 Rotational Viscometer.....	58
4.2.2 Capillary Viscometer.....	60
4.2.3 Paste Preparation.....	61
4.2.4 Solid Concentration Determination.....	64
4.2.4.1 Supercritical Fluid Extraction	64
4.2.4.2 Hexane Extraction	66
4.2.5 Calibration of Equipment	66
4.2.5.1 Calibration of Haake Viscometer	67
4.2.5.2 Calibration of Capillary Viscometer.....	68
4.2.6 Procedure for Determining Consistency Coefficient and Flow Behavior Index of Canola Pastes	69
4.2.7 Procedure for Determining Slip Factor of Canola Pastes	74
4.3 Screw Extruder	75
4.3.1 Design of the Single-screw Extruder	75
4.3.2 Hydraulic Drive System	89
4.3.3 Pressure and Temperature Measurement and Data Acquisition System.....	91
4.3.4 Equipment Calibration	96
4.3.4.1 Calibration of EXP-16 Interface and DAS-8 A/D Board.....	96
4.3.4.2 Calibration of Pressure Sensors and Ther- mocouples	98
4.3.5 Procedure for Extrusion Experiments	104
4.3.5.1 Extrusion of Newtonian Fluid	104
4.3.5.2 Extrusion of Canola Paste	104
CHAPTER 5. RESULTS AND DISCUSSION.....	107
5.1 Introduction.....	107
5.2 Apparent Viscosity of Canola Pastes	107
5.2.1 Dependency on Shear Rate	107
5.2.2 Dependency on Temperature	129
5.2.3 Dependency on Concentration	132
5.2.4 Dependency on Shear Rate, Temperature and Con- centration	134
5.3 Extrusion of Canola Paste.....	137
5.3.1 Experimental Results.....	137
5.3.2 Comparison between Experimental Results and Pre- dictions	141

5.3.3	Determination of Slip Factor	142
5.3.4	Discharge Pressure and Discharge Rate as a Function of Flight Angle	145
5.3.4.1	Discharge Pressure as a Function of Flight Angle	146
5.3.4.2	Discharge Rate as a Function of Flight Angle	148
5.3.5	Discharge Pressure and Discharge Rate as Functions of Screw Rotational Speed	150
5.3.5.1	Discharge Pressure as a Function of Screw Rotational Speed	150
5.3.5.2	Discharge Rate as a Function of Screw Rotational Speed	152
5.3.6	The Relationship Between Discharge Pressure and Discharge Rate	156
5.3.7	Effects of Slip Factor	156
5.3.8	Detailed Flow Patterns in the Screw Extruder Channel	162
5.3.8.1	Down Channel Flow	162
5.3.8.2	Cross Channel Flow	172
5.3.9	Accuracy of Numerical Simulations	177
5.4	The Effect of Extrusion on Oil Extraction	180
CHAPTER 6. CONCLUSIONS		183
CHAPTER 7. RECOMMENDATIONS		186
NOMENCLATURE		189
REFERENCES		192
APPENDIX		208
A.1	Detailed Derivation of Equations	208
A.1.1	Flow Equations	208
A.1.2	Shear Rate Equation for a Power Law Fluid in a Rotational Viscometer	211
A.1.3	Flow Rate of a Power Law Fluid with a Yield Stress in a Circular Tube	214
A.2	Effects of Yield Stress and Flow Behavior Index on Plug Flow in a Circular Tube	217
A.3	List of Extruder Drawings	221
A.4	Circuit Diagrams of EXP-16	228
A.5	List of Experimental Result	229
A.6	Listing of Computer Programs	239
A.6.1	FORTRAN Program for Extruder Simulation	239
A.6.2	BASIC Program for Calibrating the Data Acquisition Interface	254
A.7	List of Material Suppliers	256

LIST OF FIGURES

Figures	Captions	Page
Figure 1-1:	Schematic picture of continuous high-pressure jet extraction of viscous materials (Stahl <i>et al.</i> , 1984).....	6
Figure 1-2:	A single-screw extruder used in supercritical fluid extraction (Eggers <i>et al.</i> , 1985).	7
Figure 2-1:	Schematic diagram of a single-screw extruder.	12
Figure 2-2:	Dimensionless discharge rate as a function of down channel dimensionless pressure gradient. The parameter is the flow behavior index, n , in the power law (Kroesser and Middleman, 1965).....	20
Figure 2-3:	Dimensionless down channel velocity gradient in channel height direction between parallel plates: (a) shear rate is positive at all points; (b) shear rate is positive above the minimum velocity and negative below it.	22
Figure 2-4:	Dimensionless discharge rate versus down channel dimensionless pressure gradient calculated according to: (1) superposition of pressure and drag flow for a Newtonian fluid; (2) superposition of pressure and drag flow for a non-Newtonian fluid; (3) combined flow excluding cross channel flow; (4) combined flow including cross channel flow (Kroesser and Middleman, 1965)..	23
Figure 2-5:	Dimensionless correction factor χ versus ratio of flight height to channel width, H/W (Metzner, 1961).	25

Figure 2-6: Shape correction factor F_p^* as a function of height to width ratio and the flow behavior index n for the power law model (Wheeler and Wissler, 1961; Middleman, 1962).	26
Figure 2-7: Dimensionless discharge rate versus dimensionless pressure gradient for a power law fluid. The combined pressure and drag flows are compared with results from infinite parallel plates and a duct ($H/W=2$) (Middleman, 1965).	27
Figure 3-1: Schematic representation of an extruder section (two channels in parallel).	34
Figure 3-2: Geometry of the uncurled screw channel.	35
Figure 3-3: Flow domain.	39
Figure 3-4: Flow domain in dimensionless form.	42
Figure 3-5: Notation for lattice points.	47
Figure 3-6: Notation used for calculating one sided derivatives.	52
Figure 3-7 Flow chart of the computer program to calculate the velocities and pressures in the extruder	57
Figure 4-1: Schematic diagram of the grooved stationary cup and the rotating cylinder for the Haake Rotovisco RV12 viscometer. The dimensions are listed in the Table 4-1.	59
Figure 4-2: Schematic diagram of the capillary viscometer (tube dimensions: 1500 mm long, 3.06 mm ID).	62
Figure 4-3: Seed crusher	63
Figure 4-4: Schematic diagram of the supercritical fluid extraction system.	65
Figure 4-5: Calibration results for the Rotovisco RV12 sensor MV IP (Viscosity Standard 104.640 Pa·s @ 25 °C).	70

Figure 4-6: Calibration results for the Rotovisco RV12 sensor MV IIP (Viscosity Standard 104.640 Pa·s @ 25 °C).....	71
Figure 4-7: Calibration results for the Rotovisco RV12 sensor SV IIP (Viscosity Standard 104.640 Pa·s @ 25 °C).....	72
Figure 4-8: Calibration results for the capillary viscometer (Viscosity stan- dard 130.00 Pa·s @ 20 °C).....	73
Figure 4-9: Drag and pressure flow shape factors (Booy, 1963)	79
Figure 4-10: Pressure flow end correction factor (Booy, 1967)	81
Figure 4-11: Drag flow end correction factor (Booy, 1967).....	82
Figure 4-12: Drag flow curvature correction factor (Booy, 1963).....	83
Figure 4-13: Pressure flow curvature correction factor (Booy, 1963)	84
Figure 4-14: Sectional view of the assembled extruder	87
Figure 4-15: Detailed drawing of the screw shaft.....	88
Figure 4-16: Schematic diagram of the hydraulic drive equipment.	92
Figure 4-17: Details of a pressure transducer mounted on the screw bar- rel (all units are in mm).....	94
Figure 4-18: Details of a thermocouple mounted on the screw barrel.	95
Figure 4-19: Diagram of the noise-free DC voltage supply.....	97
Figure 4-20: Calibration curve for pressure transducer #1 (PX600-3K6V)	100
Figure 4-21: Calibration curve for pressure transducer #2 (PX600-3K6V)	101
Figure 4-22: Calibration curve for pressure transducer #3 (PX600-5K6V)	102
Figure 4-23: Calibration curve for pressure transducer #4 (PX600- 10K6V).....	103

Figure 4-24: Extrusion with a Newtonian viscosity standard ($\theta = 5.98^\circ$, $N = 66.5$ rpm, $Q = 2.27$ kg/h).....	106
Figure 5-1: Total shear stress as a function of shear rate at a Canola concentration of 35.3% (g solid/g liquid) using the rotational viscometer.	108
Figure 5-2: Total shear stress as a function of shear rate at a Canola concentration of 53.4% (g solid/g liquid) using the rotational viscometer.	109
Figure 5-3: Total shear stress as a function of shear rate at a Canola concentration of 64.5% (g solid/g liquid) using the rotational viscometer.	110
Figure 5-4: Total shear stress as a function of shear rate at a Canola concentration of 84.2% (g solid/g liquid) using the rotational viscometer.	111
Figure 5-5: Total shear stress as a function of shear rate at a Canola concentration of 95.7% (g solid/g liquid) using the rotational viscometer.	112
Figure 5-6: Shear stress difference ($\tau - \tau_0$) as a function of shear rate at a Canola concentration of 35.3% (g solid/g liquid) using the rotational viscometer.	114
Figure 5-7: Shear stress difference ($\tau - \tau_0$) as a function of shear rate at a Canola concentration of 53.4% (g solid/g liquid) using the rotational viscometer.	115
Figure 5-8: Shear stress difference ($\tau - \tau_0$) as a function of shear rate at a Canola concentration of 64.5% (g solid/g liquid) using the rotational viscometer.	116
Figure 5-9: Shear stress difference ($\tau - \tau_0$) as a function of shear rate at a Canola concentration of 84.2% (g solid/g liquid) using the rotational viscometer.	117

Figure 5-10: Shear stress difference ($\tau - \tau_0$) as a function of shear rate at a Canola concentration of 95.7% (g solid/g liquid) using the rotational viscometer.	118
Figure 5-11: Apparent viscosity as a function of shear rate at a Canola concentration of 35.3% (g solid/g liquid) using the rotational viscometer.	122
Figure 5-12: Apparent viscosity as a function of shear rate at a Canola concentration of 53.4% (g solid/g liquid) using the rotational viscometer	123
Figure 5-13: Apparent viscosity as a function of shear rate at a Canola concentration of 64.5% (g solid/g liquid) using the rotational viscometer..	124
Figure 5-14: Apparent viscosity as a function of shear rate at a Canola concentration of 84.2% (g solid/g liquid) using the rotational viscometer..	125
Figure 5-15: Apparent viscosity as a function of shear rate at a Canola concentration of 95.7% (g solid/g liquid) using the rotational viscometer..	126
Figure 5-16: Torque readings as a function of time for Canola paste at a Canola concentration of 95.7% (g solid/g liquid) and temperature of 25 °C using the rotational viscometer at a speed of 0.01 rpm.....	128
Figure 5-17: Apparent viscosity as a function of temperature for different Canola concentrations at a shear rate of 10 s ⁻¹ using the rotational viscometer.	131
Figure 5-18: Apparent viscosity as a function of Canola concentration for different temperatures at a shear rate of 10 (s ⁻¹) using the rotational viscometer.	133
Figure 5-19: Pressure variation with time at different locations from the inlet: curve (1) at 190 mm; curve (2) at 288 mm; curve (3) at	

386 mm and curve (4) at 435 mm. Flight angle 7.97° , rotational speed 66.5 rpm, discharge rate 3.75 kg/hr of Canola paste at a concentration of 146% g solid/g liquid.138

Figure 5-20: Pressure variation with time at different locations from the inlet: curve (1) is at 190 mm; curve (2) 288 mm; curve (3) 386 mm and curve (4) 435 mm (Flight angle 7.97° , rotational speed 88.5 rpm, discharge rate 7.42 kg/hr of Canola paste at a concentration of 146% g solid/g liquid).....139

Figure 5-21: Pressure variation with time at different locations from the inlet: curve (1) is at 190 mm; curve (2) 288 mm; curve (3) 386 mm and curve (4) 435 mm (Flight angle 7.97° , rotational speed 100.5 rpm, discharge rate 3.07 kg/hr of Canola paste at a concentration of 146% g solid/g liquid).....140

Figure 5-22: Discharge rate as a function of discharge pressure and rotational speed. The curves were obtained from the present three-velocity model with no slip; the symbols denote the experimental results obtained with a screw flight angle of 5.98° at a Canola concentration of 146%).143

Figure 5-23: Discharge pressure as a function of flight angle. The curve is obtained by the present three-velocity model and the symbols represent experimental measurements (discharge rate 5.0 kg/h, rotational speed 66.5 rpm, slip factor 0.3, Canola concentration 146% g solid/g liquid)147

Figure 5-24: Discharge pressure as a function of flight angle (obtained by the present three-velocity model and Booy's model, discharge rate 1.0 kg/hr, rotational speed 66.5 rpm, no slip with a Newtonian fluid having a viscosity of 621 Pa·s).149

Figure 5-25: Discharge rate as a function of flight angle (the solid curves were obtained from the present three-velocity model with Canola paste having a concentration of 146% g solid/g liquid and a slip factor of 0.3; the dashed curve was obtained

from Booy's model using a Newtonian fluid with a viscosity of 621 Pa·s and no slip; rotational speed 66.5 rpm. The symbols represent the experimental measurements)151

Figure 5-26: Discharge pressure as a function of screw rotational speed and flight angle. The curves are obtained from the present three-velocity model and the symbols are the experimental measurements (discharge rate 5 kg/hr, slip factor 0.3, Canola concentration 146% g solid/g liquid)153

Figure 5-27: Discharge rate as a function of screw rotational speed and flight angle. The curves are obtained from the present three-velocity model and the symbols are experimental measurements (discharge pressure 20 MPa, slip factor 0.3, Canola concentration 146% g solid/g liquid).154

Figure 5-28: Discharge rate of corn syrup extruded in a 2.5" diameter extruder as a function of rotational speed. Lines indicate predicted values from Booy's model with the assumption $F_d = F_p = 1.0$. The symbols represent experimental data obtained by Maddock (Tadmor, 1969).....155

Figure 5-29: Discharge rate as a function of discharge pressure and rotational speed at a flight angle of 5.98°. The curves are calculated from the present three-velocity model with a slip factor of 0.3. The symbols represent experimental results obtained with a Canola paste concentration of 146% (g solid/g liquid).157

Figure 5-30: Discharge rate as a function of discharge pressure and rotational speed at a flight angle of 7.97°. The curves are calculated from the present three-velocity model with a slip factor of 0.3. The symbols represent experimental results obtained with a Canola paste concentration of 146% (g solid/g liquid).158

Figure 5-31: Discharge rate as a function of discharge pressure and rotational speed at a flight angle of 9.94°. The curves are cal-

- culated from the present three-velocity model with a slip factor of 0.3. The symbols represent experimental results obtained with a Canola paste concentration of 146% (g solid/g liquid).159
- Figure 5-32: Discharge rate as a function of discharge pressure and rotational speed at a flight angle of 5.98° . The curves are calculated from the present three-velocity model with slip factors of 0, 0.3 and 1. The symbols represent experimental results obtained with a Canola paste concentration of 146% (g solid/g liquid)161
- Figure 5-33: Comparison of pressure distribution along a screw extruder using different models: (1) single velocity model, (2) the present three-velocity model with $\kappa = 0$, (3) the present three-velocity model with $\kappa = 0.3$. The symbols represent experimental results for rotational speed 88.5 rpm, discharge rate 2.85 kg/hr, Canola concentration 146% (g solid/g liquid), flight angle 5.98° 163
- Figure 5-34: Dimensionless down channel velocity w (rotational speed 100.5 rpm, discharge pressure 10 MPa, discharge rate 11.8 kg/hr, flight angle 5.98° , slip factor 0.3, paste concentration 146% g solid/g liquid, flight height 4.9mm)165
- Figure 5-35: Dimensionless down channel velocity, w , at $y = W/2$ (discharge pressure 10 MPa, discharge rate 11.8 kg/hr, rotational speed 100.5 rpm, flight angle 5.98° , slip factor 0.3, paste concentration 146% g solid/g liquid, flight height 4.9mm)166
- Figure 5-36: Dimensionless down channel velocity w (rotational speed 66.5 rpm, discharge pressure 30 MPa, discharge rate 2.3 kg/hr, flight angle 5.98° , slip factor 0.3, paste concentration 146% g solid/g liquid, flight height 4.9mm)167
- Figure 5-37: Dimensionless down channel velocity, w , at $y = W/2$ (discharge pressure 30 MPa, discharge rate 2.3 kg/hr, rota-

- tional speed 66.5 rpm, flight angle 5.98° , slip factor 0.3, paste concentration 146% g solid/g liquid, flight height 4.9mm).....168
- Figure 5-38: Dimensionless down channel velocity w (rotational speed 66.5 rpm, discharge pressure 30 MPa, discharge rate 8.7 kg/hr, flight angle 5.98° , slip factor 0, paste concentration 146% g solid/g liquid, flight height 4.9mm).....169
- Figure 5-39: Dimensionless down channel velocity, w , at $y = W/2$ (discharge pressure 30 MPa, discharge rate 8.7 kg/hr, rotational speed 66.5 rpm, flight angle 5.98° , slip factor 0, paste concentration 146% g solid/g liquid, flight height 4.9mm)170
- Figure 5-40: Dimensionless down channel velocity contours at $z = L/2$ (discharge pressure 30 MPa, discharge rate 2.3 kg/hr, rotational speed 66.5 rpm, flight angle 5.98° , slip factor 0.3, paste concentration 146% g solid/g liquid, flight height 4.9mm).....171
- Figure 5-41: Stream function contours (flight angle 5.98° , rotational speed 66.5 rpm, discharge pressure 10 MPa, discharge rate 15.5 kg/hr, slip factor 0, paste concentration 146% g solid/g liquid, flight height 4.9mm).....173
- Figure 5-42: Stream function contours (flight angle 5.98° , rotational speed 66.5 rpm, discharge pressure 30 MPa, discharge rate 8.7 kg/hr, slip factor 0, paste concentration 146% g solid/g liquid, flight height 4.9mm).....174
- Figure 5-43: Stream function contours (flight angle 5.98° , rotational speed 66.5 rpm, discharge pressure 10 MPa, discharge rate 11.8 kg/hr, slip factor 0.3, paste concentration 146% g solid/g liquid, flight height 4.9mm)175
- Figure 5-44: Stream function contour (flight angle 5.98° , rotational speed 66.5 rpm discharge pressure 30 MPa, discharge rate 2.3

kg/hr, slip factor 0.3, paste concentration 146% g solid/g liquid, flight height 4.9mm).....	176
Figure 5-45: Effect of discharge pressure on supercritical fluid extraction of Canola oil. The pastes were either not extruded (0 Pa) or extruded at discharge pressures of 10.7 MPa, 18.4 MPa, 29.6 MPa	182
Figure A.1.2-1: Notation of a fluid element from a rotational viscometer	212
Figure A.2-1: Dimensionless velocity distribution in a circular tube. (1) $n = 1$, $\tau_0 = 0$; (2) $n = 0.5$, $\tau_0 = 0$; (3) $n = 0.5$; $\tau_0 = 2000$ Pa; (4) $n = 0.5$, $\tau_0 = 2850$ Pa; (5) $n = 0.5$, $\tau_0 = 4000$ Pa; (6) $n = 0.1$, $\tau_0 = 0$; (7) $n = 0.1$, $\tau_0 = 2850$ Pa.....	220
Figure A.3-1: Drawing 3 left bearing holder	222
Figure A.3-2: Drawing 4 restrictor locker nut	223
Figure A.3-3: Drawing 5 cone restrictor	224
Figure A.3-4: Drawing 6 inlet section barrel.....	225
Figure A.3-5: Drawing 7 outlet section barrel.....	226
Figure A.3-6: Drawing 8 thrust bearing holder.....	227
Figure A.5-1: Recorded pressure distribution along the extruder. Flight angle 5.98° , rotational speed 66.5 rpm, paste concentration 146% (g solid/g liquid).....	230
Figure A.5-2: Recorded pressure distribution along the extruder. Flight angle 5.98° , rotational speed 88.5 rpm, paste concentration 146% (g solid/g liquid)	231
Figure A.5-3: Recorded pressure distribution along the extruder. Flight angle 5.98° , rotational speed 100.5 rpm, paste concentration 146% (g solid/g liquid)	232

Figure A.5-4: Recorded pressure distribution along the extruder. Flight angle 7.98°, rotational speed 66.5 rpm, paste concentration 146% (g solid/g liquid)	233
Figure A.5-5: Recorded pressure distribution along the extruder. Flight angle 7.97°, rotational speed 88.5 rpm, paste concentration 146% (g solid/g liquid)	234
Figure A.5-6: Recorded pressure distribution along the extruder. Flight angle 7.97°, rotational speed 100.5 rpm, paste concentration 146% (g solid/g liquid)	235
Figure A.5-7: Recorded pressure distribution along the extruder. Flight angle 9.94°, rotational speed 66.5 rpm, paste concentration 146% (g solid/g liquid)	236
Figure A.5-8: Recorded pressure distribution along the extruder. Flight angle 9.94°, rotational speed 88.5 rpm, paste concentration 146% (g solid/g liquid)	237
Figure A.5-9: Recorded pressure distribution along the extruder. Flight angle 9.94°, rotational speed 100.5 rpm, paste concentration 146% (g solid/g liquid)	238

LIST OF TABLES

Tables	Page
Table 4-1: Dimensions of the grooved cups and cylinders (see Figure 4-1).....	60
Table 4-2: Solid concentration of Canola paste.....	67
Table 4-3: Calibration factors for the rotational viscometer	69
Table 4-4: Screw dimensions.....	85
Table 4-5: Regression results of pressure transducer calibration	99
Table 4-6: Calibration results for the Iron-Constantan thermocouples.	99
Table 5-1: Consistency coefficient (m) and flow behavior index (n) for Canola pastes at various temperatures and concentrations.....	119
Table 5-2: Experimental and predicted apparent viscosities at a shear rate of 10 s^{-1}	135
Table 5-3: Slip factors for Canola pastes obtained from that capillary viscometer experiments at a temperature of 20°C	145
Table 5-4: Simulated dimensionless down channel velocities adjacent to the flight for different mesh sizes (flight angle 5.98° , discharge pressure 20 MPa, discharge rate 5.93 kg/hr, slip factor 0.3, paste concentration 146% g solid/g liquid, flight height 0.49 mm).....	178
Table 5-5: Simulated dimensionless down channel velocities at $y = W/2$ for different mesh sizes (flight angle 5.98° , discharge pressure 20 MPa, discharge rate 5.93 kg/hr, slip factor 0.3, paste concentration 146% g solid/g liquid, flight height 0.49 mm).	179

Table A.2-1 Comparison of curves (2) and (4) for dimensionless velocities at $\Delta p = 20$ MPa, $L=1.5$ m and $R = 1/16''$	219
Table A.3-1 Extruder part list for Figure 4-15.....	221

ACKNOWLEDGMENTS

The author wishes to express his sincere gratitude to his supervisor Dr. A. Meisen for his patient guidance, corrections and financial support which played a very important role in the completion of the study.

The author also wishes to thank Mrs. D. Wiebe for her very helpful proof reading.

Thanks are due to the technical staff of the Chemical Engineering Department for their assistance in the construction of the experimental equipment.

Finally, special thanks to my wife Zhengyi, daughter Yan and my parents who were constant sources of moral support and motivation during the entire course of this study.

CHAPTER ONE

INTRODUCTION

1.1 Introduction

Solvent extraction is a traditional, widely used separation technique. During the last decade, partly due to the energy crisis and toxicity considerations, supercritical fluids, *i. e.*, fluids above their critical points, have been actively studied as solvents. The term supercritical fluid extraction (SFE) has been given to extraction processes using such fluids.

1.2 Background

1.2.1 Supercritical Fluid Extraction

A supercritical fluid usually has a lower viscosity and higher density than that of the corresponding liquid and gas, respectively. The fact that supercritical fluids have comparatively low viscosities for a given density, facilitates their penetration into solid structures and can, therefore, result in improved extraction. It is in the extraction of solids, therefore, that one major potential application of supercritical fluids lies.

Numerous applications of the supercritical fluid extraction of solids have been reported. For instance, Prasad *et al.* (1981), Qian (1984) and Pearce (1988)

described the use of supercritical CO₂ ($T_c=31.4^\circ$, $P_c=7.81$ MPa) to decaffeinate coffee by passing such a fluid through a fixed bed of beans. The caffeine, which dissolved in the supercritical CO₂ was then removed from the CO₂ by a water wash. Researchers in the United States (Friedrich *et al.*, 1982) used supercritical CO₂ to extract lipids from soybeans. Choi *et al.* (1987), in a single step, extracted most of the neutral lipids and part of the glycolipids from algae with supercritical CO₂. Japanese researchers found that the phospholipid content of the oil obtained from SFE was about 500 ppm lower than that of oil extracted with hexane (Liu, 1986). A lower phospholipid content improves the quality of cooking oil. Fattori (1985) thoroughly investigated the extraction of oil from Canola by passing supercritical CO₂ through a fixed bed of seed fragments. The results of his study demonstrated that supercritical CO₂, under the appropriate conditions, can be an effective solvent for extracting oil from Canola seeds.

Another promising area for the application of supercritical fluid extraction is presented by the coal industry. Supercritical fluids can be used in the desulfurization of high sulfur coals to generate high BTU gases (Muchmore *et al.*, 1985; Chen *et al.*, 1985; Yueruem *et al.*, 1990; Hippo *et al.*, 1991). The extracted compounds have potential uses as chemical feed stocks and sulfiding agents. Supercritical fluid extraction may therefore lead to clean coals which can be burned with less environmental impact than unprocessed coals.

Many recent publications have indicated that supercritical fluid extraction may be used to treat contaminated soil and water. PCB and DDT in contaminated soils were successfully extracted with supercritical CO₂ (Brady *et al.*, 1985, 1987;

Irvin *et al.*, 1987, Roop *et al.*, 1989; Yeo *et al.*, 1990, Ghonasgi *et al.*, 1990 and Haan *et al.*, 1992). The attractive feature of this process is that CO₂, being virtually inert, leaves no harmful solvent residue in the processed soil. Furthermore, the ease of separation of the extracted solute from supercritical CO₂ results in smaller waste volumes and facilitates the efficiency of subsequent disposal processes such as combustion. Funazukuri *et al.* (1985) used supercritical fluids to extract oil from used automotive tire samples. He found that more than 50% (by weight) of the sample was converted to liquid oils when the extraction was finished.

1.2.2 Canola Oil Processing

Over the centuries, four basic methods have been used to extract edible oils from oil seeds. The first was the basic wet rendering process in which the oil-bearing material was boiled in water leading to a partial separation of oil, which was skimmed off the top of the vessel. The second was the cage-press in which pressure was applied to a stationary bed of seeds by levers, screw jacks or hydraulic cylinders. The oil flowed from the compressed mass to collecting vats below. Both of these methods are now virtually obsolete (Bredeson, 1983). The third method is the mechanical screw press and the fourth is solvent extraction. Both are widely used in today's vegetable oil industry. Hexane is one of the most popular solvents used to extract oil from seeds.

The world-wide rape seed production was 25 million metric tonnes and in Canada, 3.3 million metric tonnes of Canola seeds (one kind of rape seed) were produced in 1990 (FAO, 1991). However, there are several problems

associating with vegetable oil production. On the one hand, when Canola seeds are processed in a screw press, a somewhat dark colored oil is obtained which needs refining and bleaching before being saleable. On the other hand, hexane extracted oil contains unwanted gums which must be removed in a separate refining process. Furthermore, since hexane is a petroleum product, it is subject to price increases and uncertainties of supply (Friedrich and List, 1982). A more efficient and selective process for Canola seed processing is, therefore, needed. Supercritical fluid extraction is promising because it can produce an oil which is essentially gum-free (Friedrich and List, 1982) due to the selectivity of certain supercritical fluids.

1.2.3 Principal Problems Associated with Supercritical Fluid Extraction of Solids

1.2.3.1 Solubility

Although the solvent ability of supercritical CO₂ has been demonstrated, the solubility of extracts may be too low for many commercial processes. For example, the solubility of Canola oil in supercritical CO₂ is 11.8 mg oil/g CO₂ at 36 MPa and 55 °C (Fattori, 1985). To increase the solubility of supercritical CO₂, entrainers have been suggested (Brunner and Peter, 1982; Peter, 1984; Van Alsten, 1985). Entrainers are compounds which are added to supercritical fluids to improve their solvation power. Although not yet fully understood, the efficiency of entrainers may result from hydrogen bonding with the extracts.

1.2.3.2 Continuous Feeding of Solids

As mentioned before, it is in the extraction of solids that a major advantage of supercritical fluid extraction may lie. Supercritical fluid extractors must operate near or above the critical pressure of the solvent, which is quite high for most promising solvents. It is difficult to introduce solids continuously into high pressure extractors without leakage and little research has been reported on feeding solids into supercritical extractors.

In coal liquefaction, where water is often used as the supercritical fluid extractant, Davies and Whitehead (1982) used liquid water as the feed carrier and designed a reciprocating pump with double ball check valves at the inlet and outlet for pumping a coal slurry into an extractor operating at approximately 20 MPa. However, this method is not well suited to the supercritical extraction of biomaterials (like oil seeds) using CO₂ since CO₂ is a gas with a much lower density than that of biomaterials under ambient conditions. Therefore, CO₂ cannot be used as a carrier fluid. Stahl *et al.* (1984) reported to have used a continuous extractor in which the supercritical fluid and solid material flow concurrently, as shown in Figure 1-1. However, the feeding of the solid into the hopper is still a batch operation.

Since biomaterials are soft and may contain free oils, German researchers (Eggers *et al.*, 1985) have made some preliminary studies on screw extruders to feed rape seeds into an extractor. As the soft, oil-bearing biomaterial is forced through the extruder (Figure 1-2), it fills the space between the screw and casing thereby preventing the leakage of pressurized fluid from the extractor

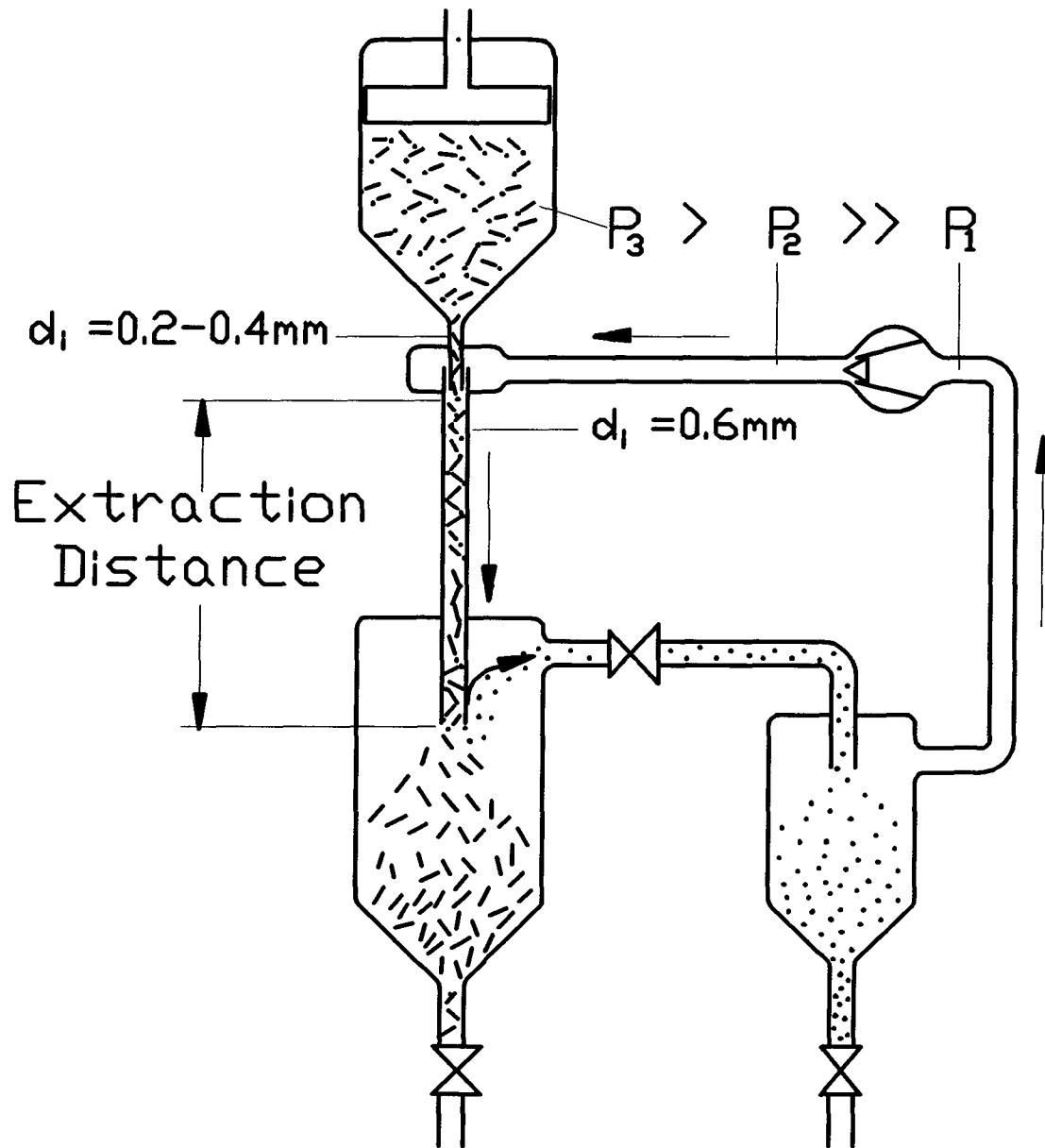


Figure 1-1: Schematic picture of continuous high-pressure jet extraction of viscous materials (Stahl *et al.*, 1984).

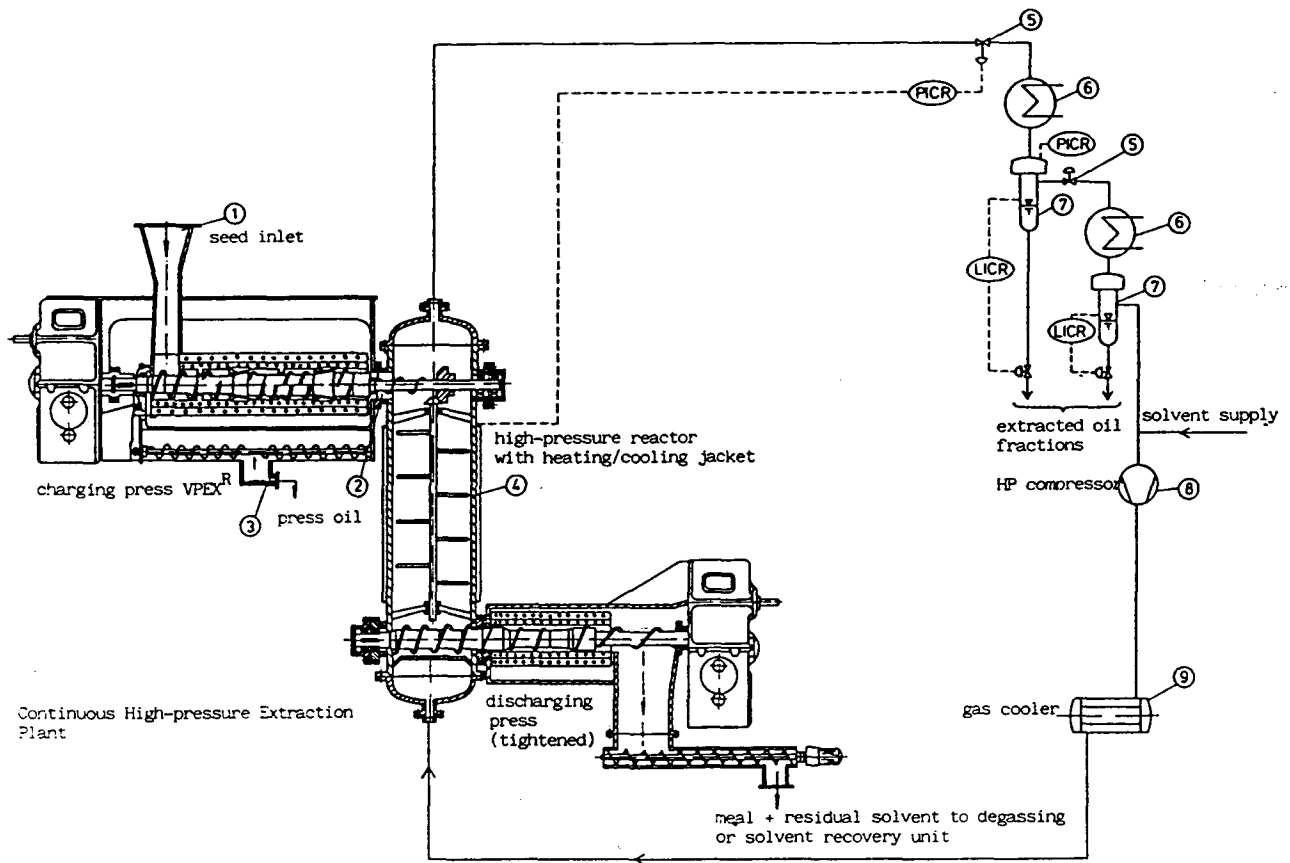


Figure 1-2: A single-screw extruder used in supercritical fluid extraction (Eggers *et al.*, 1985).

which is located at the extruder exit.

Although the experiments reported by Eggers *et al.* have been promising, they have not been extensive and practical shortcomings remain to be overcome. For example, biomaterials tend to adhere to the screw and spin synchronously with the screw thereby resulting in a low feed rate. Furthermore, improved design procedures are needed for screw extruders which feed solids into supercritical fluid extractors operating at high pressures.

1.2.3.3 Solvent-Solute and Solvent-Solid Separation

After the oil is extracted by supercritical CO₂, the seed particles must be separated from the fluid and the oil must be separated from the supercritical CO₂. Ely (1983) suggested recovering the oil from CO₂ by decreasing the density of the supercritical phase, *i. e.*, either by reducing the pressure at a constant temperature or by raising the temperature at a constant pressure. However, little information has thus far been reported on the separation of extracted solids from high pressure solvent.

1.2.3.4 Discharge of Extracted Solids

The extracted solid should be moved continuously from the high pressure extractor without any leakage of pressurized solvent. Eggers *et al.* (1985) claimed that a screw extruder can also be used to move solid material out of the high pressure extractor while keeping the system pressure steady (see Figure 1-2).

1.2.4 Principal Advantages of Screw Feeders

Screw extruders are probably one of most common equipment items used in the food industry today. Screw extruders could not only be used as feeding and discharging devices, but they may also be utilized to pretreat biomaterials. It is well known that some biomaterials, such as oil seeds, require pretreatment before extraction in order to improve both the quality and yield of the oil (Clandinin, 1981; Beach, 1983). While the material is conveyed in an extruder, the pressure is raised and frictional heat is produced. Furthermore, the screw feeder could be easily heated externally. Thus in the extruder, the seeds may be crushed and partially cooked. It would be worthwhile determining how these effects influence the subsequent extraction of Canola oil.

1.3 Thesis Objectives

In order to evaluate the application of screw extruders as feeders for supercritical fluid extractors, physical properties, basic experimental screw extruder data and mathematical models are needed. The current study is aimed at providing such information. The general objective of the present research project is to examine the use of extruders for continuously feeding Canola seed paste at elevated pressures. The specific objectives of the study are:

- To determine the rheological characteristics of pastes consisting of oil and Canola seed fragments;

- To develop laboratory equipment to investigate the use of single-screw extruders as continuous feeders for elevated pressure extraction processes;
- To determine the effects of extruder parameters on the performance of single-screw feeders;
- To develop a mathematical model for screw extruders (based on previous models intended for the plastic industry) and make the model suitable for predicting the performance of extruders when they are used as feeders of Canola seeds for supercritical fluid extractors;
- To compare the model predictions with measured results obtained from laboratory experiments;
- To determine the effect of high pressure extrusion on the extractibility of Canola pastes.

The research project was carried out in a number of stages. In the initial stage, the rheological behavior of Canola pastes was investigated at different concentrations and temperatures. In the second stage, the rheological data were used to design a laboratory-scale single-screw feeder by means of a simplified method. In the next stage, the equations governing the flow of the Canola pastes in the screw channel and the pressure increase along the screw were developed and solved numerically. The results predicted by this mathematical model were then compared with experimental data. In the final stage, the pastes which were extruded at different pressures were extracted by supercritical CO₂.

CHAPTER TWO

LITERATURE REVIEW

2.1 Introduction

The word "extrude" originates from the Latin words "ex" (out) and "trudere" (to thrust). This closely describes the extrusion process itself as the "shaping" of a deformable material by a force acting through a die. Extrusion is a widely used process in the food and polymer processing industries. When screw extruders are used to pump Newtonian fluids, they are also called screw viscosity pumps (Rowell, 1922). The salient feature of screw extruders is an Archimedian screw located in a cylindrical barrel. A typical single-screw extruder is shown Figure 2-1. When the screw is rotated, the flight on the screw pushes the plasticized material forward and creates the pressure to force the material through the exit opening.

2.2 History of Screw Extruders

Screw extruders have been used extensively for the past 150 years and were largely developed to meet the needs of the rubber and plastic industries. However, they have also found considerable application in the food industry (Janssen, 1978; Harper, 1981). The first extruder used in the plastic industry was a ram extruder, apparently developed by Henry Bewley and Richard Rooman in 1845 in England (Kaufman, 1969). The ram extruder operated in

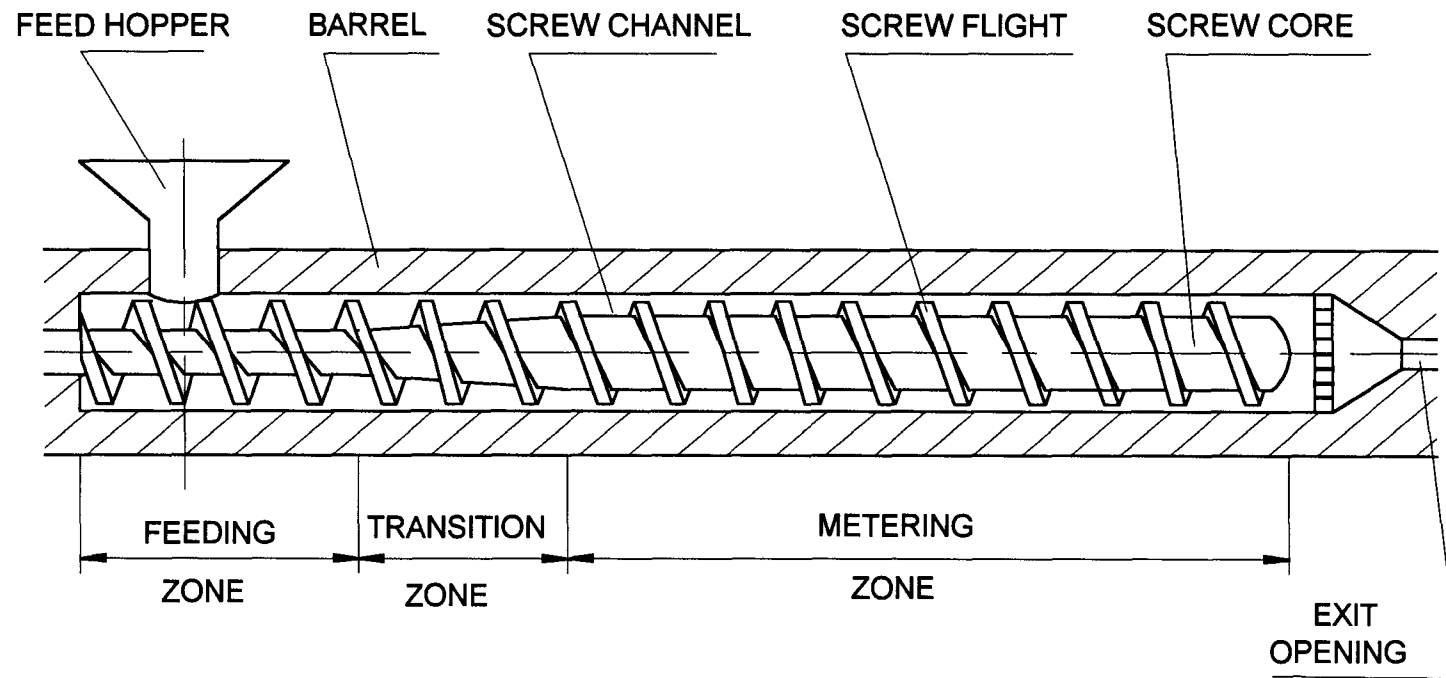


Figure 2-1: Schematic diagram of a single-screw extruder.

an intermittent fashion which is unsuitable for the high capacities usually required by industry today. The need for continuous extrusion brought about the screw extruder. Circumstantial evidence indicates that A. G. DeWolfe, in the United States, might have developed the first screw extruder in the early 1860s (Hovey, 1961). The Phoenix Gummiwerke has published a drawing of a screw dated 1873 (Schenkel, 1966), and William Kiel and John Prior, in the United States, both claimed the development of such a machine in 1876 (White, 1969). However, the birth of the screw extruder is most clearly linked to the patent of Matthew Gray issued in England in 1879 (Gray, 1879). This patent is the first clear description of this type of machine. Independent of Gray, Francis Shaw in England developed a screw extruder in 1879, as did John Royle in the United States in 1880 (Tadmor and Gogos, 1979).

2.3 Modeling of Screw Extrusion

A typical screw extruder can be divided into three main sections: the feed, transition and metering sections (see Figure 2.1). Different mathematical models have been developed for each section.

2.3.1 Feed Section

The feed section (also called the "*solid conveying zone*" in thermoplastic processing) has received less attention by extruder analysts than the metering zone (Darnell and Mol, 1956) due to the extreme difficulty of describing the movement of discontinuous solid materials such as crushable seeds. One of the earliest treatments of the subject was given by Decker (1941) who derived equations which led to some correct conclusions even though the predictions did

not correlate well with the experimental results. He recommended attaining low friction between the screw surface and polymer by polishing the screw and maintaining a high coefficient of friction between the polymer and barrel by roughening the barrel surface. Pawlowski (1949) created a more realistic model. He assumed that there is no internal shear in the solid and made a force and torque balance on the solid plug (Darnell and Mol, 1956). Maillefer (1954) also discussed the solid conveying section, but his analysis did not apply to curved channels where torques are involved and, therefore, did not include all forces acting upon the solid plug. Simonds (1952) introduced the balance of torques, but his treatment can only predict whether or not the solid will be conveyed. Jackson *et al.* (1958) performed a similar analysis to that of Maillefer, but included the normal force that the flight exerts on the plug. However, because they did not take into consideration the essential balance of torques, the equations have little value (Tadmor, 1970). The most thorough analysis of the solid conveying zone was performed by Darnell and Mol (1956) even though they did not consider the effect of void fraction in the solid material. Based on the physical model by Darnell and Mol (1956), Pend *et al.* (1985) presented a mathematical model and their results proved that the friction between extrudate and barrel is the most important factor affecting extruder performance. Contrary to the plug flow model presented by Darnell and Mol (1956), Zhu *et al.* (1989) considered that plastic pellets in the screw channel behave in a similar manner to fluids but their model does not satisfy the assumption of pressure isotropy, thus the three main stresses at any point are not identical. Their model may be regarded as a non-plug flow model. Their experimental results were reported as agreeing well with numerical simulations based on the model.

2.3.2 Transition Section

In thermoplastic extrusion, the characteristic of this section is that the solid polymer is converted into a melt. It is, therefore, also called the *melting zone* in thermoplastic extrusion. Similarly, in the extrusion of food stuffs, the material may change from a raw or uncooked state into a plastic, dough-like state (Harper, 1981).

The melting of plastics in screw extruders was first investigated by Maddock (1959) and Streeter (1961). They developed an experimental technique which led to the development of a qualitative analysis for the melting zone through visual observation. The experimental technique used to study the melting mechanism operating in a plasticating extruder is, first, to feed the extruder with a mixture of natural colored (3-5%) polymer. When steady state is reached, the extruder is suddenly frozen by cooling the barrel and screw. The original conditions existing in the extruder channel during the steady state operation are, therefore, retained, and the molten and partially mixed polymer will exhibit flow lines, while the unmelted polymer will remain in the initial solid form. This technology provided them with detailed information for modeling this section.

Several other authors (Maillefer, 1963; Tadmor, 1966; Tadmor and Klein, 1970; Edmondson and Fenner, 1975; Shapiro *et al.*, 1976) have presented different model analyses of the melt-pool melting processes but no successful analysis has yet been given to predict the mode of melting (Pearson, 1985).

2.3.3 Metering Section

The term metering section originates from the common practice of designing the last section of the screw preceding the die to control or "meter" the flow rate through an extruder. The fluid flow in this section is considered to be fully developed. Therefore, modeling this section is relatively easy compared with the previous sections and has received more attention. The first mathematical model for this section was derived for screw viscosity pumps (Rowell and Finlayson, 1922, 1928). It assumes that the flow is Newtonian, steady, laminar, fully developed, incompressible, without slippage at the walls and with negligible gravitational effects. It also assumes that the normal velocity between the screw core and the barrel is zero; the other two velocity components are independent of the down-channel coordinate. With these assumptions, the three components of the equation of motion in rectangular coordinates can be reduced to a linear partial differential equation with boundary value conditions:

$$\begin{aligned}
 \frac{\partial p}{\partial z} &= \mu \left(\frac{\partial^2 v_z}{\partial x^2} + \frac{\partial^2 v_z}{\partial y^2} \right) \\
 v_z\{0, y\} &= 0 \\
 v_z\{H, y\} &= V_z \\
 v_z\{x, 0\} &= 0 \\
 v_z\{0, W\} &= 0 \\
 \frac{\partial p}{\partial x} &= \mu \frac{\partial^2 v_x}{\partial x^2} \\
 v_x\{0\} &= 0 \text{ and } v_x\{H\} = V_x
 \end{aligned} \tag{2-1}$$

The velocity profile in a channel having a rectangular cross section has been solved by several authors (Boussinesq, 1868; Rowell and Finlayson, 1922,

1928) and presented in different forms. Meskat (1955) showed that the various solutions are equivalent. The down channel velocity, w , may be expressed by the following Fourier series:

$$\frac{w}{V_z} = \frac{4}{\pi} \sum_{i=1,3,5,\dots}^{\infty} \frac{\sinh(i\pi y/W)}{i \sinh(i\pi H/W)} \sin\left(\frac{i\pi x}{W}\right) - \left(\frac{1}{2\mu} \frac{\partial p}{\partial z} \frac{H^2}{V_z} \right) \left\{ \left(\frac{y}{H} \right)^2 - \frac{y}{H} + \frac{8}{\pi^3} \sum_{i=1,3,5,\dots}^{\infty} \frac{\cosh\left[i\pi \frac{W}{H} \left(\frac{x}{W} - \frac{1}{2} \right) \right]}{i^3 \cosh\left(\frac{i\pi W}{2H} \right)} \sin\left(\frac{i\pi y}{H} \right) \right\} \quad (2-2)$$

Equation (2-2) shows that the solution is composed of two independent terms. The first term on the right hand side is due to the drag that the moving boundary exerts on the fluid in the channel and, accordingly, is termed the "drag flow." The second term is due to the pressure gradient $\partial p/\partial z$ and is called "pressure flow". The pressure gradient is maintained by a restriction at the exit of the screw extruder. If there is no restriction, the pressure flow disappears, and pure drag flow results. This is also called "open discharge" flow.

The solution in the form of two independent terms results from the Newtonian nature of the fluid. A Newtonian fluid gives rise to a linear differential equation. If the fluid is non-Newtonian, the solution is more complicated and it is impossible to speak about drag and pressure flows since the momentum equations become coupled and cannot be solved analytically.

Early attempts to model the behavior of non-Newtonian fluids in the metering section were based on Newtonian fluid concepts using the superposition principle, *i. e.*, the linear addition of drag and pressure flows with an appropriate method of calculating the average apparent viscosity of the non-Newtonian fluid. However, this idealization is inadequate for fluids which depart from Newtonian behavior.

Mori and Matsumoto (1958) and Jacobi (1963) recalculated the pressure flow term by using a "power law" model for the fluid viscosity. Subsequently, they superimposed it on the drag flow and assumed that the error was insignificant. However, Glyde and Holmes-Walker (1962) and later Kroesser and Middleman (1965) showed that the error from this approach might be substantial and, by using this method, the discharge of a pseudoplastic fluid can be greatly overestimated. When calculating the average apparent viscosity, other researchers (Kroesser and Middleman, 1965) considered the positive pressure gradient only. However, in plasticating extruders negative pressure gradients also exist. In these cases, the discharge calculated by superposition is underestimated. The physical reason for the error is that the average apparent viscosity is shear rate dependent. Since the shear rate profile of a pure pressure flow is quite different from the shear rate profile in "combined" pressure and drag flow, merely superimposing the pressure and drag velocity profiles results in a velocity profile which is different from the real profile.

DeHaven (1958) and Yashida *et al.* (1957) chose a special case of the Ellis model to describe the average apparent viscosity of pseudoplastic polymer melts,

$$-\frac{dv_x}{dy} = \frac{\tau}{\mu_0} (1 + c\tau^2) \quad (2-3)$$

Furthermore, they assumed that the fluid flow was equivalent to that between two parallel plates. This assumption may cause some error, but the main disadvantage of DeHaven's method is that the fluid model does not generally fit flow data over a wide experimental range.

The following more general Ellis fluid model in tensor operation form was used by Ram and Narkis (1967) in their studies on plastic extrusion:

$$\tau = \frac{\mu_0}{1 + B \left| \frac{1}{2} \dot{\gamma} : \dot{\gamma} \right|^{(\alpha-1)/2}} \Delta \quad (2-4)$$

The advantage of using this model is that it overcomes the difficulties of the power law model at low shear rates (or stresses) because the model converges, under these conditions, to the Newtonian model. Since the authors only considered positive shear rates, their solution cannot be regarded as complete.

Because of the existence of pressure flow, shear rates are not always positive. Glyde and Holmas-Walker (1962) and Kroesser and Middleman's calculation (1965) demonstrated that the discharge rate, as shown in Figure 2-2, is very different at a positive shear rate condition than under the conditions (depicted in the Figure 2-3) where both positive and negative shear rates exist. The fluid model is based on the power law and the flow is between two infinite parallel plates.

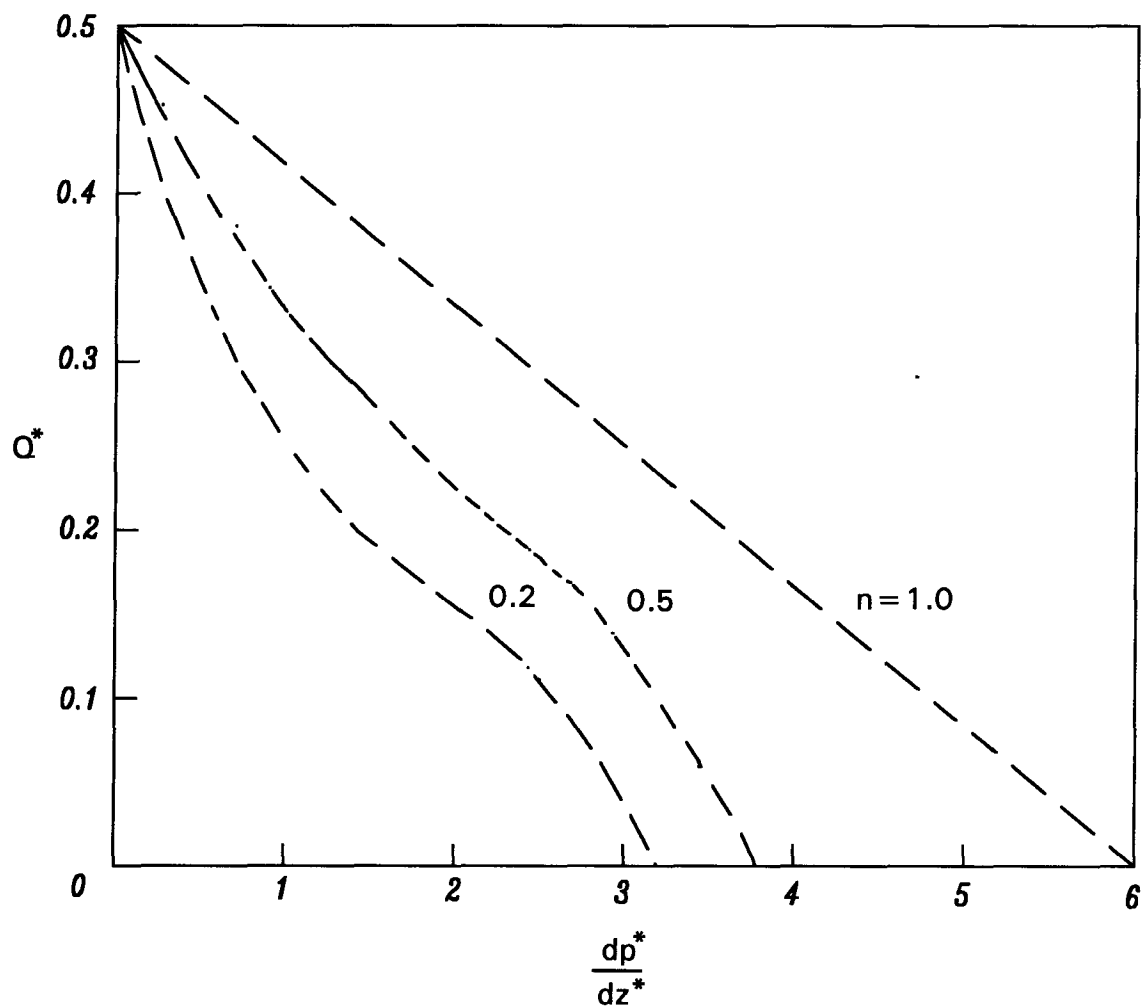
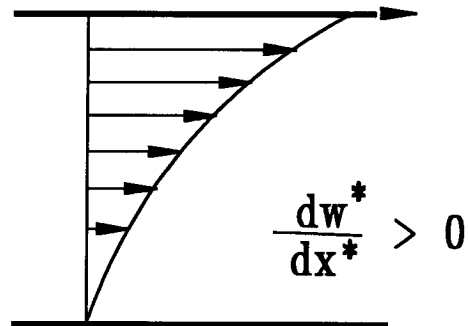


Figure 2-2: Dimensionless discharge rate as a function of down channel dimensionless pressure gradient. The parameter is the flow behavior index, n , in the power law (Kroesser and Middleman, 1965).

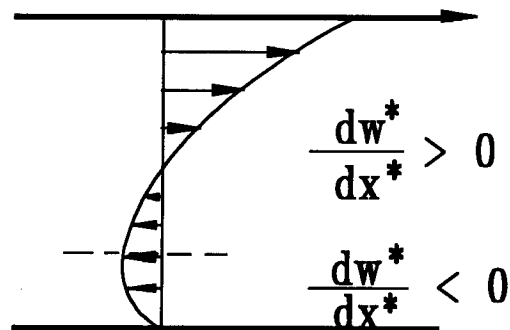
The previously cited studies all focus on one-dimensional flow between two infinite parallel plates. In reality, the direction of the "moving barrel" may cause significant cross channel flow (transverse flow) in the screw channel. This flow affects the extruder discharge indirectly by changing the fluid's apparent viscosity when the fluid in a screw channel is non-Newtonian. Griffith (1962) solved this two-dimensional problem numerically with the aid of a digital computer by assuming that the two velocity components are functions of x (parallel to the flight height) only. A comparison of Griffith's solution with that of Kroesser and Middleman (1965) gives an indication of the importance of the effect of the transverse flow on extruder output (see Figure 2-4).

The effect of flights on the discharge of a non-Newtonian fluid has not yet been discussed. As a first approximation, a shape factor can be used to modify the effect of flight on discharge rate in the case of Newtonian fluids (Booy, 1963). Since for non-Newtonian fluids, one cannot separate drag and pressure flow terms, Tadmor (1970) suggested using an average value for the shape factor. The effect of the non-Newtonian character of the fluid can be estimated by comparing the effect of the flights on the pressure flow of a non-Newtonian fluid in a rectangular duct with that of a Newtonian fluid. A study of power law fluids flowing under laminar conditions in rectangular ducts has been reported by Metzner (1961) and resulted in a correction factor, χ , to modify the extruder discharge rate, *i. e.*,

$$Q = \frac{1}{\chi} \left(\frac{1}{1 + H/W} \right)^{1/n} \left[\frac{1}{2m} \left(- \frac{\partial P}{\partial z} \right) \right]^{1/n} W H^{2+1/n} \quad (2-3)$$



(a)



(b)

Figure 2-3: Dimensionless down channel velocity gradient in channel height direction between parallel plates: (a) shear rate is positive at all points; (b) shear rate is positive above the minimum velocity and negative below it.

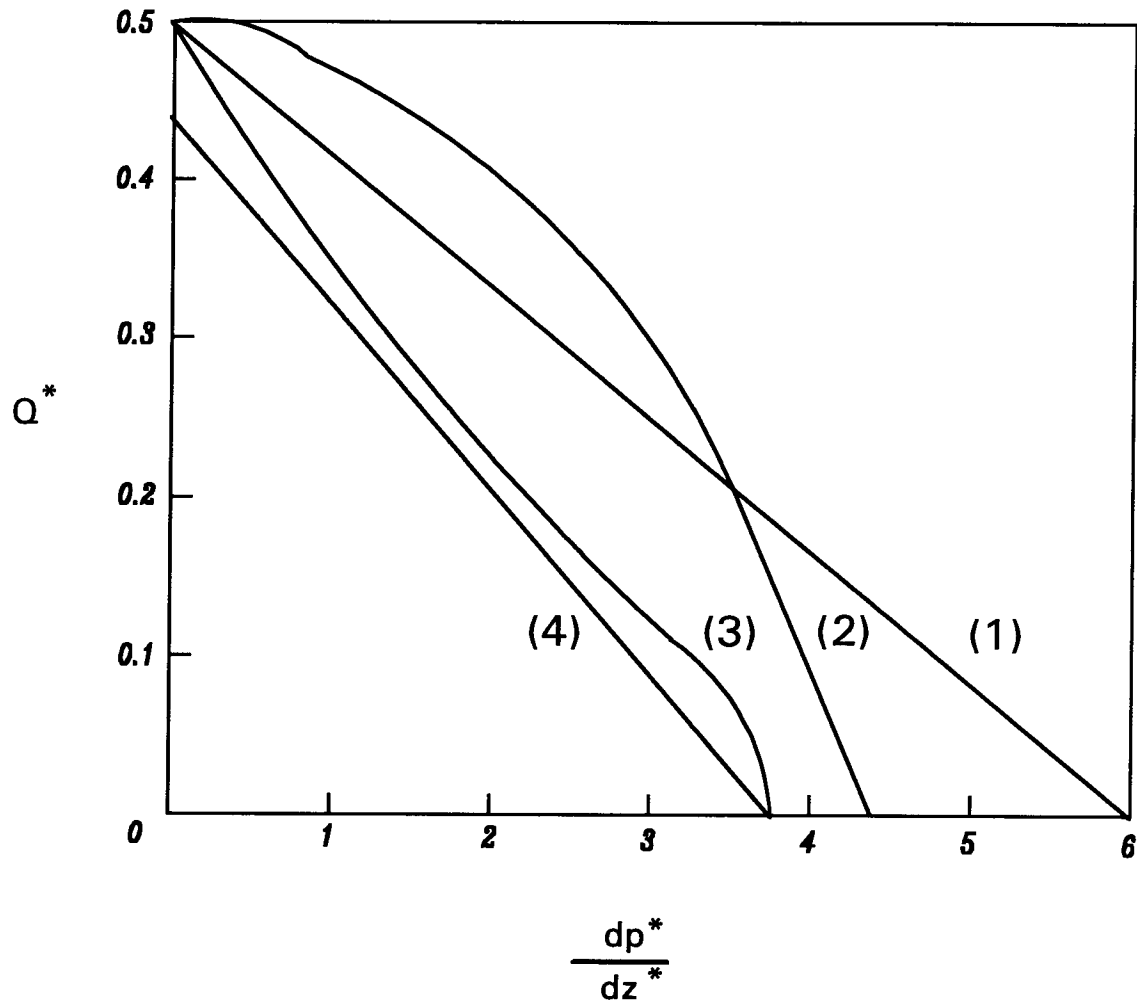


Figure 2-4: Dimensionless discharge rate versus down channel dimensionless pressure gradient calculated according to: (1) superposition of pressure and drag flow for a Newtonian fluid; (2) superposition of pressure and drag flow for a non-Newtonian fluid; (3) combined flow excluding cross channel flow; (4) combined flow including cross channel flow (Kroesser and Middleman, 1965).

The factor χ was found to be a function of the ratio of the flight height and channel width (see Figure 2-5).

Other researchers (Wheeler and Wissler, 1965) related the shape factor to the Fanning friction factor, since the rheological parameters were based on pipe data. In other words, the geometry of the pipe and the pipe conditions affect the extrusion discharge. The relationship between shape factor and ratio of the height of flight and width of channel is illustrated by Figure 2-6.

It should be pointed out that when both pressure and drag flows exist, additional errors may be introduced by using individually derived shape factors. This follows from the nonlinear nature of the partial differential equations describing the motion of non-Newtonian fluids. Middleman (1965) summarized these differences in the plot presented in Figure 2-7.

Besides the effect of flight height on extruder performance, the curvature of the screw should be considered because the fluid does not flow between a pair of parallel plates. To determine the effect of curvature on discharge, McKelvey (1962) suggested a curvature correction factor based on the ratio of discharge rates between concentric cylinders and parallel plates. Booy (1963) introduced cylindrical coordinates and solved the ordinary differential equations analytically. This resulted in a pair of curvature correction factors to modify the drag and pressure flows. The correction factor determined by McKelvey (1962) at zero helix angle converges to Booy's curvature correction factor. Since the correction factors are based on Newtonian fluids, if they are used, the pressure and drag flows have to be calculated first. This cannot be done with non-Newtonian fluids.

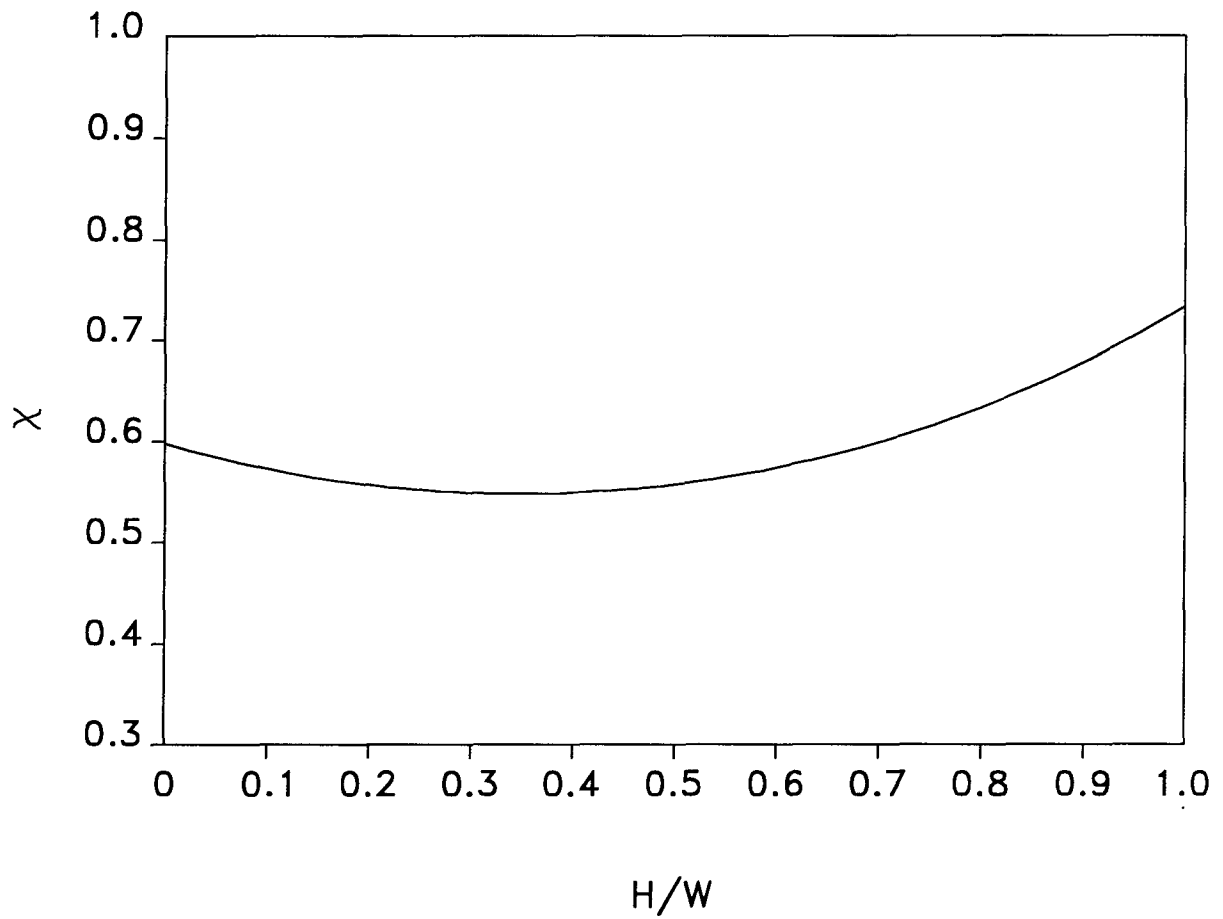


Figure 2-5: Dimensionless correction factor χ versus ratio of flight height to channel width, H/W (Metzner, 1961).

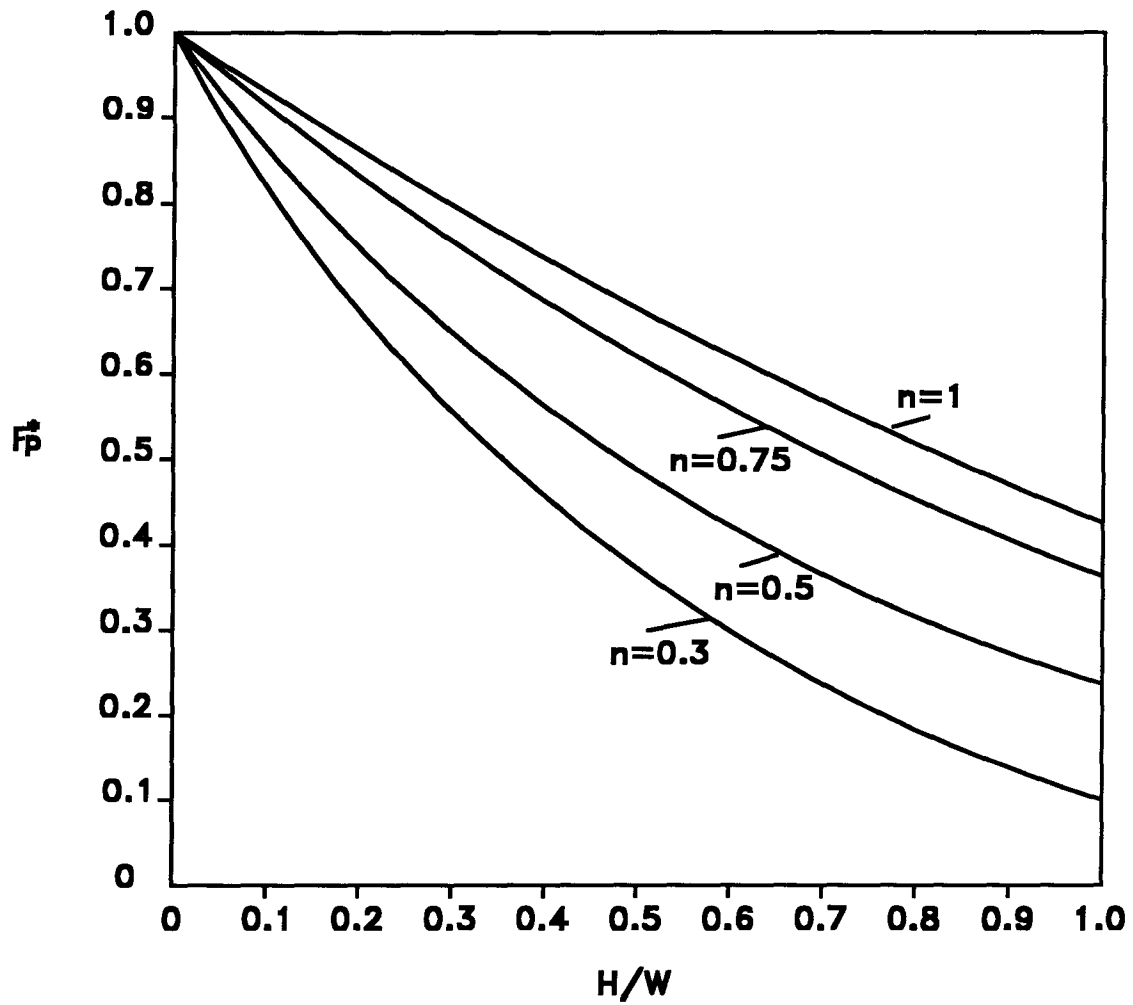


Figure 2-6: Shape correction factor F_p^* as a function of height to width ratio and the flow behavior index n for the power law model (Wheeler and Wissler, 1961; Middleman, 1962).

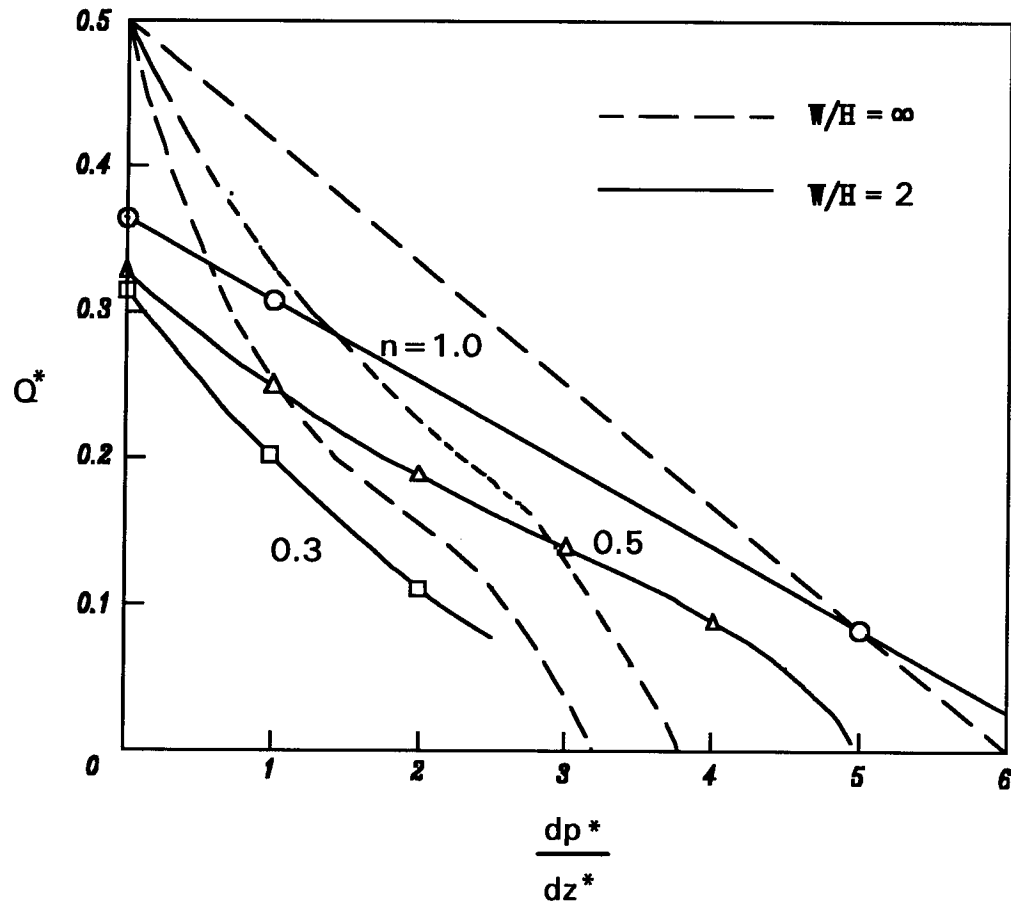


Figure 2-7: Dimensionless discharge rate versus dimensionless pressure gradient for a power law fluid. The combined pressure and drag flows are compared with results from infinite parallel plates and a duct ($H/W=2$) (Middleman, 1965).

This method is, therefore, of less significance when it is applied to non-Newtonian fluids.

When dealing with non-Newtonian fluids, it is difficult to solve the momentum equation for square ducts because they possess less symmetry than round pipes, concentric annuli, or parallel plates. Hence, even for a simple fluid model, one must solve at least one nonlinear partial differential equation which is only possible with the aid of fast computers.

With the help of a modern computer, Martin (1969) solved the problem numerically. He assumed that the non-Newtonian fluid moves in an uncurled rectangular channel and obeys the power law model. He considered three velocity components in a straight rectangular channel and assumed each velocity component as being a function of the coordinates x and y .

Martin's study still has drawbacks in analyzing the flow in single-screw extruders because he neglected the curvature of the channel and flights for deep screw channels. The significance of Martin's study is that it provides some means of quantitatively estimating the effects of the flight walls on the discharge rate by comparing it with the data that can be obtained for very wide channels ($W \rightarrow \infty$). Others, for example Atkinson *et al.* (1970), Kiparissides and Vlachopoulos (1976) and Caswell and Tanner (1978), used finite element methods to solve the same physical model as Martin chose. Choo *et al.* (1981) obtained a numerical solution when curvature effects are taken into account using cylindrical coordinates.

More recently, literature (Gotsis and Kalyon, 1990; Lawal and Kalyon, 1992) on wall slip in single-screw extruders has been published. Researchers (Payne, 1965; Yilmazer *et al.*, 1989 and Gotsis *et al.*, 1990) considered that slippage was inevitable for a highly filled suspension like melt thermoplastics. Therefore, the customary no-slip boundary conditions may not be used in the simulation of flows involving these materials. In fact, they found that slippage-induced flow can become the dominant mode of flow under certain stress levels (Yilmazer and Kalyon, 1989).

2.4 Rheological Properties of Concentrated Fluid Biomaterials

Concentrated fluid biomaterials frequently arise in the food industry and their rheological properties must be known for the accurate design and evaluation of handling and processing equipment.

A majority of these concentrated fluid biomaterials behave with non-Newtonian characteristics. Their feature is that the flow curve (τ_{yx} versus dy/dx) is not linear through the origin at a given temperature and pressure. By analogy to Newtonian fluids, an "apparent viscosity" is customarily defined (Skelland, 1967).

Numerous equations for apparent viscosity, η , of concentrated fluids can be found in the literature. These may be divided into two major categories: theoretical equations and empirical ones (Thomas, 1965). Yet there is no commonly accepted theoretical treatment for concentrated suspensions partly because our knowledge about their properties is very limited. Other reasons are the difficulties of the analysis coupled with a lack of agreement among different

experimental investigations (Thomas, 1965; Lefebvre, 1982). The empirical treatment, therefore, is more widely used in studying the behavior of concentrated biomaterials.

Several papers have been published on empirical models which describe the apparent viscosities or consistency characteristics of biomaterials (Hand *et al.*, 1955; Robinson *et al.*, 1956; Whittenberger and Nutting, 1957, 1958; Smit and Nortje, 1958; Ezell, 1959). However, in the early stages, the viscosities or consistencies reported were the results of single measurements. Although the investigators have generally recognized that single viscosity measurements have only limited value for non-Newtonian fluids, lack of time or suitable instrumentation prevented more complete studies. Harper and Sahrighi (1965) were the first to conduct a thorough investigation into tomato concentrates at different concentrations and temperatures. The results showed that the power-law model is adequate to describe tomato concentrates up to 30%.

Gill and Tung (1976) found a power-law model with a yield stress term which can be used to describe rape seed protein dispersions and soybean protein gels at different concentrations and temperatures. More recently, Speer and Tung (1986) studied the flow behavior of xanthan gum dispersions with the aid of power-law model. They described the experimental results as:

$$\ln\{\eta\} = \ln\{396 C^{1.22} e^{668/T}\} - 0.642 \ln \dot{\gamma} \quad (2-4)$$

According to Equation (2-4), the logarithm of the apparent viscosity varies linearly with the logarithm of the shear rate. However, their experimental results

showed that the slope varied with concentration. Therefore, the index of the concentration term cannot be constant.

Canola paste is a typical biomaterial, but no reports are available on its rheological behavior.

PAGINATION ERROR.

ERREUR DE PAGINATION.

TEXT COMPLETE.

LE TEXTE EST COMPLET.

NATIONAL LIBRARY OF CANADA.

BIBLIOTHEQUE NATIONALE DU CANADA.

CANADIAN THESES SERVICE.

SERVICE DES THESES CANADIENNES.

CHAPTER THREE

MATHEMATICAL MODEL FOR A SINGLE-SCREW EXTRUDER

3.1 Mathematical Model of the Fully Developed Flow in a Single-screw Extruder

3.1.1 Flow Equations and Boundary Conditions

An enlarged section of a right-handed, single-screw extruder is shown in Figure 3-1. D is the screw diameter, H the channel depth, W and e the channel and flight widths, respectively (measured perpendicular to the flight surface), l_e is the length of the flight pitch and θ is the helix angle (measured at the flight tips). The number of channels in parallel, or number of 'starts' to the screw, is denoted by i (in Figure 3-1 $i=2$). The screw is assumed to rotate at N revolutions per unit time.

The first step towards the analysis of viscous flow in a single-screw extruder is to set up a mathematical model to describe the flow. Martin's (1969) three velocity component model is used as the basis for the present mathematical model. The following assumptions are made:

1. The sides of the flights are perpendicular to the screw axis.

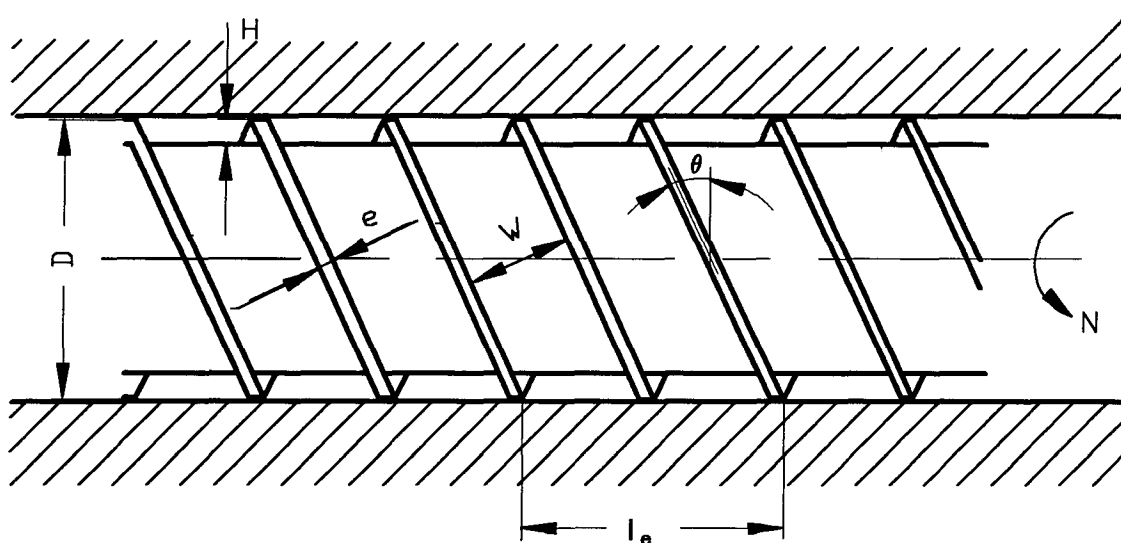


Figure 3-1: Schematic representation of an extruder section (two channels in parallel).

2. Due to the high viscosity of the paste, the fluid velocity is very low.
3. Body forces (e. g., gravity) are negligible in comparison with viscous and pressure forces.
4. Inertial forces are negligible because of the low speeds.
5. The channel may be unrolled, the length of unrolled channel is based on the top diameter of flight and treated as rectilinear and Cartesian coordinates are used.
6. The Canola paste is considered as incompressible and the density of the extrudate is constant.
7. The flow is steady and fully developed.
8. Slip occurs between the barrel metal surfaces and the paste.

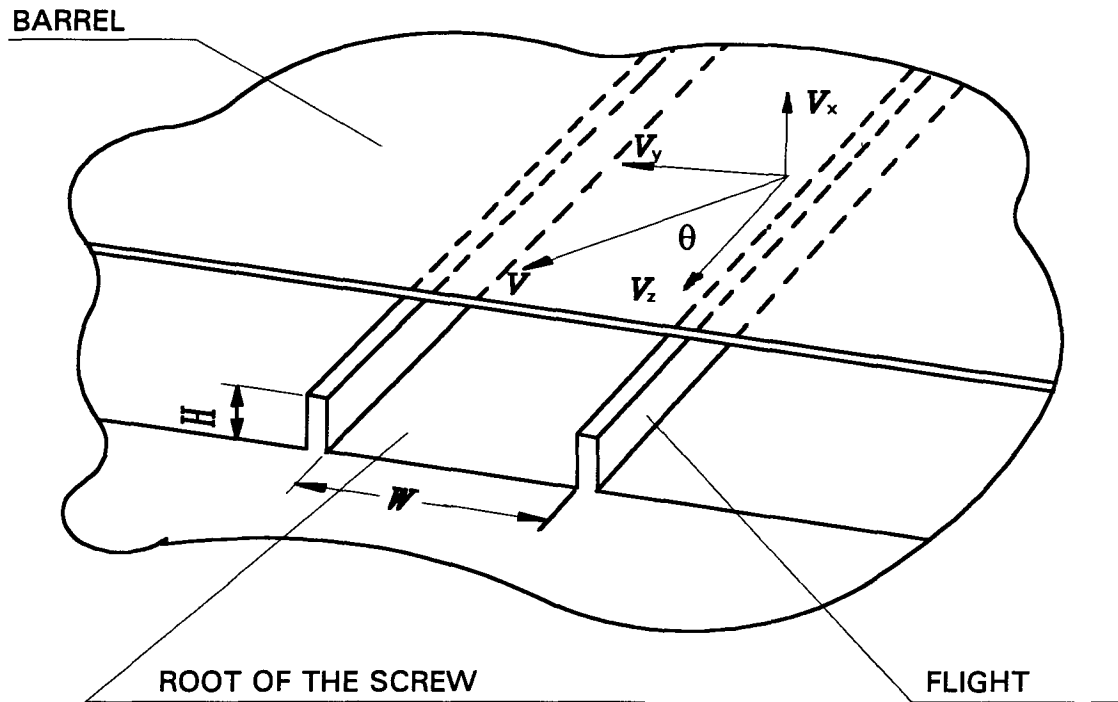


Figure 3-2: Geometry of the uncurled screw channel.

9. The limited yield stress of Canola paste may be ignored.

If the channel is uncurled, the Canola paste can be considered to flow in a rectangular channel with the coordinates shown in Figure 3-2. For the sake of convenience, the top side of the channel is regarded as moving and the other three sides are stationary. The paste is therefore dragged by the force originating from the top.

The general equations of motion governing a flow in a rectangular channel are:

$$\rho \left(\frac{\partial v_x}{\partial t} + v_x \frac{\partial v_x}{\partial x} + v_y \frac{\partial v_x}{\partial y} + v_z \frac{\partial v_x}{\partial z} \right) = -\frac{\partial p}{\partial x} - \left(\frac{\partial \tau_{xx}}{\partial x} + \frac{\partial \tau_{yx}}{\partial y} + \frac{\partial \tau_{zx}}{\partial z} \right) + \rho g_x \quad (3-1)$$

$$\rho \left(\frac{\partial v_y}{\partial t} + v_x \frac{\partial v_y}{\partial x} + v_y \frac{\partial v_y}{\partial y} + v_z \frac{\partial v_y}{\partial z} \right) = -\frac{\partial p}{\partial y} - \left(\frac{\partial \tau_{xy}}{\partial x} + \frac{\partial \tau_{yy}}{\partial y} + \frac{\partial \tau_{zy}}{\partial z} \right) + \rho g_y \quad (3-2)$$

$$\rho \left(\frac{\partial v_z}{\partial t} + v_x \frac{\partial v_z}{\partial x} + v_y \frac{\partial v_z}{\partial y} + v_z \frac{\partial v_z}{\partial z} \right) = -\frac{\partial p}{\partial z} - \left(\frac{\partial \tau_{xz}}{\partial x} + \frac{\partial \tau_{yz}}{\partial y} + \frac{\partial \tau_{zz}}{\partial z} \right) + \rho g_z \quad (3-3)$$

The first subscript of τ indicates the direction normal to the direction of the applied force. The second subscript of τ denotes the direction of the force. According to the previous assumptions, the momentum equations reduce to:

$$\frac{\partial p}{\partial x} = - \left(\frac{\partial \tau_{xx}}{\partial x} + \frac{\partial \tau_{yx}}{\partial y} + \frac{\partial \tau_{zx}}{\partial z} \right) \quad (3-4)$$

$$\frac{\partial p}{\partial y} = - \left(\frac{\partial \tau_{xy}}{\partial x} + \frac{\partial \tau_{yy}}{\partial y} + \frac{\partial \tau_{zy}}{\partial z} \right) \quad (3-5)$$

$$\frac{\partial p}{\partial z} = - \left(\frac{\partial \tau_{xz}}{\partial x} + \frac{\partial \tau_{yz}}{\partial y} + \frac{\partial \tau_{zz}}{\partial z} \right) \quad (3-6)$$

For non-Newtonian fluid flow, the relationship between the shear stresses and the velocity gradients are given by (M. M. Denn, 1980):

$$\tau_{yx} = \tau_{xy} = \tau_0 - \eta \left(\frac{\partial v_x}{\partial y} + \frac{\partial v_y}{\partial x} \right) \quad (3-7)$$

$$\tau_{yz} = \tau_{zy} = \tau_0 - \eta \left(\frac{\partial v_z}{\partial y} + \frac{\partial v_y}{\partial z} \right) \quad (3-8)$$

$$\tau_{zx} = \tau_{xz} = \tau_0 - \eta \left(\frac{\partial v_x}{\partial z} + \frac{\partial v_z}{\partial x} \right) \quad (3-9)$$

Equations (3-8) and (3-9) can be further simplified because the velocity components do not depend on z , *i. e.*:

$$\tau_{yz} = \tau_{zy} = \tau_0 - \eta \left(\frac{\partial v_z}{\partial y} \right) \quad (3-10)$$

$$\tau_{zx} = \tau_{xz} = \tau_0 - \eta \left(\frac{\partial v_z}{\partial x} \right) \quad (3-11)$$

Canola pastes exhibit viscoplasticity, *i. e.*, they possess a limited yield stress below which they experience little or no deformation and hence flow in a plug-like manner. Since the yield stress is constant, the yield stress is eliminated when Equations (3-7) to (3-9) are incorporated into Equations (3-4) to (3-6). In solving the equations, the yield stress may be ignored without causing significant errors as shown in Appendix A.2.

The normal stresses caused by viscosity are very small compared with the absolute pressure (Denn, 1980), *i. e.*:

$$\tau_{xx} = 2\eta \frac{\partial v_x}{\partial x} \approx 0 \quad (3-12)$$

$$\tau_{yy} = 2\eta \frac{\partial v_y}{\partial y} \approx 0 \quad (3-13)$$

$$\tau_{zz} = 2\eta \frac{\partial v_z}{\partial z} \approx 0 \quad (3-14)$$

Substituting Equations (3-7) and (3-10) to (3-14) into Equations (3-4) to (3-6) yields:

$$\frac{\partial p}{\partial x} = 2\frac{\partial}{\partial x}\left(\eta \frac{\partial v_x}{\partial x}\right) + \frac{\partial}{\partial y}\left(\eta \frac{\partial v_x}{\partial y} + \eta \frac{\partial v_y}{\partial x}\right) \quad (3-15)$$

$$\frac{\partial p}{\partial y} = \frac{\partial}{\partial x}\left(\eta \frac{\partial v_x}{\partial y} + \eta \frac{\partial v_y}{\partial x}\right) + 2\frac{\partial}{\partial y}\left(\eta \frac{\partial v_y}{\partial y}\right) \quad (3-16)$$

$$\frac{\partial p}{\partial z} = \frac{\partial}{\partial x}\left(\eta \frac{\partial v_z}{\partial x}\right) + \frac{\partial}{\partial y}\left(\eta \frac{\partial v_z}{\partial y}\right) \quad (3-17)$$

There are four variables in the three equations, Equations (3-15) to (3-17), and the continuity equation must therefore also be used.

Equations (3-15) to (3-17) are solved in a rectangular domain with impermeable boundaries. Three of its boundaries are stationary and one is moving as shown in Figure 3-3. The boundary conditions of the equations are:

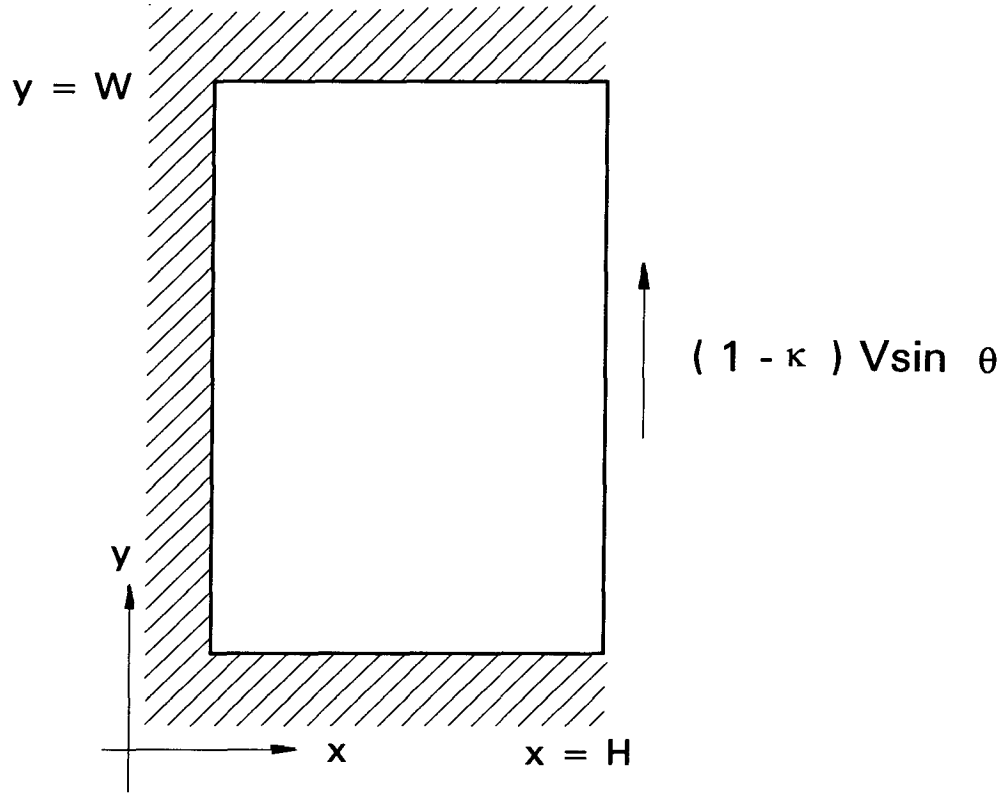


Figure 3-3: Flow domain.

$$\left. \begin{array}{l} v_x = 0 \\ v_y = 0 \\ v_z = 0 \end{array} \right\} \text{ at } x = 0 \text{ for } 0 \leq y \leq W \quad (3-18)$$

$$\left. \begin{array}{l} v_x = 0 \\ v_y = (1 - \kappa)V \sin \theta \\ v_z = (1 - \kappa)V \cos \theta \end{array} \right\} \text{ at } x = H \text{ for } 0 \leq y \leq W \quad (3-19)$$

$$\left. \begin{array}{l} v_x = 0 \\ v_y = 0 \\ v_z = 0 \end{array} \right\} \text{ at } y = 0, y = W \text{ for } 0 \leq x \leq H \quad (3-20)$$

$$p = p_o \quad \text{at} \quad z = 0 \quad (3-21)$$

where $V = \pi DN$ is the linear rotation speed and κ is the slip factor according to the assumption 8. The physical definition of the κ factor is that the paste velocity at the boundary is $(1 - \kappa)$ less than the "barrel speed."

It is reported (Gotsis *et. al.*, 1990; Lawal *et. al.*, 1992) that the slip factor is zero at the screw root surface and a maximum at the barrel surface. The slip factors at the flight surfaces are very small compared with the slip factor at the barrel surface. Therefore, it was decided, in the present model, to neglect slip at the screw flight and root surfaces.

Unlike the case for Newtonian fluids, the apparent viscosity, η , is regarded as a function of the velocity gradients, *i. e.*:

$$\begin{aligned} \eta &= m \left\{ 2 \left[\left(\frac{\partial v_x}{\partial x} \right)^2 + \left(\frac{\partial v_y}{\partial y} \right)^2 + \left(\frac{\partial v_z}{\partial z} \right)^2 \right] + \right. \\ &\quad \left. + \left(\frac{\partial v_y}{\partial x} + \frac{\partial v_x}{\partial y} \right)^2 + \left(\frac{\partial v_z}{\partial y} + \frac{\partial v_y}{\partial z} \right)^2 + \left(\frac{\partial v_z}{\partial z} + \frac{\partial v_x}{\partial x} \right)^2 \right\}^{\frac{(n-1)}{2}} \\ &= m \left\{ 2 \left[\left(\frac{\partial v_x}{\partial x} \right)^2 + \left(\frac{\partial v_y}{\partial y} \right)^2 \right] \left(\frac{\partial v_y}{\partial x} + \frac{\partial v_x}{\partial y} \right)^2 \left(\frac{\partial v_z}{\partial y} \right)^2 \left(\frac{\partial v_z}{\partial y} \right)^2 \right\}^{\frac{(n-1)}{2}} \quad (3-22) \end{aligned}$$

The coefficients m and n depend on the temperature and concentration of the paste and have to be determined experimentally.

3.1.2 Dimensionless Equations and Boundary Conditions

Equations (3-15) to (3-17) can be recast in dimensionless forms by defining:

$$x^* = \frac{x}{H}, \quad y^* = \frac{y}{H}, \quad z^* = \frac{z}{H}$$

$$u^* = \frac{v_x}{V}, \quad v^* = \frac{v_y}{V}, \quad w^* = \frac{v_z}{V}$$

$$p^* = \frac{p H^n}{m V^n}$$

$$\eta^* = \frac{\eta H^{n-1}}{m V^{n-1}}$$

Multiplying both sides of Equations (3-15) to (3-17) and the continuity equation by $\frac{H^{n+1}}{m V^n}$ gives the dimensionless equations for fully developed steady state flow in a single-screw extruder:

$$\frac{\partial p^*}{\partial x^*} = 2 \frac{\partial}{\partial x^*} \left(\eta^* \frac{\partial u^*}{\partial x^*} \right) + \frac{\partial}{\partial y^*} \left(\eta^* \frac{\partial u^*}{\partial y^*} + \eta^* \frac{\partial v^*}{\partial x^*} \right) \quad (3-23)$$

$$\frac{\partial p^*}{\partial y^*} = 2 \frac{\partial}{\partial x^*} \left(\eta^* \frac{\partial u^*}{\partial y^*} + \eta^* \frac{\partial v^*}{\partial x^*} \right) + 2 \frac{\partial}{\partial y^*} \left(\eta^* \frac{\partial u^*}{\partial y^*} \right) \quad (3-24)$$

$$\frac{\partial p^*}{\partial z^*} = 2 \frac{\partial}{\partial x^*} \left(\eta^* \frac{\partial w^*}{\partial x^*} \right) + \frac{\partial}{\partial y^*} \left(\eta^* \frac{\partial w^*}{\partial y^*} \right) \quad (3-25)$$

$$0 = \frac{\partial u^*}{\partial x^*} + \frac{\partial v^*}{\partial y^*} \quad (3-26)$$

and

$$\eta^* = \left\{ 2 \left[\left(\frac{\partial u^*}{\partial x^*} \right)^2 + \left(\frac{\partial v^*}{\partial y^*} \right)^2 \right] + \left(\frac{\partial v^*}{\partial x^*} + \frac{\partial u^*}{\partial y^*} \right)^2 + \left(\frac{\partial w^*}{\partial x^*} \right)^2 + \left(\frac{\partial w^*}{\partial y^*} \right)^2 \right\}^{\frac{n-1}{2}} \quad (3-27)$$

In dimensionless form, the notation in Figure 3-3 for the flow domain then becomes that shown in Figure 3-4.

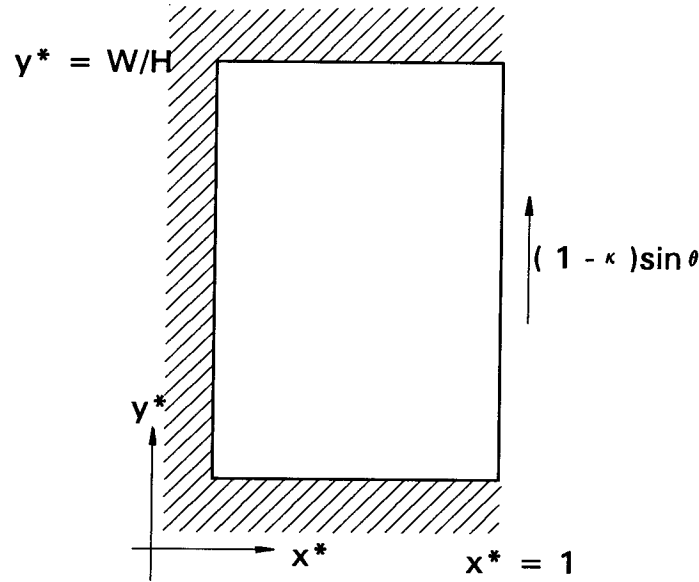


Figure 3-4: Flow domain in dimensionless form.

The boundary conditions are:

$$\left. \begin{array}{l} u^* = 0 \\ v^* = 0 \\ w^* = 0 \end{array} \right\} \text{ at } x^* = 0 \text{ for } 0 \leq y^* \leq W/H \quad (3-28)$$

$$\left. \begin{array}{l} u^* = 0 \\ v^* = (1 - \kappa) \sin \theta \\ w^* = (1 - \kappa) \cos \theta \end{array} \right\} \text{ at } x^* = 1 \text{ for } 0 \leq y^* \leq W/H \quad (3-29)$$

$$\left. \begin{array}{l} u^* = 0 \\ v^* = 0 \\ w^* = 0 \end{array} \right\} \text{ at } y^* = 0, y^* = W/H \text{ for } 0 \leq x^* \leq 1 \quad (3-30)$$

$$p^* = p_0^* \text{ at } z^* = 0 \quad (3-31)$$

The advantage of the dimensionless equations is that the results can be more concisely presented and extruders with similar geometry can be designed without reference to their absolute dimensions.

For convenience, the superscript stars are omitted from the formulas in all subsequent discussion.

3.1.3 Transverse Flow Equations

Introducing the stream function defined by:

$$u = -\frac{\partial \psi}{\partial y}, \quad v = \frac{\partial \psi}{\partial x} \quad (3-32)$$

the velocity components can then be eliminated from Equations (3-23) to (3-24) yielding (see Appendix A.1 for details):

$$\begin{aligned}
\eta \nabla^4 \psi &= \left(\frac{\partial^2 \psi}{\partial y^2} - \frac{\partial^2 \psi}{\partial x^2} \right) \left(\frac{\partial^2 \eta}{\partial x^2} - \frac{\partial^2 \eta}{\partial y^2} \right) - 4 \frac{\partial^2 \eta}{\partial x^2} \frac{\partial^2 \eta}{\partial y^2} - \\
&\quad - 2 \frac{\partial \eta}{\partial x} \left(\frac{\partial^3 \psi}{\partial x \partial y^2} + \frac{\partial^3 \psi}{\partial x^3} \right) - 2 \frac{\partial \eta}{\partial y} \left(\frac{\partial^3 \psi}{\partial y \partial x^2} + \frac{\partial^3 \psi}{\partial y^3} \right) \\
&= F\{x, y\}
\end{aligned} \tag{3-33}$$

where ∇^4 denotes the biharmonic operator defined by:

$$\nabla^4 = \frac{\partial^4}{\partial x^4} + 2 \frac{\partial^4}{\partial x^2 \partial y^2} + \frac{\partial^4}{\partial y^4} \tag{3-34}$$

The right-hand-side of Equation (3-33) can be further simplified by introducing the vorticity function, Ω , i. e.:

$$\frac{\partial^2 \psi}{\partial x \partial y^2} + \frac{\partial^3 \psi}{\partial x^3} = \frac{\partial}{\partial x} \left(\frac{\partial^2 \psi}{\partial x^2} + \frac{\partial^2 \psi}{\partial y^2} \right) = - \frac{\partial \Omega}{\partial x} \tag{3-35}$$

$$\frac{\partial^2 \psi}{\partial y \partial x^2} + \frac{\partial^3 \psi}{\partial y^3} = \frac{\partial}{\partial y} \left(\frac{\partial^2 \psi}{\partial x^2} + \frac{\partial^2 \psi}{\partial y^2} \right) = - \frac{\partial \Omega}{\partial y} \tag{3-36}$$

Substitution of Equations (3-35) and (3-36) into Equation (3-33) enables the equations to be written as:

$$\nabla^2 \Omega = -F\{x, y\}/\eta \quad (3-37)$$

It is interesting to note that even when the fluid is Newtonian, Equation (3-37) is complex because the fluid viscosity is temperature dependent.

The complexity and high differential order of Equation (3-33) make solving the equation very difficult. Martin (1969) suggested using the following pair of reduced equations to replace equations (3-33):

$$\begin{aligned} \nabla^2(\eta \Omega) &= -2 \left(\frac{\partial^2 \eta}{\partial y^2} \frac{\partial^2 \psi}{\partial x^2} - 2 \frac{\partial^2 \eta}{\partial x \partial y} \frac{\partial^2 \psi}{\partial x \partial y} + \frac{\partial^2 \eta}{\partial x^2} \frac{\partial^2 \psi}{\partial y^2} \right) \\ &= f\{\psi\} \end{aligned} \quad (3-38)$$

and

$$\eta \nabla^2 \psi = -(\eta \Omega) \quad (3-39)$$

The combined variable $\eta\Omega$ is regarded as a single variable and η cannot be canceled from Equation (3-39). For convenience, the right-hand-side of Equation (3-38) is denoted by $G\{x, y\}$ and the function $\eta\Omega$ is replaced by ξ . The Poisson Equations (3-38) and (3-39) then become by:

$$\eta \nabla^2 \psi = -\xi \quad (3-40)$$

$$\nabla^2 \xi = -2G \quad (3-41)$$

The boundary conditions for Equations (3-40) and (3-41) and their determination will be discussed in detail in next section.

To the author's knowledge, no analytical solutions are available for Equations

(3-40) and (3-41). The only practical way of solving the equations are by numerical methods. A finite difference method was adopted in this thesis to solve the equations of fluid flow. The reduced Equations (3-40) and (3-41) much be solved simultaneously and therefore iteratively since the solution of Equation (3-40) is needed to compute the right-hand-side of Equation (3-41), whereas the right-hand-side of Equation (3-40) depends on ξ .

3.2 Discretization of Flow Equations and Boundary Conditions

For points in the interior of the domain indicated by Figure 3-5, the Poisson Equations (3-40) and (3-41) are approximated by a second-order central difference expression which provides a second order truncation error:

$$\begin{aligned}\nabla^2 \psi &= \frac{\psi_{i+1,j} - 2\psi_{i,j} + \psi_{i-1,j}}{\Delta x^2} + \frac{\psi_{i,j+1} - 2\psi_{i,j} + \psi_{i,j-1}}{\Delta y^2} \\ &\quad + O(\Delta x^2) + O(\Delta y^2) \\ &= -\frac{\xi_{i,j}}{\eta_{i,j}}\end{aligned}\tag{3-42}$$

$$\begin{aligned}\nabla^2 \xi &= \frac{\xi_{i+1,j} - 2\xi_{i,j} + \xi_{i-1,j}}{\Delta x^2} + \frac{\xi_{i,j+1} - 2\xi_{i,j} + \xi_{i,j-1}}{\Delta y^2} \\ &\quad + O(\Delta x^2) + O(\Delta y^2) \\ &= 2G_{i,j}\end{aligned}\tag{3-43}$$

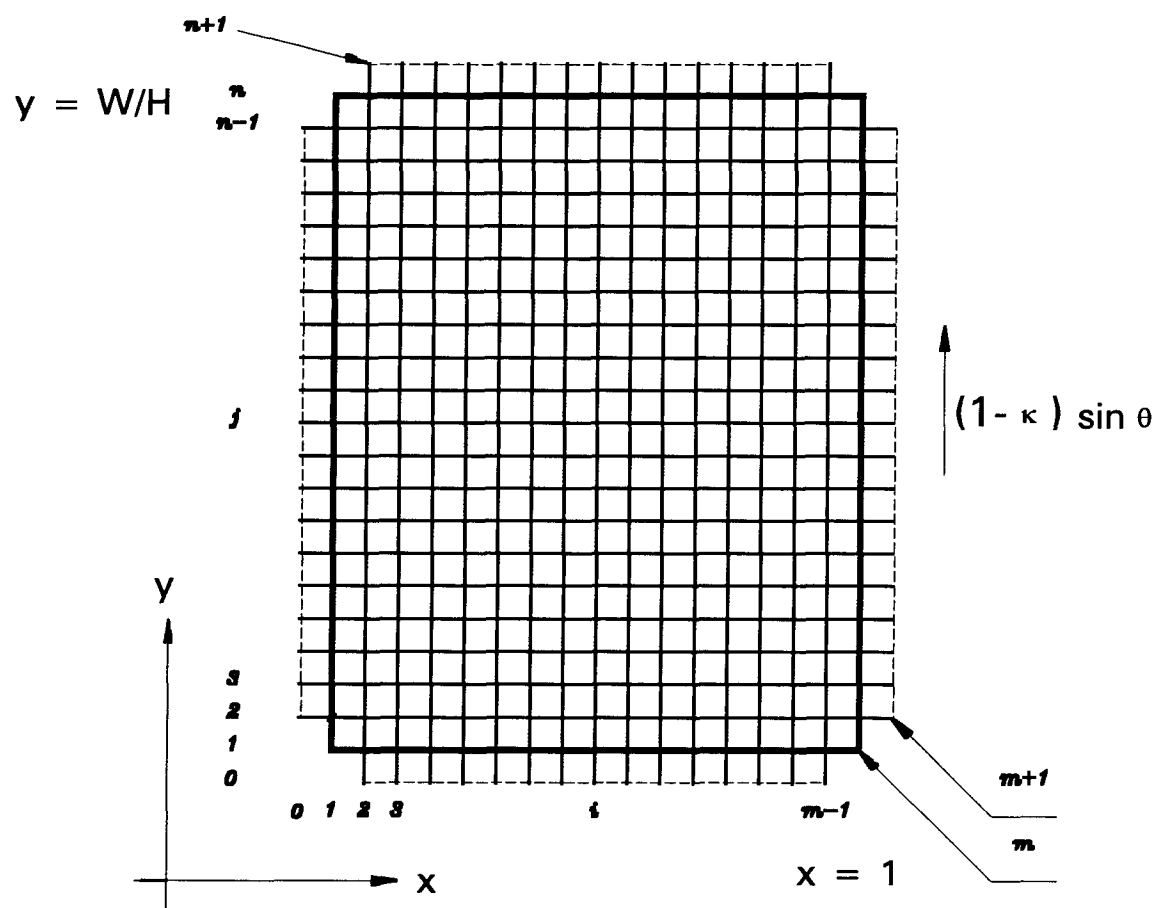


Figure 3-5: Notation for lattice points.

For the interior points, the dimensionless apparent viscosity is calculated from:

$$\eta_{i,j} = \left\{ 4 \left(\frac{\partial^2 \psi}{\partial x \partial y} \right)^2 + \left(\frac{\partial^2 \psi}{\partial y^2} - \frac{\partial^2 \psi}{\partial x^2} \right)^2 + \left(\frac{\partial w}{\partial x} \right)^2 + \left(\frac{\partial w}{\partial y} \right)^2 \right\}^{\frac{n-1}{2}} \quad (3-44)$$

where central difference expressions are used to describe the first derivatives of the down channel velocity w with respect to x and y ; this also gives a second order truncation error.

The right-hand-side of Equation (3-41) is therefore approximated by:

$$\begin{aligned} & -2 \left[\frac{\eta_{i,j+1} - 2\eta_{i,j} + \eta_{i,j-1}}{\Delta y^2} \frac{\psi_{i+1,j} - 2\psi_{i,j} + \psi_{i-1,j}}{\Delta x^2} \right] \\ & + 4 \left[\frac{\eta_{i+1,j+1} - \eta_{i-1,j+1} - \eta_{i+1,j-1} + \eta_{i-1,j-1}}{4\Delta y \Delta x} \frac{\psi_{i+1,j+1} - \psi_{i-1,j+1} - \psi_{i+1,j-1} + \psi_{i-1,j-1}}{4\Delta y \Delta x} \right] \quad (3-45) \\ & -2 \left[\frac{\eta_{i+1,j} - 2\eta_{i,j} + \eta_{i-1,j}}{\Delta x^2} \frac{\psi_{i,j+1} - 2\psi_{i,j} + \psi_{i,j-1}}{\Delta y^2} \right] + O(\Delta x^2) + O(\Delta y^2) \end{aligned}$$

Since all walls coincide with streamlines and are impermeable, any constant value may be selected for the stream function ψ there. The conventional choice is $\psi = 0$ at the walls (Roache, 1972), *i. e.*:

$$\begin{aligned}
\eta \nabla^2 \psi &= -(\xi) \\
\psi \{0, y\} &= 0 \\
\psi \{x, 0\} &= 0 \\
\psi \left\{x, \frac{W}{H}\right\} &= 0 \\
\psi \{1, y\} &= 0
\end{aligned} \tag{3-46}$$

The boundary conditions for Equation (3-41) can be calculated using the results of Equation (3-42) because both the apparent viscosity and vorticity may be expressed in terms of ψ .

From the known velocities at the walls, the stream function values adjacent to the wall are obtained by:

at $x = 0$

$$\begin{aligned}
v &= \frac{\partial \psi}{\partial x} \\
&= \frac{\psi_{2,j} - \psi_{0,j}}{2\Delta x} + O(\Delta x^2) \\
&= 0
\end{aligned} \tag{3-47}$$

thus

$$\psi_{0,j} \approx \psi_{2,j} \tag{3-47a}$$

at $x = 1$

$$\begin{aligned}
v &= \frac{\partial \psi}{\partial x} \\
&= \frac{\psi_{m+1,j} - \psi_{m-1,j}}{2\Delta x} + O(\Delta x^2) \\
&= (1 - \kappa) \sin \theta
\end{aligned} \tag{3-48}$$

thus

$$\psi_{m+1,j} \approx \psi_{m,j} + 2\Delta x (1 - \kappa) \sin\theta \quad (3-48a)$$

at $y = 0$

$$\begin{aligned} u &= -\frac{\partial \psi}{\partial y} \\ &= -\frac{\psi_{i,2} - \psi_{i,0}}{2\Delta y} + O(\Delta y^2) \\ &= 0 \end{aligned} \quad (3-49)$$

thus

$$\psi_{i,0} \approx \psi_{i,2} \quad (3-49a)$$

at $y = W/H$

$$\begin{aligned} u &= -\frac{\partial \psi}{\partial y} \\ &= -\frac{\psi_{i,n+1} - \psi_{i,n-1}}{2\Delta y} + O(\Delta y^2) \\ &= 0 \end{aligned} \quad (3-50)$$

thus

$$\psi_{i,n+1} \approx \psi_{i,n-1} \quad (3-50a)$$

The vorticity values at the boundary are then given by:

at $x = 0$

$$\begin{aligned} \Omega_{1,j} &= -\left(\frac{\psi_{2,j} - 2\psi_{1,j} + \psi_{0,j}}{\Delta x^2} + \frac{\psi_{1,j+1} - 2\psi_{1,j} + \psi_{1,j-1}}{\Delta y^2} \right) \\ &\quad + O(\Delta x^2) + O(\Delta y^2) \\ &\approx -\frac{2\psi_{2,j}}{\Delta x^2} \end{aligned} \quad (3-51)$$

at $x = 1$

$$\begin{aligned}\Omega_{m,j} &= - \left(\frac{\psi_{m+1,j} - 2\psi_{m,j} + \psi_{m-1,j}}{\Delta x^2} + \frac{\psi_{m,j+1} - 2\psi_{m,j} + \psi_{m,j-1}}{\Delta y^2} \right) \\ &\quad + O(\Delta x^2) + O(\Delta y^2) \\ &\approx -2 \frac{\psi_{m-1,j} + \Delta x (1 - \kappa) \sin \theta}{\Delta x^2}\end{aligned}\quad (3-52)$$

at $y = 0$

$$\begin{aligned}\Omega_{i,1} &= - \left(\frac{\psi_{2,j} - 2\psi_{1,j} + \psi_{0,j}}{\Delta x^2} + \frac{\psi_{1,j+1} - 2\psi_{1,j} + \psi_{1,j-1}}{\Delta y^2} \right) \\ &\quad + O(\Delta x^2) + O(\Delta y^2) \\ &\approx - \frac{2\psi_{i,2}}{\Delta y^2}\end{aligned}\quad (3-53)$$

at $y = W/H$

$$\begin{aligned}\Omega_{i,n} &= - \left(\frac{\psi_{i+1,n} - 2\psi_{i,n} + \psi_{i-1,n}}{\Delta x^2} + \frac{\psi_{i,n+1} - 2\psi_{i,n} + \psi_{i,n-1}}{\Delta y^2} \right) \\ &\quad + O(\Delta x^2) + O(\Delta y^2) \\ &\approx - \frac{2\psi_{i,n-1}}{\Delta y^2}\end{aligned}\quad (3-54)$$

For the points on the stationary wall, forward and backward difference expressions were chosen (White, 1974) to approximate the down channel velocity gradients (see Figure 3-6 for subscript notations) with second order truncation error:

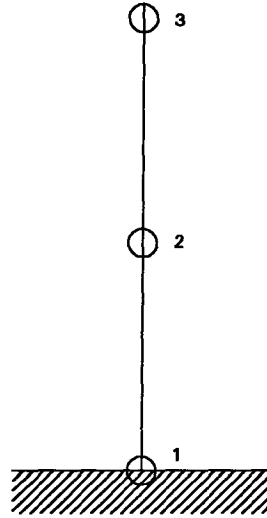


Figure 3-6: Notation used for calculating one sided derivatives.

$$\frac{df}{dx} = -\frac{3f_1 - 4f_2 + f_3}{2\Delta x} + O(\Delta x^2) \quad (3-55)$$

The dimensionless apparent viscosities, η , at the boundaries are therefore given by:

at $x = 0$

$$\eta_{1,j} = \left[\left(\frac{2\psi_{2,j}}{\Delta x^2} \right)^2 \left(\frac{3w_{1,j} - 4w_{2,j} + w_{3,j}}{2\Delta x} \right)^2 \right]^{\frac{n-1}{2}} + O(\Delta x^2) \quad (3-56)$$

at $x = 1$

$$\eta_{m,j} = \left[\left(\frac{2(\Delta x \sin \theta - \psi_{m-1,j})}{\Delta x^2} \right)^2 + \left(\frac{3w_{m,j} - 4w_{m-1,j} + w_{m-2,j}}{2\Delta x} \right)^2 \right]^{\frac{n+1}{2}} + O(\Delta x^2) \quad (3-57)$$

at $y = 0$

$$\eta_{i,1} = \left[\left(\frac{2\psi_{i,2}}{\Delta y^2} \right)^2 + \left(\frac{3w_{i,1} - 4w_{i,2} + w_{i,3}}{2\Delta y} \right)^2 \right]^{\frac{n+1}{2}} + O(\Delta y^2) \quad (3-58)$$

at $y = W/H$

$$\eta_{i,n} = \left[\left(\frac{2\psi_{i,n-1}}{\Delta y^2} \right)^2 + \left(\frac{3w_{i,n} - 4w_{i,n-1} + w_{i,n-2}}{2\Delta y} \right)^2 \right]^{\frac{n+1}{2}} + O(\Delta y^2) \quad (3-59)$$

The boundary values for Equation (3-41) can then be calculated from Equations (3-47) to (3-59).

Although the boundary conditions for Equations (3-40) and (3-41) have been discussed in detail, initial estimates of Equations (3-40) and (3-41) have to be specified to start the iteration. The flow of a Newtonian fluid is chosen to give the starting values. The corresponding equations are:

$$\nabla^2 \psi = -\Omega \quad (3-60)$$

$$\psi = 0 \text{ at all border nodes}$$

$$\nabla^2 \Omega = 0 \quad (3-61)$$

The right-hand-side of Equation (3-60) is set to zero and the boundary conditions for Equation (3-61) are calculated from the ψ values given by Equation (3-60). These ψ values are then used to calculate the boundary conditions and right-hand-side of Equation (3-41).

After the stream function, ψ , has been obtained, the velocities u and v are calculated from the finite difference form of Equation (3-32). The down channel velocity, w , is computed by Equation (3-25) subject to the following boundary conditions:

$$\begin{aligned} w &= 0 \quad \text{at } x = 0, \quad y = 0, \quad y = W/H \\ w &= (1 - \kappa) \cos \theta \quad \text{at } x = 1 \end{aligned} \quad (3-62)$$

The discharge rate of paste from the extruder is given by:

$$Q = V H^2 \int_0^1 \int_0^{W/H} \rho w \, dx \, dy \quad (3-63)$$

Iteration is one of the most common method used to solve nonlinear equations. In this thesis, the equations were solved by using a successive relaxation technique defined by:

$$\psi^{k+1} = \psi^k + \lambda_\psi (\psi^k - \psi^{k-1}) \quad (3-64)$$

$$\Omega^{k+1} = \Omega^k + \lambda_{\Omega}(\Omega^k - \Omega^{k-1}) \quad (3-65)$$

and

$$w^{k+1} = w^k + \lambda_w(w^k - w^{k-1}) \quad (3-66)$$

where λ_{ψ} , λ_{Ω} and λ_w denote the relaxation factors; superscript k represents the k th iteration.

3.3 Computer Program Flow Chart

The general flow chart for the program (refer to Appendix A.6.1) is shown in Figure 3-7.

In essence, the program calculates the discharge pressure for a specified discharge rate. The length of screw channel was divided into 17 small sections. For each section, the discharge rate was the same according to the law of mass conservation, the flight height was constant. The temperature for each section was regarded as constant and was taken from experimental measurements.

The first loop in the program determines the initial stream function values by assuming that the Canola paste behaves like a Newtonian fluid.

The second loop finds the values for the stream function, vorticity, ξ and subsequently velocities u and v .

The new velocities u and v are then used to find new apparent viscosity which is incorporated into the third loop to obtain the down channel velocity, w , by solving Equation (3-25).

In the fourth loop, the discharge rate is used to find the down channel pressure gradient and pressure at the section exit.

When the above four loops have been converged, the exit results are used as the initial values for next section and loop five is performed until the exit of the extruder has been reached.

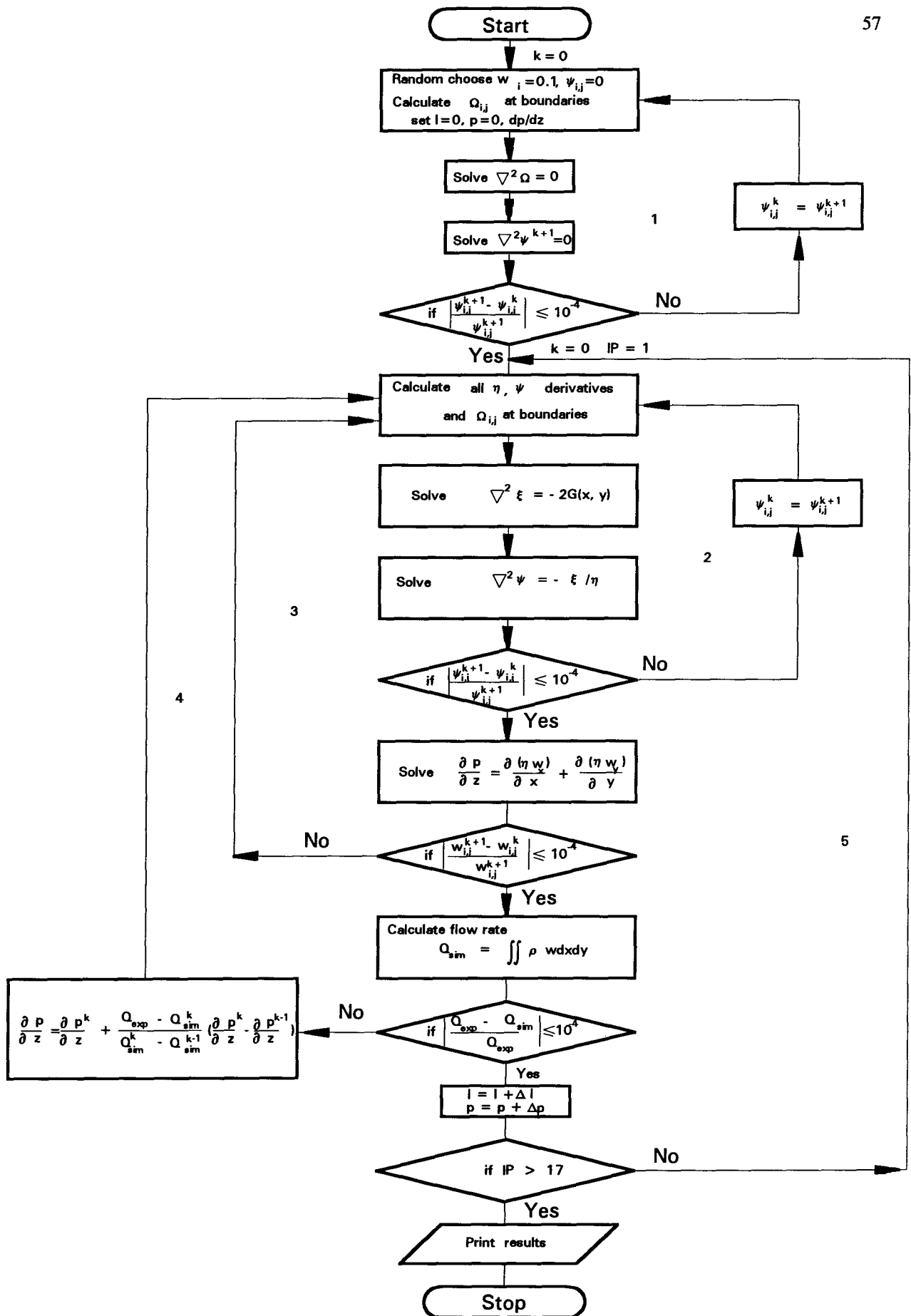


Figure 3-7: Flow chart of the computer program to calculate the velocities and pressures in the extruder.

CHAPTER FOUR

EXPERIMENTAL EQUIPMENT AND PROCEDURES

4.1 Introduction

In order to study the behavior of Canola seed pastes in screw extruders, both rheological and extrusion experiments were conducted. This chapter contains a description of the rheological equipment, single-screw extruder and measurement equipment. In addition, the pretreatment of Canola seeds to prepare the paste for both rheological and extrusion experiments is described.

4.2 Rheological Equipment

Although extrusion of Canola seeds is widely practiced in the food industry, detailed rheological data were not available and consequently had to be obtained experimentally.

4.2.1 Rotational Viscometer

A Haake Rotovisco RV12 viscometer (Haake Mess-Technik GmbH Co., Karlsruhe, Federal Republic of Germany) was chosen to determine the apparent viscosity of Canola pastes as a function of shear rate, concentration and temperature. The Haake Rotovisco RV12 consists essentially of a stationary

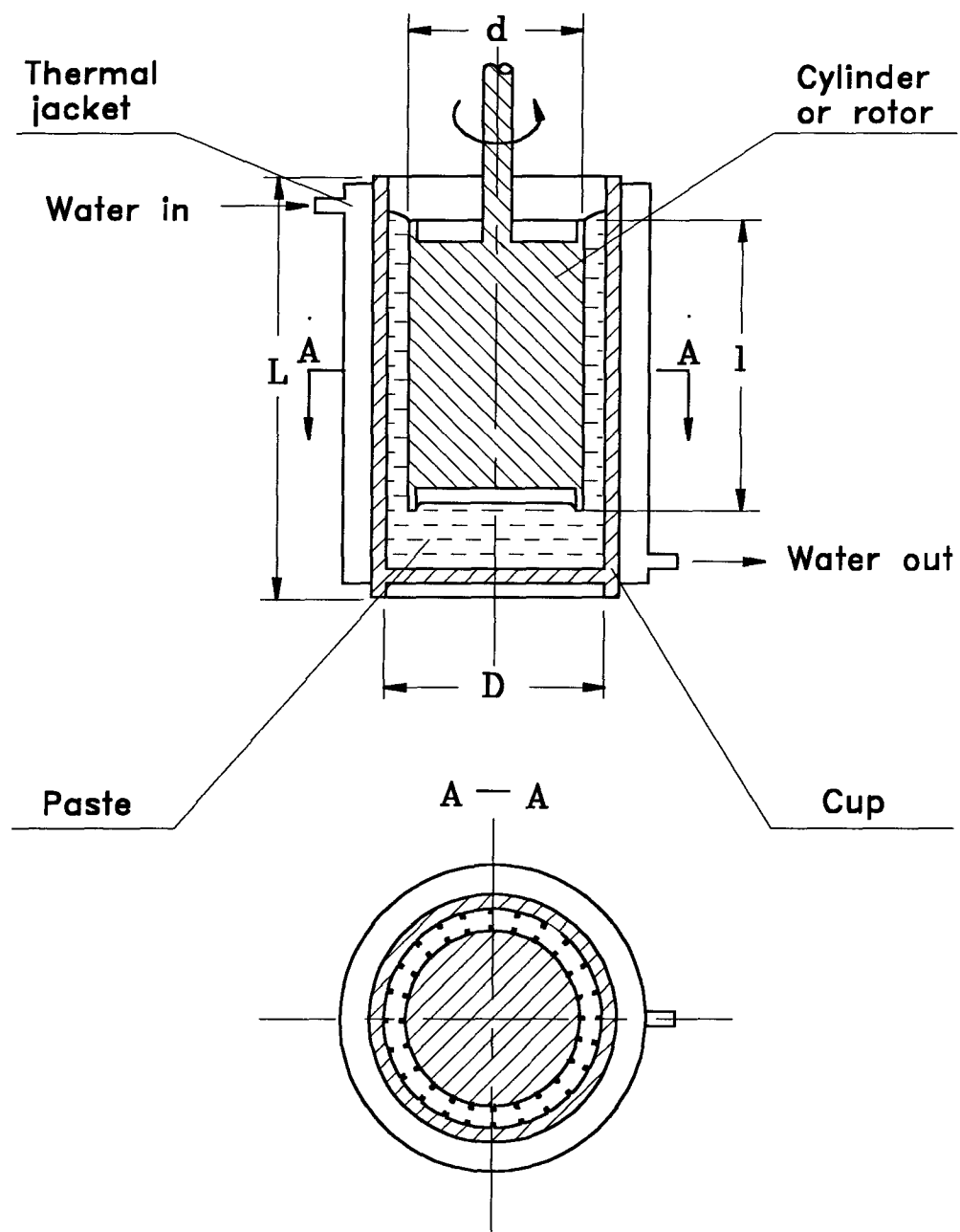


Figure 4-1: Schematic diagram of the grooved stationary cup and the rotating cylinder for the Haake Rotovisco RV12 viscometer. The dimensions are listed in the Table 4-1.

cup and an inner rotating cylinder as shown in Figure 4-1. It is basically a torque measuring instrument whose speed can be controlled very accurately.

Three different cups and cylinders (manufactured to precise tolerances) were used and their dimensions are listed in Table 4-1. To reduce slippage of the paste at the surfaces of the cup and cylinder, the surfaces were grooved as shown in Figure 4-1.

The cup and cylinder were surrounded by a thermal jacket whose temperature could be controlled within ± 0.01 °C in the range -10 °C to 100 °C. In the present experiments, the temperatures were varied from 15 °C to 50 °C in 5 °C intervals.

Table 4-1 Dimensions of the grooved cups and cylinders for Haake Rotovisco RV12 (see Figure 4-1).

Model	D (mm)	L (mm)	d (mm)	l (mm)
MV IP	42.00	120.00	40.08	60.00
MV IIP	42.00	120.00	36.80	60.00
SV IIP	23.10	60.00	20.20	19.60

4.2.2 Capillary Viscometer

The original Canola paste had a solid concentration of 146%, where the percentage is based on the ratio of the mass of oil-free solid to the mass of liquid

(i. e. 100 x g solid/g liquid). For such a high solid concentration paste, it is likely that slip between the paste and a moving surface will occur when the paste is forced to flow in a screw extruder. A capillary viscometer was therefore used to determine the slip factor and also to verify the results obtained with the rotational viscometer.

As shown in Figure 4-2, the capillary viscometer consisted essentially of a high pressure nitrogen cylinder, a pressure regulator, a 200 mL high pressure reservoir and a 1.5 m long, 3.06 mm ID stainless steel capillary tube. The pressure exerted on the surface of the paste inside the reservoir forced the paste through the capillary tube. The recorded pressure drop, the flow rate acquired by the ratio of the mass of collected paste to the time, the geometric data of the tube and the paste's rheological properties obtained by the rotational viscometer could be related to determine the slip factor of the Canola pastes.

4.2.3 Paste Preparation

The Canola paste samples used in the present rheological studies were prepared in a manner similar to that used for preparing peanut butter and sesame pastes in the food industry. Canola seeds provided by Canbra Food Ltd. (Lethbridge, Alberta) were crushed by a roller crusher (see Figure 4-3). To determine the rheological properties of a paste containing solid particles with a rotational or capillary viscometer, the dimensions of the particles had to be less than 1/10 of the gap between the cup and cylinder or the diameter of the tube (Tung, 1988). The crushed seed was therefore screened through a 125 μm sieve. The residual material was recrushed and rescreened until all solids passed through the sieve.

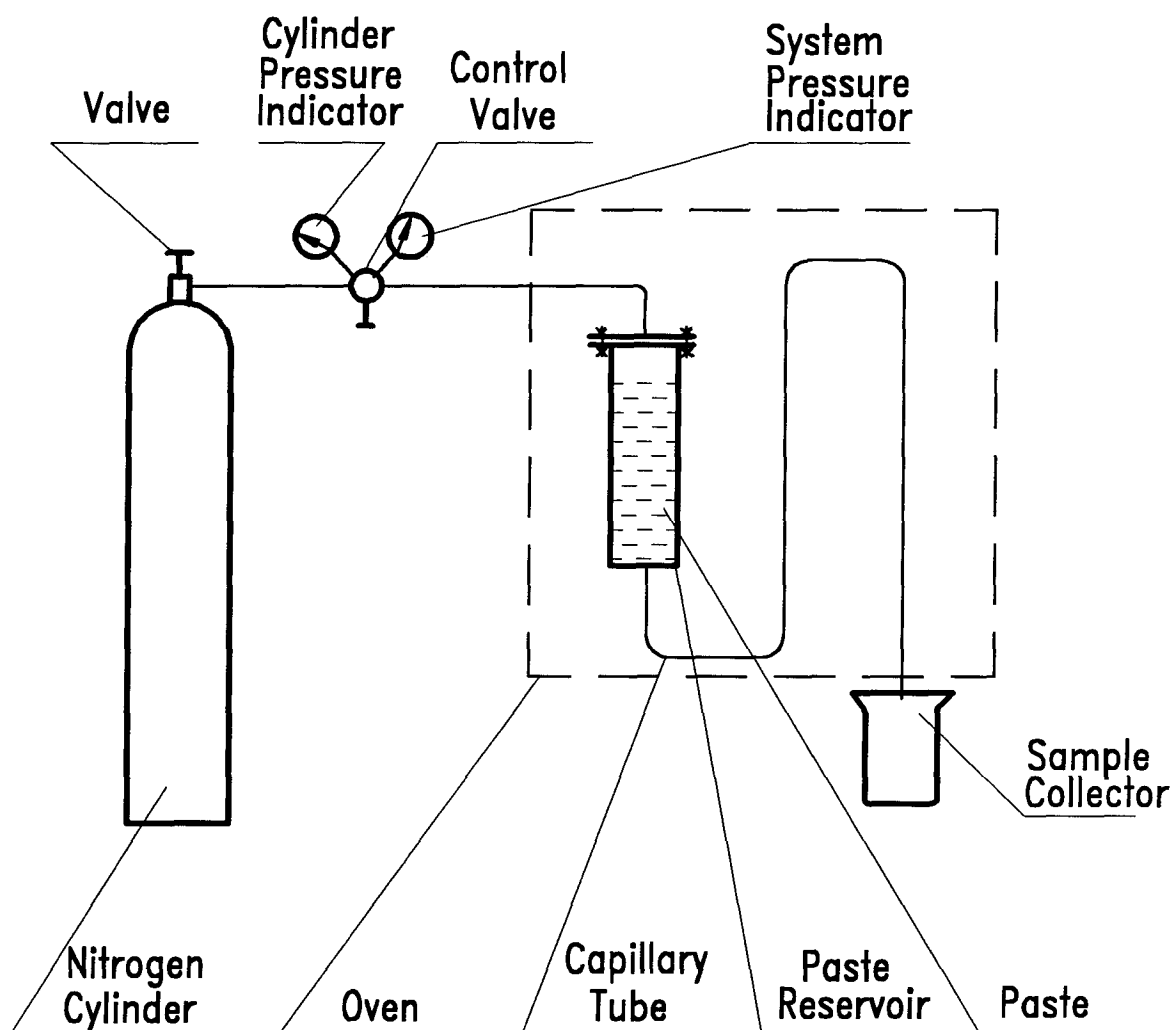


Figure 4-2: Schematic diagram of the capillary viscometer (tube dimensions: 1500 mm long, 3.06 mm ID).

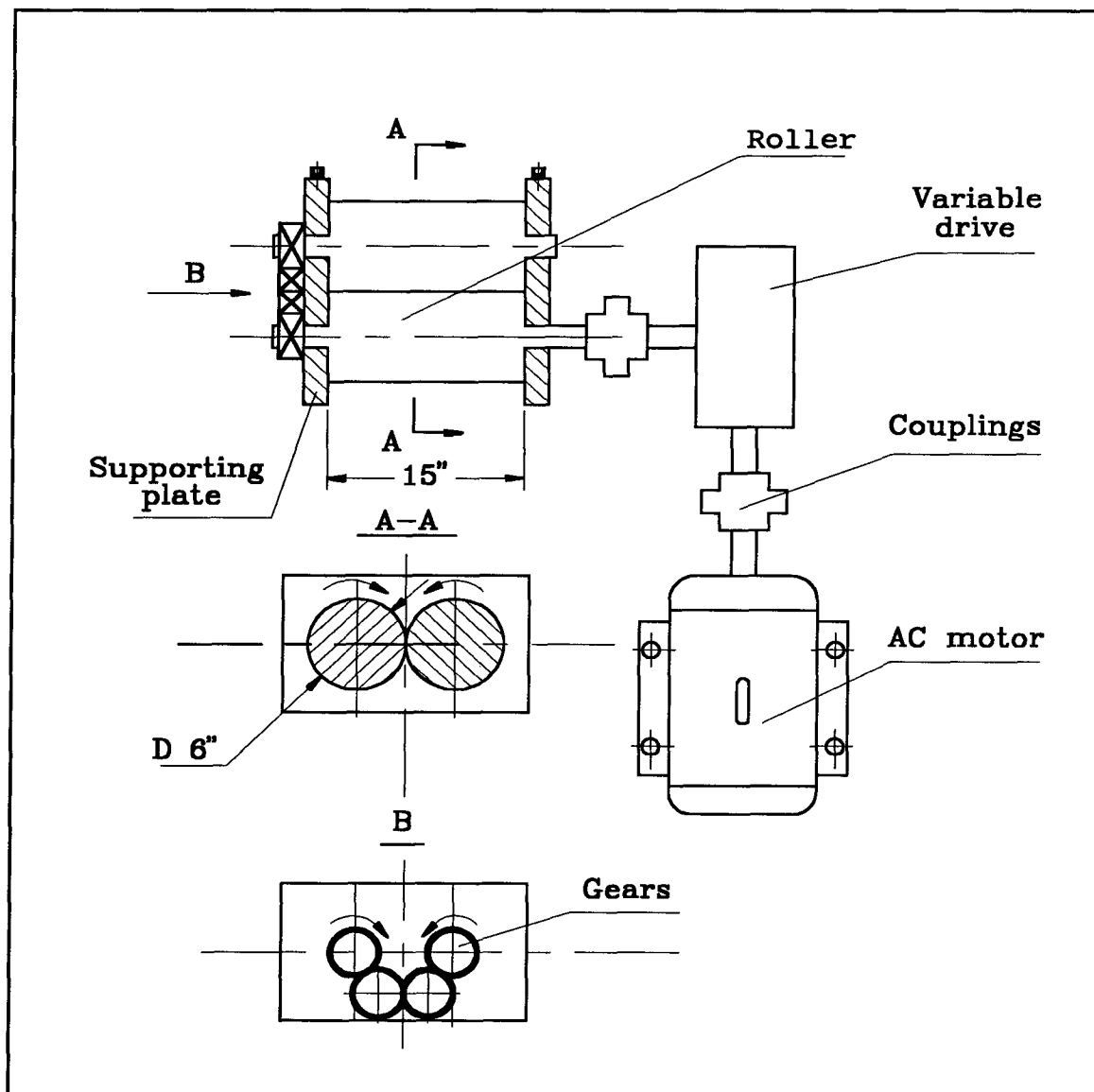


Figure 4-3: Seed crusher.

To obtain Canola pastes with different solid concentrations, the crushed and sieved seeds were mixed with raw Canola oil supplied by Canbra Food Ltd. Five batches having the following solid concentrations were prepared: 35.3, 53.4, 64.5, 84.2 and 95.7% (g solid/g liquid). The batches were kept refrigerated at approximately 0 °C until required.

4.2.4 Solid Concentration Determination

The solid components in the Canola pastes in this study are defined as materials which cannot be extracted with solvents such as *n*-hexane and supercritical CO₂. In the case of Canola pastes, the solids are lignin, seed coat fibers, proteins and other forms of hydrocarbon. The total solid concentration of the Canola paste was determined by subtracting the portion of extractable oil from the total paste weight. The oil was recovered by supercritical CO₂ extraction and the standard *n*-Hexane extraction method recommended by IUPAC (Paguot, 1986).

4.2.4.1 Supercritical Fluid Extraction

The supercritical fluid extraction equipment used to determine the oil content of Canola pastes is shown in Figure 4-4. A pre-weighed amount of paste, typically 27 g, was placed into the extractor (24.5 mm ID x 98 mm in length, shown in Figure 4-4) and extracted with supercritical CO₂ at 35 MPa and 55°C for 72 hours at a liquid CO₂ flow rate of 2.5 mL/min. To ensure that most of the

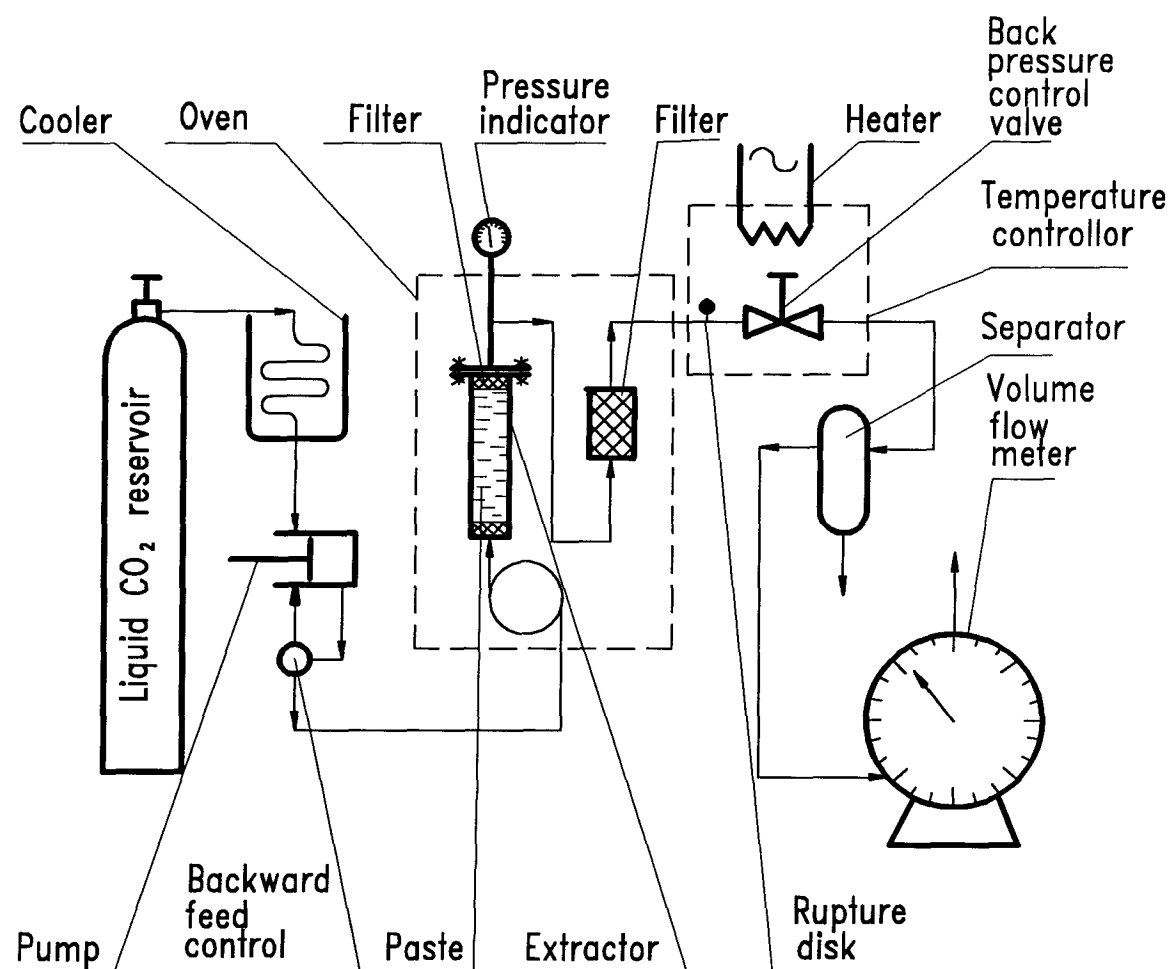


Figure 4-4: Schematic diagram of the supercritical fluid extraction system.

oil in the paste sample was extracted, the weights of extracted oil and paste after 48 hours were compared with the corresponding weights after 72 hours. The difference was less than 1%. The solid concentration was then expressed as the ratio of the residual solid weight to the weight of oil extracted from the paste. The extraction was repeated twice and the final accepted value of the solid concentration in the paste was taken as the arithmetic mean of the three values, *i. e.*, the two supercritical CO₂ extractions and the result from the IUPAC method described in the next section.

4.2.4.2 Hexane Extraction

A pre-weighed amount of about 30 g of paste was placed into a Soxhlet cup (24.5 mm ID x 75 mm long) and extracted by *n*-hexane for six hours at 60 °C. The extracted paste was then allowed to cool in a current of air for 12 hours in order to evaporate most of the hexane. It was then placed into an air convection oven at 40 °C for 24 hours to evaporate the remaining hexane. The residual solid was subsequently finely ground and extracted again for two hours. After allowing the sample to be cooled and dried by the process described above, the residual solid was considered to be the solid content of the initial sample. Typical solid concentration results are listed in the Table 4-2.

4.2.5 Calibration of Equipment

The rotational and tubular viscometers were calibrated with fluids of known viscosities before the rheological experiments were performed.

Table 4-2: Solid concentrations of Canola paste.

Method	Initial Paste mass (g)	Residual Solid mass (g)	Solid concentration % (g solid/g liquid)
SFE	27.164	16.11	145.8
SFE	28.075	16.77	148.3
IUPAC	33.421	19.79	145.0
Average			146.4

4.2.5.1 Calibration of Haake Viscometer

An oil of known viscosity and exhibiting Newtonian behavior was used for the calibration. For such a fluid, the relationship between the shear stress, τ , and viscosity, μ , is:

$$\tau = \mu \frac{\pi N}{15} \frac{R_o^2}{R_o^2 - R_i^2} \quad (4-1)$$

or

$$\tau = \mu NM \quad (4-1a)$$

where M is the "shear rate factor" (min/s) which depends on the geometry of the system; N is the rotational speed of the rotor (rpm); μ is the viscosity of the Newtonian fluid (Pa·s); and R_o and R_i are the radii of the cup and cylinder (m), respectively. The shear stress can be found from the measured torque S ; *i.e.*

$$\tau = A \cdot S \quad (4-2)$$

where A is the "shear stress factor" which depends on the geometry of the cylinder, cup, torque measuring spring and the electrical specifications of the viscometer. Combining Equations (4-1a) and (4-2) gives:

$$A \cdot S = \mu \dot{M} \quad (4-3)$$

The aim of the calibration is to find the shear stress factor A for each combination of cup and cylinder using a Newtonian fluid with a known viscosity. The constant A will be used subsequently to determine the shear stress, τ , with Equation (4-2), when the viscometer is applied to non-Newtonian fluids.

The calibration procedure is as follows. The cup was filled 1/3 full with the oil of known viscosity and slid into the thermal-jack holder. The cylinder was immersed into the cup until the fluid rose slightly over the edge of the cylinder which was also lower than the edge of the cup. The oil was then left for about 30 minutes to reach a steady temperature of 25°C. The fluid was then subjected to shear at different speeds of rotation and the corresponding torques were recorded. The rotary viscometer calibration results are listed in Table 4-3 and Figures 4-4 to 4-6.

4.2.5.2 Calibration of Capillary Viscometer

The capillary viscometer was calibrated with a silicon oil having a viscosity of 130 Pa·s at 20 °C, which was supplied by Canon Instrument Company, PA (viscosity standard N30000). As the tube length is 500 times the tube diameter, the tube inlet and outlet effects were insignificant. The line in Figure 4-8 is the

predicted discharge rate as a function of the applied pressure drop using the Hagen-Poiseuille equation, *i. e.*, without considering the end effects.

Table 4-3: Calibration factors for the rotational viscometer.

Models	A Pa/scale grad.	M min/s	Squared residuals R ²
MV IP	3.32	2	0.999
MV IP	3.86	0.88	0.998
SV IIP	38.69	0.78	0.998

4.2.6 Procedure for Determining Consistency Coefficient and Flow Behavior Index of Canola Pastes

Like many other biomaterials, it was found that the shear stress of Canola pastes follows a power law relationship with a yield stress, *i. e.*,

$$\tau = \tau_0 + m \left(\dot{\gamma} \right)^n \quad (4-4)$$

where m is the consistency coefficient and n the is flow behavior index. The aim of the rheological experiments was to determine τ_0 , m and n of Canola pastes at

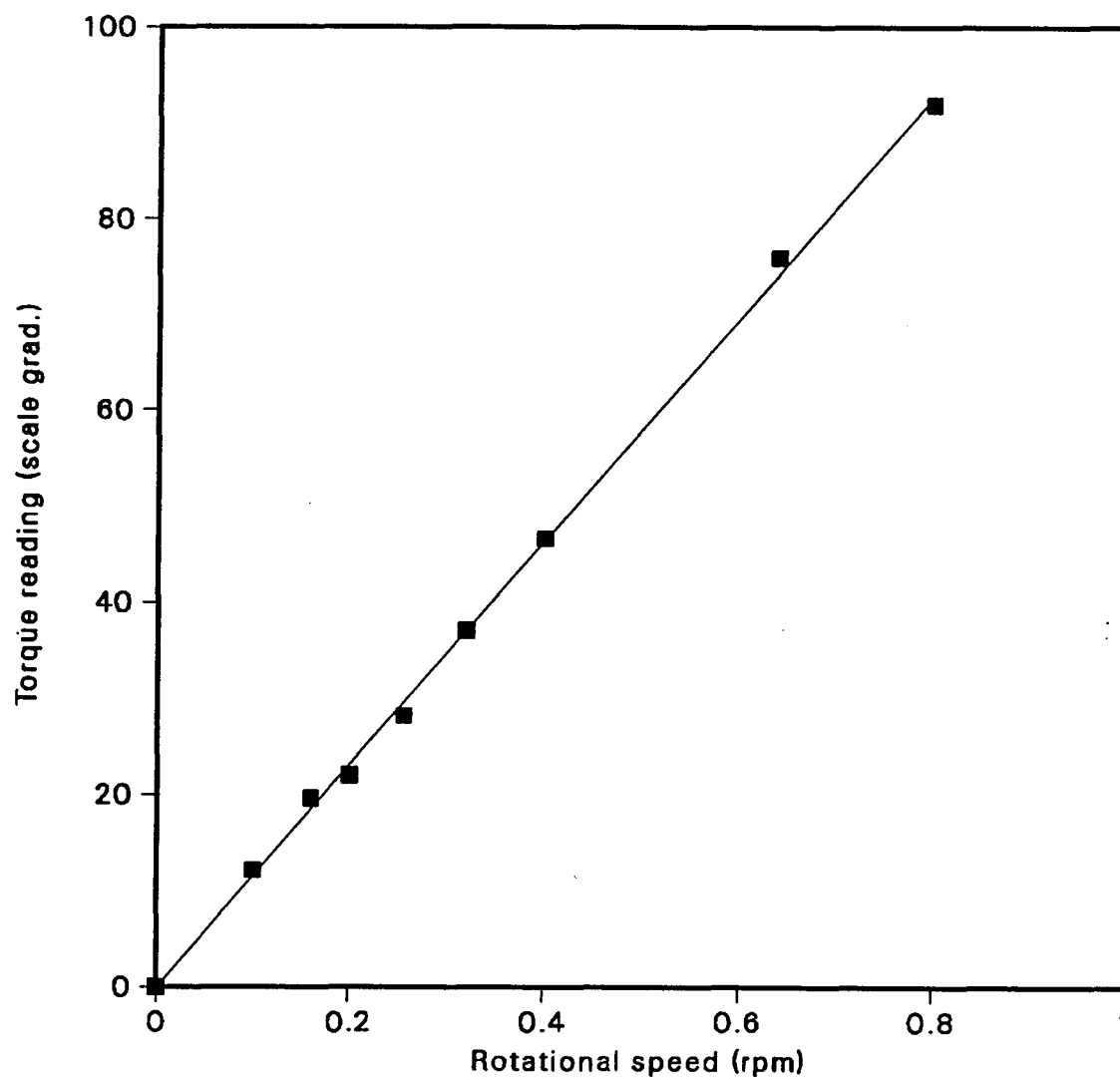


Figure 4-5: Calibration results for the Rotovisco RV12 sensor MV IP (Viscosity Standard 104.640 Pa·s @ 25 °C).

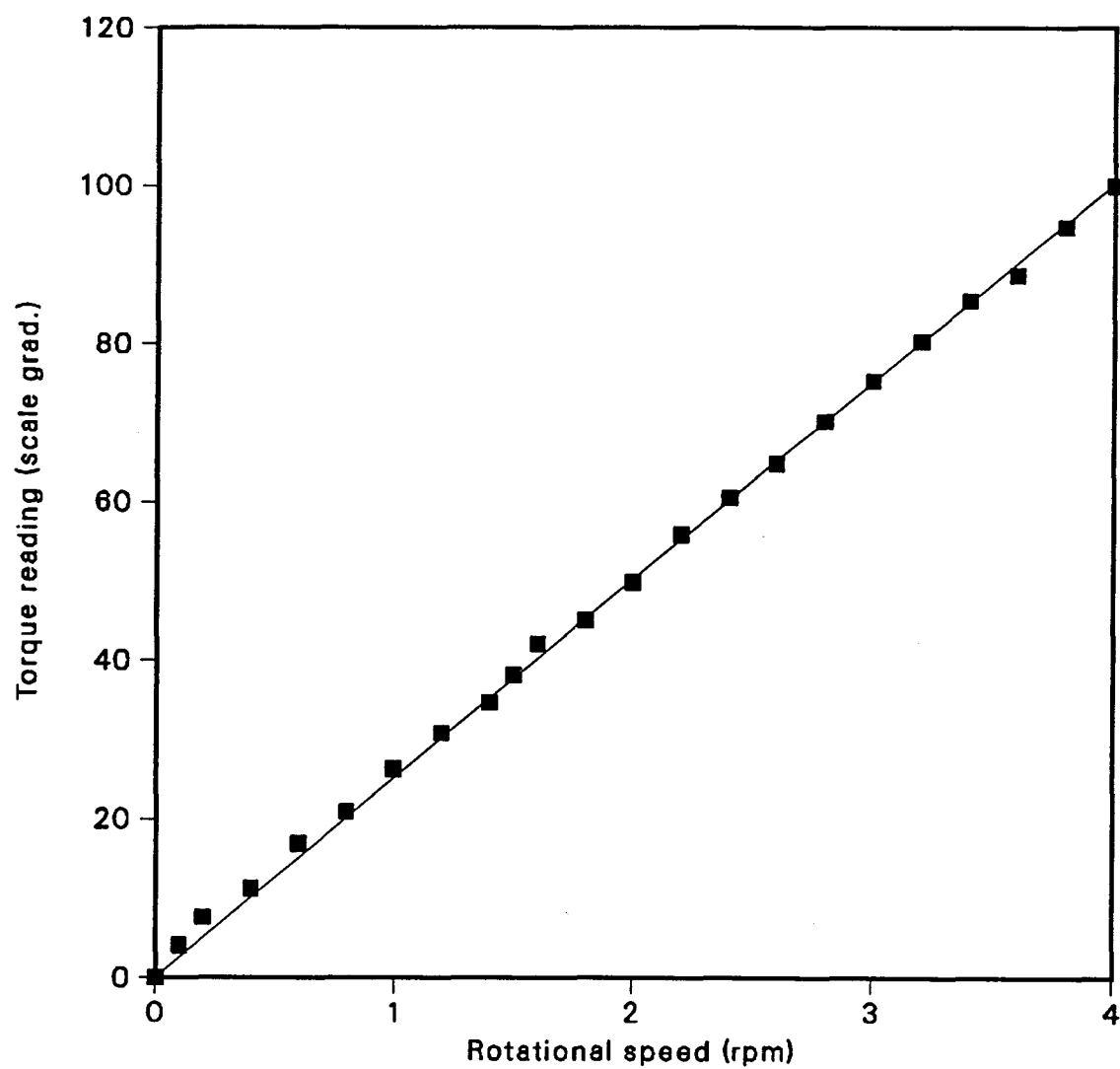


Figure 4-6: Calibration results for the Rotovisco RV12 sensor MV IIP (Viscosity Standard 104.640 Pa·s @ 25 °C).

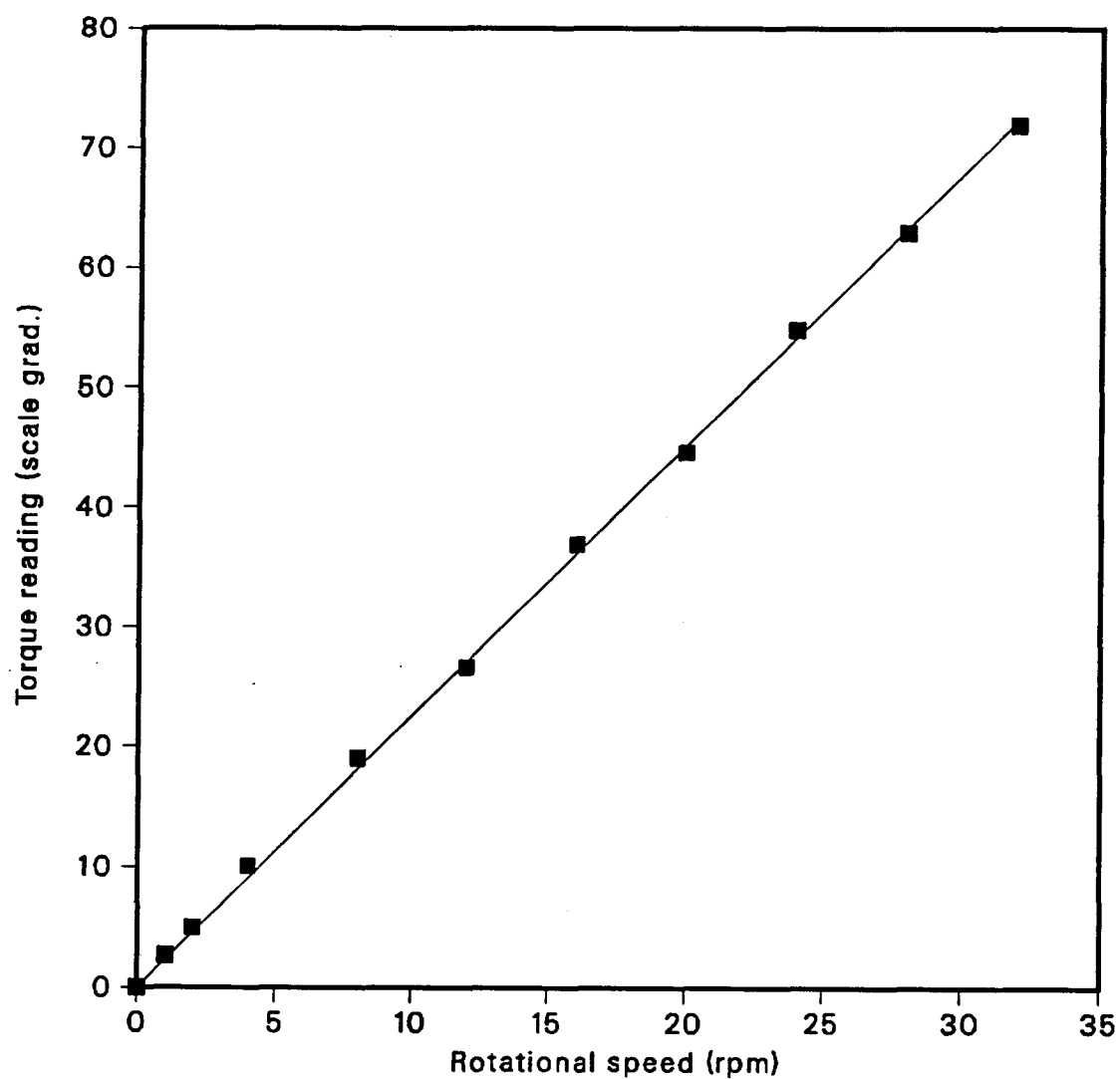


Figure 4-7: Calibration results for the Rotovisco RV12 sensor SV IIP (Viscosity Standard 104.640 Pa·s @ 25 °C).

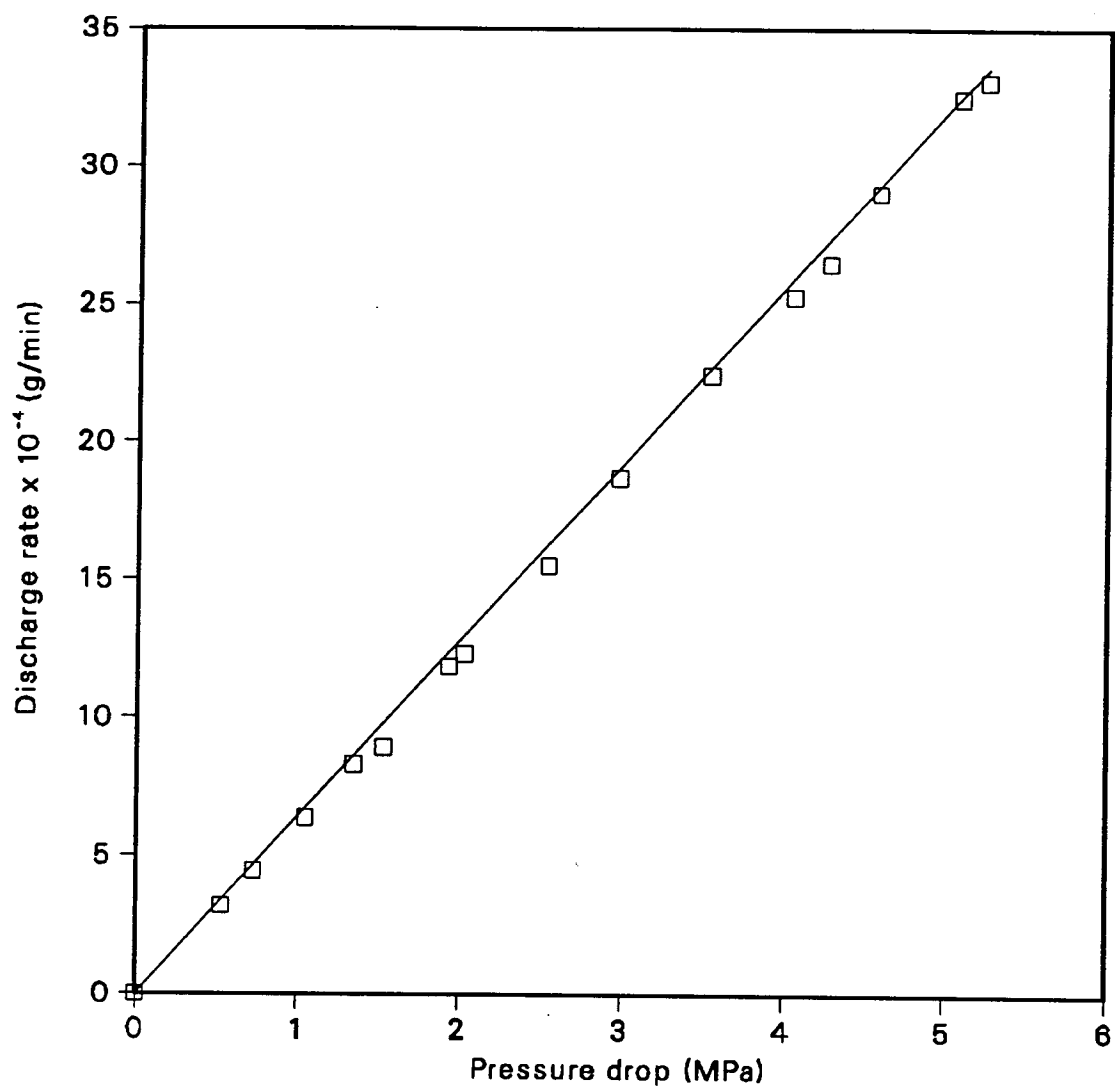


Figure 4-8: Calibration results of the tube viscometer
(Viscosity standard 130.00 Pa·s @ 20 °C).

different concentrations and temperatures.

The shear stress in Equation (4-4) was obtained by:

$$\tau = A \cdot S \quad (4-5)$$

where A and S were defined in section 4.2.5.1.

The shear rate in Equation (4-4) is given by (c. f. Appendix A.1.2):

$$\dot{\gamma} = \frac{1}{2} \left(\frac{R_o^{2/n}}{R_o^{2/n} - R_i^{2/n}} + \frac{R_i^{2/n}}{R_o^{2/n} - R_i^{2/n}} \right) \frac{\pi}{15n} N \quad (4-6)$$

A nonlinear multiple regression procedure was used to find τ_0 , m and n . At the beginning, n was set to 1 which is the value for a Newtonian fluid. The n value obtained from the latest regression procedure was used in Equation (4-6) to get a new set of shear rates. These newly obtained shear rates were used in the regression again until the difference in successive n values was less than a preset tolerance, say 0.001.

4.2.7 Procedure for Determining Slip Factor of Canola Pastes

The capillary viscometer was used to determine the slip factor of the Canola pastes. The procedure was to fill the paste reservoir (c. f. Figure 4-2) with about 100 mL of the paste, measure the discharge volume of the paste from the tube at a certain pressure and time period. The volumetric discharge rate was obtained by the ratio of the discharge volume and time. Since the tube length was about

500 times of the diameter of the capillary tube, the contraction and expansion effects were ignored based on the calibration with a Newtonian fluid of a known viscosity. With this assumption, the pressure drop cross the control valve and tube outlet could be therefore regarded as the pressure drop cross the capillary tube. Four paste concentrations, such as 35.3%, 64.5%, 95.7% and 146% (g solid/g liquid) were tested at pressure ranges from 0.1 MPa to 20 MPa. The time periods varied from 5 min to 30 min and the experimental temperature was 20.2 °C.

The obtained experimental volumetric discharge rates were used to compare with the predicted volumetric discharge rates to determine the slip factors. The results are listed in Table 5-3 and discussed in section 5.3.3.

4.3 Screw Extruder

4.3.1 Design of the Single-screw Extruder

A single flight, single-screw extruder was chosen as the feeder to convey precrushed Canola seeds into a high pressure supercritical CO₂ extractor. Due to its complex geometry and the rheological properties of Canola pastes, an accurate design of extruders was very difficult. In accordance with common practice in the food industry, a simplified design method, adapted from the plastics industry, is used; *i. e.*, the Canola pastes are considered to be Newtonian fluids and average apparent viscosities are assumed. Since the flight angle is one of the most important factors which affect the discharge pressure, three different screws with angles of 6°, 8° and 10° were investigated in this thesis. The calculation below shows that single-screw extruders having such

flight angles should be able to reach the desired discharge pressures. In fact, the available manufacturing facility could make the single flight screw only with angles of 5.98°, 7.97° and 9.94°. The diameter of the screw D was chosen as 36.8 mm (1.5 inch), the flight height H was 4.9 mm (1/5 inch), the length of the screw L was 0.47 m (19.2 inch) and the flight thickness e was 3.5 mm (0.1429 inch) which provides sufficient rigidity to sustain the torque exerted on the side of the flight. Once the above parameters were specified, the discharge rate and pressure were calculated according to the method presented by Harper (1981). The discharge rate, Q , can be found from the following equations after the discharge pressure is determined from the operational requirements of the extractor:

$$Q = G_1 N F_{dt} + \frac{G_2}{\eta} F_{pt} \left(\frac{P_1 - P_2}{L} \right) \quad (4-4)$$

where

$$G_1 = \frac{\pi^2}{2} D^2 H \left(1 - \frac{e}{\pi D \sin \theta} \right) \sin \theta \cos \theta \quad (4-5)$$

$$G_2 = \frac{\pi}{12} D H^3 \left(1 - \frac{e}{\pi D \sin \theta} \right) \sin^2 \theta \quad (4-6)$$

$$F_{dt} = F_d F_{de} F_{dc} \quad (4-7)$$

$$F_{pt} = F_p F_{pe} F_{pc} \quad (4-8)$$

The correction factors in Equations (4-7) and (4-8) are determined from the ratios of H/W , L/D and H/D and Figures 4-9 to 4-13. Equation (4-4) was

developed on the assumption of Newtonian fluid flow. When this equation is applied to a non-Newtonian system, the average apparent viscosity replaces the viscosity. After the discharge pressure is determined, the power requirement of the extruder is calculated from:

$$E = \frac{\pi D^2 L N^2}{\sin \theta} \left[\eta \frac{W}{H} (\cos^2 \theta + 4 \sin^2 \theta) + \eta_s \frac{e}{\delta} \right] + \frac{\pi}{2} D^2 H N \left(1 - \frac{e}{\pi D \sin \theta} \right) \sin \theta \cos \theta \Delta p \quad (4-9)$$

The procedure will be illustrated by performing the calculations for the 9.94° screw and for a discharge pressure of 40 MPa. Although the screw length is 0.47 m, the effective length is taken as 0.44 m because the inlet does not correspond to the beginning of the flight (see Figure 4-14). From Equations (4-5) and (4-6), it follows that:

$$\begin{aligned} G_1 &= \frac{\pi^2}{2} D^2 H \left(1 - \frac{e}{\pi D \sin \theta} \right) \sin \theta \cos \theta \\ &= \frac{\pi^2}{2} 0.0368^2 * 0.00490 * \left(1 - \frac{0.00350}{\pi 0.0368 \sin 9.94^\circ} \right) \sin 9.94^\circ \cos 9.94^\circ \\ &= 4.577 * 10^{-6} \text{ (m}^3\text{)} \end{aligned}$$

$$\begin{aligned} G_2 &= \frac{\pi}{12} D H^3 \left(1 - \frac{e}{\pi D \sin \theta} \right) \sin^2 \theta \\ &= \frac{\pi}{12} 0.0368 * 0.00490^3 * \left(1 - \frac{0.00350}{\pi 0.0368 \sin 9.94^\circ} \right) \sin^2 9.94^\circ \\ &= 2.780 * 10^{-11} \text{ (m}^3\text{)} \end{aligned}$$

The width of the screw channel is given by:

$$\begin{aligned}
 W &= \pi D \tan\left(\frac{\theta}{i}\right) \cos\theta - e \\
 &= \pi * 0.0368 * \tan\left(\frac{9.94^\circ}{1}\right) \cos 9.94^\circ - 0.00350 \\
 &= 0.0165 \text{ (m)}
 \end{aligned}$$

The ratio of the flight height to the channel width is:

$$\begin{aligned}
 \frac{H}{W} &= \frac{0.00490}{0.0165} \\
 &= 0.298
 \end{aligned}$$

From Figure 4-9, the drag flow and pressure flow correction factors are:

$$F_d = 0.85$$

$$F_p = 0.72$$

The ratio of the screw length to the screw diameter is:

$$\begin{aligned}
 \frac{L}{D} &= \frac{0.44}{0.0368} \\
 &= 10.8
 \end{aligned}$$

From Figures 4-10 and 4-11, the pressure flow end correction factor and drag flow end factor are obtained as:

$$F_{pe} = 1.03$$

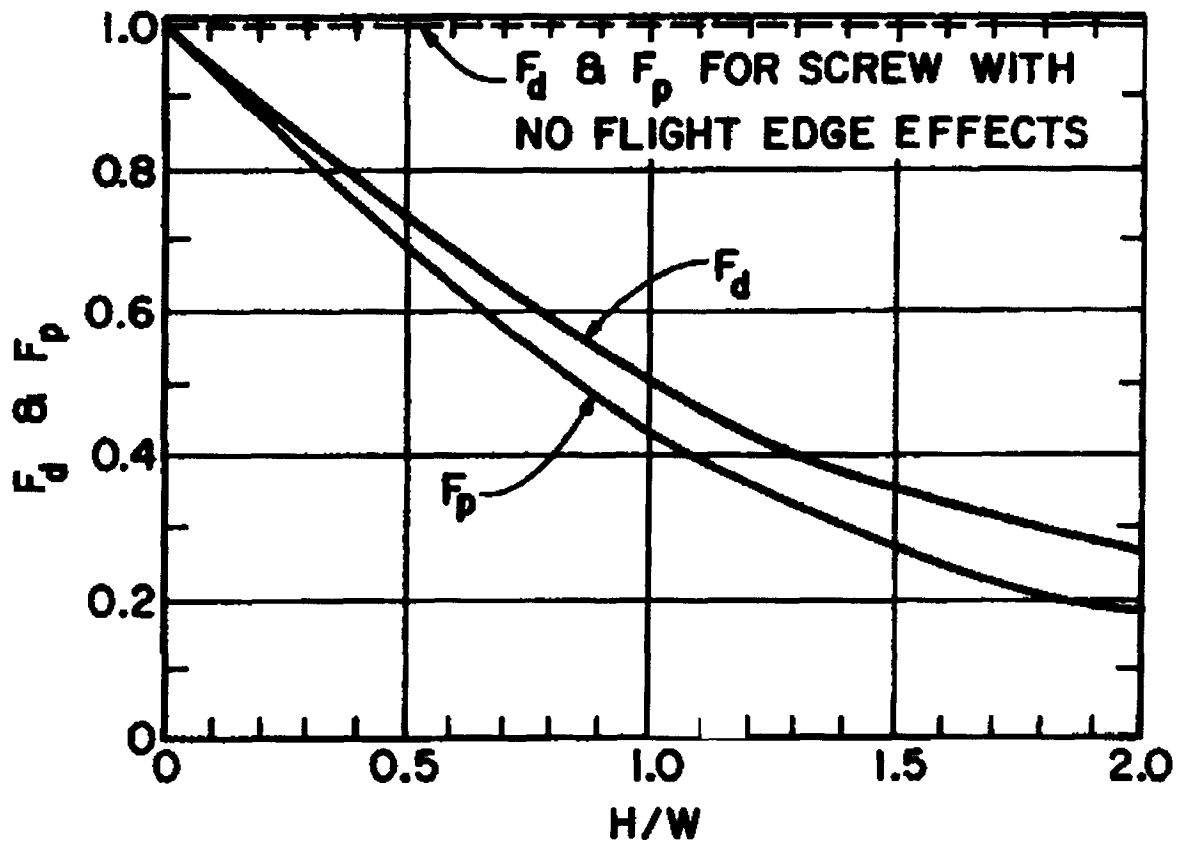


Figure 4-9: Drag and pressure flow shape factors (Booy, 1963).

$$\begin{aligned}
 F_{de} &= 1 + \tan^2 \theta - F_{pe} \tan^2 \theta \\
 &= 1 + \tan^2 9.94 - 1.03 * \tan^2 9.94 \\
 &= 0.999
 \end{aligned}$$

The ratio of the flight height to the screw diameter is given by:

$$\begin{aligned}
 H/D &= 0.00490 / 0.0368 \\
 &= 0.133
 \end{aligned}$$

The pressure flow curvature correction factor and drag flow curvature factor are taken from Figures 4-12 and 4-13:

$$\begin{aligned}
 F_{pc} &= 1.13 \\
 F_{dc} &= 1.04
 \end{aligned}$$

The total drag flow factor F_{dt} and pressure flow factor F_{pt} are functions of the three other drag and pressure factors, respectively, i. e.,

$$\begin{aligned}
 F_{dt} &= F_d F_{de} F_{dc} \\
 &= 0.85 * 0.999 * 1.04 \\
 &= 0.883
 \end{aligned}$$

$$\begin{aligned}
 F_{pt} &= F_p F_{pe} F_{pc} \\
 &= 0.72 * 1.03 * 1.13 \\
 &= 0.838
 \end{aligned}$$

The average shear rate in the screw channel may be estimated from:

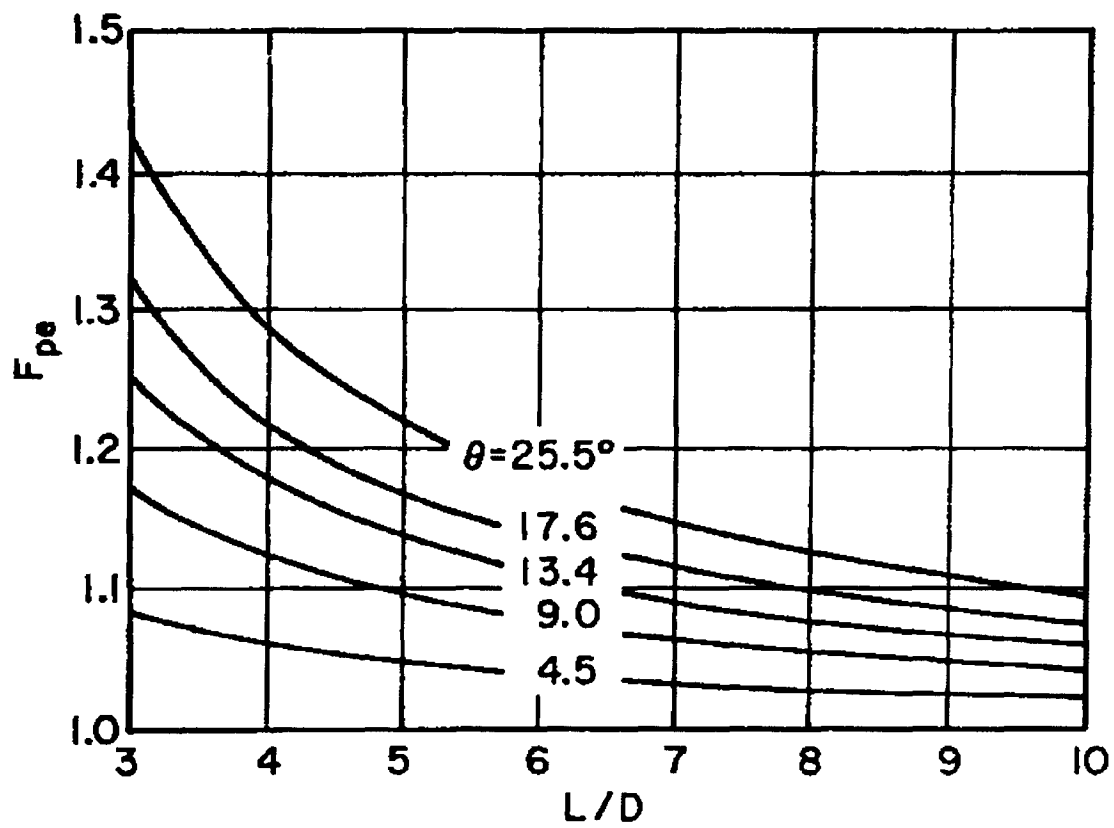


Figure 4-10: Pressure flow end correction factor
(Booy, 1967).

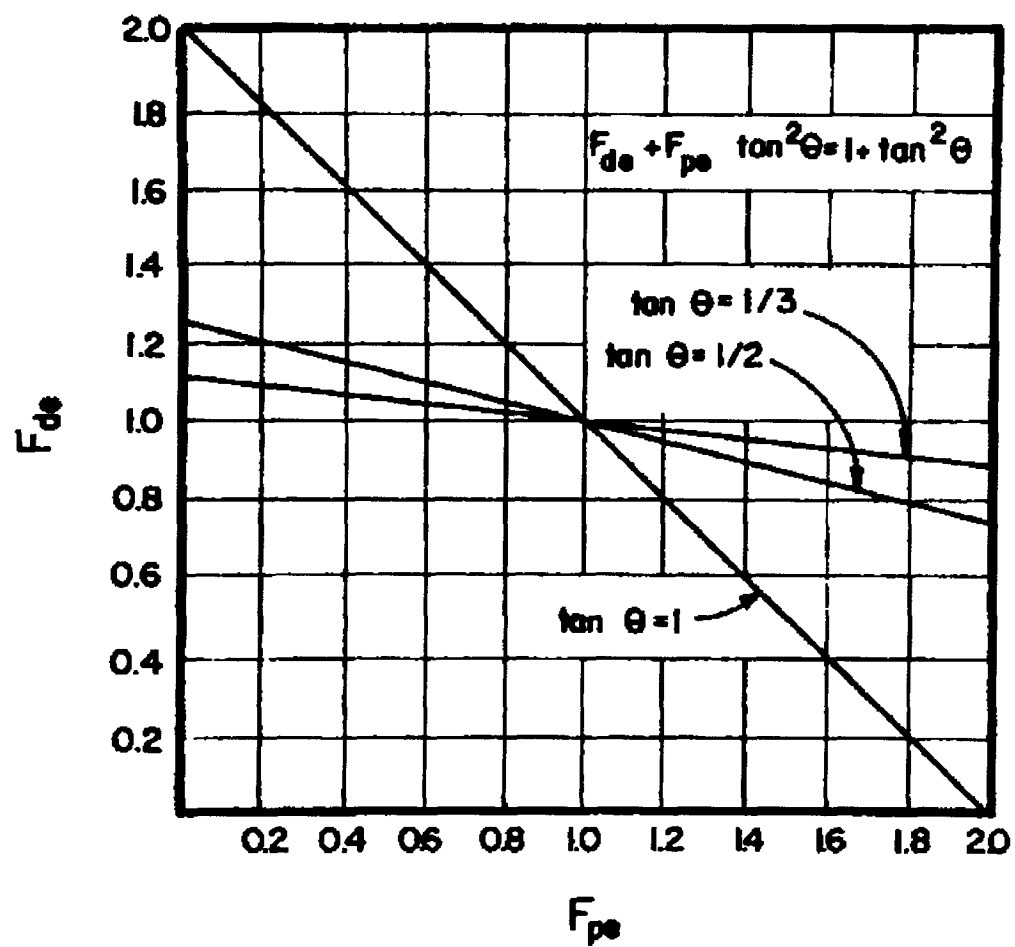


Figure 4-11: Drag flow end correction factor (Booy, 1967).

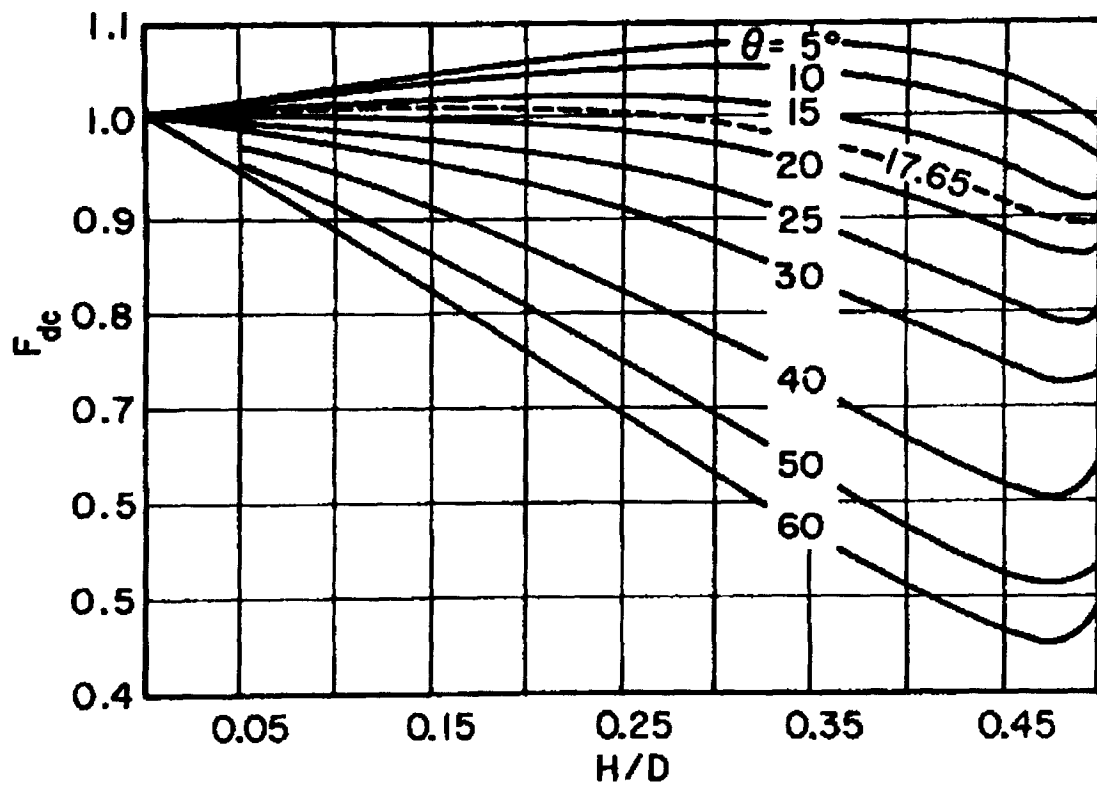


Figure 4-12: Drag flow curvature correction factor (Booy, 1963).

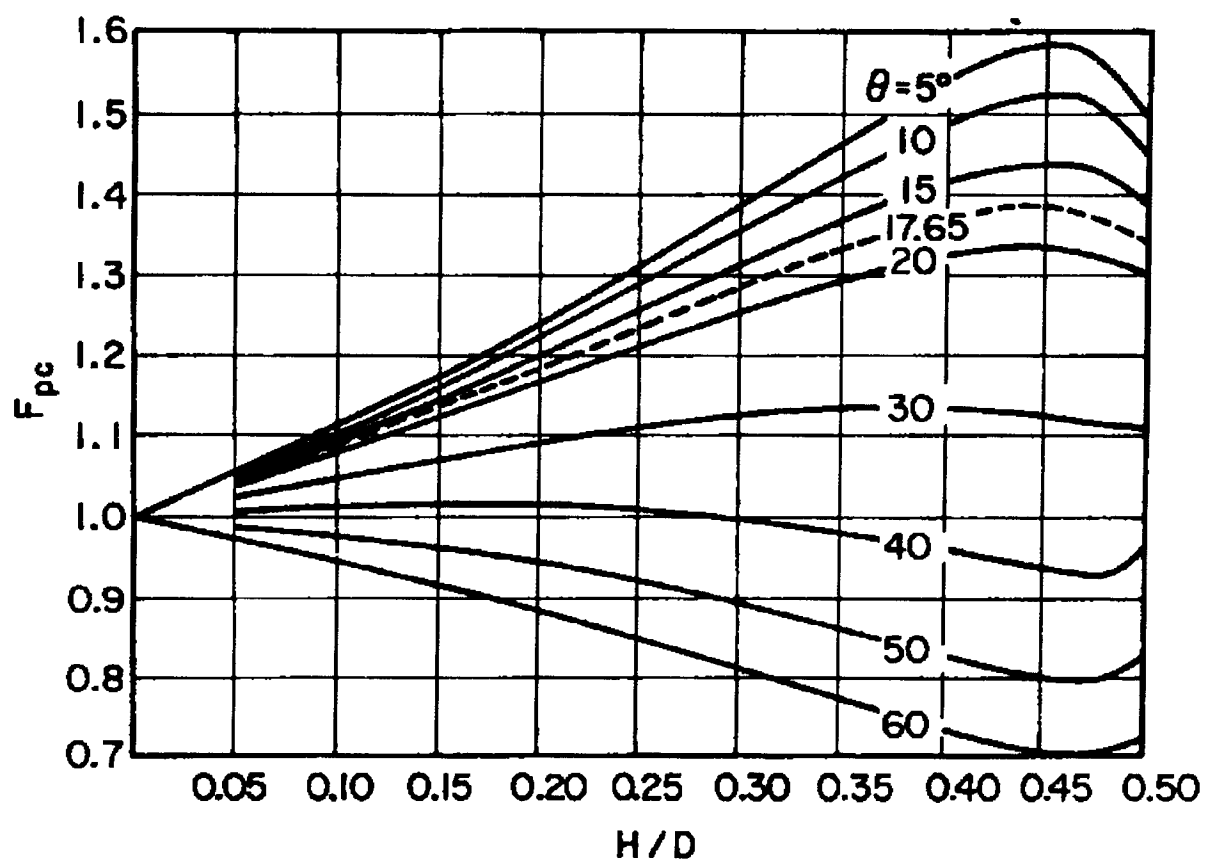


Figure 4-13 Pressure flow curvature correction factor
(Booy, 1963).

$$\begin{aligned}
 \dot{\gamma} &= \frac{\pi DN}{60H} \\
 &= \frac{\pi * 0.036 * 66.5}{60 * 0.0046} \\
 &= 26.1 \text{ (s}^{-1}\text{)}
 \end{aligned}$$

The average apparent viscosity in the screw channel is then computed from Equation (5-9) presented in Chapter 5:

$$\begin{aligned}
 \eta &= 0.205 \left(\dot{\gamma} \right)^{-0.444 C^{0.197}} C^{4.85} \exp \left(\frac{19500}{T R_c} \right) \\
 &= 0.205 \text{ } 26.1^{-0.444 * 1.46^{0.197}} 1.46^{4.85} \exp \left(\frac{19500}{303 * 8.314} \right) \\
 &= 621 \text{ (Pa} \cdot \text{s)}
 \end{aligned}$$

The discharge rate at a discharge pressure of 40 MPa is then given by Equation (4-4):

$$\begin{aligned}
 Q &= G_1 N F_{dt} + \frac{G_2}{\eta} F_{pt} \left(\frac{p_1 - p_2}{L} \right) \\
 &= 4.58 * 10^{-6} * \frac{66.5}{60} * 0.883 + \frac{2.78 * 10^{-11}}{621} * 0.838 \left(\frac{-400 * 10^5}{0.44} \right) \\
 &= 6.52 * 10^{-7} \text{ (m}^3\text{/s)} \\
 &= 2.35 \text{ (L/h)}
 \end{aligned}$$

The design dimensions of the three screws are listed in the Table 4-4 and the drawings of the extruder are shown in Figures 4-14 and 4-15. Additional detailed drawings are found in Appendix A.3.

Table 4-4: Screw dimensions.

Screw #	θ (°)	D (mm)	i	H (mm)	W (mm)	e (mm)	L (mm)
1	5.98	36.75	1	4.9	8.527	3.5	470
2	7.97	36.75	1	4.9	12.51	3.5	470
3	9.94	36.75	1	4.9	16.43	3.5	470

The power consumption of the screw extruder is estimated from Equation (4-9) recommended by Harper (1981). The gap, δ , between the flight tip of the screw and the barrel was designed as 0.02 mm. The apparent viscosity in the gap, η_δ , in Equation (4-9) was also replaced by the average apparent viscosity in the screw channel. The total power consumed by the extruder is then given as:

$$\begin{aligned}
 E &= \frac{(\pi D)^2 L N^2}{\sin \theta} \left[\eta \frac{W}{H} (\cos^2 \theta + 4 \sin^2 \theta) + \eta_\delta \frac{e}{\delta} \right] + \frac{\pi}{2} D^2 H N \left(1 - \frac{e}{\pi D \sin \theta} \right) \sin \theta \cos \theta \Delta p \\
 &= \frac{(0.0368\pi)^2 * 0.44 (100/60)^2}{\sin 9.94^\circ} \left[621 * \frac{0.016}{0.0049} (\cos^2 9.94^\circ + 4 * \sin^2 9.94^\circ) + 621 * \frac{0.00350}{0.00002} \right] + \\
 &\quad + \frac{\pi}{2} * 0.0368^2 * 0.00490 \left(\frac{100}{60} \right) \left(1 - \frac{0.00350}{0.0368\pi \sin 9.94^\circ} \right) \sin 9.94^\circ \cos 9.94^\circ * 400 * 10^5 \\
 &= 9.01 * 10^3 \text{ (Nm/s)} \\
 &= 9.01 \text{ (kW)} \\
 &= 12.1 \text{ (hp)}
 \end{aligned}$$

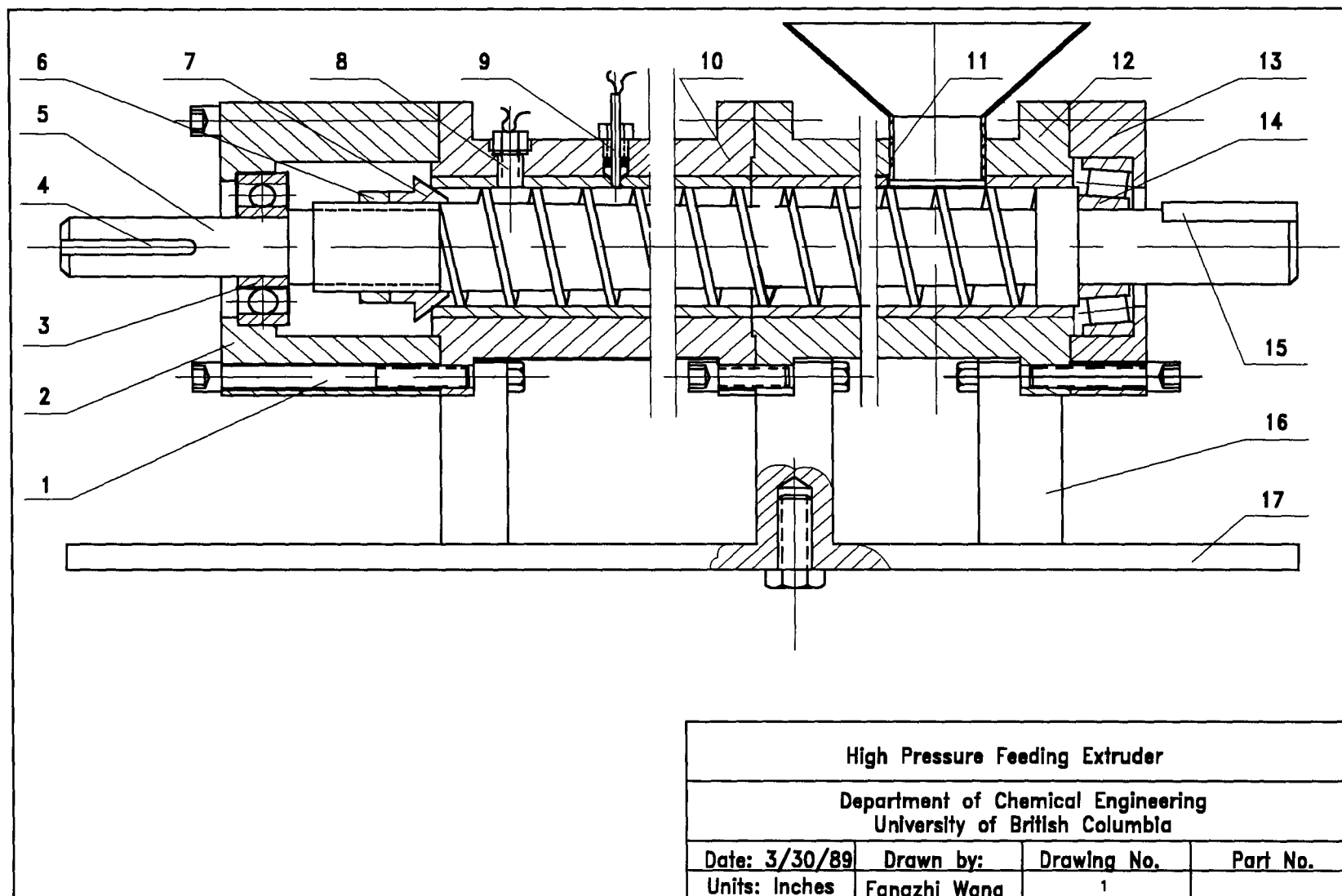


Figure 4-14: Sectional view of the assembled extruder.

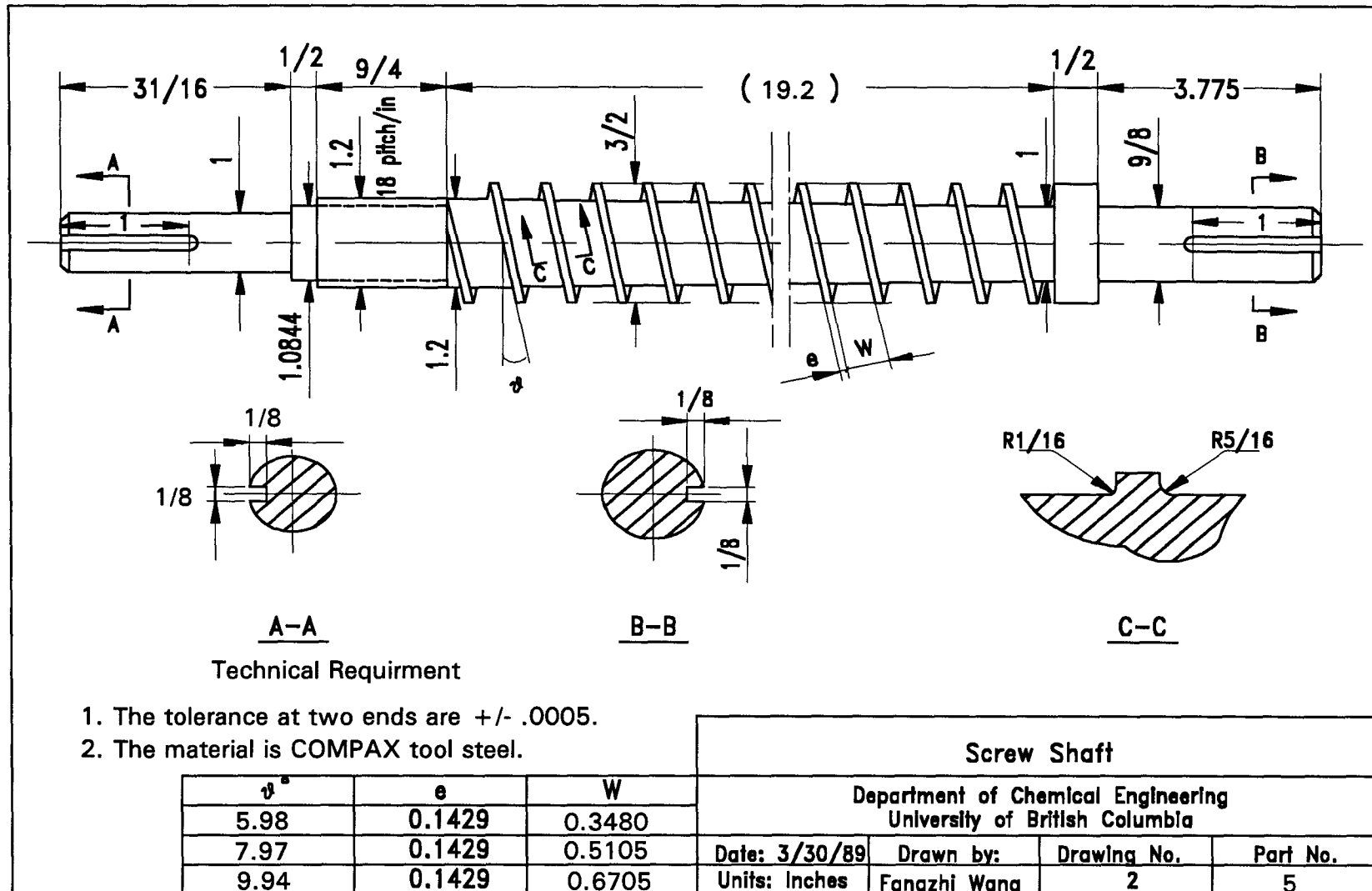


Figure 4-15: Detailed drawing of the screw shaft.

The required input torque, T_e , can, therefore, be calculated from the ratio of the power consumption, E , and the screw rotation speed, N :

$$\begin{aligned} T_e &= \frac{E}{N} \\ &= \frac{9010}{100 / 60} \\ &= 5406 \text{ (N} \cdot \text{m)} \end{aligned}$$

When selecting an electric motor, a safety factor of 1.2 was chosen, which was proved to be suitable experimentally. Therefore, the required power of the electric motor is:

$$\begin{aligned} N_p &= 12.1 * 1.2 \\ &= 14.5 \\ &\approx 15 \text{ (hp)} \end{aligned}$$

The drawing of the assembled extruder is shown in Figure 4-14 and the custom designed parts, *i. e.*, parts #2, #5, #6, #7, #10, #12 and #13 can be found in Figure 4-15 and Appendix A.3.

4.3.2 Hydraulic Drive System

Hydraulic motors offer significant advantages over electric variable speed motors. Hydraulic motors generate higher torques and a wider range of continuous speeds than electric motors at a similar price level. Furthermore, hydraulic motors are flexible in changing the direction of rotation which is especially beneficial in high pressure extrusion experiments. Another significant characteristic of hydraulic motors is that they provide almost constant torque

when the motor speed is increased. Hydraulic motors can give a starting torque approaching that of the running torque and they can run very smoothly at very low speeds. Their inertia is also much lower than that of most other drives, so they accelerate to the set speed almost instantaneously. This feature is very important in screw extruder operation because stationary pastes in the screw channel strongly resist a moving screw.

Two hydraulic motors (Char-Linn 103-1032, Eaton Corp., Eden Prairie, MN) were chosen to drive the screw extruder and each motor was connected to one end of the screw shaft as shown in Figure 4-16. A single hydraulic motor could provide a torque of 4,090 N·m. Therefore, the total torque of the two motors is 8,180 N·m. Since the actual required torque was 5,406 N·m, the two motors could provide 50 percent more torque than was needed.

Utilizing two motors to drive a single shaft synchronously without damaging the shaft and motors could probably be done only with a hydraulic drive system. Since the two hydraulic motors were arranged in parallel and connected to the same power fluid line, they were both driven by an isobaric fluid. This configuration also ensured that the two motors rotated at the same speed. If one of the motors slowed down, the other one would drag it to a faster pace resulting in the lower pressure at the slow end. This would cause more fluid to flow to this end. Consequently, the two motors rotated at the same speed. In addition, the two motors provided two supports for the screw shaft which ensured that the screw shaft remained centered in the barrel.

One of the drawbacks of the hydraulic drive system is that it consumes more power than electric motors of the same output power. As a result, the hydraulic

drive system may generate more heat than a corresponding electric drive system. The heat increases the temperature of the hydraulic fluid. To keep the hydraulic fluid at a relatively low temperature, the amount of hydraulic fluid in the system should be four times the hydraulic motor's full flow capacity according to standard hydraulic design guide lines (Ciolfitto, 1989). The flow rate required by each hydraulic motor to operate at full capacity was 38 L/min. Therefore, the full flow rate of the two hydraulic motors was 76 L/min. The reservoirs (see Figure 4-16) were designed to hold 350 liters of hydraulic fluid which was four and half times the motors' full flow capacity. Furthermore, the baffle plates installed inside the reservoirs, as shown in Figure 4-16, reduced short circuiting of the fluid and kept the fluid outside the motors as long as possible to allow cooling.

4.3.3 Pressure and Temperature Measurement and Data Acquisition System

To enable a theoretical analysis of extruder operation, four fast response pressure transducers (PX-600, Omega Engineering INC., Stamford, CT) and six Iron-Constantan thermocouples (ICSS-12, Omega Engineering INC.) were mounted onto the extruder barrel. The surfaces of the transducers and tips of the thermocouples were placed as close to the inner surface of the barrel as possible to measure the real pressures and temperatures at the tip of the flight. The gap between the pressure transducer surface and the inner surface of the barrel was less than 0.12 mm. Details of the pressure transducer and thermocouple mounts are shown in Figures 4-17 and 4-18. The four pressure transducers were placed on the barrel at positions 190 mm, 288 mm, 386 mm and 435 mm respectively from the inlet; the six thermocouples were located at positions 190 mm, 239 mm, 288 mm, 337 mm, 386 mm and 435 mm from the inlet as shown in Figure A.3-5.

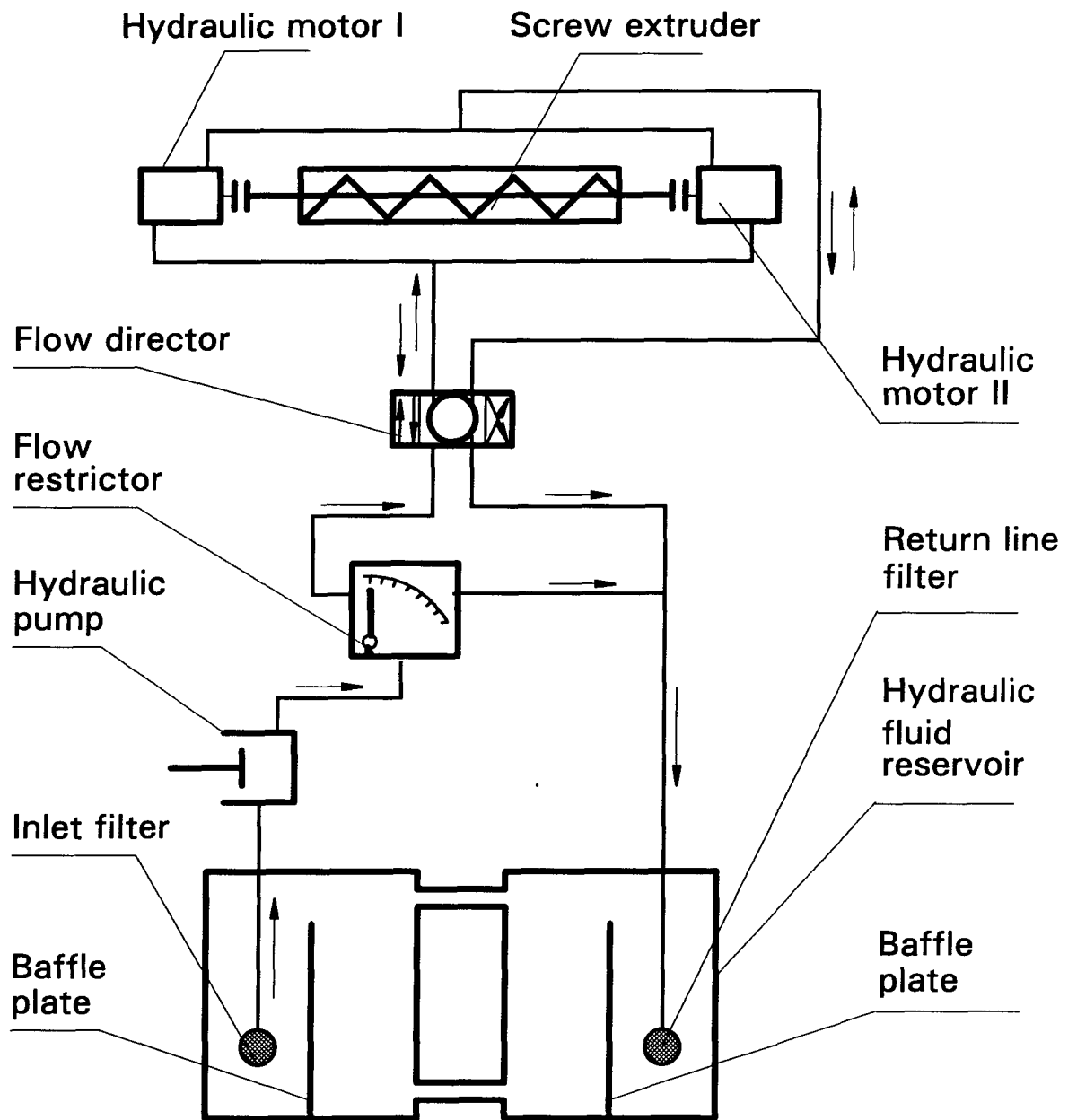


Figure 4-16: Schematic diagram of the hydraulic drive equipment.

The analog pressure and temperature signals were amplified by an interface EXP-16 (Omega Engineering INC.), converted by an analog-digital board DAS-8 (Omega Engineering INC.) and transferred to a 286-AT IBM PC compatible computer.

The DAS-8 is a half length, single input-ended A/D board featuring a high speed, 12-bit successive approximation conversion. The conversion period can reach 25 μsec (35 μsec maximum) which results in a data throughput rate of more than 30 kHz if the A/D board is used with high speed personal computers and supported with proper software. The DAS-8 also provides a fixed ± 5 VDC input with a resolution to 0.00244 volts using a common ground (single-ended) and could withstand continuous voltage overloading of ± 30 VDC with transients to several hundred volts. The IBM PC bus power supply (+5, +12 and -12V) and other I/O connections allow additional user-designed interfaces for input signal conditioning and multiplexers.

The EXP-16 is a multiplexer/amplifier interface which has 16 differential analog input channels all of which are connected to one analog output channel which, in turn, is connected to the DAS-8 A/D board. It provides signal amplification, filtering and conditioning. The high grade instrumentation amplifier has switch selectable gains of 0.5, 1, 2, 10, 50, 100, 200 and 1000 plus programming gain capability. The interface is also equipped with cold-junction sensing and compensation circuitry for J, K, T, E, S, R and B type thermocouples.

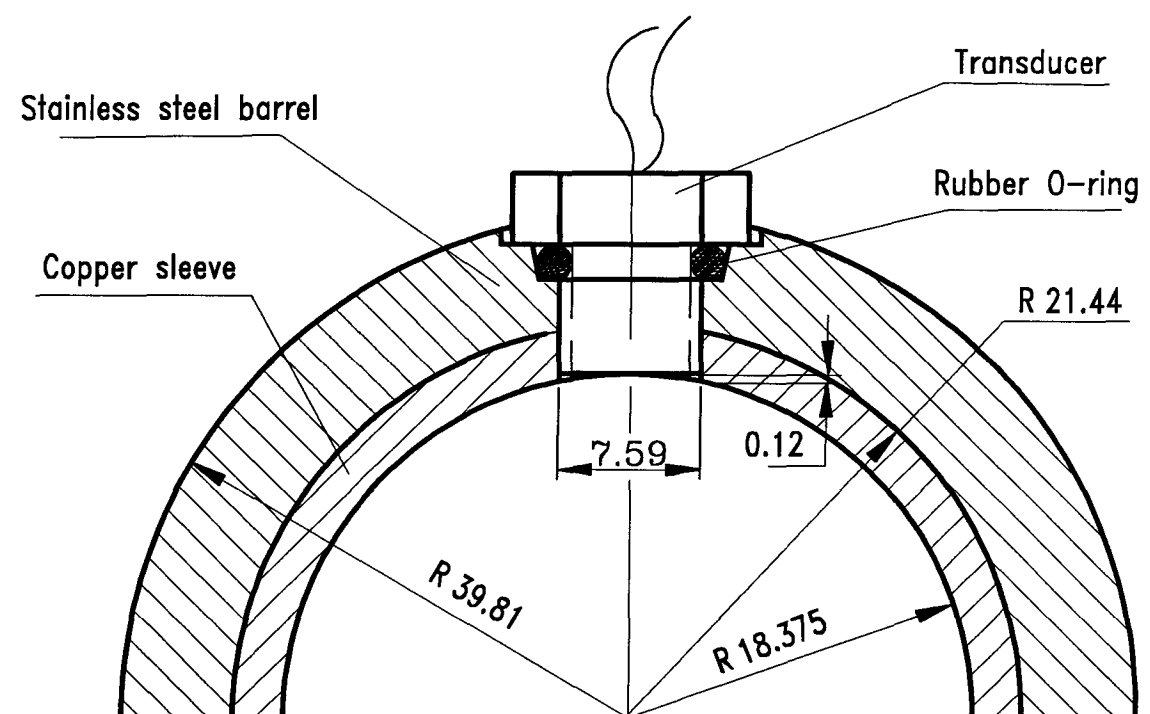


Figure 4-17: Details of a pressure transducer mounted on the screw barrel (all units are in mm).

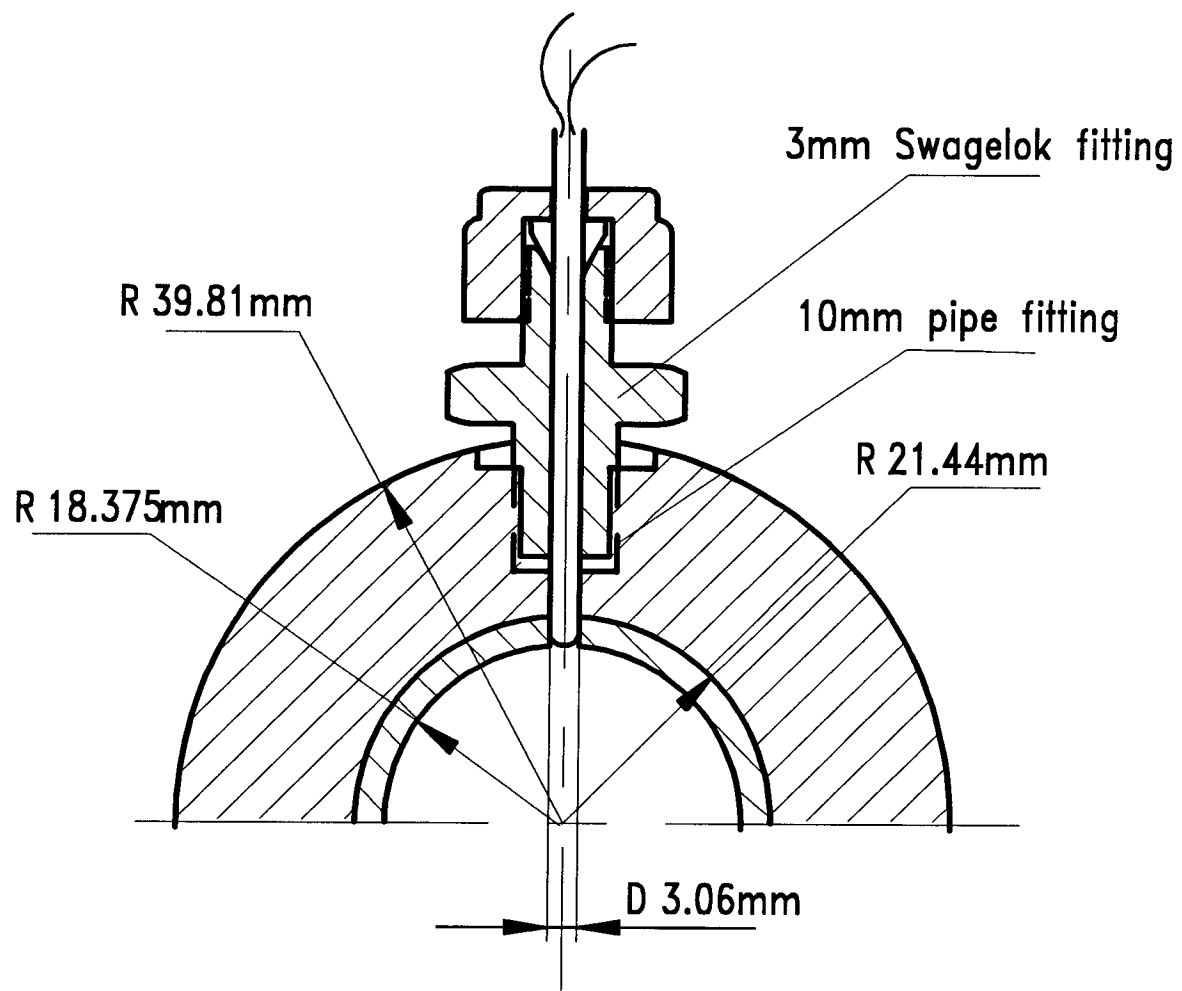


Figure 4-18: Details of a thermocouple mounted on the screw barrel.

The software used to perform the data acquisition was Labtech Notebook purchased from Laboratory Technologies Corporation (Wilmington, WA). The pressure signals fluctuated periodically at a rate of less than 1.5 cycles per second. To record the complete pressure signals, the sampling rate had to be at least 10 times that of the pressure signal fluctuating rate. The sampling rate was, therefore, chosen as 30 to 50 per second.

4.3.4 Equipment Calibration

4.3.4.1 Calibration of EXP-16 Interface and DAS-8 A/D Board

The EXP-16 multiplexer was calibrated with a 4 1/2 digit digital multimeter, HP3455A (EXP-16 Manual), and a custom-made, finely regulated voltage supply which is completely noise free. The circuit is shown in Figure 4-19 and the calibration procedure was as follows.

At both the highest and lowest gain modes, each input channel's high, low and ground connectors were joined. The multimeter was then connected to the output channel and the ground. The related potentiometer, R75 (refer to Appendix A.5, EXP-16 circuit diagram) was adjusted until the output value shown on the multimeter was zero. The low and ground connectors were then joined, the gain dip switch was set to 100, a noise free 50 mVDC voltage signal from the DC supplier was sent to each of the 16 input channels on the EXP-16 and the gain potentiometer was adjusted until the reading from the meter was $+5.000 \text{ VDC} \pm 0.001 \text{ VDC}$. The final step in the calibration of the EXP-16 was the calibration of the cold junction circuit built in the multiplexer. A digital voltmeter was connected to the ground connector and one of the cold junction

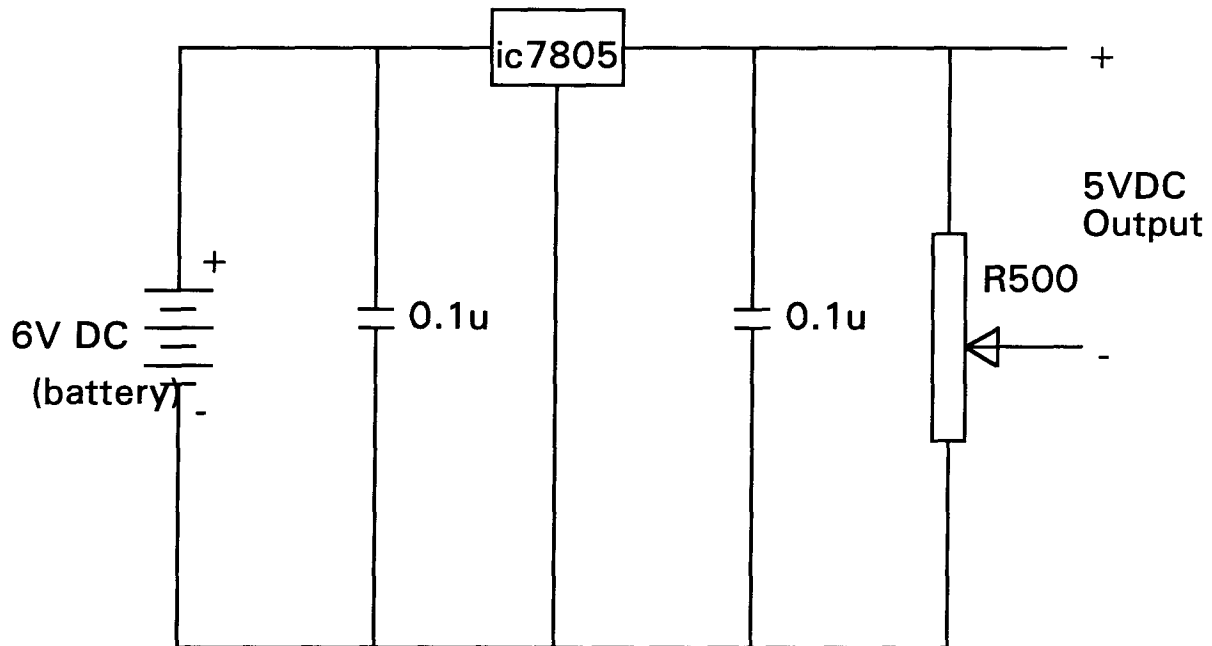


Figure 4-19: Diagram of the noise free DC voltage supply.

compensation channels and the environmental temperature in the vicinity of the EXP-16 board was precisely measured. The cold junction circuit potentiometer was adjusted until the digital voltmeter showed a number which was equal to the value of the multiplication of $24.4 \text{ mV}/^{\circ}\text{C}$ to the environmental temperature.

The DAS-8 A/D conversion board was calibrated to retain full accuracy with the 4 1/2 digit digital multimeter. To perform a satisfactory calibration, the calibration was conducted using the program, CALDAS8.BAS provided by MetraByte Corp.(Taunton, MA), see Appendix 6.2.

The DAS-8 A/D board was plugged into one of the eight slots in the 286-AT computer and a - 4.9988 VDC voltage was applied to the analog input channel of DAS-8. Then, the - F. S. potentiometer (c f the DAS-8 circuit diagram in Appendix A.4) was adjusted so that the digital output which was shown on the computer screen was flickering between - 2047 and - 2048. Finally, a + 4.9963 VDC voltage was applied to the board, and the + F. S. potentiometer was adjusted so that the output was between + 2046 and + 2047.

Adjustments were done on "half" bit intervals to obtain a reading flickering 50/50 between two adjacent values. This is more precise than applying whole bit values such as - 5.0000 V, 0.0000 V etc. and gives a better calibration (DAS-8 Manual, 1988).

4.3.4.2 Calibration of Pressure Sensors and Thermocouples

The four pressures transducers were calibrated with a more precise pressure transducer (Model AB from Data Instruments Inc., Lexington MA) equipped with a LCD digital meter and a large Bourdon gauge. All pressure transducers and the Bourdon gauge were connected to a 1 L high pressure reservoir which could withstand a pressure of 70 MPa. Each transducer had its own DC power supply as shown in Figure 4-19 to reduce background noise. The output from the transducers was recorded by the computer and the pressures were taken as the average reading displayed by the LCD and the Bourdon gauge. The calibration results are plotted in Figures 4-20 to 4-23 and the corresponding linear least square regression results are listed in the Table 4-5.

Table 4-5: Regression results of pressure transducer calibration.

Sensor #	X Coef. a	Std. Err. of Y Est.	R ²	Std. Err. of Coef.
1 (PX600-3K6V)	13.75	3.613	0.9962	0.0967
2 (PX600-3K6V)	14.62	2.921	0.9975	0.0831
3 (PX610-5K6V)	32.66	6.36	0.9969	0.2211
4 (PX610-10K6V)	48.40	11.47	0.9936	0.4576

Iron-Constantan thermocouples were calibrated by using room temperature (19.6 °C) and the boiling point of distilled water (99.1 °C at 756 mm Hg). The results are shown in Table 4-6:

Table 4-6: Calibration results for the Iron-Constantan thermocouples.

Thermocouple #	Temperature Reading at 19.6 °C	Temperature Reading at 99.1 °C
1	19.0	98.4
2	19.5	99.4
3	20.1	98.3
4	19.1	98.3
5	19.7	99.3
6	18.9	98.3

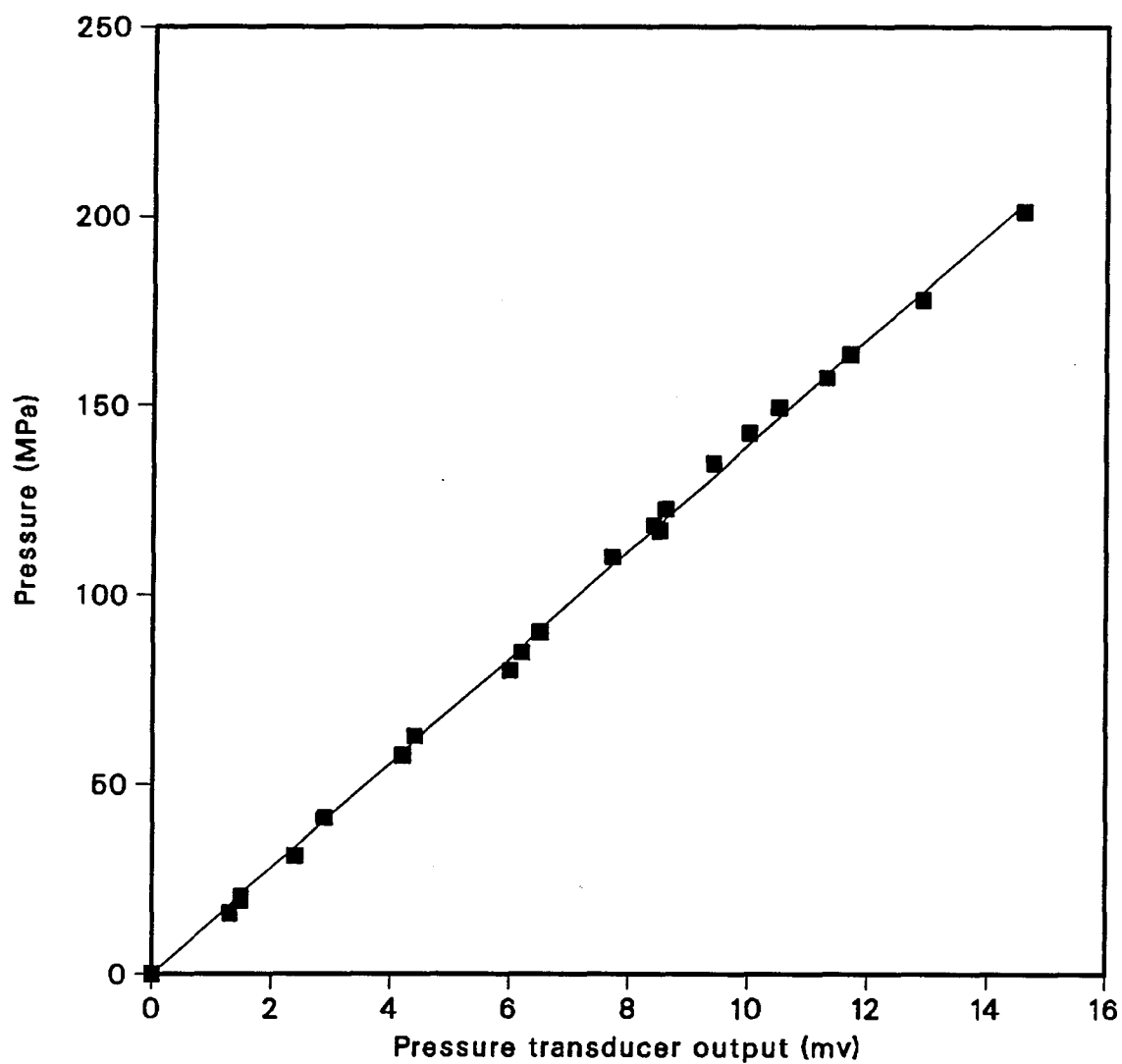


Figure 4-20: Calibration curve for pressure transducer #1 (PX600-3K6V).

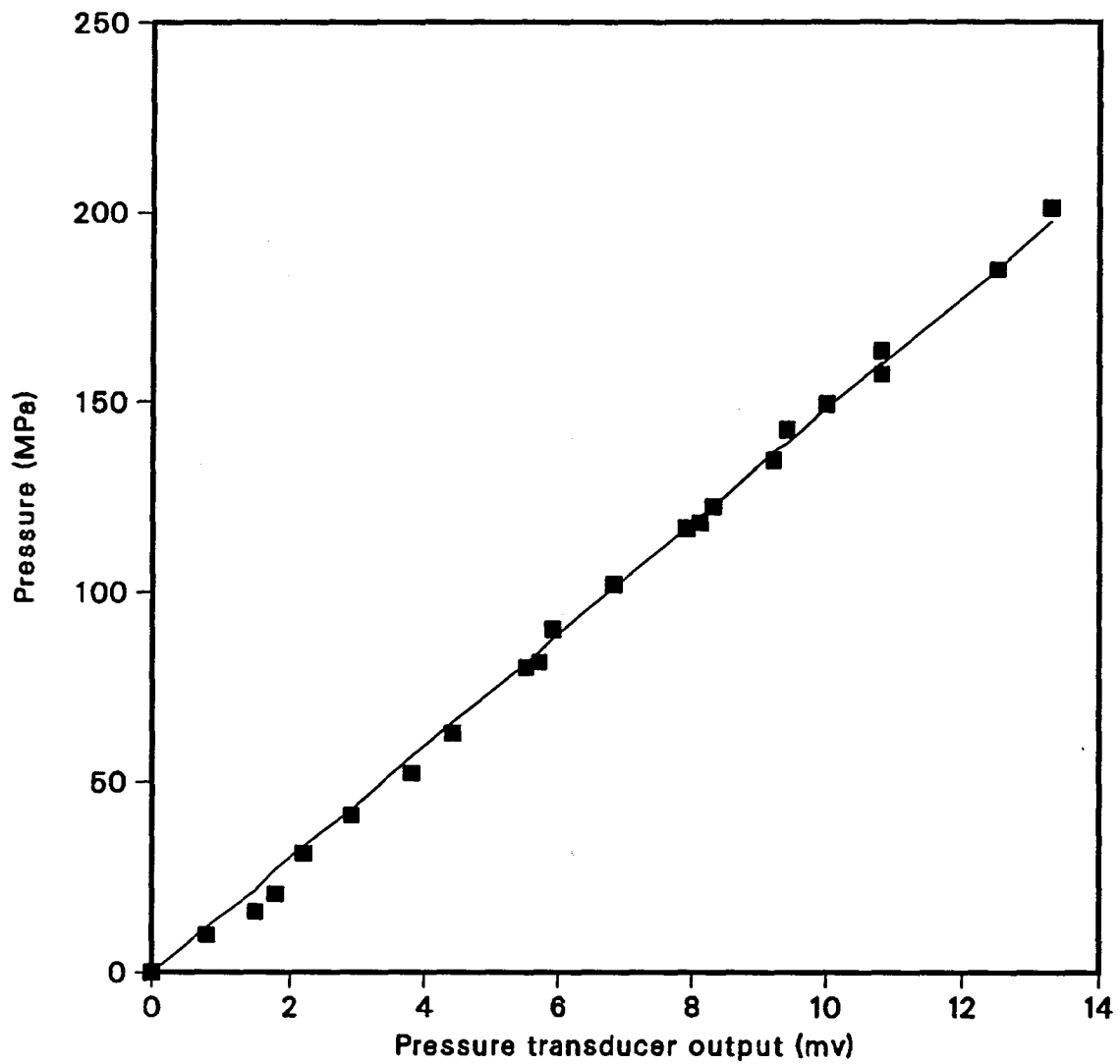


Figure 4-21: Calibration curve for pressure transducer #2 (PX600-3K6V).

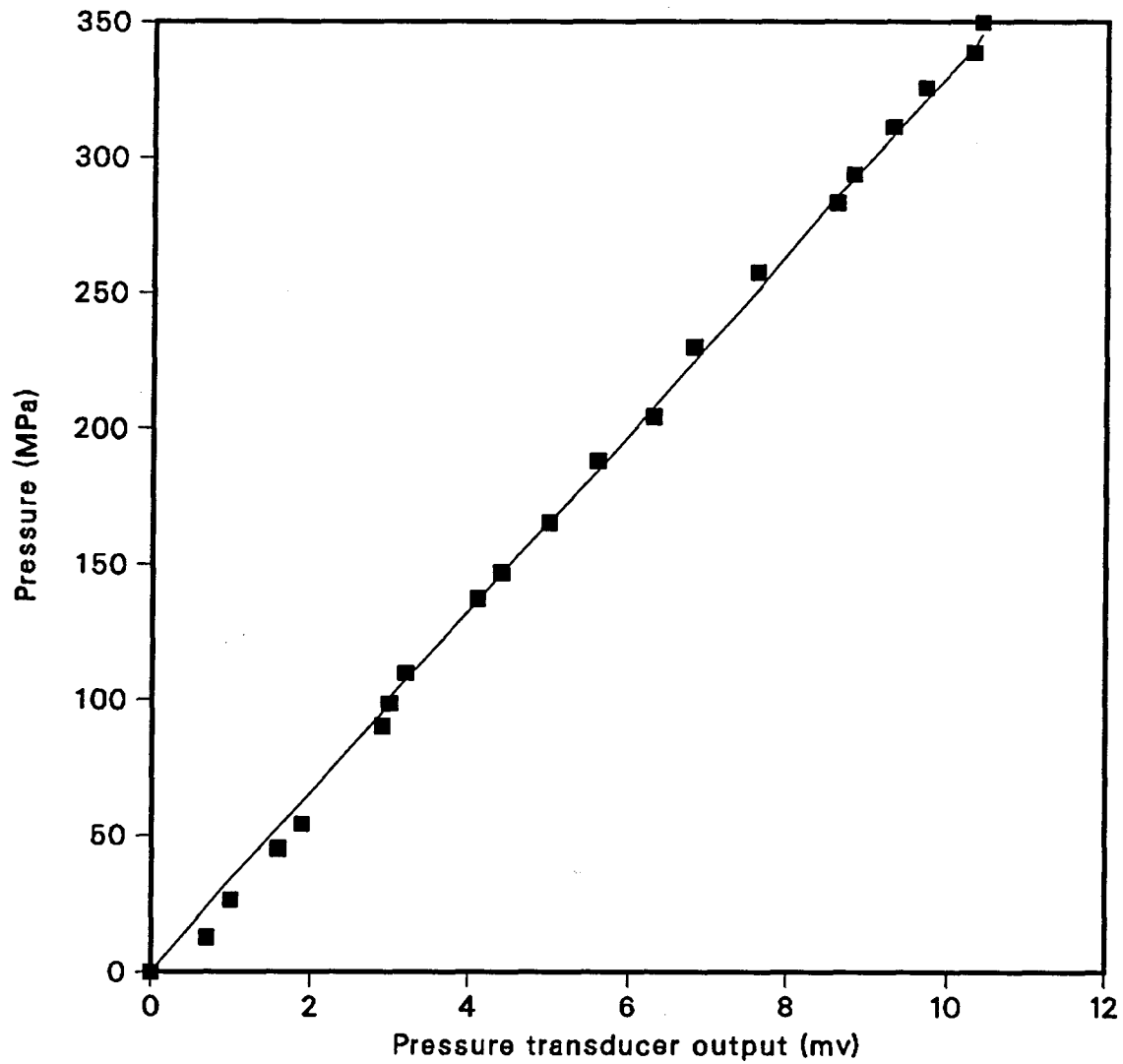


Figure 4-22: Calibration curve for pressure transducer #3 (PX600-5K6V).

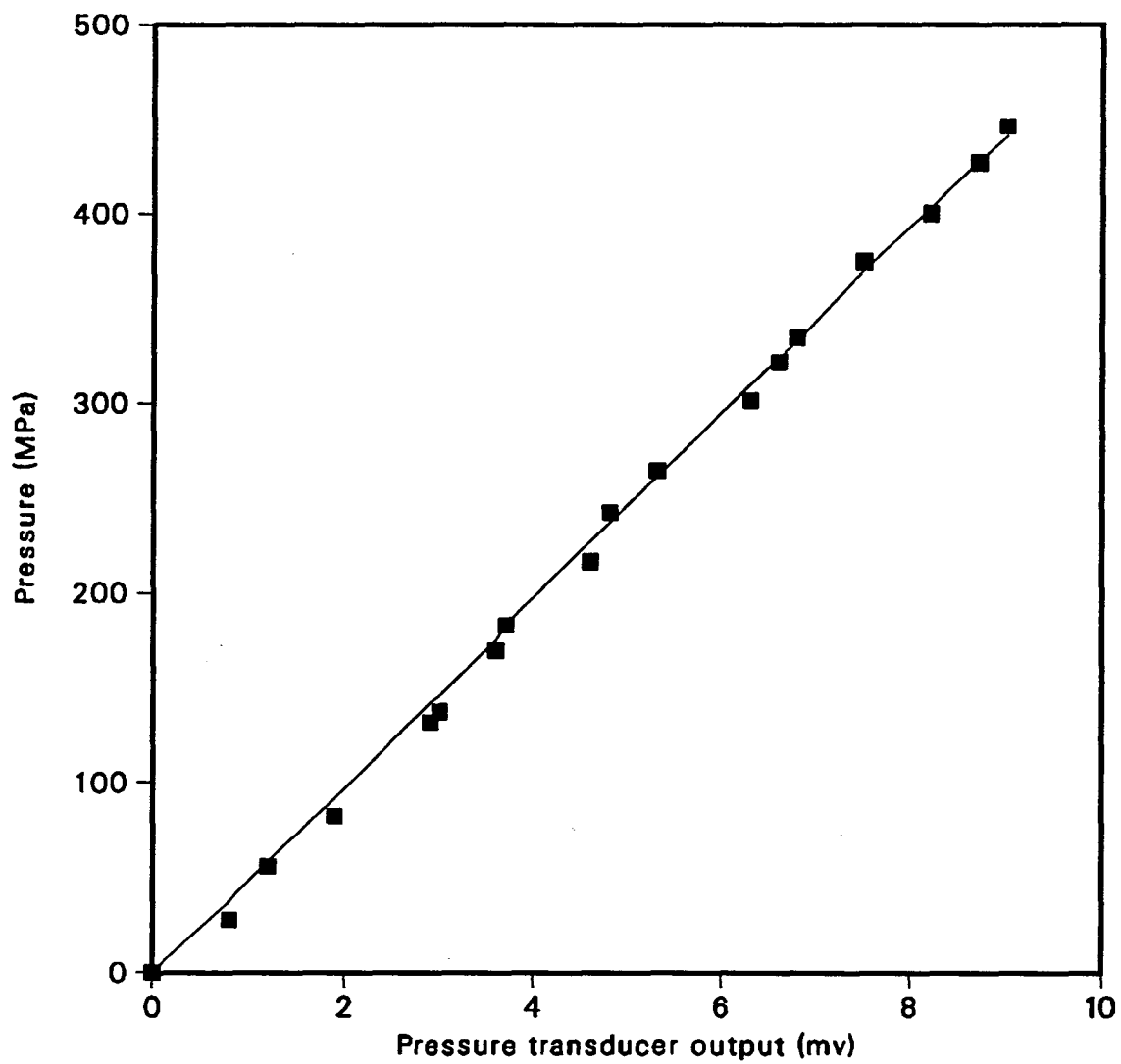


Figure 4-23: Calibration curve for pressure transducer #4 (PX600-10K6V).

4.3.5 Procedure for Extrusion Experiments

4.3.5.1 Extrusion of Newtonian Fluid

The screw extruder was first tested with an oil of known viscosity (130 Pa·s @ 20°C) and which exhibits Newtonian behavior. Typical results are shown in Figure 4.24. The mathematical model used to calculate the predicted values in the figure was presented in Chapter 3. Figure 4.24 indicates that the predicted values exceed the experimental results by about 20% to 50%. The discrepancy is probably due to ignoring the clearance between the screw and the barrel and the temperature gradient in the radial direction. From the figure, it can also be seen that the differences between the predicted values and experimental ones are larger for the points close to the extruder inlet. This is probably caused by the inlet effects. The reasonably good agreement between the predicted results and the experimental measurements using a Newtonian fluid shows that the mathematical model may be predicting the extrusion process well when it is applied to the Canola paste.

4.3.5.2 Extrusion of Canola Pastes

Before the extrusion experiments, the precrushed Canola seed paste was placed in a centrifuge and subjected to 1000 rpm for one minute to expel air trapped in the paste. Experiments showed that higher speeds and longer times caused the solid and liquid in the paste to separate.

The thermocouple used for measuring the room temperature, which was chosen as a reference temperature, was connected to the first channel of the

A/D board DAS-8. Channels from number 2 to 7 were linked to the thermocouples, and channels number 8 to 11 were assigned to the pressure transducers. The sampling rate for each channel was set to 30 readings per second and the sampling period was 10 seconds. At steady state, this sampling period could take at least 6 full pressure signal waves, which was found to be enough for data analysis. The temperatures were converted from mV into °C with a 5th order polynomial in the software LabTech. To speed the data logging process, all the acquired data from the D/A board were stored in a RAM drive and later transferred to floppy disks. It was found that a 286-AT personal computer equipped with a floating-point-coprocessor had the minimum capacity required to fulfill this data logging task.

The screw speeds were chosen as 66.5, 88.5 and 100.5 rpm as higher speeds would cause high temperatures and shear rates which might not be covered by the available rheological data. The speed of the hydraulic motors was checked using a tachometer (Jaquet model 629) within the tested range.

The power fluid in the hydraulic drive system was set to the by-pass position before the electric motor was turned on to make the electric motor easier to start. The highly viscous paste was then pushed into the extruder by the gravitational force of the falling brass plunger which generated about 0.04 MPa pressure. The extruder was left running for about 5 minutes to reach steady state so that the temperature of the discharged extrudate did not change. The computer was then started to record the pressure and temperature for a 10 second period. The extruder discharge rate and discharge pressure were controlled by adjusting the cone (see part number 7 in the Figure 4-14) at the extruder's outlet and the discharge rate was obtained by noting the discharge and corresponding time.

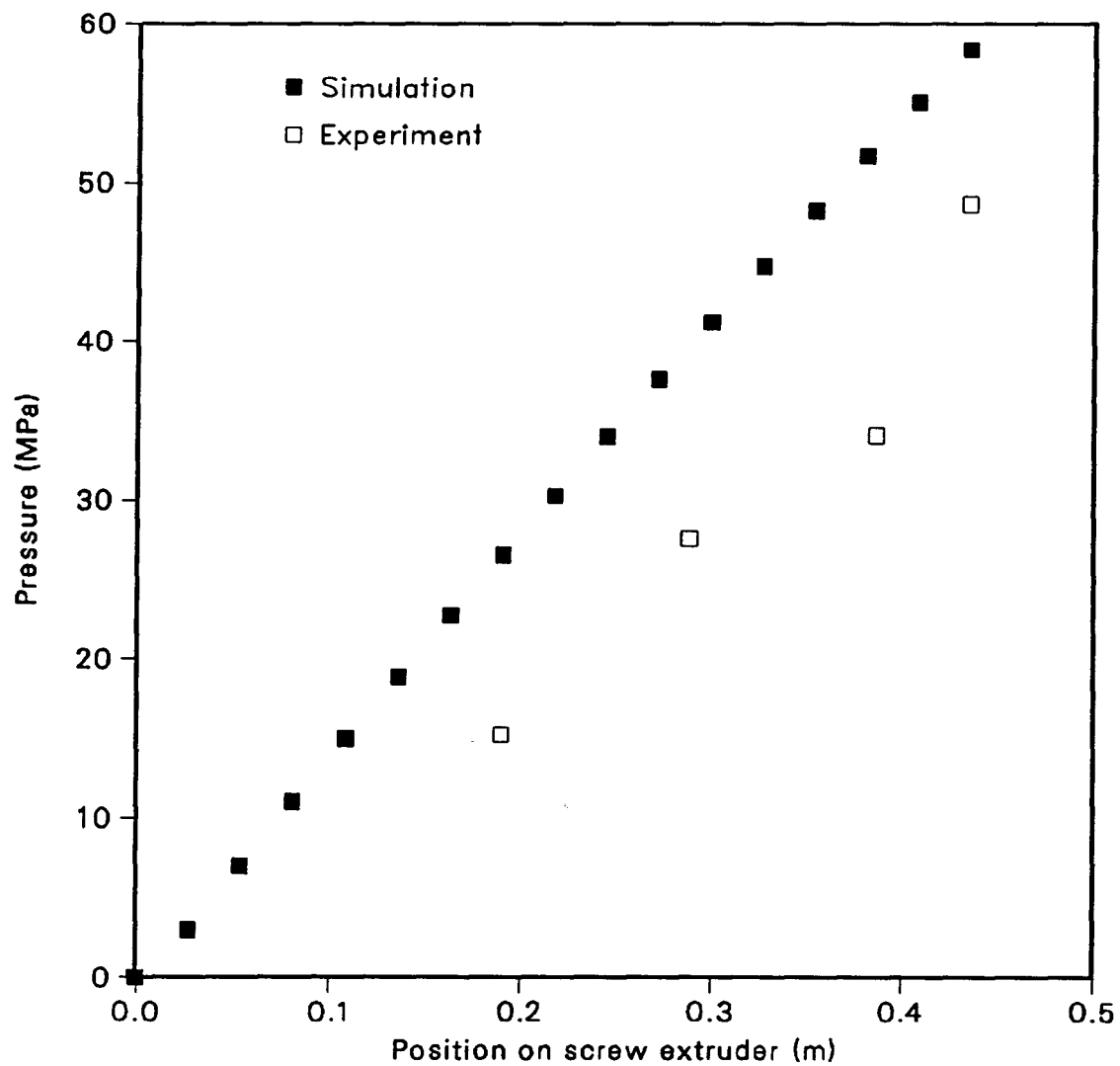


Figure 4-24: Extrusion with a Newtonian viscosity standard ($\theta = 5.98^\circ$, $N = 66.5$ rpm, $Q = 2.27$ kg/h).

CHAPTER FIVE

RESULTS AND DISCUSSION

5.1 Introduction

This chapter is divided into three principal parts. In the first part, the apparent viscosity of Canola paste is presented as a function of temperature, concentration and shear rate. The second part deals with the results from the extruder mathematical model and compares them with the experimental findings. The last part addresses the extractibility of extruded pastes using supercritical carbon dioxide.

5.2 Apparent Viscosity of Canola Pastes

5.2.1 Dependency on Shear Rate

The apparent viscosities were determined using a rotational viscometer at operating shear rates ranging from 0.15 to 100 s⁻¹.

Figures 5-1 to 5-5 show the total shear stress (τ) as a function of shear rate for different temperatures and concentrations. In these figures, the symbols represent experimental data and the curves are the predicted values from the regression analyses. From these figures, it is difficult to see what kind of

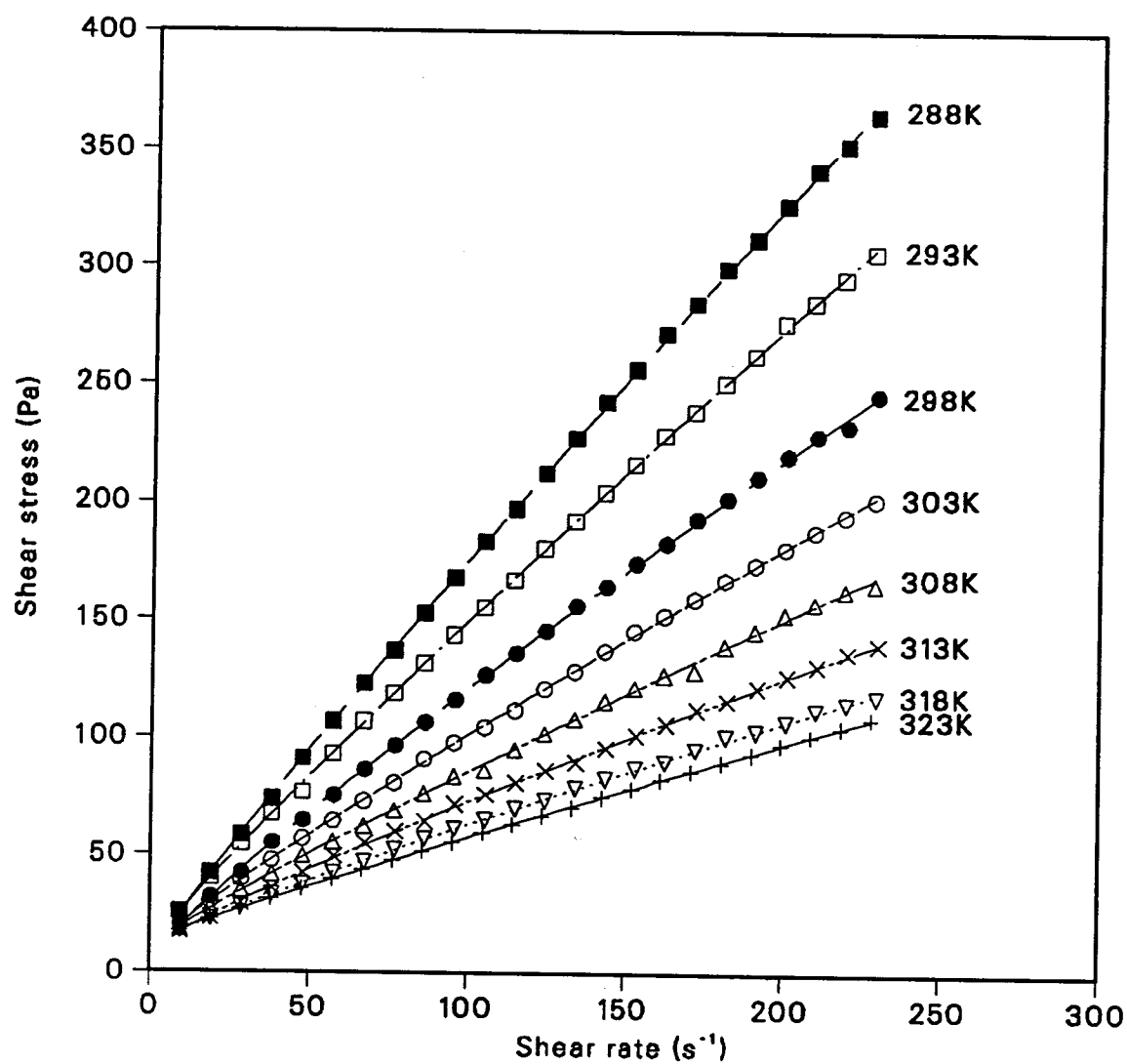


Figure 5-1: Total shear stress as a function of shear rate at a Canola concentration of 35.3% (g solid/g liquid) using the rotational viscometer.

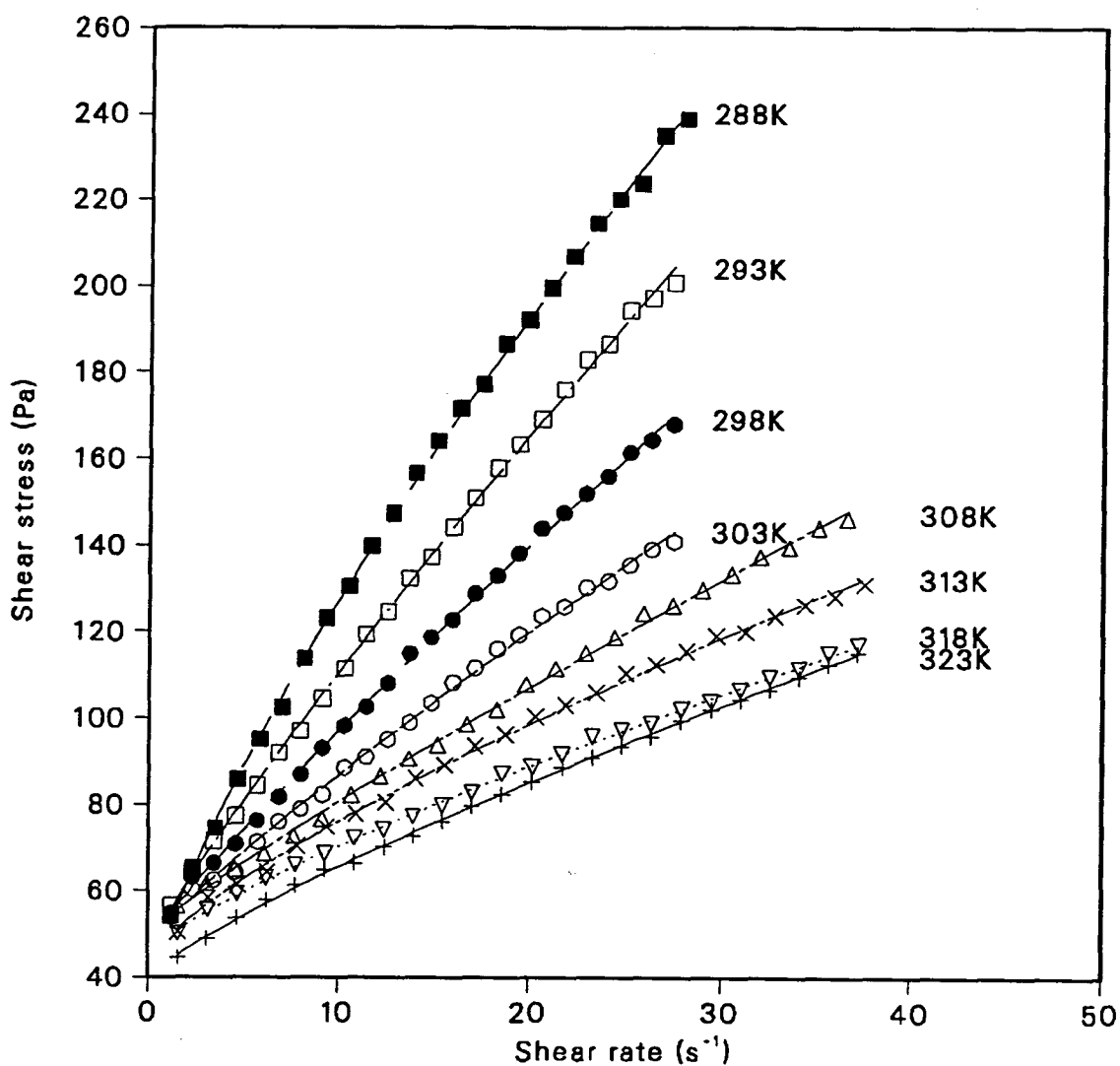


Figure 5-2: Total shear stress as a function of shear rate at a Canola concentration of 53.4% (g solid/g liquid) using the rotational viscometer.

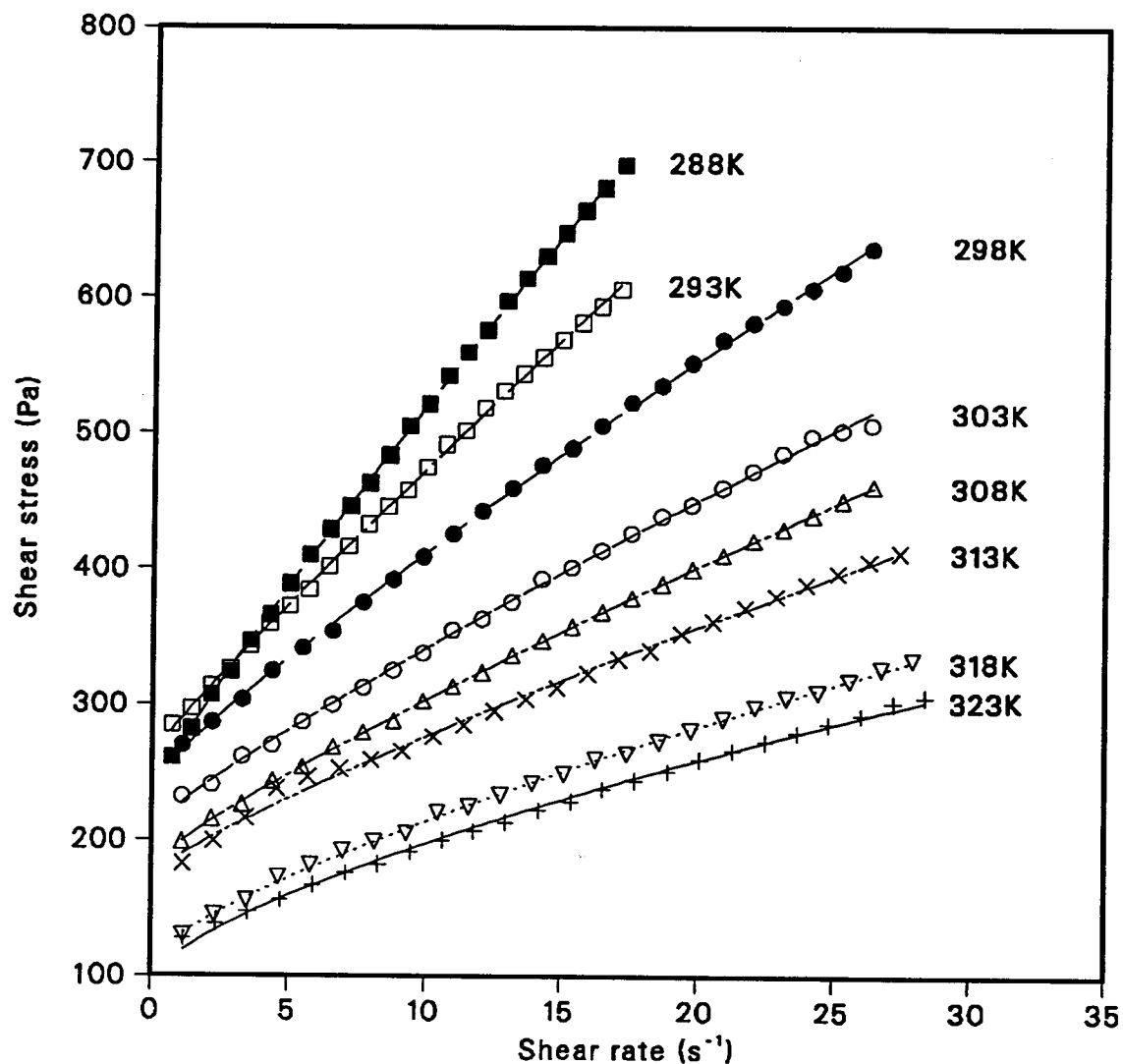


Figure 5-3: Total shear stress as a function of shear rate at a Canola concentration of 64.5% (g solid/g liquid) using the rotational viscometer.

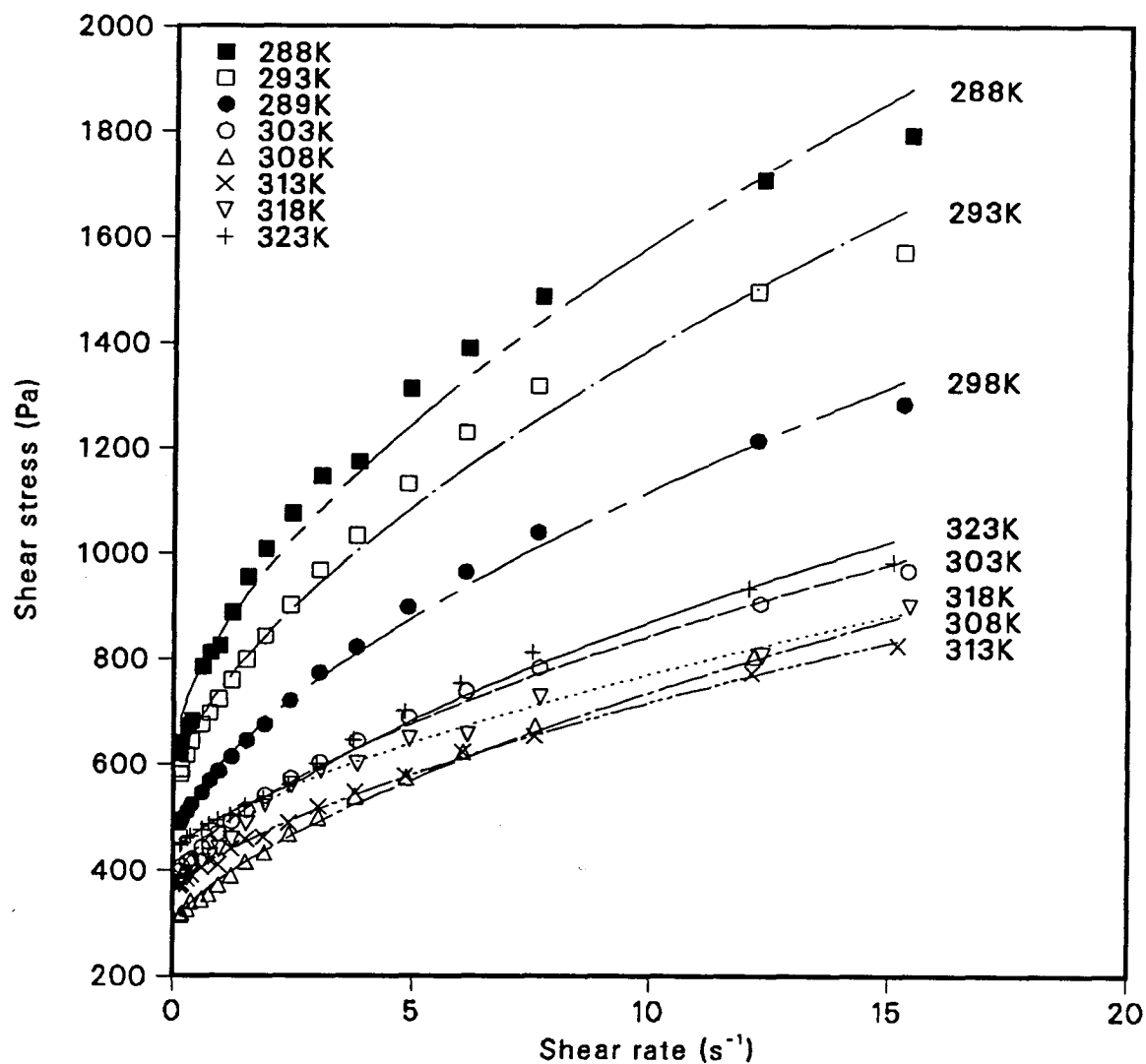


Figure 5-4: Total shear stress as a function of shear rate at a Canola concentration of 84.2% (g solid/g liquid) using the rotational viscometer.

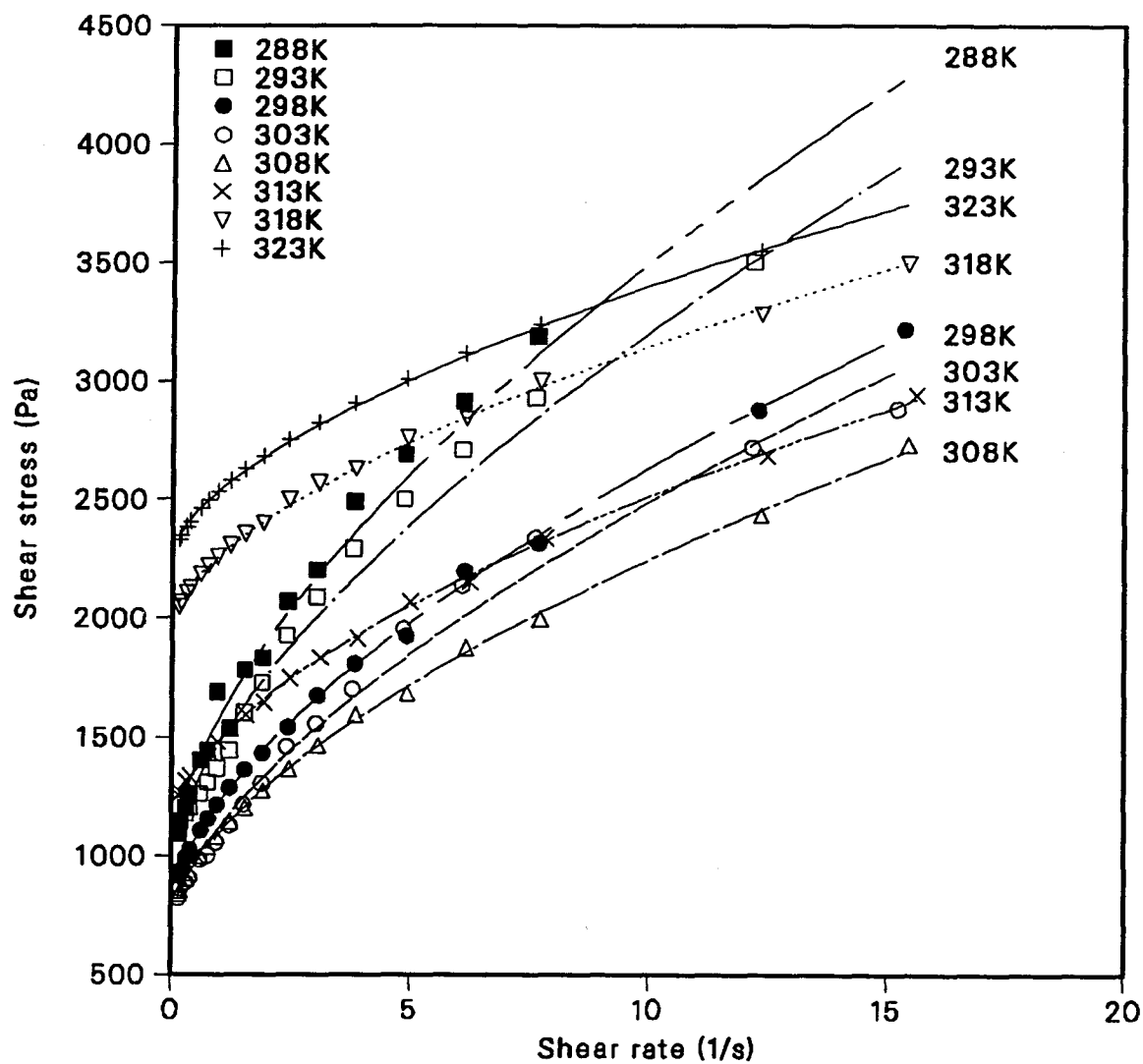


Figure 5-5: Total shear stress as a function of shear rate at a Canola concentration of 95.7% (g solid/g liquid) using the rotational viscometer.

relationship exists between the shear stresses and shear rates. If the shear stress differences ($\tau - \tau_0$) are plotted against the shear rates as shown in Figures 5-6 to 5-10, it can be seen that Canola pastes exhibit pseudoplastic behavior similar to many other biomaterials and it is evident that Canola pastes follow a power law expression with a flow behavior index $n < 1$, i. e.,

$$\tau - \tau_0 = m \left(\dot{\gamma} \right)^n \quad (5-1)$$

The experimental data were regressed using the above equation and the results are shown in Table 5-1. The quality of the various fits was expressed in terms of the correlation coefficient, R^2 , defined as:

$$R^2 = \frac{\sum (\tau_{obe} - \tau_{ave})^2 - \sum (\tau_{obe} - \tau_{reg})^2}{\sum (\tau_{obe} - \tau_{ave})^2} \quad (5-2)$$

where τ_{obe} is the experimental data, τ_{ave} is the arithmetic average of the data and τ_{reg} is the regressed value. The correlation coefficient values given in Table 5-1 show that the regression is satisfactory and that the power law is able to describe the rheological behavior of Canola pastes within the ranges of shear rates, temperatures and concentrations studied.

Similar to the definition of viscosity for a Newtonian fluid, the apparent viscosity, η , of a non-Newtonian fluid is defined as:

$$\Delta\tau = \eta \dot{\gamma} \quad (5-3)$$

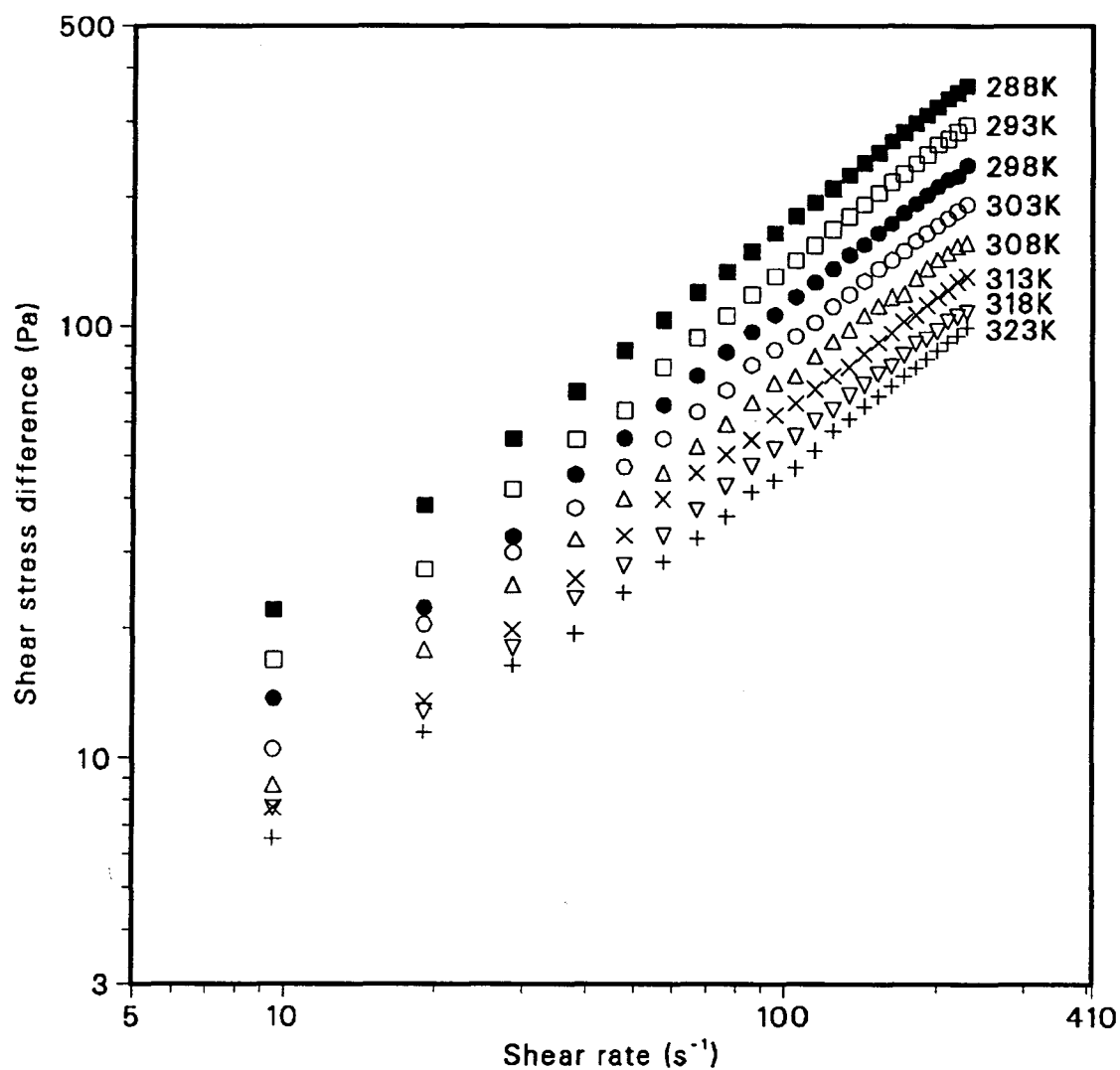


Figure 5-6: Shear stress difference ($\tau - \tau_0$) as a function of shear rate at a Canola concentration of 35.3% (g solid/g liquid) using the rotational viscometer.

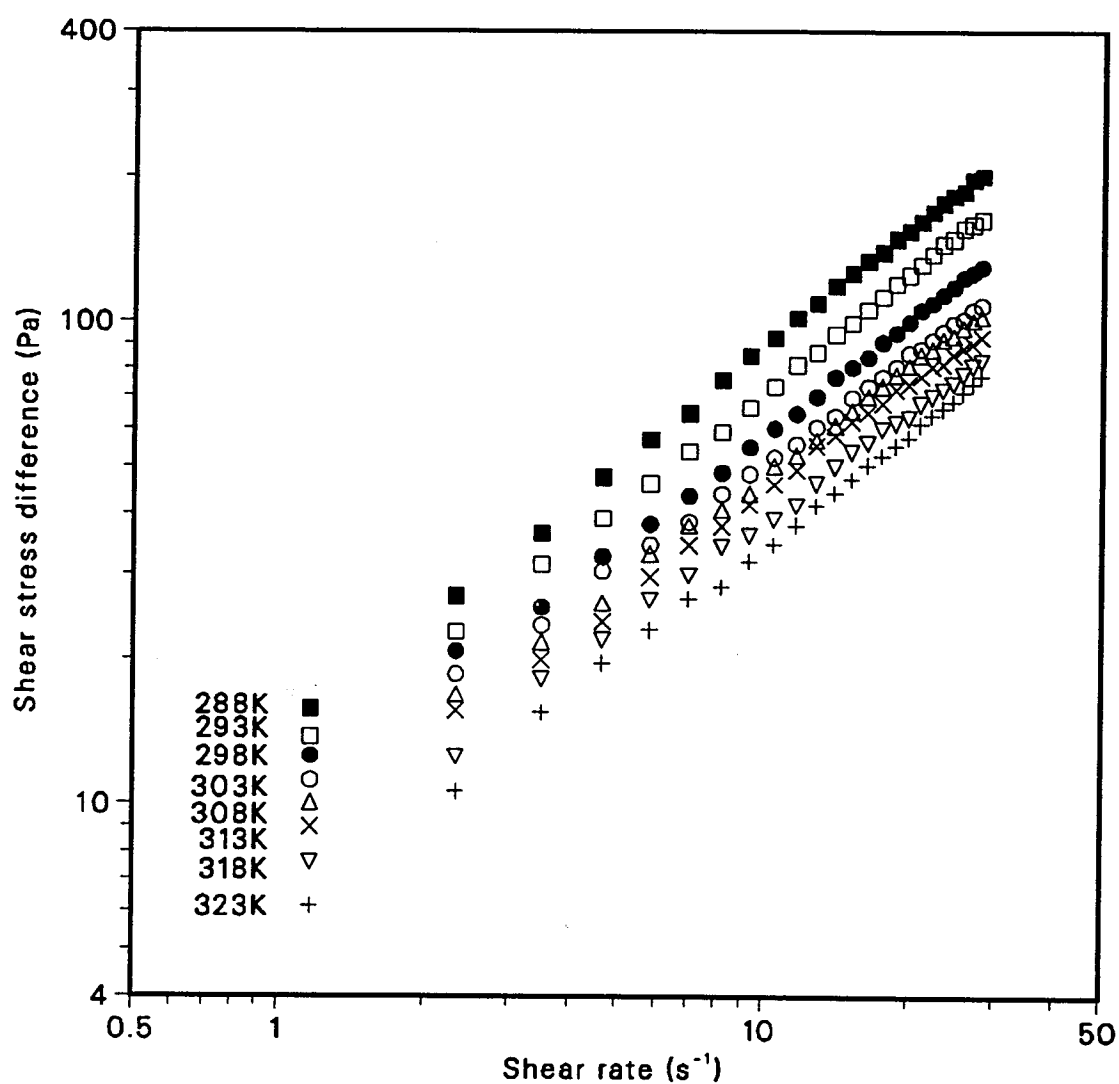


Figure 5-7: Shear stress difference ($\tau - \tau_0$) as a function of shear rate at a Canola concentration of 53.4% (g solid/g liquid) using the rotational viscometer.

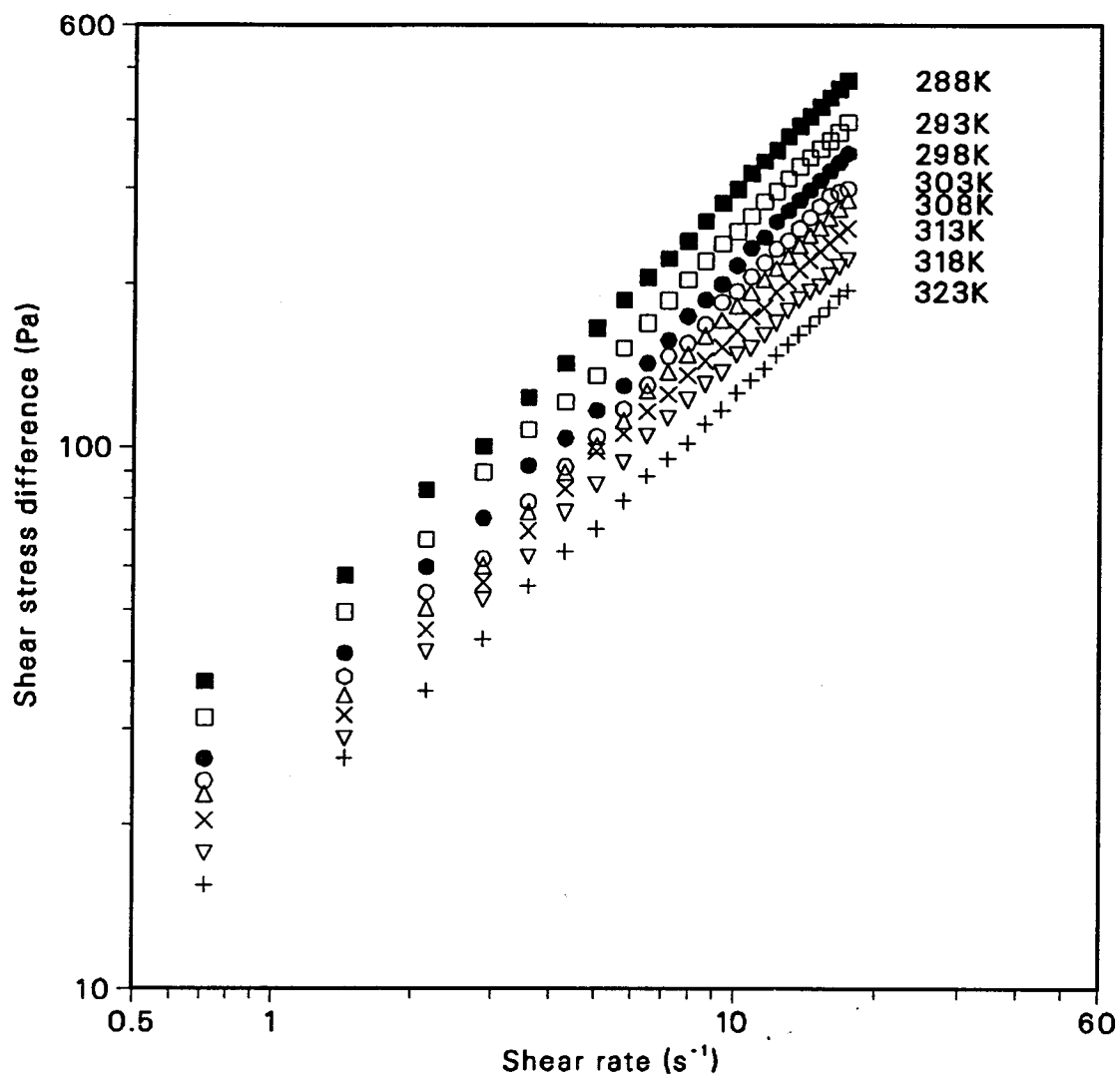


Figure 5-8: Shear stress difference ($\tau - \tau_0$) as a function of shear rate at a Canola concentration of 64.5%(g solid/g liquid) using the rotational viscometer.

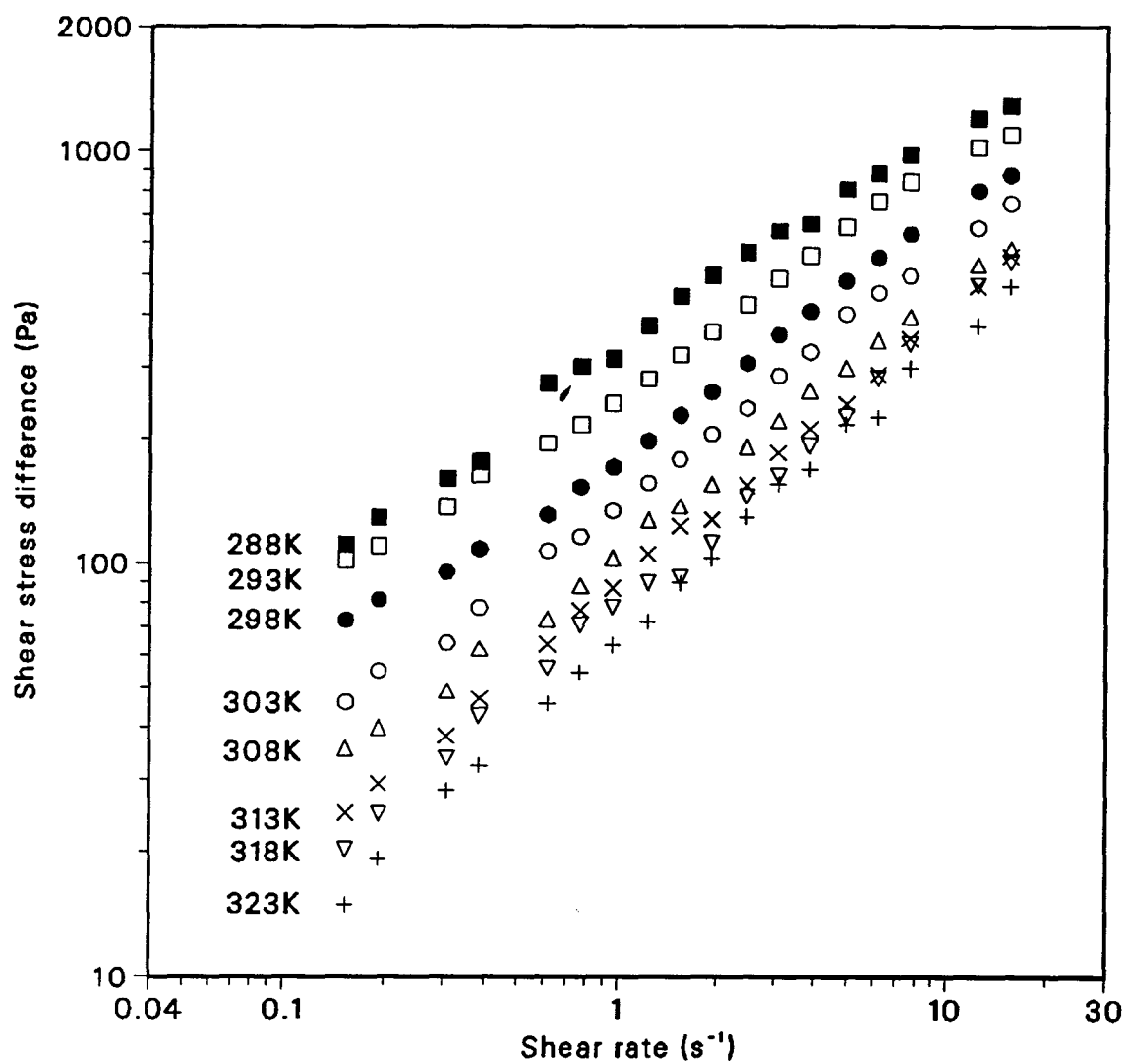


Figure 5-9: Shear stress difference ($\tau - \tau_0$) as a function of shear rate at a Canola concentration of 84.2% (g solid/g liquid) using the rotational viscometer.

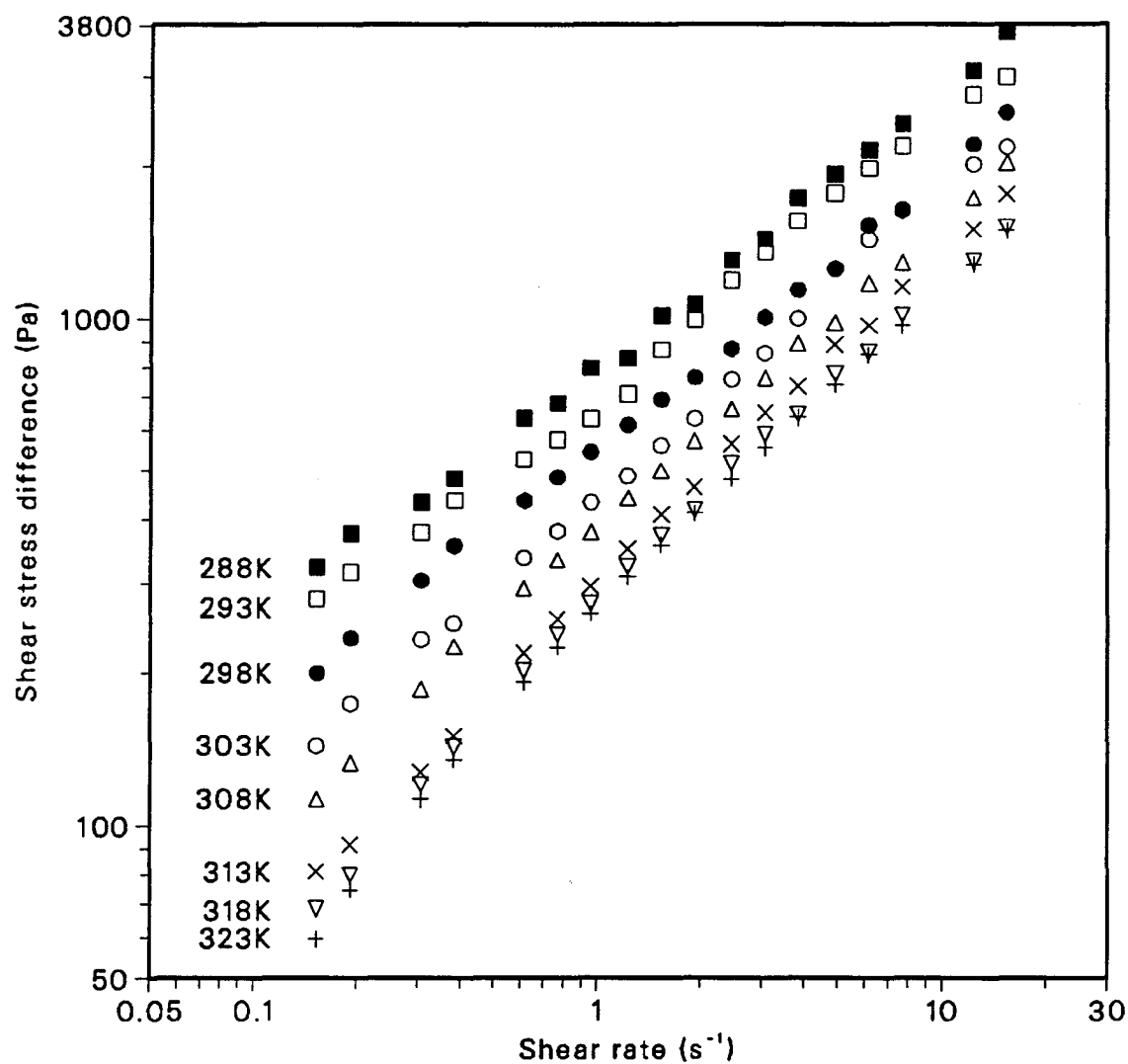


Figure 5-10: Shear stress difference ($\tau - \tau_0$) as a function of shear rate at a Canola concentration of 95.7% (g solid/g liquid) using the rotational viscometer.

Table 5-1: Consistency coefficient (m) and flow behavior index (n) for Canola pastes at various temperatures and concentrations.

Conc. (g solid/g liquid)	Temp. (K)	m (Pa s ^{n})	n	τ_0 (Pa)	R^2
0.353	288	0.83	0.9061	11.82	0.9678
0.353	293	0.66	0.9113	9.21	0.9956
0.353	298	0.64	0.9043	8.76	0.9987
0.353	303	0.47	0.9102	8.01	0.9938
0.353	308	0.39	0.9049	8.76	0.9957
0.353	313	0.41	0.8975	7.56	0.9985
0.353	318	0.30	0.9064	3.87	0.9559
0.353	323	0.20	0.8902	3.27	0.9712
0.534	288	4.81	0.8684	33.03	0.9805
0.534	293	3.84	0.8756	43.56	0.9393
0.534	298	3.56	0.8416	44.55	0.9595
0.534	303	2.77	0.8425	44.94	0.9792
0.534	308	2.22	0.8462	46.74	0.9424
0.534	313	2.26	0.8490	40.77	0.9209
0.534	318	2.02	0.8672	42.57	0.9409
0.534	323	1.57	0.8722	36.66	0.9625
0.645	288	15.8	0.755	216.3	0.9784
0.645	293	12.9	0.748	245.7	0.9505

Table 5-1: (Continuous) Consistency coefficient (m) and flow behavior index (n) for Canola pastes at various temperatures and concentrations.

0.645	298	9.1	0.807	225.9	0.9541
0.645	303	8.6	0.807	195.0	0.9790
0.645	308	7.2	0.798	169.5	0.9726
0.645	313	6.7	0.801	161.4	0.9866
0.645	318	6.1	0.758	103.2	0.9915
0.645	323	5.8	0.753	89.1	0.9920
0.842	288	107.4	0.632	574.5	0.9132
0.842	293	89.3	0.629	519.3	0.9315
0.842	298	65.8	0.636	419.4	0.9515
0.842	303	55.4	0.636	343.2	0.9628
0.842	308	45.9	0.638	266.7	0.9550
0.842	313	35.1	0.645	327.0	0.9491
0.842	318	31.9	0.671	307.8	0.9847
0.842	323	25.6	0.688	399.6	0.9600
0.957	288	251.7	0.604	722.1	0.8796
0.957	293	225.9	0.604	915.3	0.9265
0.957	298	137.5	0.576	731.7	0.9387
0.957	303	150.4	0.607	687.9	0.8991
0.957	308	147.8	0.608	669.0	0.9132
0.957	313	115.4	0.611	1047.3	0.9365
0.957	318	90.4	0.614	1851.3	0.9419
0.957	323	85.9	0.615	2122	0.9492

By comparing Equation (5-3) with Equation (5-1), it is obvious that the apparent viscosity can be expressed in terms of shear rate as:

$$\eta = m\dot{\gamma}^{n-1} \quad (5-4)$$

Figures 5-11 to 5-15 show how the apparent viscosity of Canola paste varies with shear rate at different temperatures and concentrations.

From the figures and table, it can be seen that both consistency coefficient (m) and flow behavior index (n) are functions of temperature and concentration, but that m is more sensitive than n to changes in temperature. For example, at a concentration of 35.3%, when the temperature changes from 288K to 293K, the m value varies $(0.83 - 0.66)/0.83 \cong 20\%$, whereas the n value changes $(0.9113 - 0.9061)/0.9061 \cong 1\%$ which is about an order of magnitude less than changes in m . This finding is consistent with the conclusion from Metzner (1956) who stated:

".....changes in m with temperature are usually an order of magnitude greater than changes in n ."

"The flow behavior index n may be assumed independent of temperature and concentration for small changes in such conditions....."

"The flow behavior indexdoes not change rapidly with temperature of dissolved material."

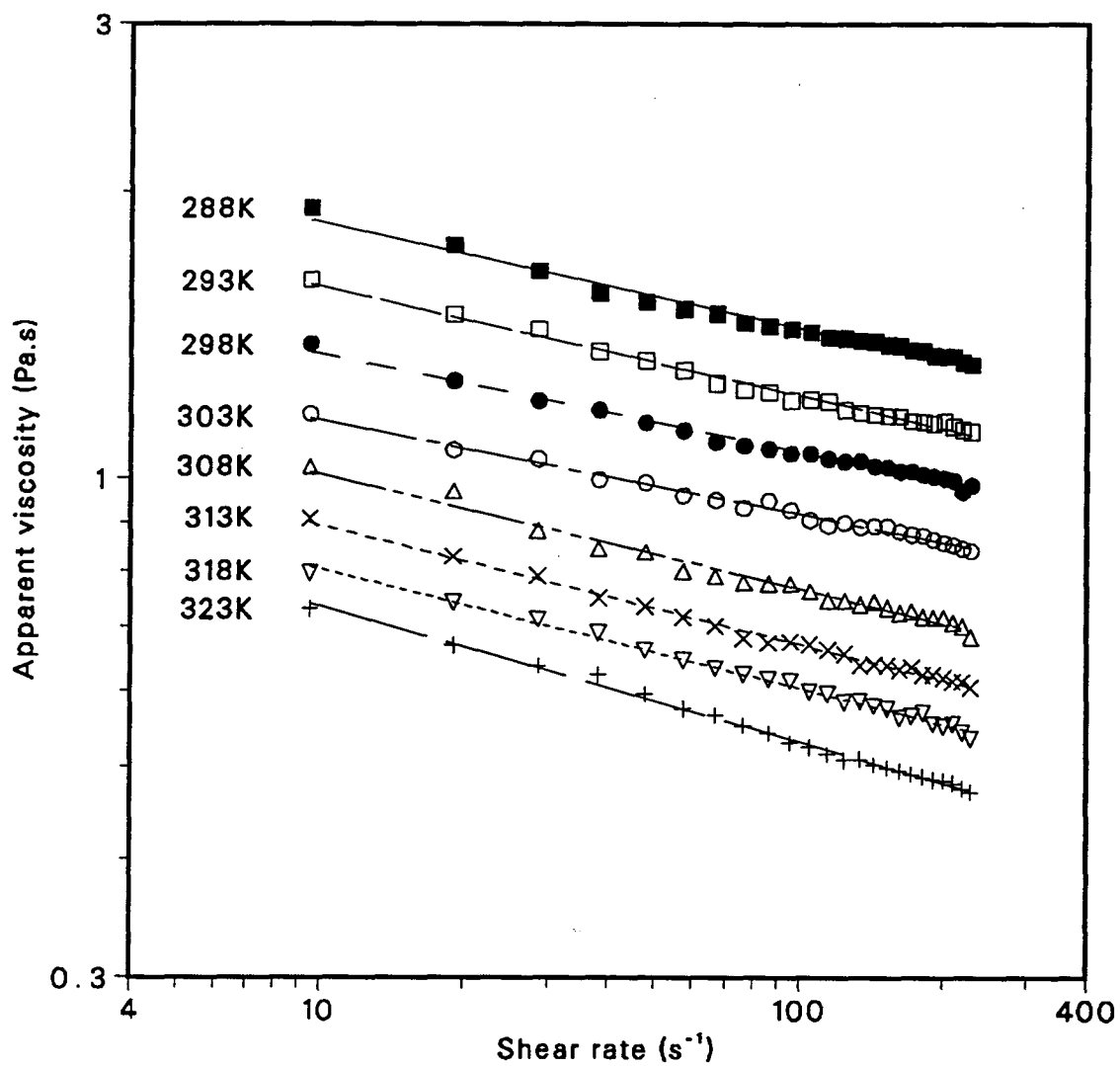


Figure 5-11: Apparent viscosity as a function of shear rate at a Canola concentration of 35.3% (g solid/g liquid) using the rotational viscometer.

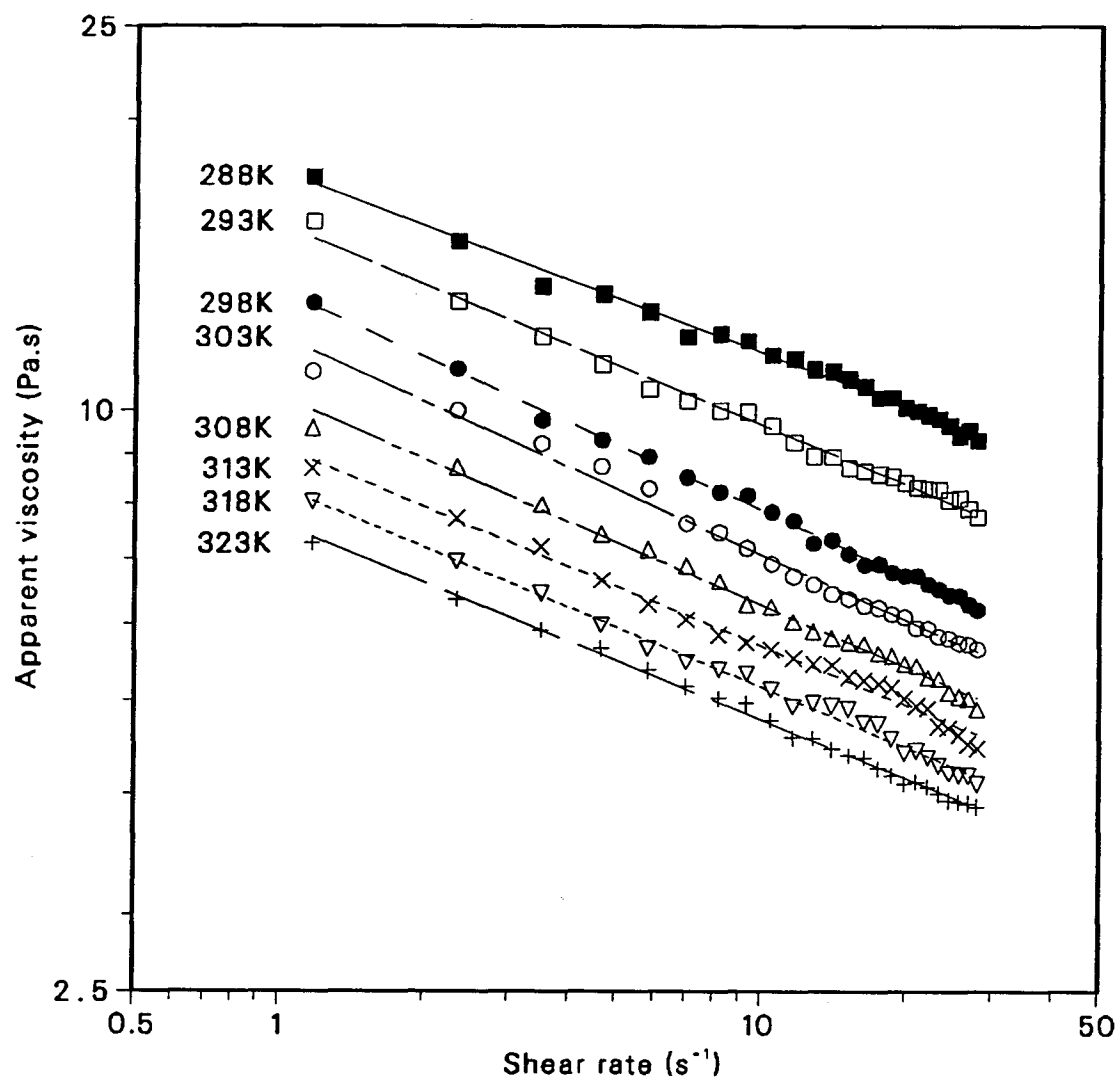


Figure 5-12: Apparent viscosity as a function of shear rate at a Canola concentration of 53.4% (g solid/g liquid) using the rotational viscometer.

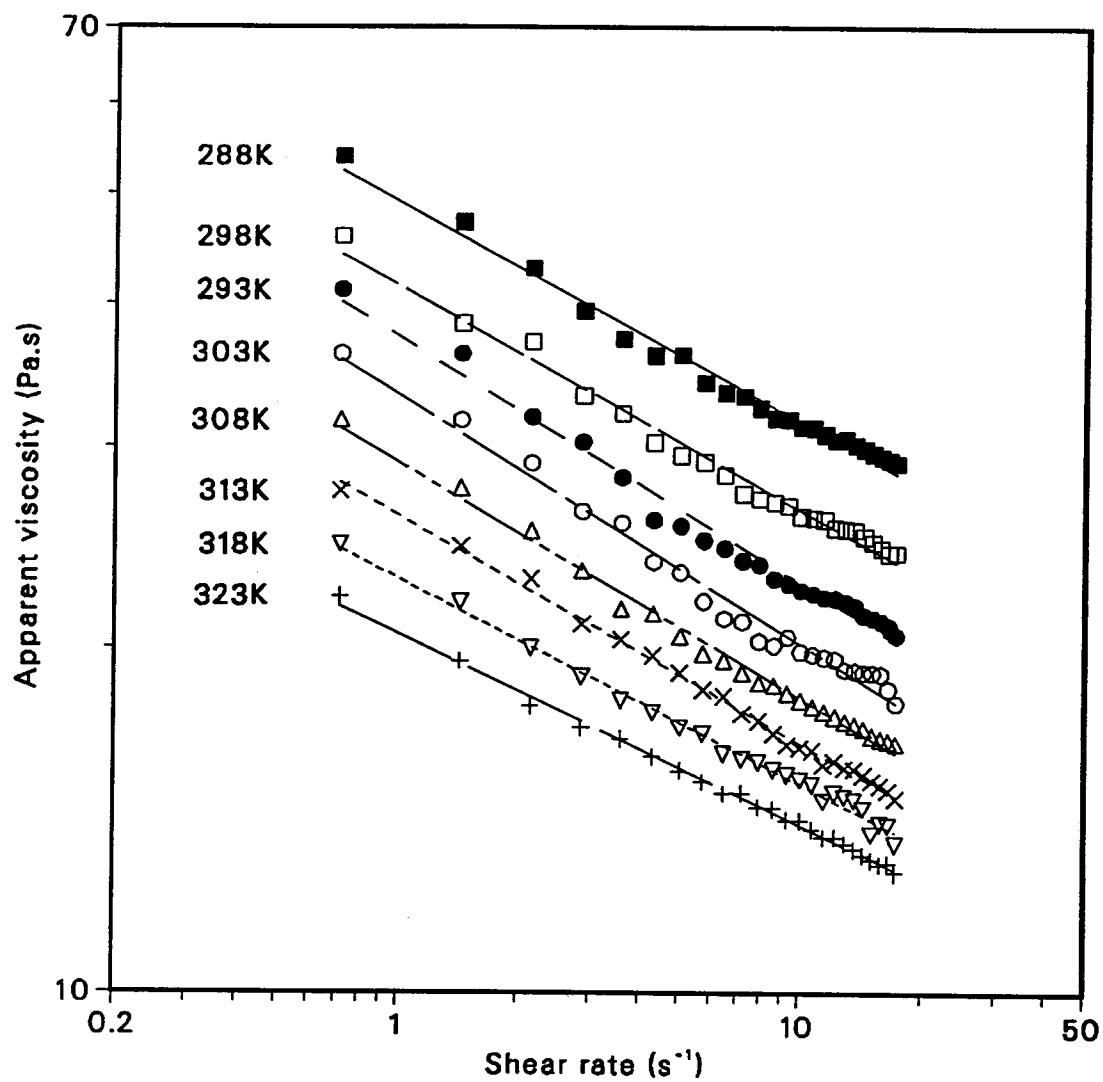


Figure 5-13: Apparent viscosity as a function of shear rate at a Canola concentration of 64.5% (g solid/g liquid) using the rotational viscometer.

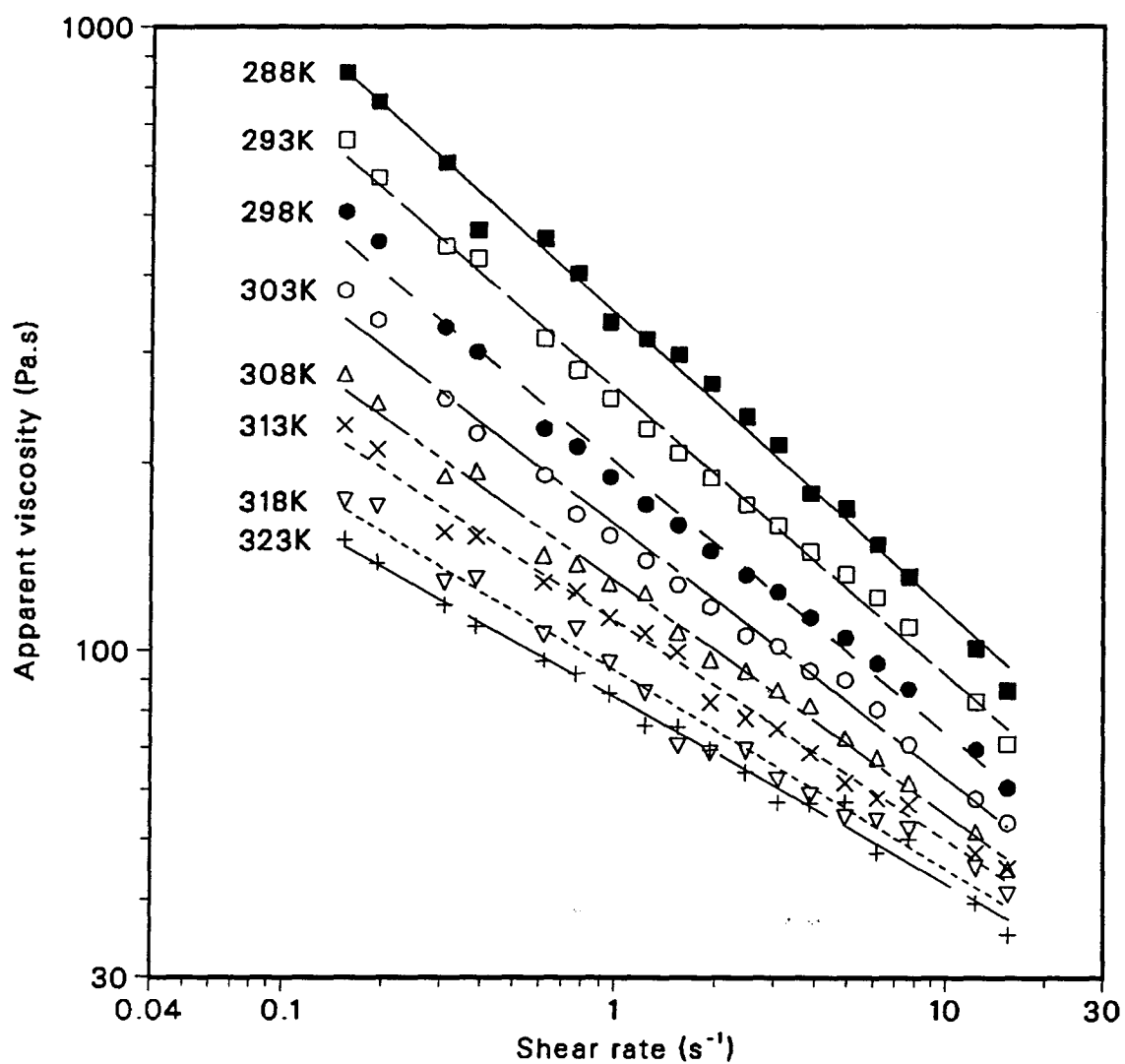


Figure 5-14: Apparent viscosity as a function of shear rate at a Canola concentration of 84.2% (g solid/g liquid) using the rotational viscometer.

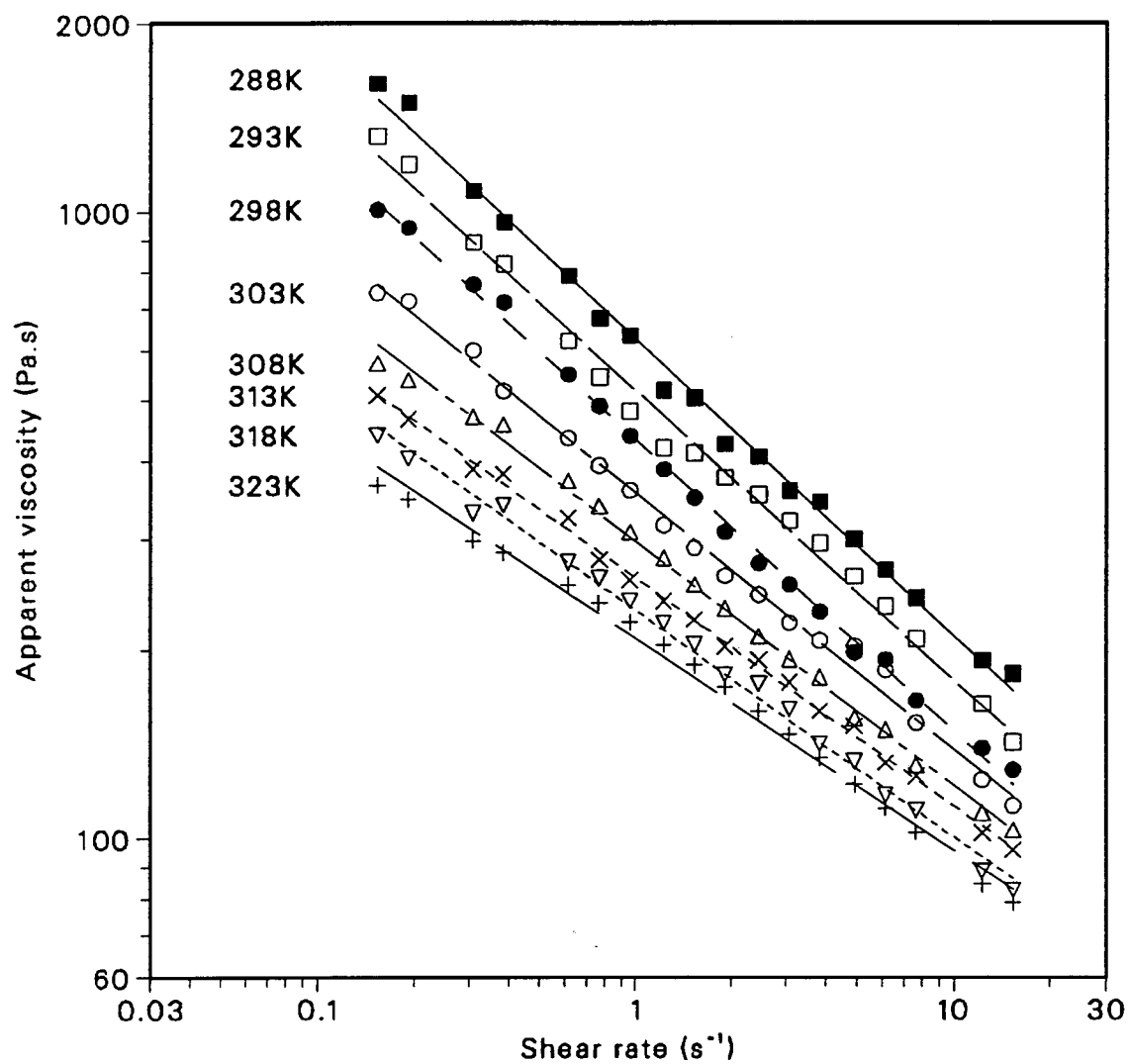


Figure 5-15: Apparent viscosity as a function of shear rate at a Canola concentration of 95.7% (g solid/g liquid) using the rotational viscometer.

The flow behavior indices (n) are the slopes of the logarithmic plots (Figures 5-6 to 5-10). The values of n range from a high of 0.91 to a low of 0.58 and, since they are less than unity, Equation (5-4) shows that the apparent viscosity decreases with an increase in shear rates. This suggests at least two possible mechanisms to account for the rheological behavior of Canola paste (Skelland, 1967):

Fluid dispersions of asymmetric molecules or particles are probably characterized by extensive entanglement of the particles when the fluid is at rest. Progressive disentanglement should occur under the influence of shearing forces, and the particles should tend to orient themselves in the direction of shear. This orienting influence is proportional to shear rate and is opposed by the randomly disorienting effects of Brownian movement, the extent of which is determined by the concentration of a given fluid.

Pseudoplastic behavior would also be consistent with the existence of highly solvated molecules or particles in the dispersion. Progressive shearing of solvated layers with increasing shear rate would result in decreasing interaction between the particles (because of their smaller effective size) and consequent reduction in apparent viscosity.

Although thixotropic fluids show apparent pseudoplastic behavior, the major difference between the shear rate sensitivity of thixotropic and pseudoplastic system lies in the time required to reach stable shear-induced conditions. This

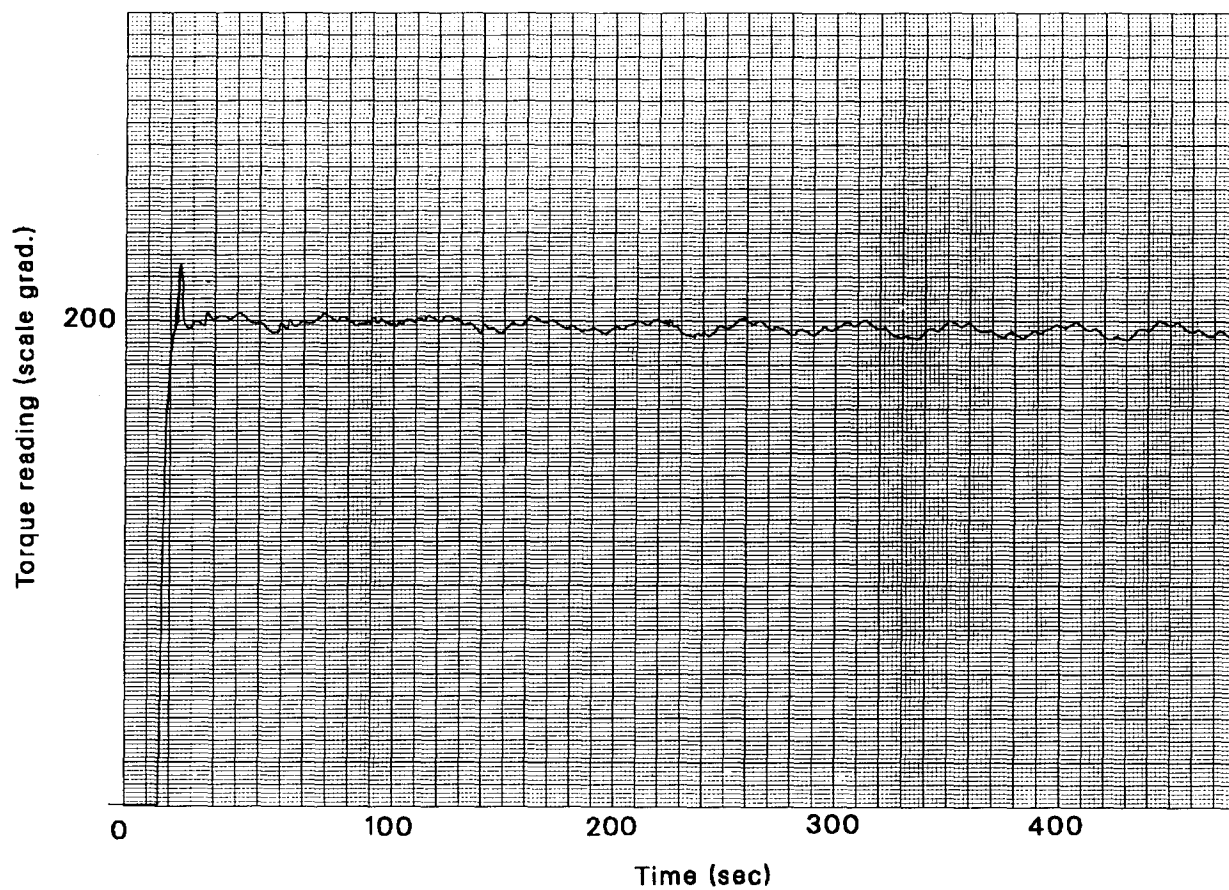


Figure 5-16: Torque readings as a function of time for Canola paste at a Canola concentration of 95.7% (g solid/g liquid) and temperature of 25 °C using the rotational viscometer at a speed of 0.01 rpm.

time is thought to be instantaneous for pseudoplastic fluids, whereas a relatively long time is required for thixotropic fluids. The latter may require several minutes or longer time before equilibrium is established. The present experimental results show (Figure 5-16) that the response time of Canola paste is very short. The paste, therefore, behaves in a non-thixotropic fashion.

Since the consistency coefficient (m) is the intercept on the η axis at unit shear rate, the apparent viscosity is proportional to the consistency coefficient. The relationship between m and temperature (T) and concentration (C) is therefore equivalent to the relationship between the apparent viscosity η and T and C .

5.2.2 Dependency on Temperature

Figure 5-17 shows the apparent viscosity of Canola paste as a function of temperature and concentration for a constant rate of 10 s^{-1} . As can be seen from the figure, η decreases with an increase in temperature according to an Arrhenius-type relationship of the form

$$\eta = a \exp\left(\frac{-\Delta E}{R_c T}\right) \quad (5-5)$$

where T is the absolute temperature, R_c is the universal gas constant, a is a parameter and ΔE is the activation energy for viscous flow. The parameter ΔE expresses the energy barrier that must be overcome before the elementary flow process can occur, and is related to the coherence of the molecules in the paste.

A high value for ΔE indicates that the paste is highly associated and that a large amount of energy is required to bring about the dissociation needed to cause flow.

It is noteworthy that the apparent viscosity decreases at a faster rate in the temperature range of 288K to 303K than in the range of 303K to 323K. Furthermore, the apparent viscosity tends to increase if the temperature is raised above 323K. This phenomenon can be explained by the free volume theory (Tung, 1988).

Free volume theory is a model used to explain the flow of simple fluid systems and draws an analogy with the movement of rigid spheres in an imperfect lattice arrangement containing vacant positions or "holes". Flow is described as a series of movements by spheres from lattice positions into adjacent holes. With each move, a hole is left behind which in turn may be occupied by another sphere, and a coordinated movement of spheres would constitute flow. This flow mechanism is favored by the presence of many holes in the system. The total volume of holes in a paste is called the free volume, thus any factor that changes the free volume in a given liquid will influence its viscosity. Temperature and pressure are two such factors that affect free volume in different ways.

In the range of 288K to 303K, an increase in temperature might increase free volume, thus reducing the paste's apparent viscosity, but in the range 303K to 323K, a further increase in temperature might cause some of the starch in the paste to start solidifying, which would either reduce the free volume or enlarge

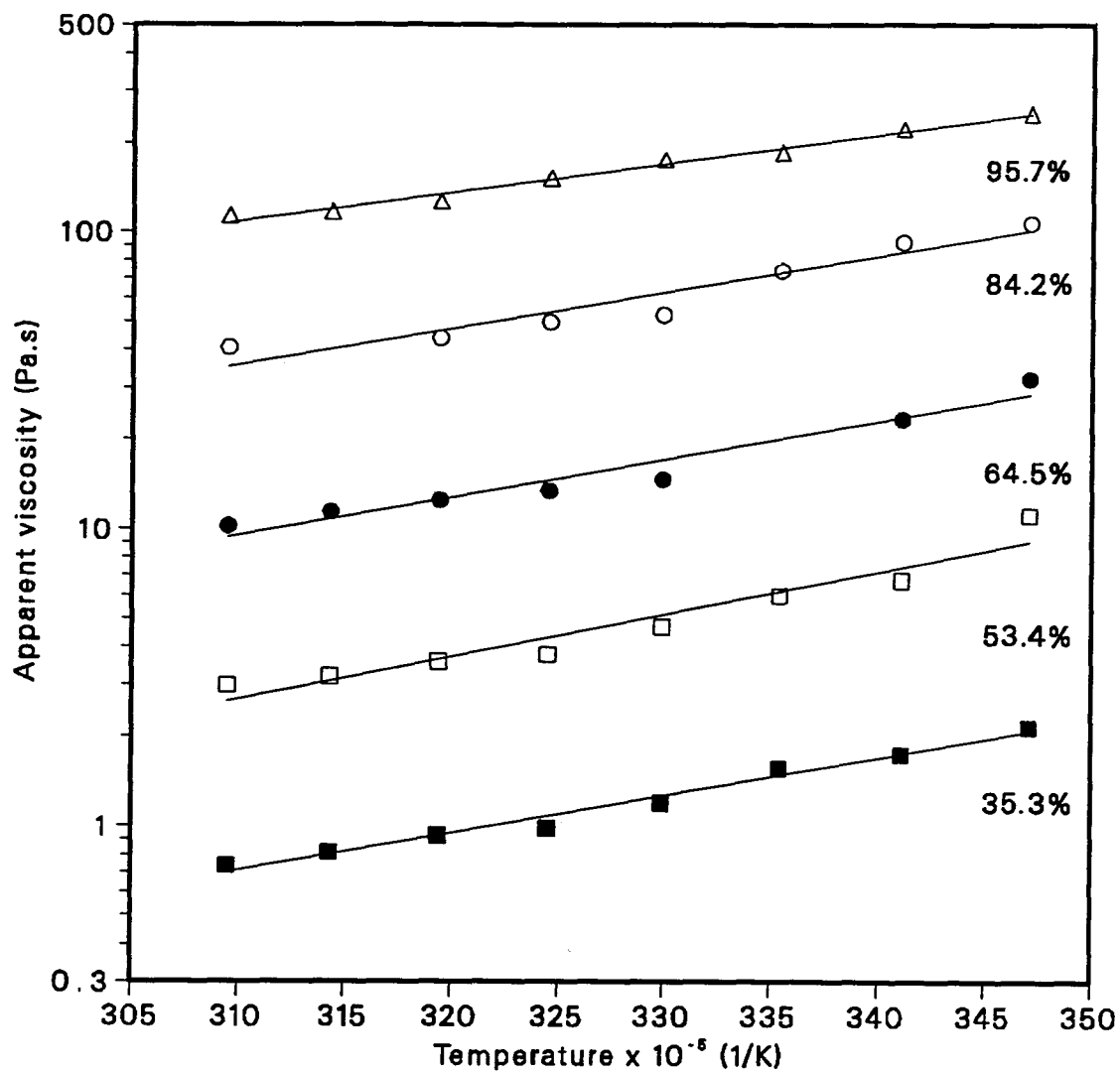


Figure 5-17: Apparent viscosity as a function of temperature for different Canola concentrations at a shear rate of 10 s^{-1} using the rotational viscometer.

the size of the particles in the paste. This creates a hindrance for the movement of the particles and results in an increase in the apparent viscosity.

5.2.3 Dependency on Concentration

The apparent viscosity is also plotted, in semi-log coordinates, as a function of concentration C and temperature T in Figure 5-18 for the same fixed shear rate of 10 s^{-1} .

It can be seen from the figure that the apparent viscosity is very sensitive to changes in concentration and, at a given temperature, it increases with increasing concentration. Microscopically, a material's viscosity is due to the interaction between the molecules in that material. The phenomenon of highly concentrated pastes having larger values of apparent viscosity might be explained as follows: as the particles in the paste come closer together, more particle collisions occur, resulting in increased interactions between the particles. An increase in apparent viscosity can therefore be observed.

Figure 5-18 suggests that the relationship between apparent viscosity and concentration can be expressed as:

$$\eta = a_c C^{b_c} \quad (5-6)$$

where a_c and b_c are constants depending on the shear rate and temperature.

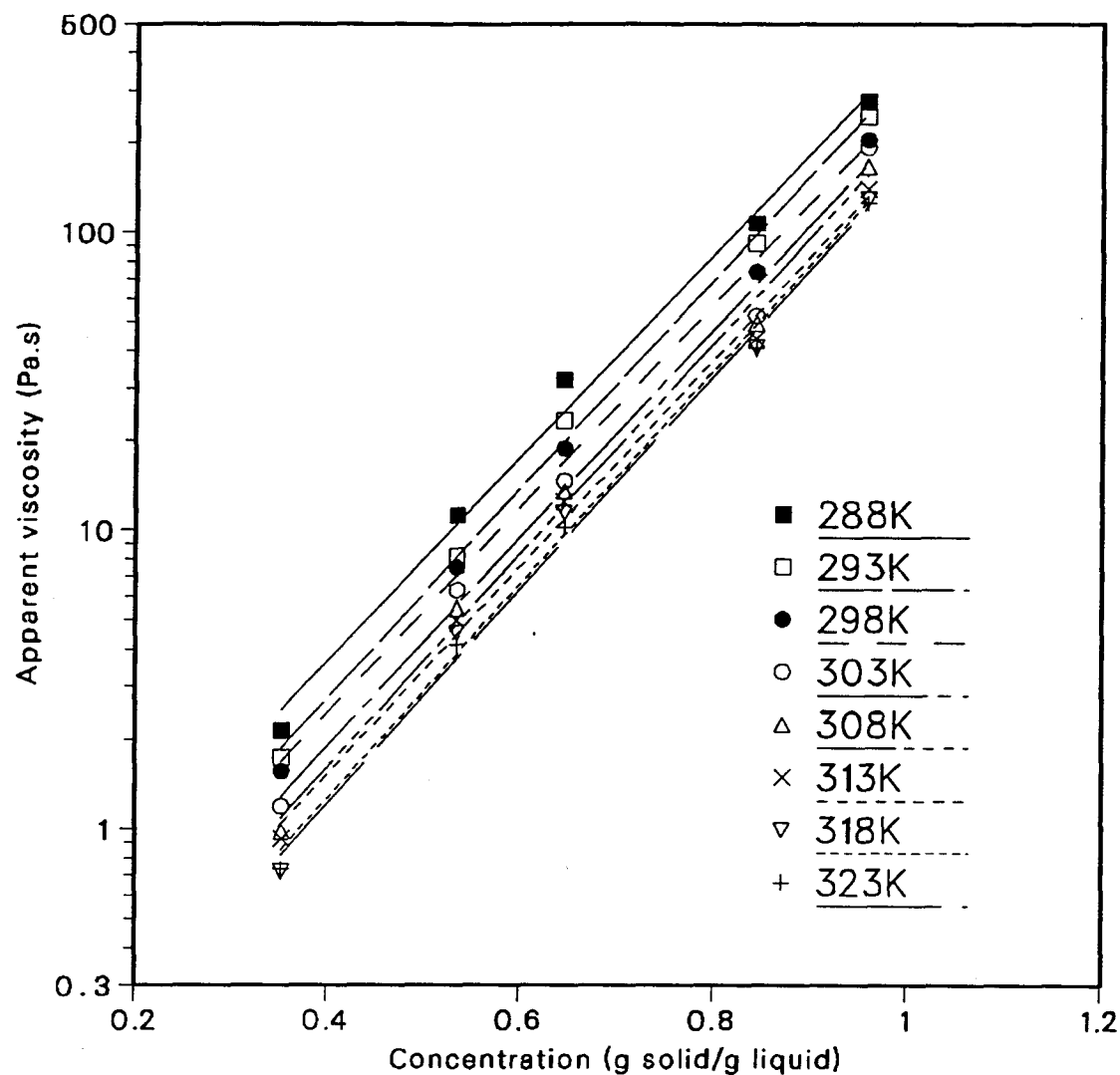


Figure 5-18: Apparent viscosity as a function of Canola concentration for different temperatures at a shear rate of $10 \text{ (s}^{-1}\text{)}$ using the rotational viscometer.

5.2.4 Dependency on Shear rate, Temperature and Concentration

Having discussed the relationship between apparent viscosity and each single variable, it is possible to relate the apparent viscosity (η) jointly to the shear rate ($\dot{\gamma}$), temperature (T) and concentration (C). The following empirical equation is suggested

$$\eta = \alpha \left(\dot{\gamma} \right)^{\beta C^{\varepsilon}} C^{\sigma} \exp\left(\frac{-\Delta E}{T R_c}\right) \quad (5-7)$$

and the coefficients α , β , ε , σ and ΔE were found by using a multiple regression procedure. The resulting relationship is:

$$\eta = 0.205 \left(\dot{\gamma} \right)^{-0.444 C^{0.197}} C^{4.85} \exp\left(\frac{19500}{T R_c}\right) \quad (5-8)$$

The overall correlation coefficient is 0.9598 and, since it was based on 846 data points, Equation 5-5 provides a fairly good fit within the experimental range. Table 5-2 lists the experimental and regressed values for η determined at a shear rate of 10 s⁻¹.

Since it was not possible to use the rotational viscometer for a paste concentration of 146% (g solid/g liquid), Equation (5-8) was used to predict the apparent viscosity at this concentration. The predictions were then compared with the results obtained from the capillary viscometer (*c. f.* Table 5-3 in Section 5.3.2). It was found that the difference between these two evaluations was

Table 5-2: Experimental and predicted apparent viscosities at a shear rate of 10 s^{-1} .

C (g solid/g liquid)	T K	η_{exp} Pa·s	η_{pre} Pa·s
35.3	288	1.94	1.97
35.3	293	1.63	1.71
35.3	298	1.45	1.50
35.3	303	1.29	1.31
35.3	308	1.21	1.16
35.3	313	0.95	1.03
35.3	318	0.91	0.91
35.3	323	0.85	0.81
53.4	288	12.51	13.64
53.4	293	11.91	11.87
53.4	298	9.79	10.38
53.4	303	7.93	9.11
53.4	308	7.05	8.04
53.4	313	6.25	7.12
53.4	318	5.62	6.33
53.4	323	5.02	5.64
64.2	288	31.15	32.94
64.2	293	26.06	28.67

Table 5-2: (Continuous) Experimental and predicted apparent viscosities at shear rate of 10 s^{-1} .

64.2	298	22.45	25.06
64.2	303	19.84	22.01
64.2	308	17.35	19.41
64.2	313	16.35	17.19
64.2	318	15.34	15.28
64.2	323	14.13	13.63
84.2	288	117.5	114.07
84.2	293	95.5	99.27
84.2	298	79.3	86.79
84.2	303	68.9	76.22
84.2	308	63.8	67.22
84.2	313	57.3	59.52
84.2	318	49.4	52.90
84.2	323	44.7	47.20
95.7	288	211.3	206.94
95.7	293	180.7	180.09
95.7	298	153.3	157.46
95.7	303	138.2	138.28
95.7	308	121.9	121.95
95.7	313	113.8	107.98
95.7	318	100.7	95.98
95.7	323	93.3	85.63

about 30%. It is suspected that slip at the interface between the paste and tube wall caused the lower value for the latter device. Thus, it is felt that Equation (5-8) can provide fairly reliable predictions of the apparent viscosity for Canola paste concentrations up to 146% (g solid/g liquid).

5.3 Extrusion of Canola Pastes

5.3.1 Experimental Results

When the paste was extruded in the screw channel, it exhibited periodic pressure fluctuations. The experimental results show that the pressure signal oscillates like a sine-wave, as illustrated by Figures 5-19 to 5-21. Figures 5-19 to 5-21 were recorded at rotational speeds of 66.5, 88.5 and 100.5 rpm, respectively. As can be seen, at least for these single flight screws, the frequency of the recorded pressure signal is proportional to the rotational speed of the screw and is equal to the times that flight passes the pressure transducers per unit time.

Recording of the pressure signals shown in Figure 5-19 was begun 5 minutes after the extruder had been in operation. The starting times in Figures 5-20 and 5-21 were 12 minutes and 7 minutes, respectively. The constant pattern of the pressure signals in the figures indicate that steady state was reached within about 5 minutes of operation. Also, sufficient data were acquired in the 10 second recording time to allow a meaningful calculation of the average mean pressure values.

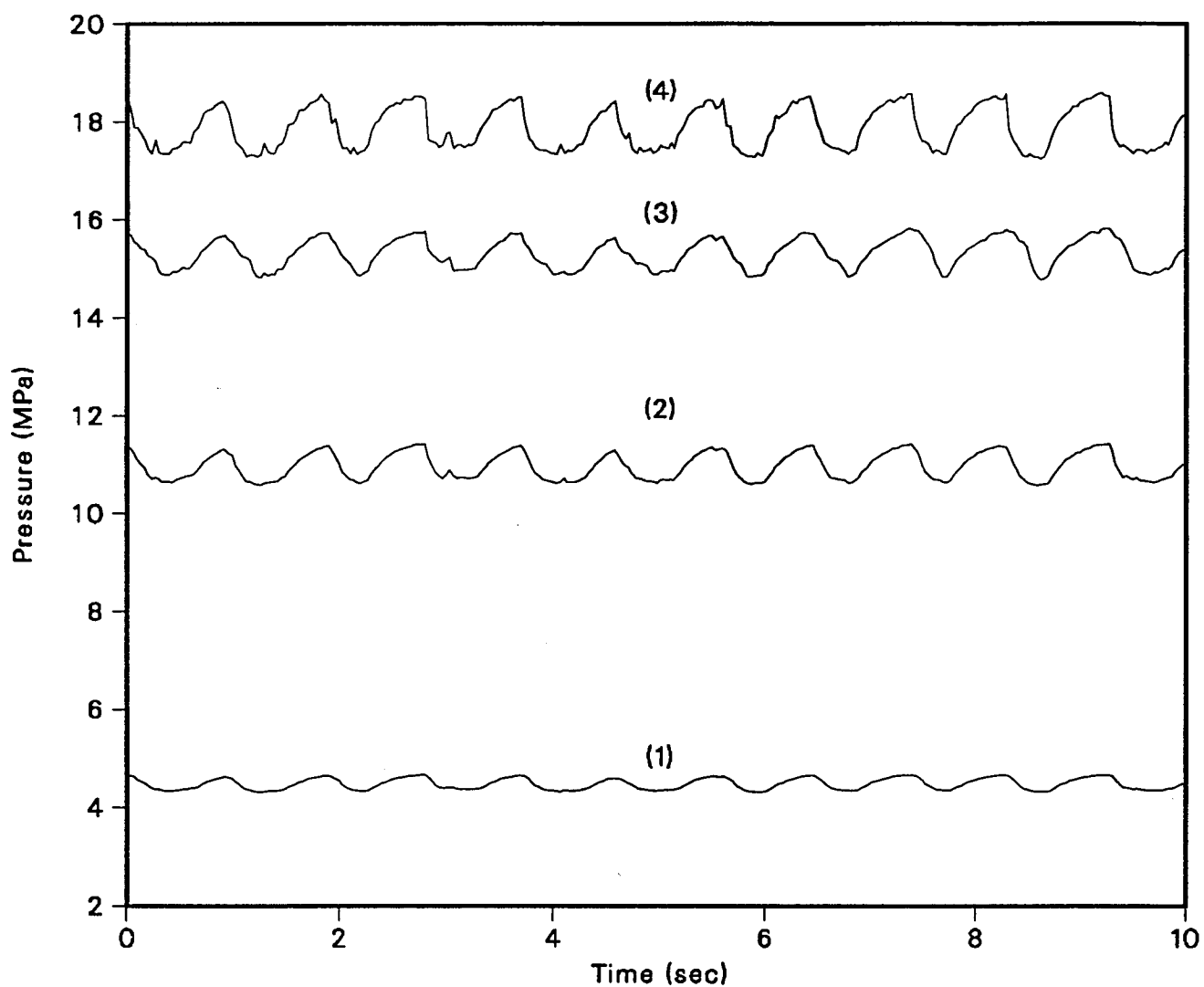


Figure 5-19: Pressure variation with time at different locations from the inlet: curve (1) at 190 mm; curve (2) at 288 mm; curve (3) at 386 mm and curve (4) at 435 mm. Flight angle 7.97° , rotational speed 66.5 rpm, discharge rate 3.75 kg/hr of Canola paste at a concentration of 146% g solid/g liquid.

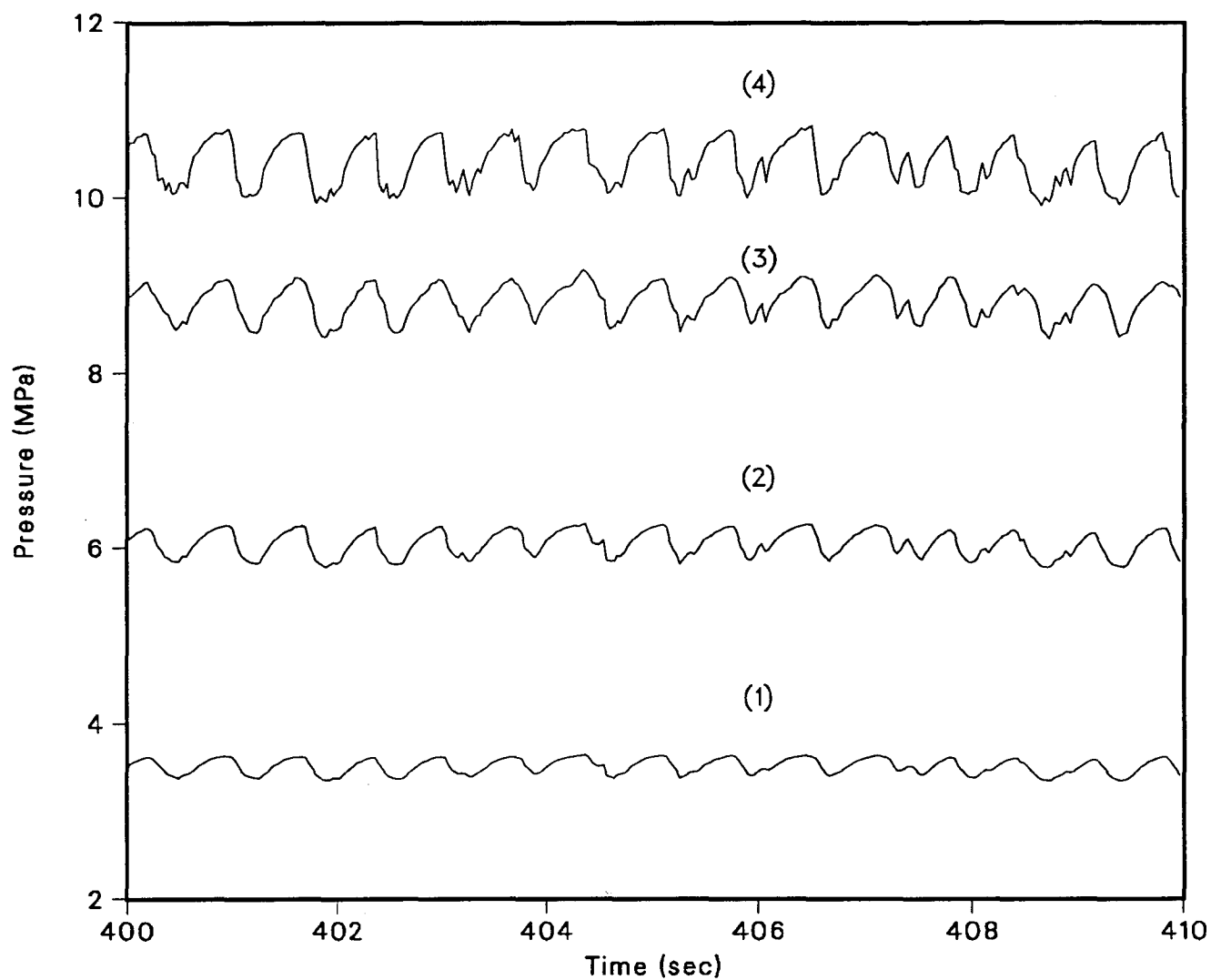


Figure 5-20: Pressure variation with time at different locations from the inlet: curve (1) is at 190 mm; curve (2) 288 mm; curve (3) 386 mm and curve (4) 435 mm (Flight angle 7.97° , rotational speed 88.5 rpm, discharge rate 7.42 kg/hr of Canola paste at a concentration of 146% g solid/g liquid).

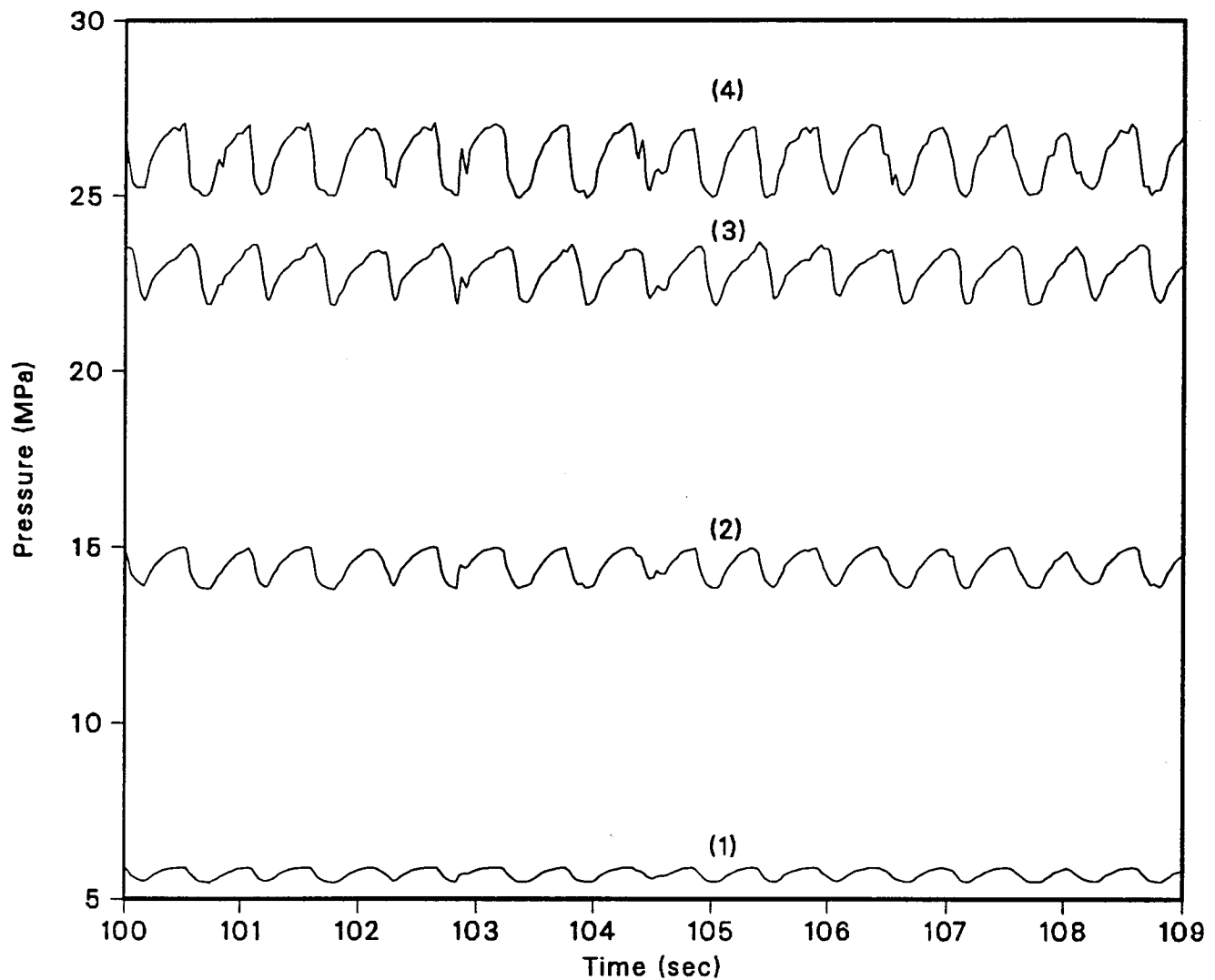


Figure 5-21 Pressure variation with time at different locations from the inlet: curve (1) is at 190 mm; curve (2) 288 mm; curve (3) 386 mm and curve (4) 435 mm (Flight angle 7.97° , rotational speed 100.5 rpm, discharge rate 3.07 kg/hr of Canola paste at a concentration of 146% g solid/g liquid).

The fluctuation range of the pressure is about 8% of the mean which is in agreement with previously reported experimental results (Maddock, 1964). The pressure fluctuation in an extruder which is utilized as a feeder for supercritical fluid extractors may benefit seed pretreatment by promoting seed rupture (Fattori, 1985).

5.3.2 Comparison Between Experimental Results and Model Predictions

Single-screw extrusion can be mathematically described by the partial differential equations which were introduced in Chapter 3. To solve this set of partial differential equations, a computer program was developed using library subroutines, such as H2GCID, H2GCSD and D03EDF, from the Crayfish and NAG (Numerical Algorithms Group) libraries available through the University Computing Service, UBC. The solutions of the equations give the detailed relationship between the output variables (*i. e.* the discharge pressure, discharge rate) and various input parameters such as flight angle and rotational speed. It also gives detailed information on the velocity distribution of the pastes flowing in the screw channel. Using the mathematical model and its associated computer program, it is possible to determine approximately the performance of a single-screw extruder. However, it is first necessary to verify the mathematical model with the experimental results.

In Figure 5-22, the discharge rate is shown as a function of the discharge pressure generated by the model together with the corresponding experimental data obtained with the 5.98° screw extruder. The figure shows that the model overpredicts the measured results and indicates that the model needs to be modified.

Two possible factors may affect the performance of screw extruders. One of them is the clearance between the flight tip and the bore of the barrel. A large clearance may cause some leakage of the paste over the flight tips, which results in lowering the discharge rates and discharge pressures. Unlike the clearance dimension of about 0.5 mm in commercial extruders, the clearance of the laboratory extruder is very small, about 0.0254 mm. Furthermore, since it has undergone only a very short period of operation, wear can be ignored. Therefore, leakage is not likely the cause of the overpredictions produced by the mathematical model.

Another reason for the overpredictions is the possible slip that occurs between the pastes and the bore of the barrel. Yilmazer and Kalyon (1989) found in their experiments that slip exists at the walls of capillary and rotational rheometers with smooth surfaces. Gotsis (1990) also pointed out that slip is inevitable with highly concentrated fluids in screw extruders. Thus the customary assumption of a no-slip boundary condition should not be used in the simulation of flows involving these materials.

Since Canola paste contains a very high percentage of solids, a slip factor was therefore introduced into the extrusion model.

5.3.3 Determination of Slip Factor

The dimensionless slip factor, κ , is defined as:

$$\kappa = \frac{u_s}{u_{max}} \quad (5-9)$$

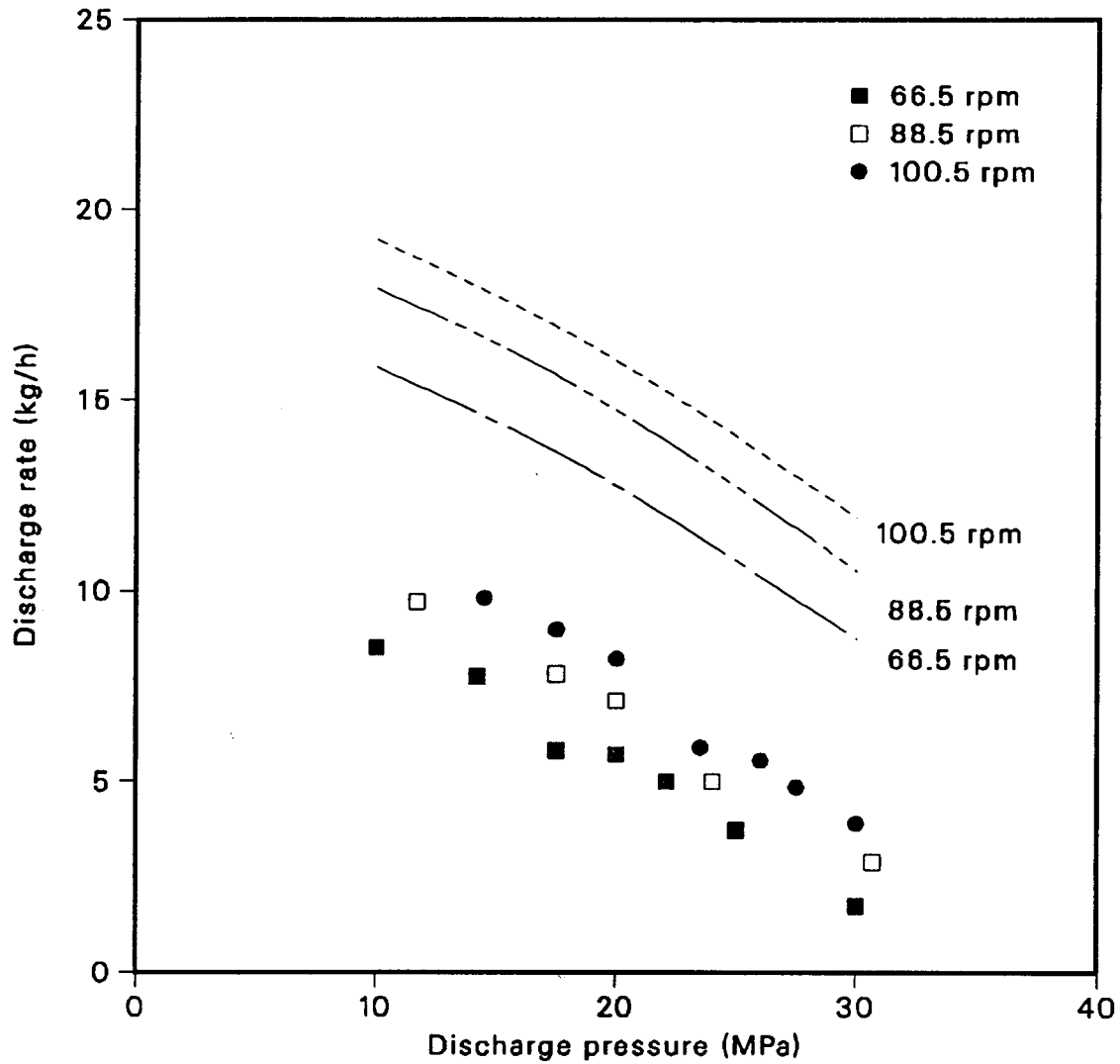


Figure 5-22 Discharge rate as a function of discharge pressure and rotational speed. The curves were obtained from the present three-velocity model with no slip; the symbols denote the experimental results obtained with a screw flight angle of 5.98° at a Canola concentration of 146%).

where u_s is the slip velocity at the surface and u_{max} is the maximum velocity in the screw channel when there is no slip occurring.

The slip velocity u_s can be found from measurements using a capillary viscometer, *i. e.*,

$$u_s = \frac{Q_{exp} - Q_{pre}}{\pi R^2} \quad (5-10)$$

where R is the tube radius; Q_{exp} is the volumetric flow rate measured from the capillary viscometer and Q_{pre} is the predicted volumetric flow rate calculated from

$$Q_{pre} = \frac{8\pi l^3 (\tau_w - \tau_0)^{1+1/n}}{(-\Delta p)^3 (1+1/n) m^{1/n}} \left\{ \tau_w^2 - \frac{2(\tau_w - \tau_0)}{2+1/n} \left[\tau_w - \frac{\tau_w - \tau_0}{3+1/n} \right] \right\} \quad (5-11)$$

where Δp and τ_w denote the pressure drop over the tube and shear stress at the tube wall, respectively. L is the length of the tube. The derivation of Equation (5-11) is given in Appendix A.1.3. For Newtonian fluids, *i.e.* $m = \mu$, $n = 1$ and $\tau_0 = 0$, Equation (5-11) reduces to the Poiseuille equation.

The maximum velocity in the tube can be determined from:

$$u_{max} = \frac{Q_{pre}}{\pi R^2} \frac{3n+1}{n+1} \quad (5-12)$$

In determining the slip factor, parameters m , n and τ_0 are adopted from the rotational viscometer experiments. Since the rotor and cup used in the rotational

viscometer were grooved, slip did not occur. The slip factors obtained for Canola pastes having four different concentrations are listed in Table 5-3. It can be seen from the table that the slip factor increases significantly with the solid concentration of Canola pastes.

Table 5-3: Slip factors for Canola pastes obtained from the capillary viscometer experiments at a temperature of 20 °C.

Concentration C (g solid/g liquid)	Pressure Δp (MPa)	Flow Rate Q_{exp} (mL/min)	Flow Rate Q_{pre} (mL/min)	Slip Velocity u_s (mm/s)	Slip Factor κ u_s/u_{max}
35.3%	0.1	15.2	14.9	0.71	0.041
64.5%	0.68	1.88	1.75	0.28	0.046
95.7%	4.0	1.46	1.27	0.43	0.085
146%	20.0	0.88	0.62	0.6	0.26

5.3.4 Discharge Pressure and Discharge Rate as Functions of Flight Angle

Discharge pressure and discharge rate are the two primary output parameters of interest. This section will examine how these two output parameters vary with the input parameter, flight angle. The predictions from the present three-velocity model will be compared with that from Booy's model and the experimental results.

5.3.4.1 Discharge Pressure as a Function of Flight Angle

The screw flight angle is one of the most important parameters which affects the performance of screw extruders. From Figure 5-23, it is obvious that screws with small flight angles achieve higher discharge pressures than screws with large flight angles provided all other conditions are the same. This finding is consistent with that of Booy's model (*c. f.* Chapter 4) using Newtonian fluids .

Two extreme conditions can be examined: very large flight angles $\theta \rightarrow 90^\circ$ and very small angles $\theta \rightarrow 0^\circ$. For $\theta \rightarrow 90^\circ$, the flight is almost parallel to the screw shaft axis. The channel is almost straight from inlet to outlet. Therefore, the curve in Figure 5-23 extends to the right with the paste yield pressure as its asymptote, and the discharge rate goes to zero as the velocity component in the z direction approaches zero.

On the other hand, if the flight angle $\theta \rightarrow 0^\circ$, the flight behaves like a blind plate positioned in the barrel with its normal almost parallel to the screw shaft axis. The curve in Figure 5-23 asymptotically approaches $\theta = 0^\circ$ and the discharge pressure becomes very large. These types of behavior are shown in Figure 5-24 which was obtained by using a Newtonian fluid having a viscosity of 621 Pa·s. This viscosity value is equivalent to the average apparent viscosity of Canola paste at the same rotational speed in the screw channel. In fact, the real maximum discharge pressure is the failure pressure of the barrel and/or screw.

For the purpose of comparison, Figure 5-24 also gives the results obtained from Booy's model for Newtonian fluids. The predictions shown in Figures 5-24

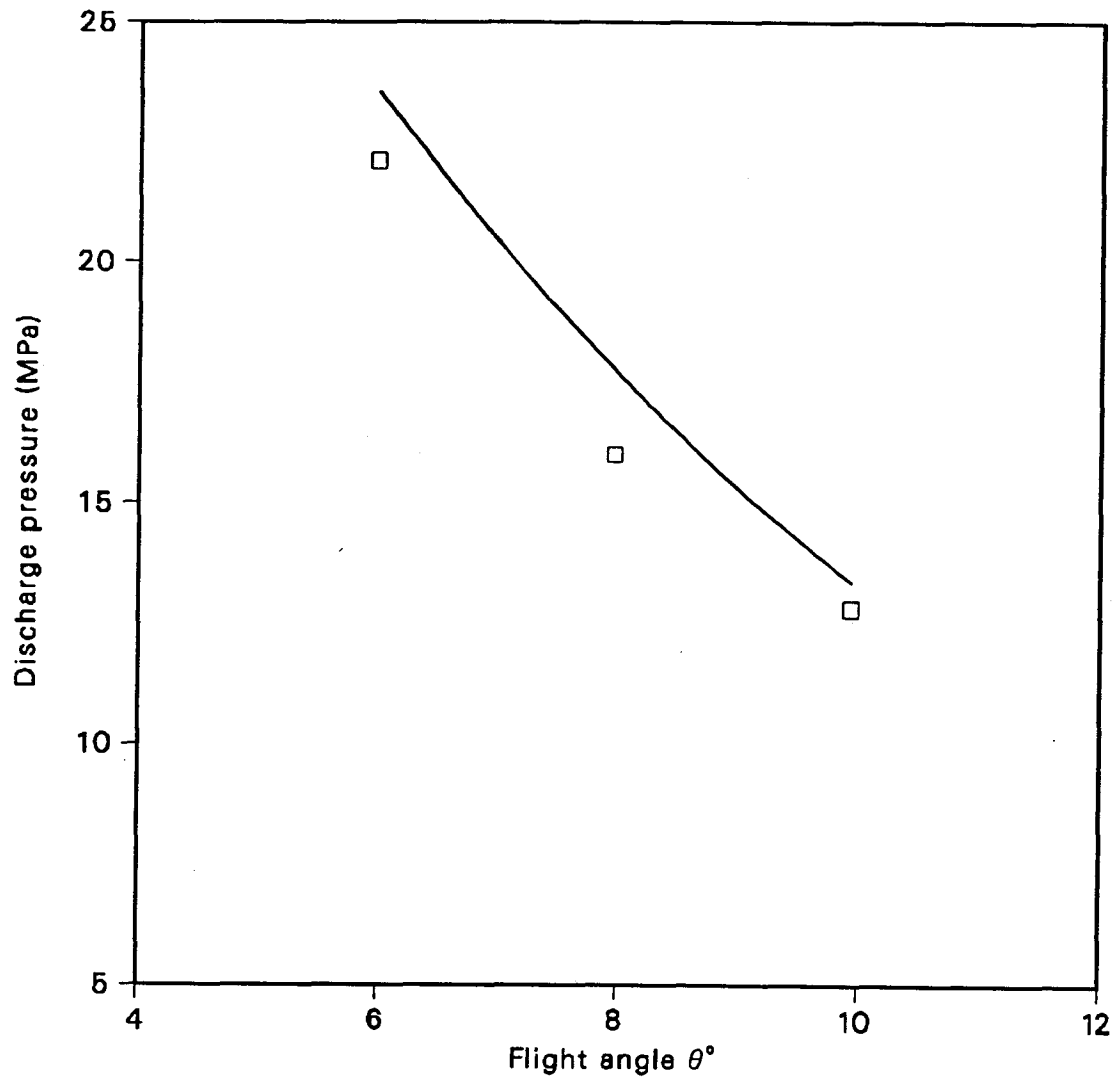


Figure 5-23: Discharge pressure as a function of flight angle. The curve is obtained by the present three-velocity model and the symbols represent experimental measurements (discharge rate 5.0 kg/h, rotational speed 66.5 rpm, slip factor 0.3, Canola concentration 146% g solid/g liquid).

demonstrate consistent trends, but Booy's model always gives higher calculated discharge pressures than does the present three-velocity model. This is because Booy's model underestimates the shear rate and ignores the cross channel flow in a screw channel. The cross channel flow will be discussed later.

5.3.4.2 Discharge Rate as a Function of Flight Angle

Figure 5-25 shows the relationship between the discharge rate and the flight angle at a rotational speed of 66.5 rpm and discharge pressures of 10, 20 and 30 MPa for Canola paste having a concentration of 146% (g solid/g liquid). As the flight angle approaches zero, the discharge rate at any discharge pressure must tend to zero because, at $\theta = 0$, the width of screw channel is zero. The discharge rate thus gradually increases with flight angle increasing from zero until it reaches a peak value depending on the discharge pressure. In the present range of discharge pressures, these peak values are in the flight angle range of $0^\circ < \theta < 10^\circ$.

The peak value can be regarded as the optimal operating condition of a screw extruder since it yields the maximum throughput at a specific discharge pressure. After the peak value is exceeded, the discharge rate decreases with increasing flight angle. This is because larger flight angles result in larger flow cross-sections which reduce the resistance to flow, causing the pressure flow to increase. Also, larger flight angles cause less momentum to be transferred from the moving boundary ($w = V \cos \theta$) to the paste by viscous forces. The combination of these effects causes a reduction of the discharge rate.

For comparison, Figure 5-25 also depicts the relationship between the

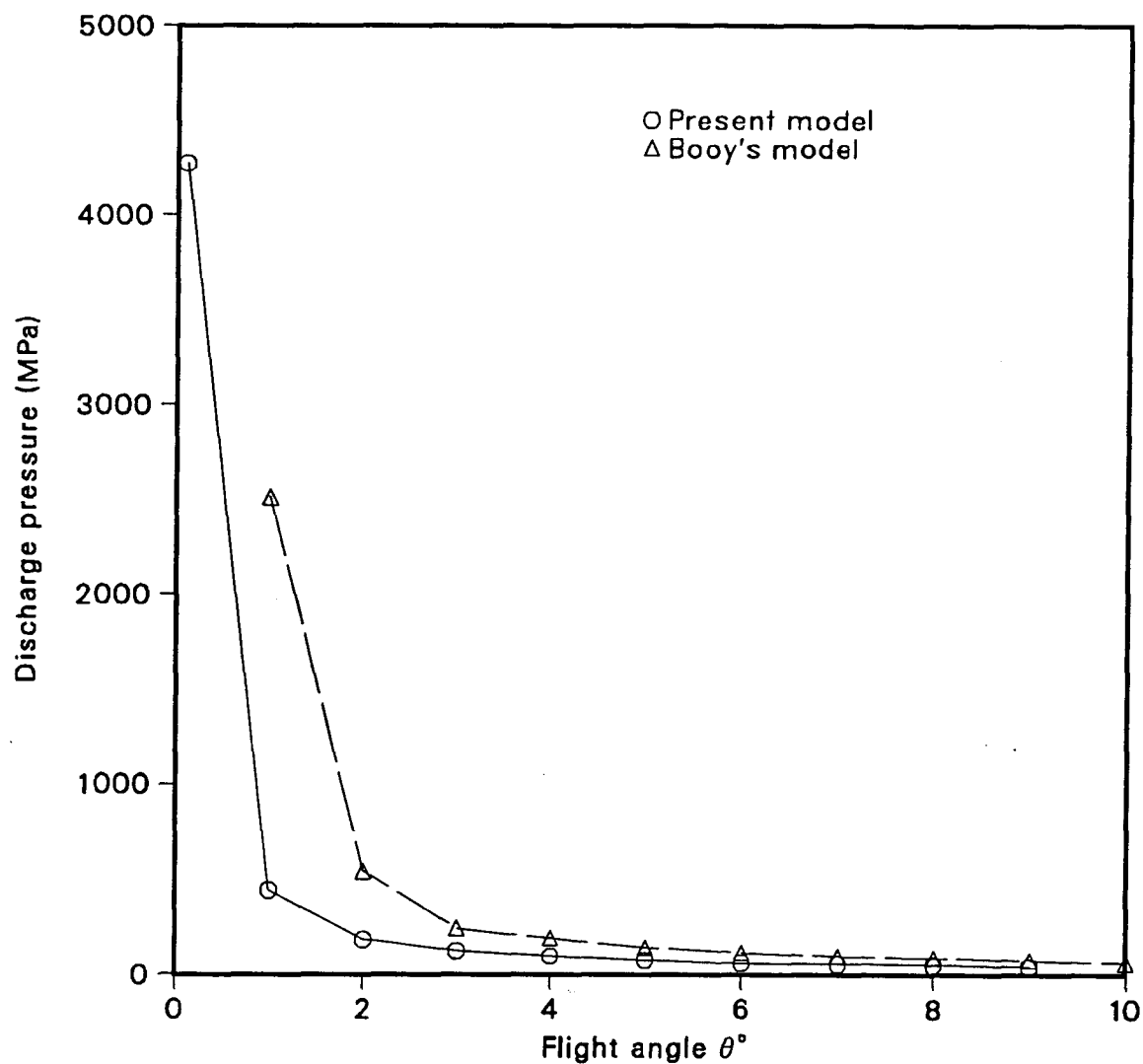


Figure 5-24: Discharge pressure as a function of flight angle (obtained by the present three-velocity model and Booy's model, discharge rate 1.0 kg/h, rotational speed 66.5 rpm, no slip with a Newtonian fluid having a viscosity of 621 Pa·s).

discharge rate and flight angle obtained by Booy's model with a Newtonian fluid having a viscosity of 621 Pa·s. It agrees, in principle, with the results achieved by the present three-velocity model.

It is noteworthy that when the flight angle approaches zero, Booy's model is unable to predict the extrusion process because the model has a singularity at $\theta = 0^\circ$ due to the term $\sin\theta$ in the denominator. Therefore, Booy's model cannot be used for $\theta \rightarrow 0^\circ$.

5.3.5 Discharge Pressure and Discharge Rate as Functions of Screw Rotational Speed

Another input parameter which strongly affects the discharge pressure and discharge rate is the screw rotational speed. The screw rotation is the most important operational parameter because it can be easily controlled and varied. This section will deal with the relationship between the rotational speed and discharge pressure and rate.

5.3.5.1 Discharge Pressure as a Function of Screw Rotational Speed

The paste in the screw channel is pushed by the flights and is thereby moved forward. The more vigorously it is pushed, the higher will be the discharge pressure generated. Therefore, at any given flight angle, an increase in screw rotational speed should result in an increase in discharge pressure. Figure 5-26 shows the relationship between the discharge pressure and rotational speed at three different flight angles.

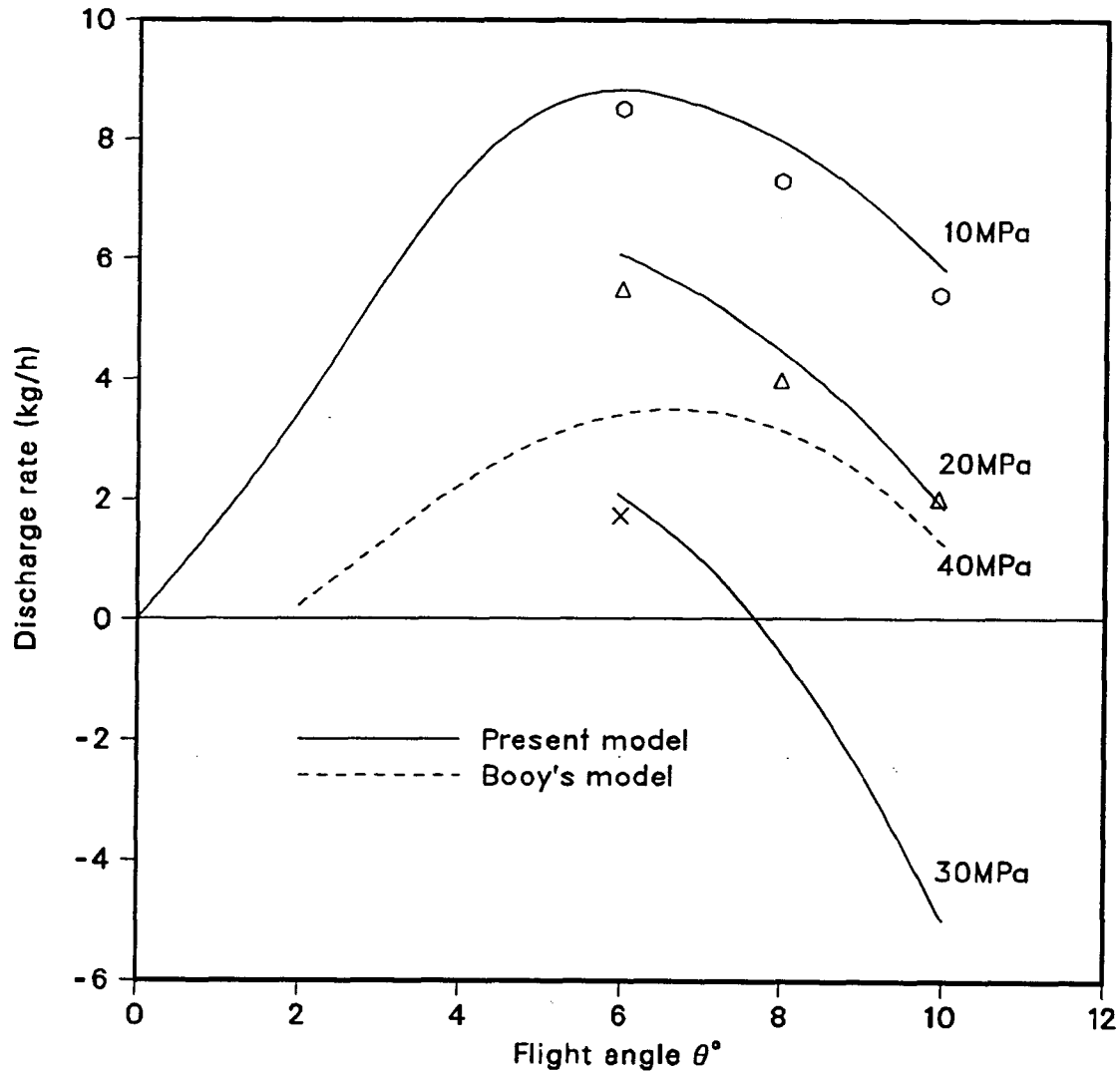


Figure 5-25: Discharge rate as a function of flight angle (the solid curves were obtained from the present three-velocity model with Canola paste having a concentration of 146% g solid/g liquid and a slip factor of 0.3; the dashed curve was obtained from Booy's model using a Newtonian fluid with a viscosity of 621 Pa·s and no slip; rotational speed 66.5 rpm. The symbols represent the experimental measurements).

Although the discharge pressure is an increasing function of rotational speed, the shape of the curves suggests that the discharge pressure may reach a saturation value beyond which it is independent of speed. In general, an increase in rotational speed causes more momentum transfer to the paste, thus raising the discharge pressure. However, because the shear rate increases, the apparent viscosity of the paste is reduced. Thus a very large increase in rotational speed may result in a sufficient decrease in apparent viscosity such that the discharge pressure remains constant. On the other hand, lowering the rotational speed results in a reduction of discharge pressure. Consequently, the curves all pass through the origin of the coordinates.

5.3.5.2 Discharge Rate as a Function of Screw Rotational Speed

Figure 5-27 indicates that the discharge rate also increases with an increase in rotational speed. The slight curvature of the lines reveals the primary differences between the behavior of non-Newtonian fluids and Newtonian fluids. Figure 5-28 gives results for a Newtonian fluid using Booy's model. It can be seen that in the latter case, the relationship between discharge rate and rotational speed is linear. The curvature in Figure 5-27 is likely caused by the pseudoplastic behavior of the Canola pastes. An increase in rotational speed causes higher shear rates in the screw channel and this lowers the apparent viscosity of the pastes. The lower apparent viscosity finally causes reduced discharge rates because the low viscosity causes less momentum transferred to the paste and decreases the drag flow.

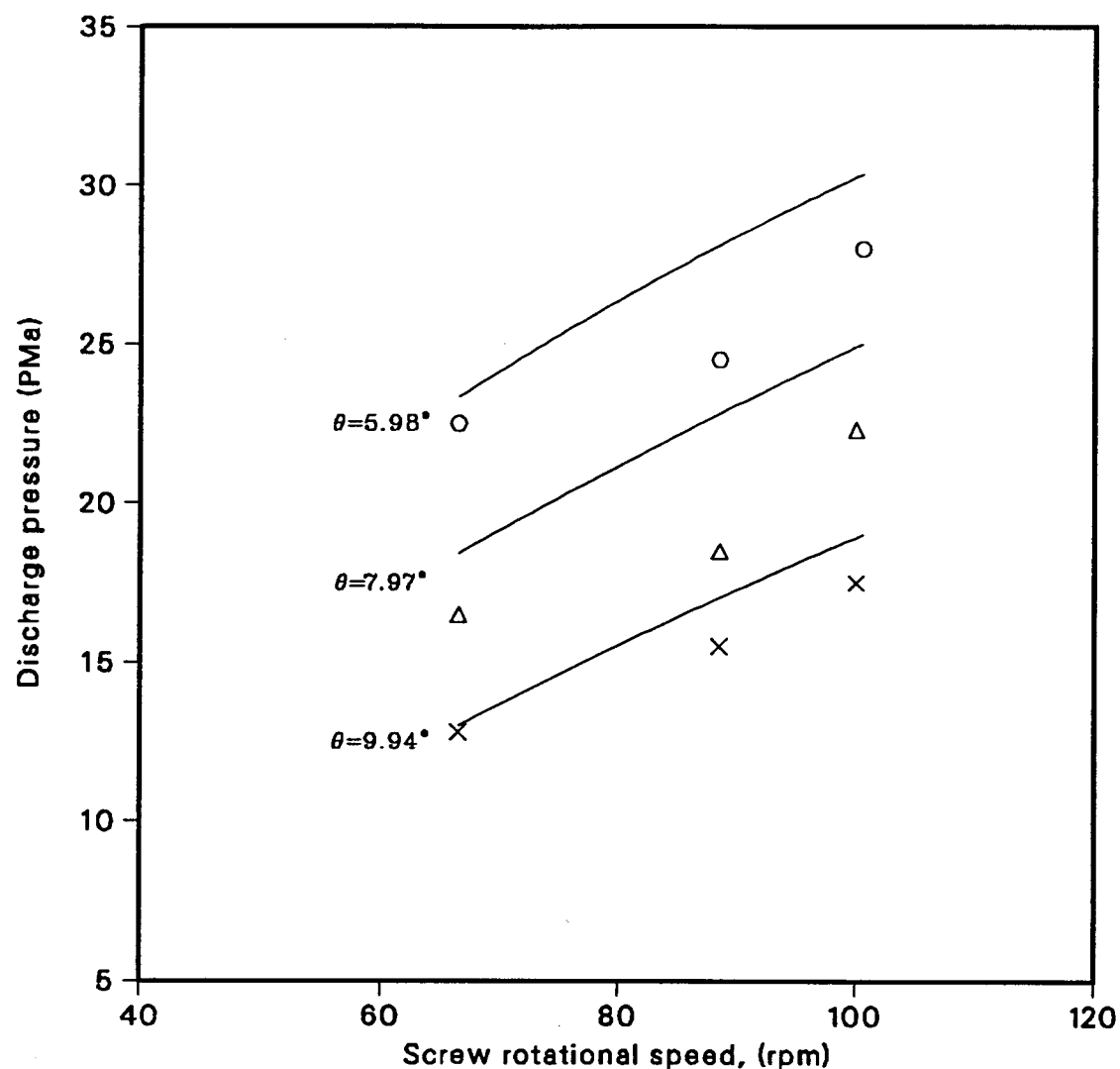


Figure 5-26: Discharge pressure as a function of screw rotational speed and flight angle. The curves are obtained from the present three-velocity model and the symbols are the experimental measurements (discharge rate 5 kg/hr, slip factor 0.3, Canola concentration 146% g solid/g liquid).

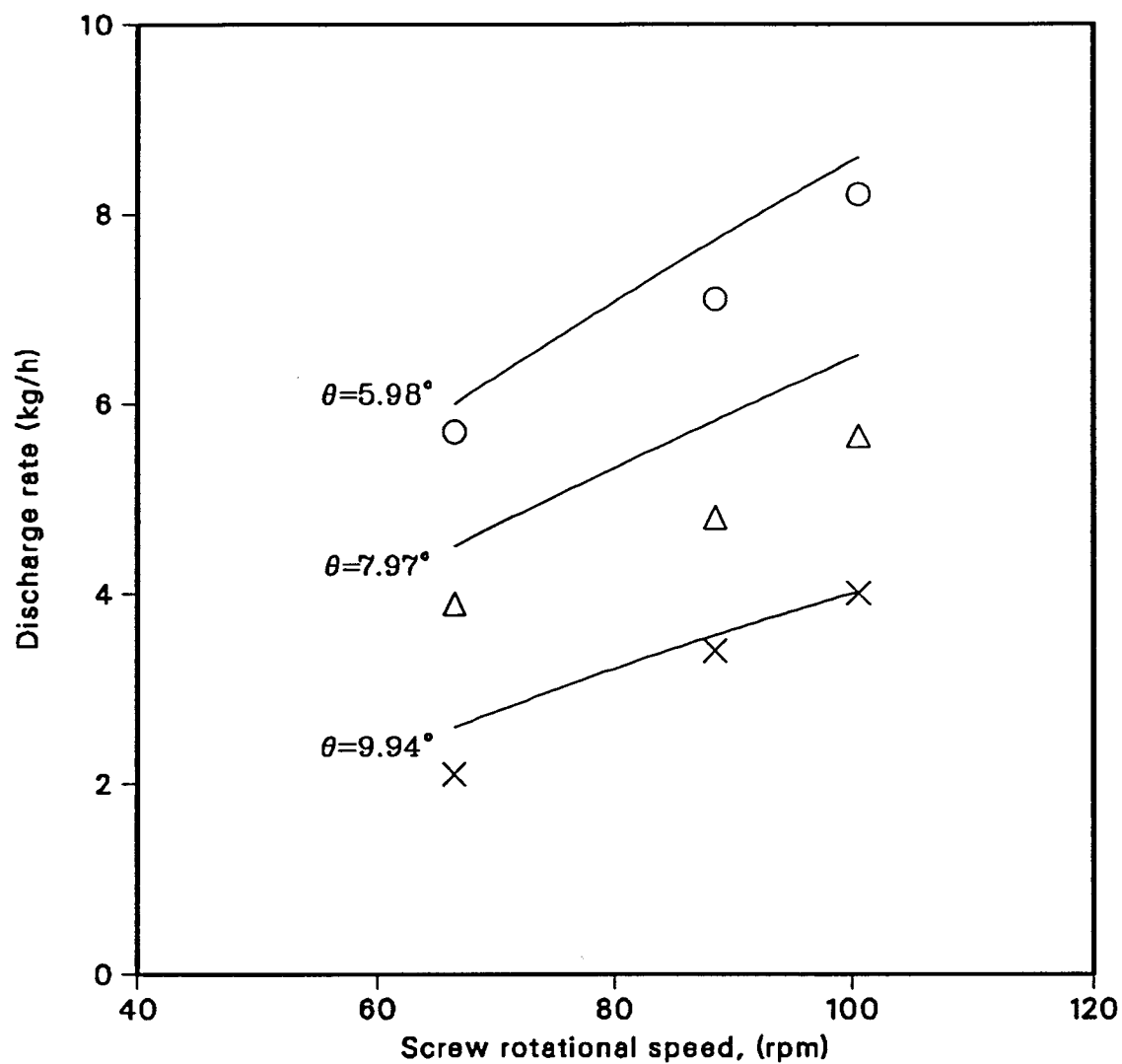


Figure 5-27: Discharge rate as a function of screw rotational speed and flight angle. The curves are obtained from the present three-velocity model and the symbols are experimental measurements (discharge pressure 20 MPa, slip factor 0.3, Canola concentration 146% g solid/g liquid).

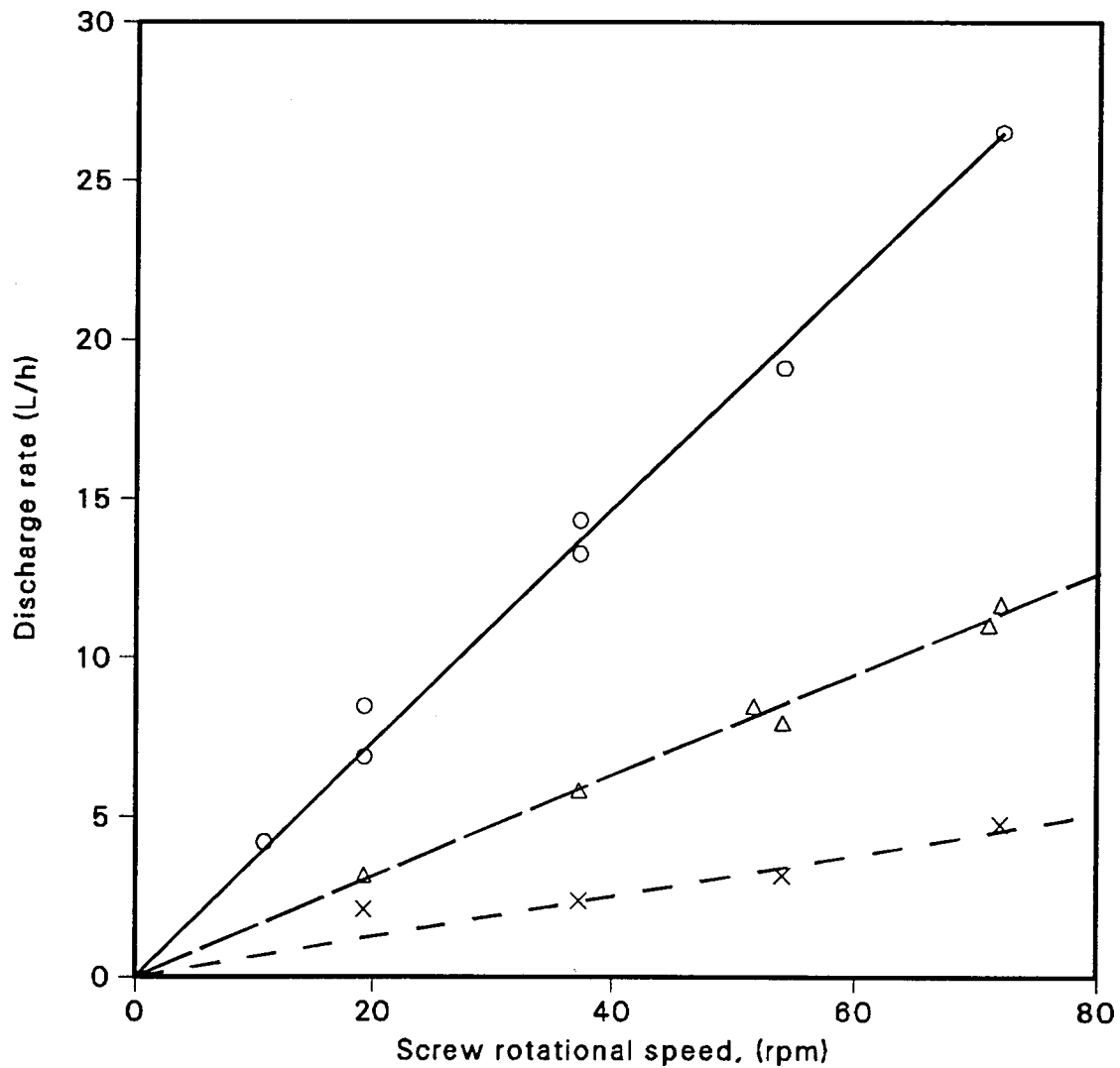


Figure 5-28: Discharge rate of corn syrup extruded in a 2.5" diameter extruder as a function of rotational speed. Lines indicate predicted values from Booy's model with the assumption $F_d = F_p = 1.0$. The symbols represent experimental data obtained by Maddock (Tadmor, 1969).

5.3.6 The Relationship Between Discharge Pressure and Discharge Rate

When the discharge pressure rises, the discharge rate normally decreases because a high pressure at the outlet constrains the discharge of the paste. In Figures 5-29 to 5-31, the discharge rates are plotted against discharge pressures; the symbols represent the experimental measurements and the curves are obtained from the present three-velocity model at $\kappa = 0.3$.

The calculated discharge pressures range from 10 MPa to 30 MPa. It is noteworthy that the negative discharge rates observed in Figures 5-30 and 5-31 indicate that the pressure flow surpasses the drag flow to such an extent that a backward flow occurs. In other words, at these discharge pressures, the pastes are simply pushed backward by the pressure existing in an extractor operating at elevated pressures.

The figures also indicate that the discharge rate of a screw extruder with a large flight angle is more sensitive to the pressure drop than is a screw extruder with a small flight angle. With each unit of pressure increase, the discharge rate obtained from a screw extruder with a large flight angle decreases more than that obtained from a screw extruder with a smaller flight angle.

5.3.7 Effects of Slip Factor

In Figure 5-32, the upper three curves were calculated with a slip factor of zero; the middle three curves were obtained with $\kappa = 0.3$ and the lowest curve was calculated with $\kappa = 1$. The symbols represent the experimental measurements obtained with a 5.98° screw extruder and a paste concentration

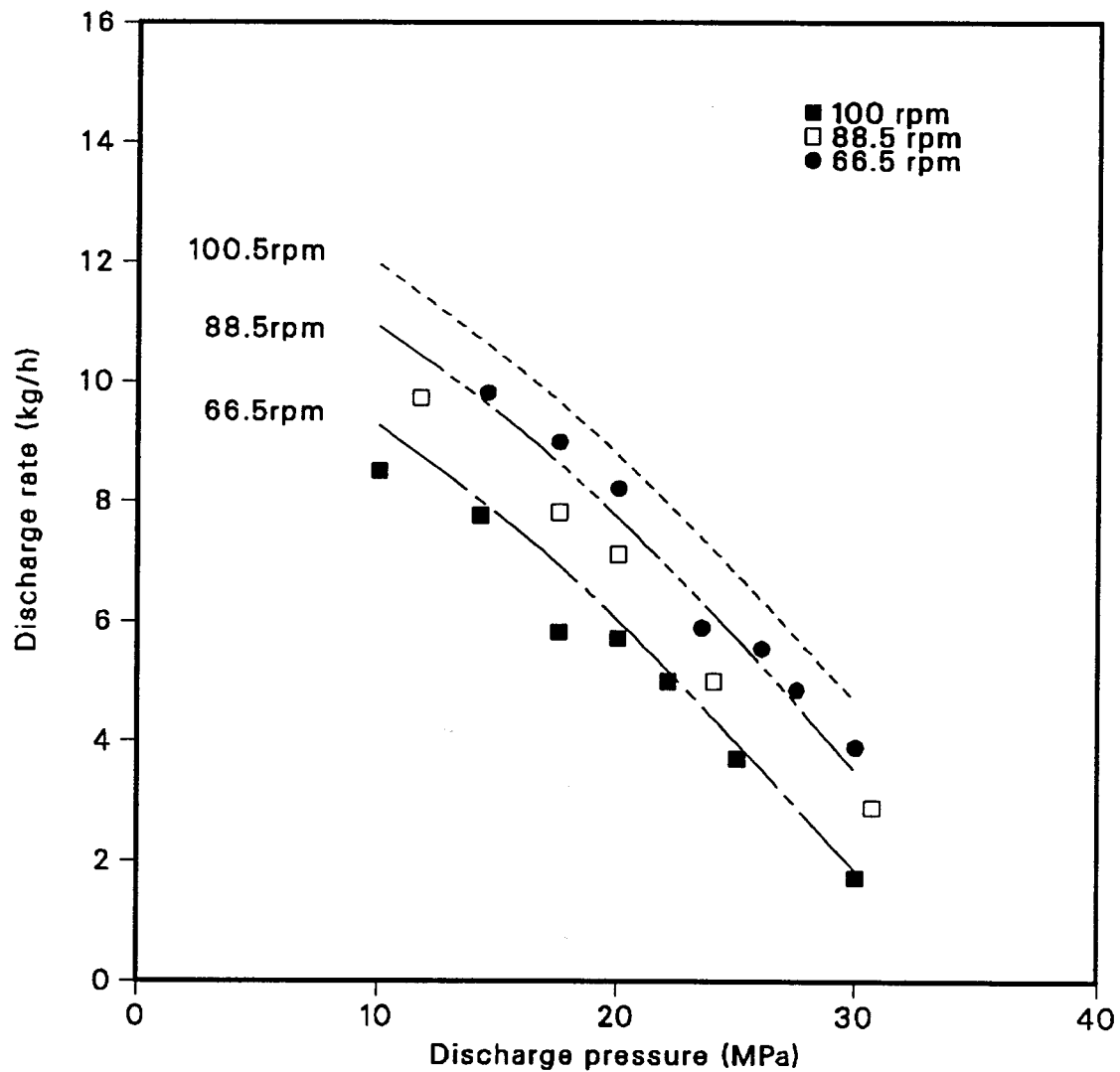


Figure 5-29: Discharge rate as a function of discharge pressure and rotational speed at a flight angle of 5.98° . The curves are calculated from the present three-velocity model with a slip factor of 0.3. The symbols represent experimental results obtained with a Canola paste concentration of 146% (g solid/g liquid).

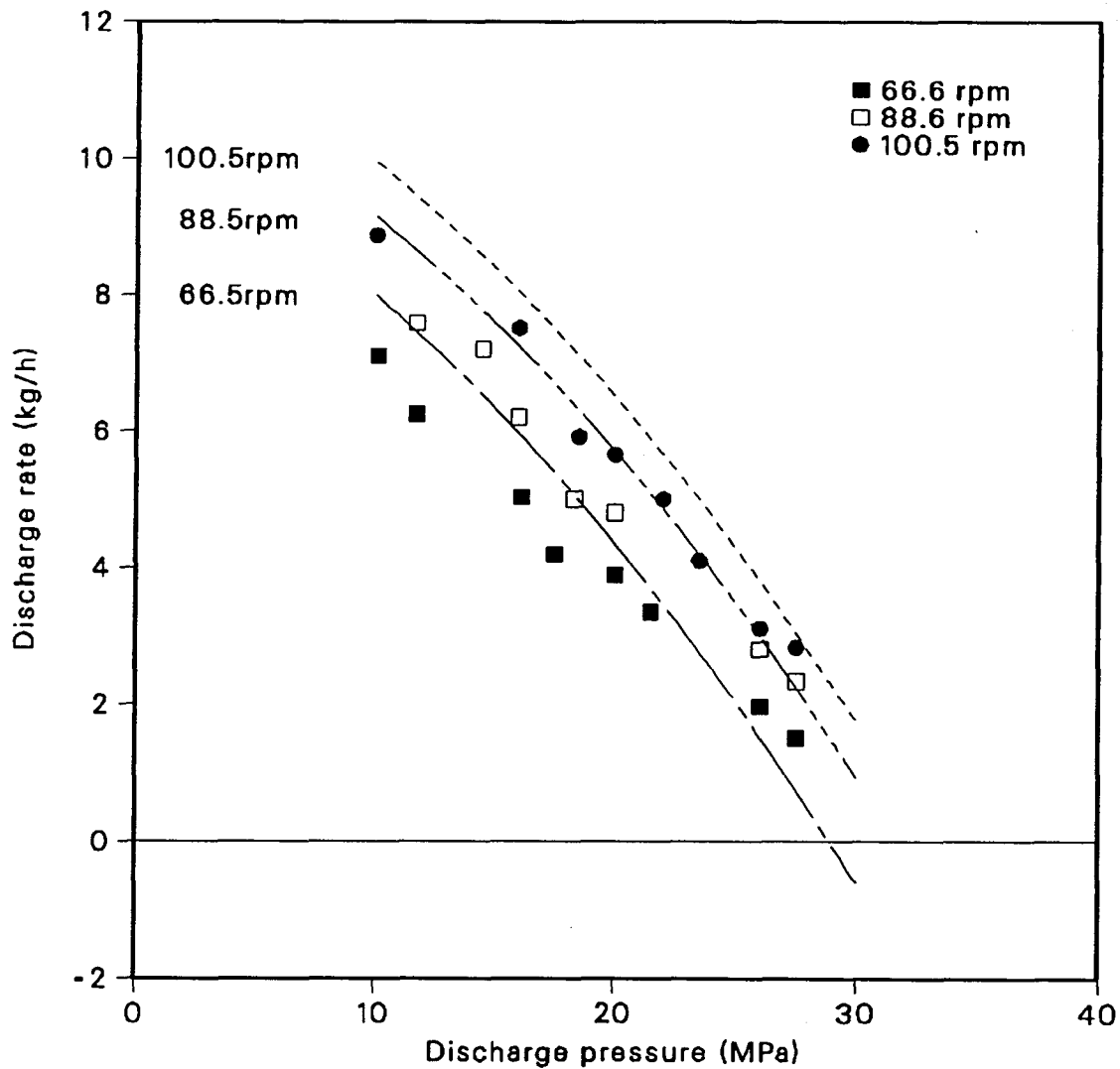


Figure 5-30: Discharge rate as a function of discharge pressure and rotational speed at a flight angle of 7.97° . The curves are calculated from the present three-velocity model with a slip factor of 0.3. The symbols represent experimental results obtained with a Canola paste concentration of 146% (g solid/g liquid).

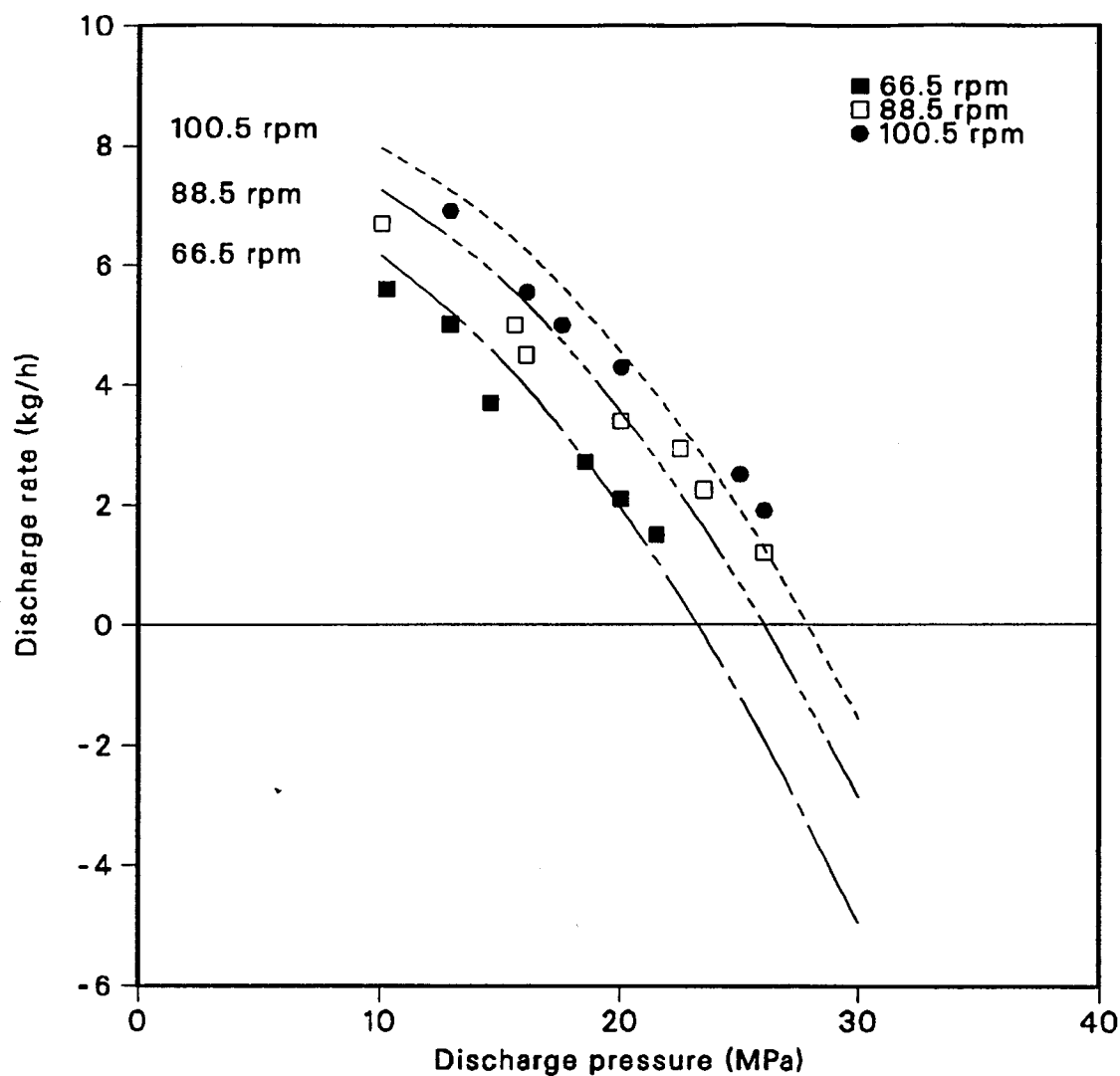


Figure 5-31: Discharge rate as a function of discharge pressure and rotational speed at a flight angle of 9.94° . The curves are calculated from the present three-velocity model with a slip factor of 0.3. The symbols represent experimental results obtained with a Canola paste concentration of 146% (g solid/g liquid).

of 146% (g solid/g liquid).

When the slip factor $\kappa = 0$, there is no slip at the interface between the paste and solid surface, *i. e.* the paste velocity at the boundary $x = 1$ is equal to the velocity components of the moving boundary (the "moving barrel"). As noted already, this results in an overprediction of the discharge pressure and rate.

For a slip factor $\kappa = 0.3$, the paste velocity at the interface is 30% less than the moving barrel's velocity because of the slip. This factor reduces the predictions to yield predicted values which agree well with the experimental results.

When the slip factor $\kappa = 1$, the local paste velocity at the surface is zero regardless of the barrel surface velocity. In this situation, as there is no viscous force from the top of the screw channel to drag the paste forward and the paste is simply pushed back by the discharge pressure.

The slip factor plays a very important role in modifying the prediction of the three-velocity model. The slip factor range is $0 \leq \kappa \leq 1$ and its value in a specific extruder depends on the material being extruded and the velocity of the solid surfaces. In Figures 5-29 to 5-31, a slip factor of 0.3 was chosen to calculate the predicted values. It can be seen that a somewhat larger slip factor would yield an even better prediction. Therefore, precise determination of the slip factor is a necessary step in accurately predicting the performance of a screw extruder.

Figure 5-33 compares the predictions from different models for the pressure

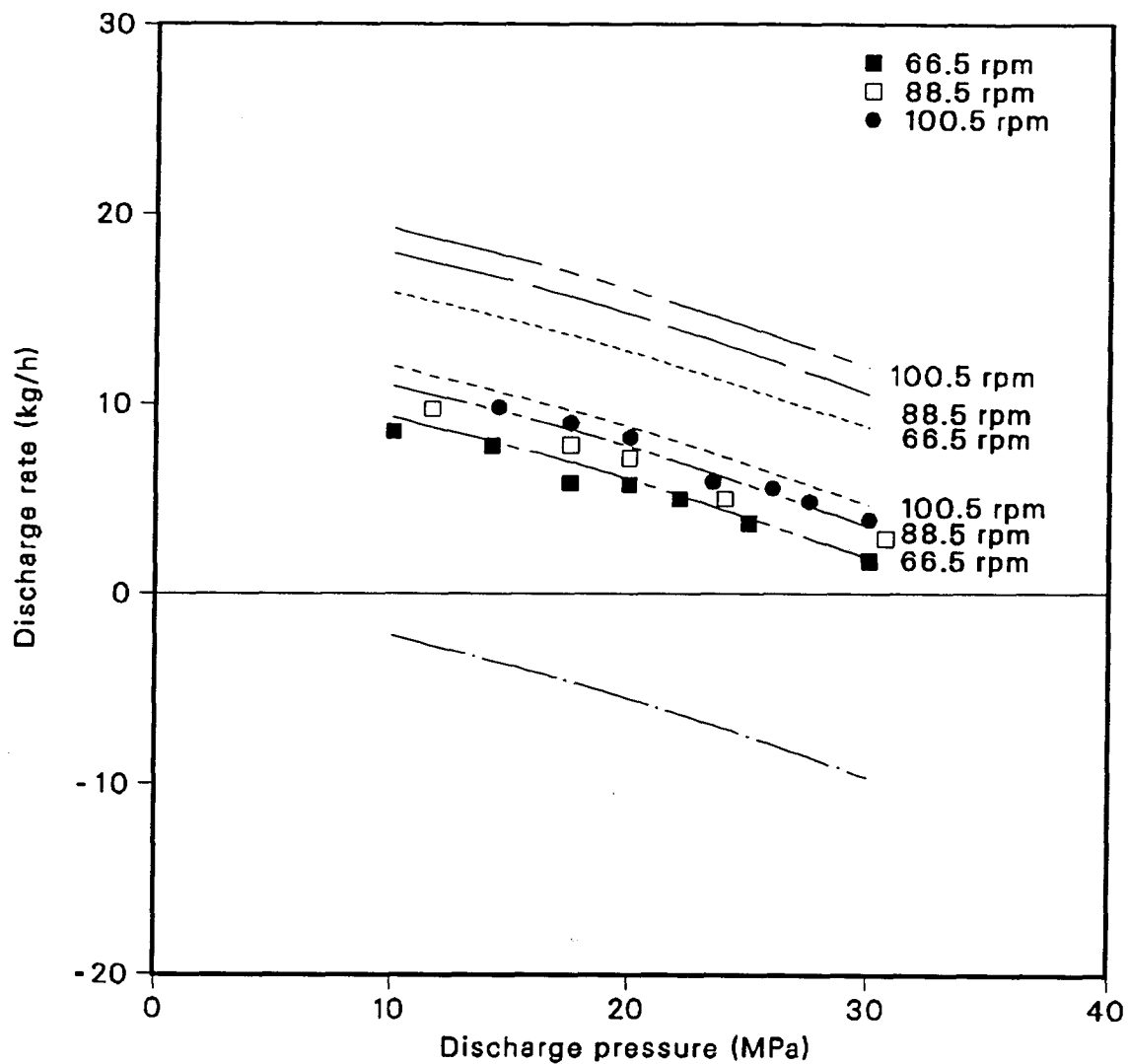


Figure 5-32: Discharge rate as a function of discharge pressure and rotational speed at a flight angle of 5.98° . The curves are calculated from the present three-velocity model with slip factors of 0, 0.3 and 1. The symbols represent experimental results obtained with a Canola paste concentration of 146% (g solid/g liquid).

distribution along the screw extruder. The top curve is obtained from Booy's model which assumes that the paste is a Newtonian fluid which simply flows in one direction, *i. e.*, the down channel direction, and does not take the slip effect into consideration. The middle curve is obtained with the present three-velocity model with a slip factor of 0 and the bottom curve results from the same model but with a slip factor of 0.3. The symbols are the typical measured pressures at various distances from the inlet of the screw extruder. It is clear that the slip factor has a strong effect on the model predictions. The slightly larger difference between the pressure measured at 0.2 m from the inlet and curve 3 may be partly due to an entrance effect in the extruder inlet. More experimental results showing the pressure distribution along the extruder can be found in Appendix A.5.

5.3.8 Detailed Flow Pattern in the Screw Extruder Channel

The motion of the fluid in the extruder is complex. An analytical description of this motion, even for an isothermal Newtonian fluid, is not feasible as it entails solving a set of complex non-linear partial differential equations. However, by using a computer and appropriate numerical approximations, a complete solution for a rectangular cross-section extruder channel becomes possible and allows one to examine the complete fluid flow patterns.

5.3.8.1 Down Channel Flow

The down channel velocity, w , which is directly affected by the discharge pressure and slip effect, is the major contributor to the discharge rate. Unlike

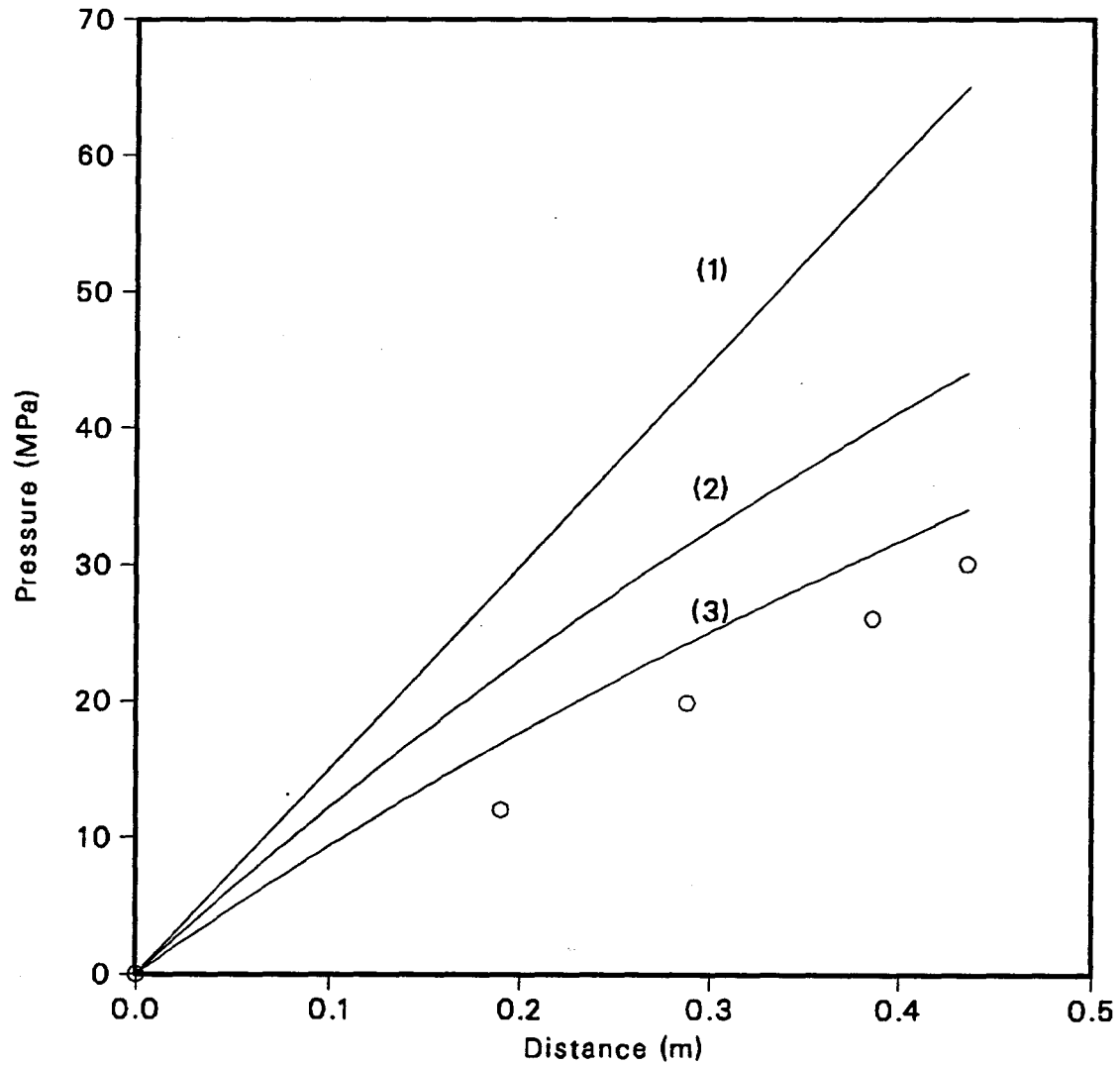


Figure 5-33: Comparison of pressure distribution along a screw extruder using different models: (1) single velocity model, (2) the present three-velocity model with $\kappa = 0$, (3) the present three-velocity model with $\kappa = 0.3$. The symbols represent experimental results for rotational speed 88.5 rpm, discharge rate 2.85 kg/hr, Canola concentration 146% (g solid/g liquid), flight angle 5.98° .

Newtonian fluid flow in a screw channel where the pressure flow and drag flow are readily distinguished, non-Newtonian fluids do not permit such a distinction.

When the discharge pressure is low, for example 10 MPa, the pressure flow is very small, as shown in Figure 5-34. The velocity profile in the plane, whose normal is parallel to the y axis (*i. e.*, the channel width, W), is approximately parabolic in profile and does not have a minimum within the range $0 \leq x \leq 1$. This can also be seen from Figure 5-35 which shows the down channel velocity distribution at $y = W/2$.

When the discharge pressure is high, for example 30 MPa, the pressure flow increases. This changes the down channel velocity distribution, as shown in Figure 5-36. The paraboloid-shaped down channel velocity distribution now has a minimum which is the result of the superimposition of the pressure and drag flows. Figure 5-37 shows the velocity profile in the plane $y = W/2$ with a minimum near $x = 0.3$. This minimum value is always closer to the $x = 0$ side because the drag flow has the smallest value at $x = 0$.

The slip factor can also change the down channel velocity distribution. Figures 5-36 and 5-37 were obtained with a slip factor of 0.3. If slip is absent at the discharge pressure of 30 MPa, the backflow would not be as significant as is shown in Figures 5-36 and 5-37. Figures 5-38 and 5-39 show the down channel velocity distribution in the absence of slip. At the same discharge pressure, the no-slip condition gives a higher discharge rate. This suggests that, to improve the extruder's performance, it is advisable to make rough flight surfaces to reduce slip.

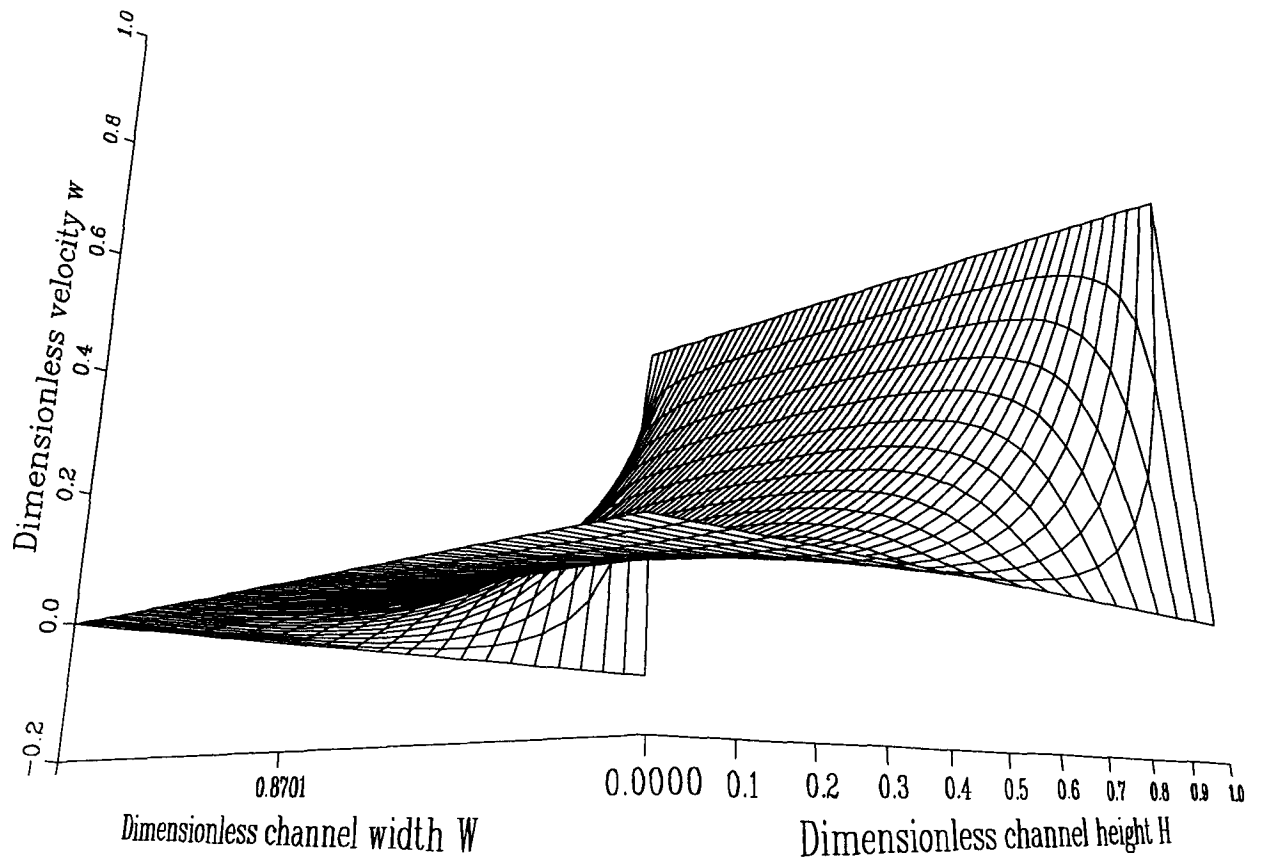


Figure 5-34: Dimensionless down channel velocity w (rotational speed 100.5 rpm, discharge pressure 10 MPa, discharge rate 11.8 kg/hr, flight angle 5.98° , slip factor 0.3, paste concentration 146% g solid/g liquid, flight height 4.9mm).

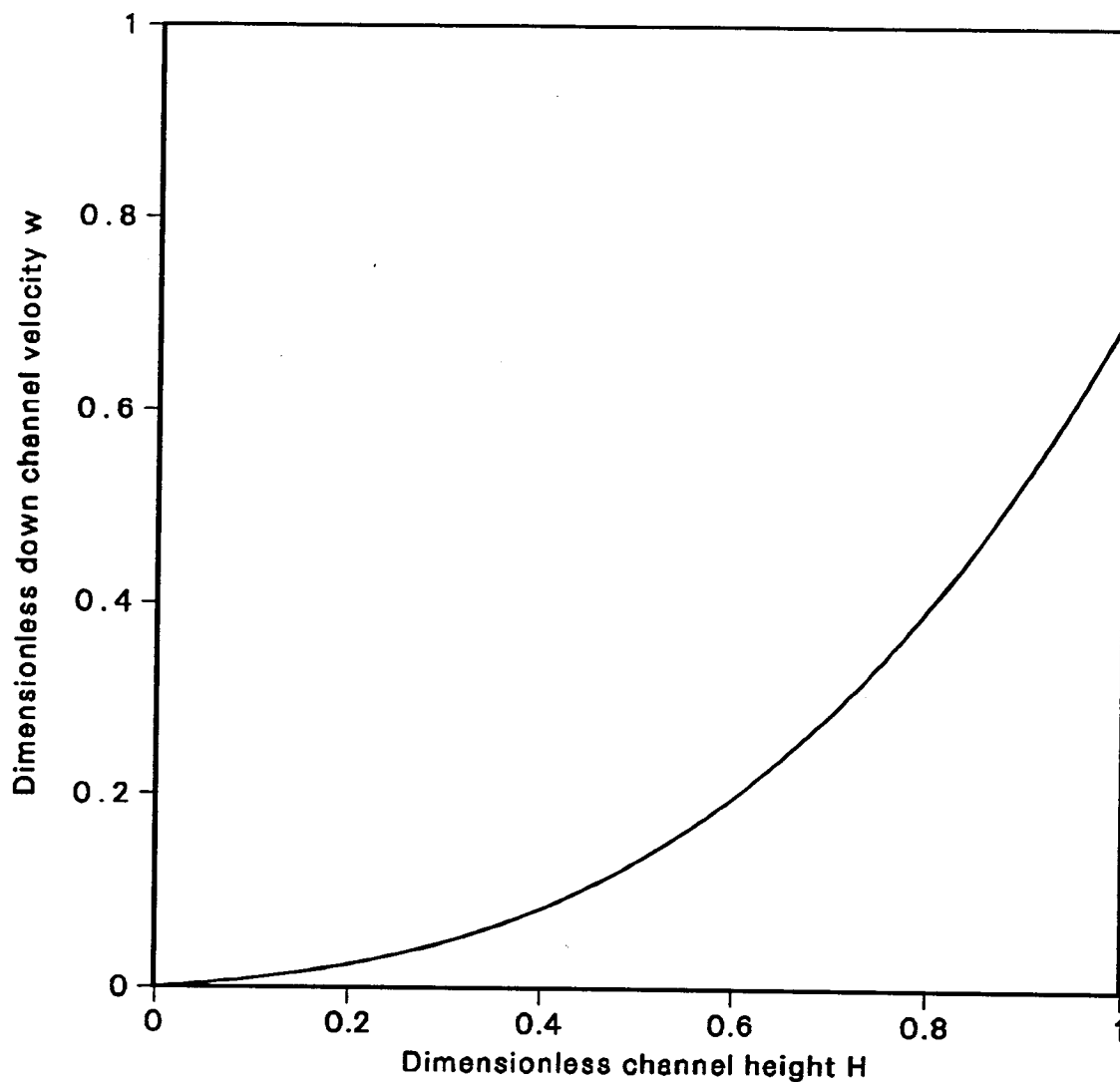


Figure 5-35: Dimensionless down channel velocity, w , at $y = W/2$ (discharge pressure 10 MPa, discharge rate 11.8 kg/hr, rotational speed 100.5 rpm, flight angle 5.98° , slip factor 0.3, paste concentration 146% g solid/g liquid, flight height 4.9mm).

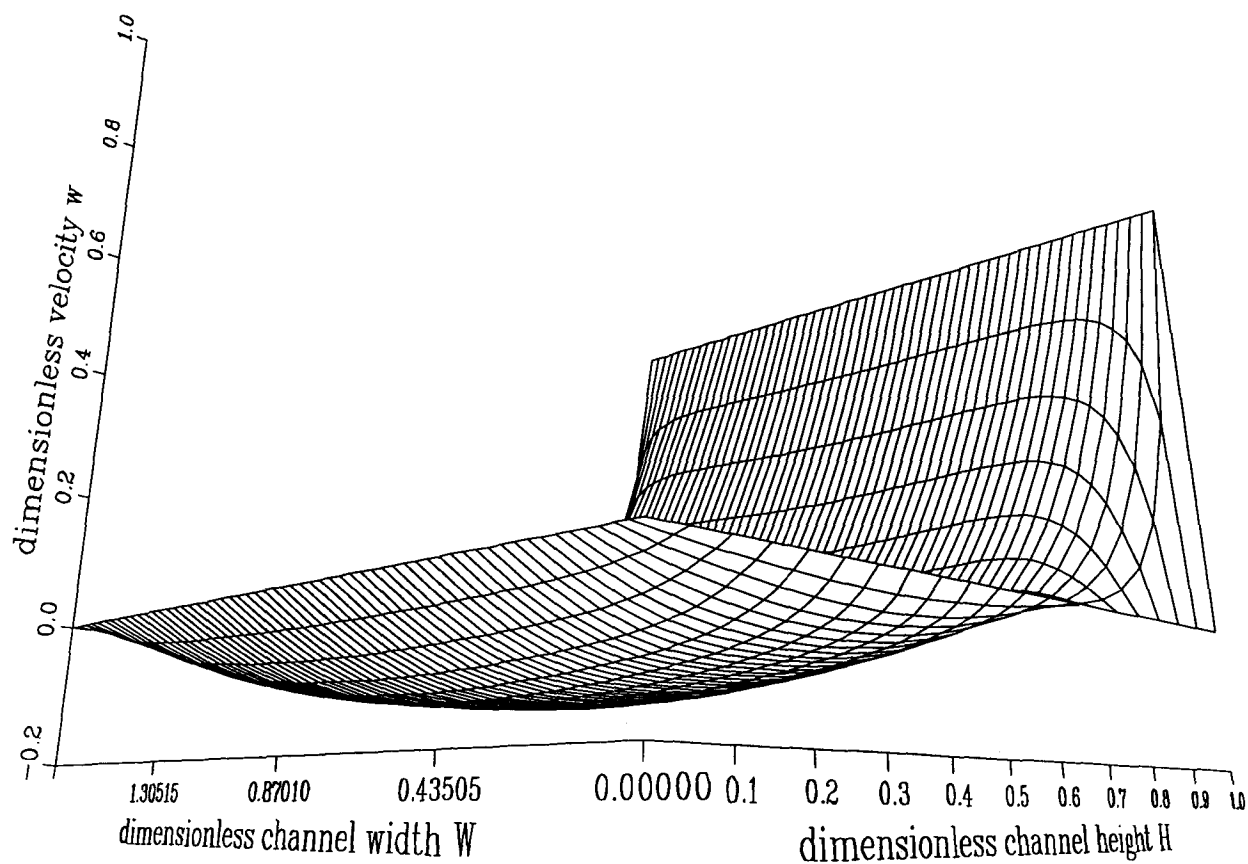


Figure 5-36: Dimensionless down channel velocity w (rotational speed 66.5 rpm, discharge pressure 30 MPa, discharge rate 2.3 kg/hr, flight angle 5.98° , slip factor 0.3, paste concentration 146% g solid/g liquid, flight height 4.9mm).

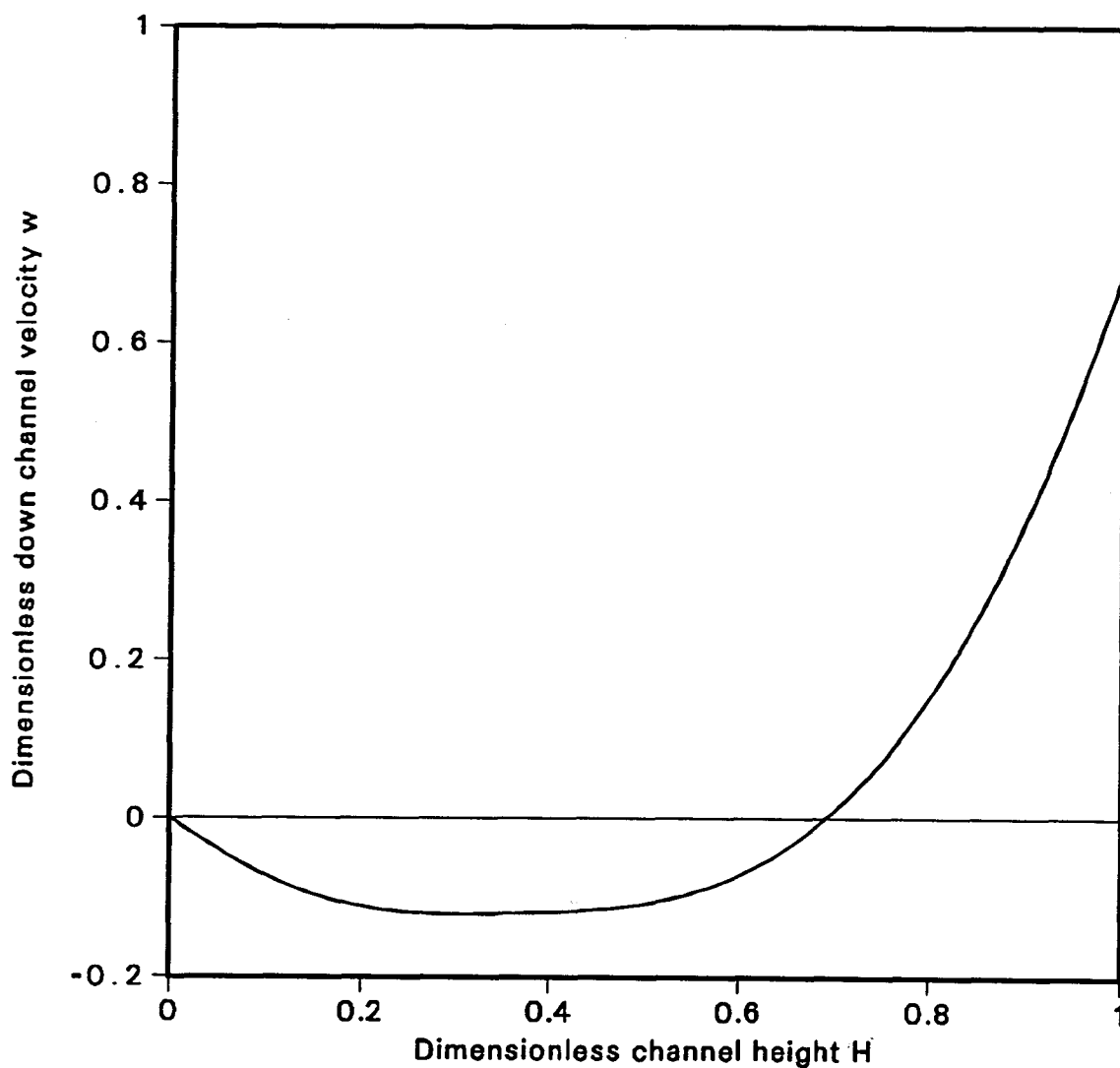


Figure 5-37: Dimensionless down channel velocity, w , at $y = W/2$ (discharge pressure 30 MPa, discharge rate 2.3 kg/hr, rotational speed 66.5 rpm, flight angle 5.98° , slip factor 0.3, paste concentration 146% g solid/g liquid, flight height 4.9mm).

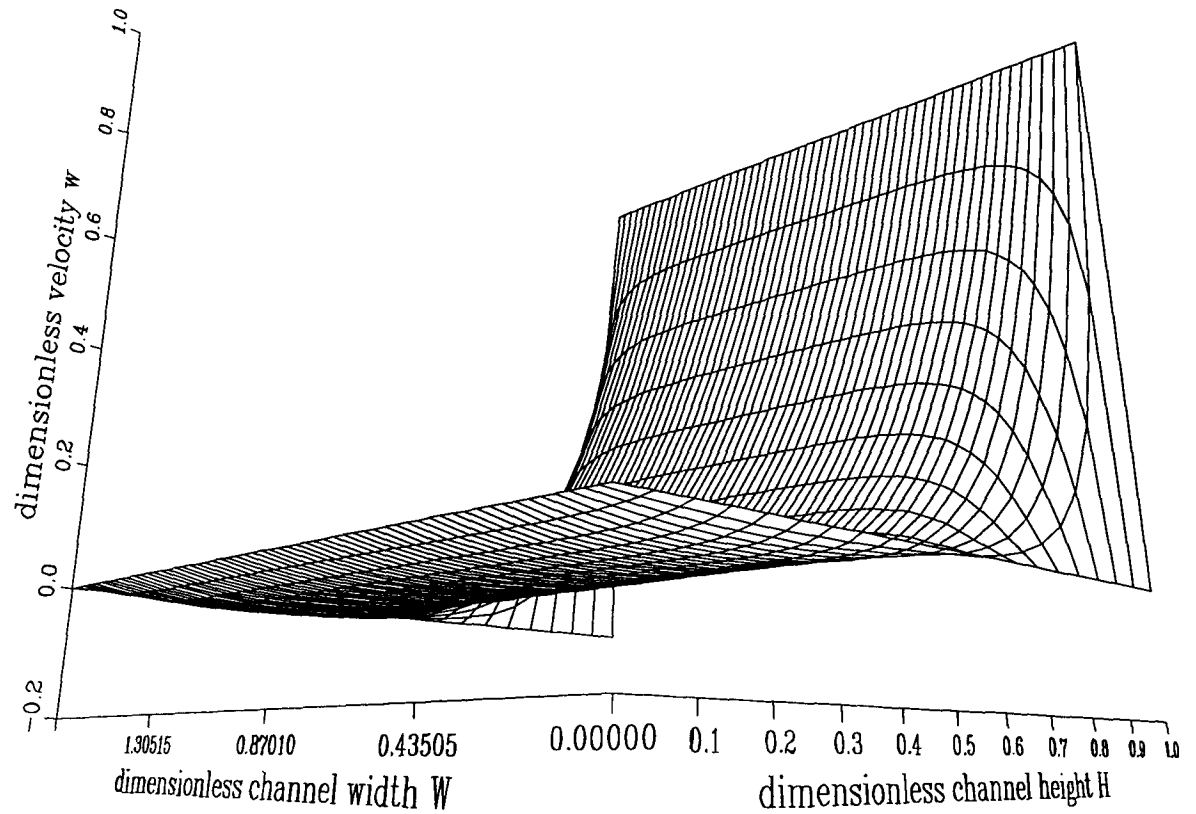


Figure 5-38: Dimensionless down channel velocity w (rotational speed 66.5 rpm, discharge pressure 30 MPa, discharge rate 8.7 kg/hr, flight angle 5.98°, slip factor 0, paste concentration 146% g solid/g liquid, flight height 4.9mm).

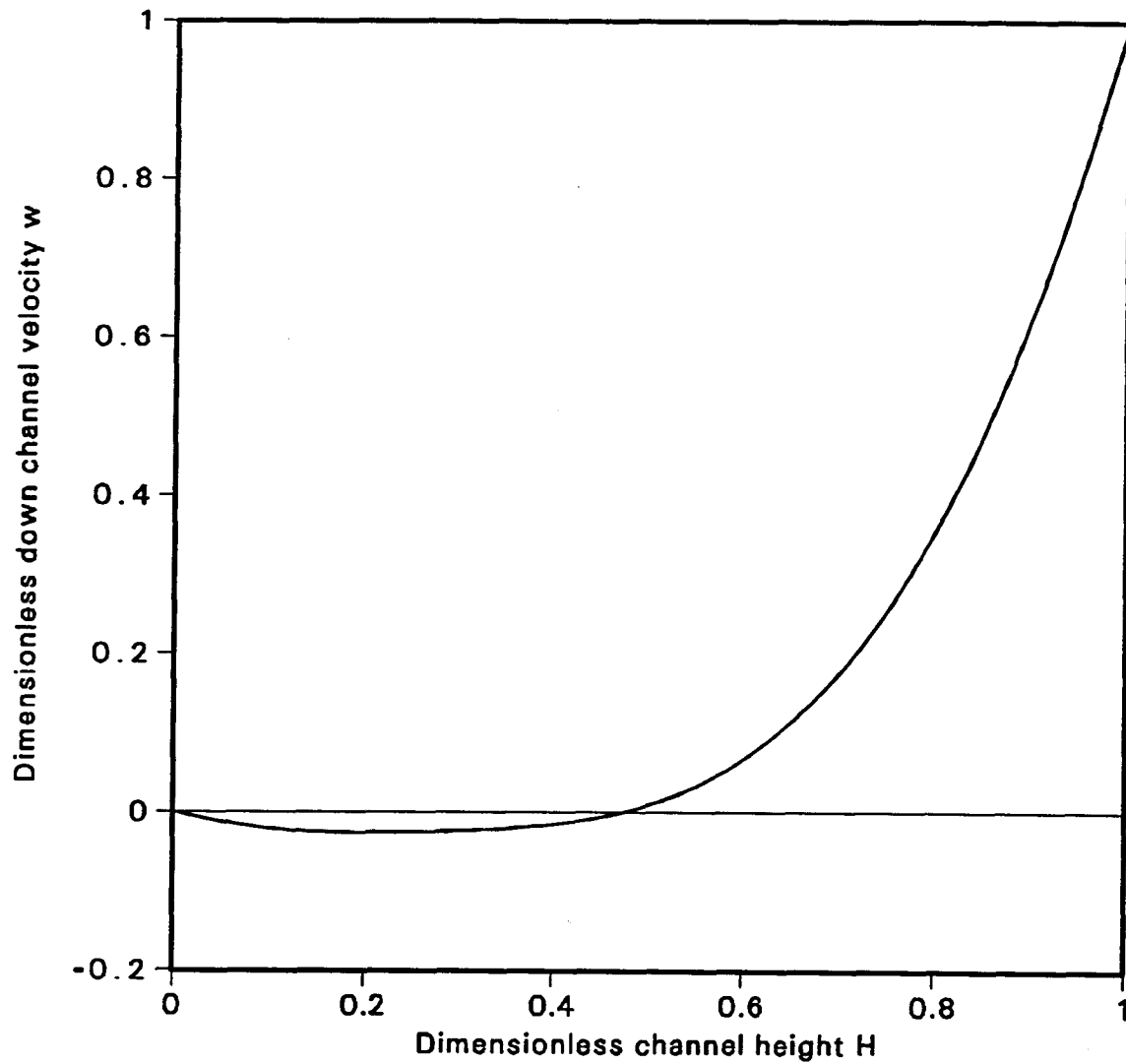


Figure 5-39: Dimensionless down channel velocity, w , at $y = W/2$ (discharge pressure 30 MPa, discharge rate 8.7 kg/hr, rotational speed 66.5 rpm, flight angle 5.98° , slip factor 0, paste concentration 146% g solid/g liquid, flight height 4.9mm).

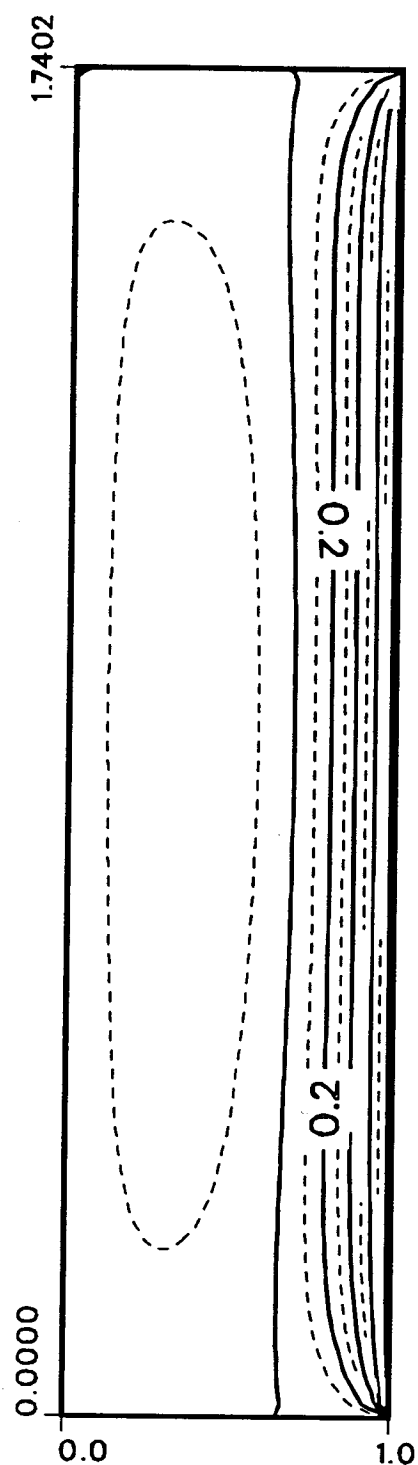


Figure 5-40: Dimensionless down channel velocity contours at $z = L/2$ (discharge pressure 30 MPa, discharge rate 2.3 kg/hr, rotational speed 66.5 rpm, flight angle 5.98° , slip factor 0.3, paste concentration 146% g solid/g liquid, flight height 4.9mm).

It is noted from Figures 3-37, 3-39 and 3-40 that a region exists in the screw channel where the flow is plug like. In the present model, this flow arises from $n < 1$. The smaller the value of n , the larger the region of plug flow (refer also to Appendix A.2). It should be noted that, in reality, the yield stress also contributes to the plug flow regime. The existence of the yield stress increases the region but, for the present case, this effect does not appear to be significant (*c. f.* Appendix A.2). Thus, ignoring the yield stress should not have a significant influence on the size of the plug flow region. To include the yield stress into the model would be extremely difficult since the size and shape of the plug-flow region is not known a priori and cannot be readily determined. Since the yield stress was not likely to compromise the accuracy of the present results, it was excluded from the extruder model.

5.3.8.2 Cross Channel Flow

The cross channel flow, also called the transverse flow, does not affect the discharge rate directly. However, the existence of a cross channel flow changes the structure of the velocity distribution, which in turn affects the apparent viscosity and results in altering the discharge rate. The values of the cross channel velocities u and v can be shown most conveniently as a stream function contour plot where the stream function is defined by Equation (3-29) and represents the locus of points tangent to the velocity vectors in the x, y plane. Figures 5-41 and 5-42, which show the stream function distribution at $z = L/2$, were obtained using $\kappa = 0$ and discharge pressures of 10 MPa and 30 MPa, respectively. It is shown that, at higher discharge pressures, the paste tends to circulate more rapidly in the channel than it does at lower discharge pressures.

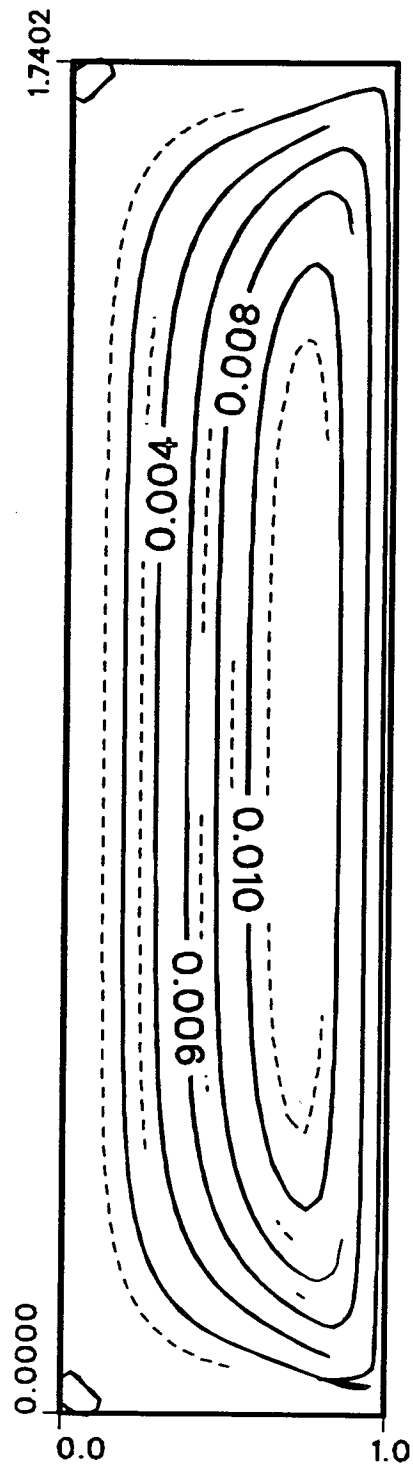


Figure 5-41: Stream function contours (flight angle 5.98° , rotational speed 66.5 rpm, discharge pressure 10 MPa, discharge rate 15.5 kg/hr, slip factor 0, paste concentration 146% g solid/g liquid, flight height 4.9mm).

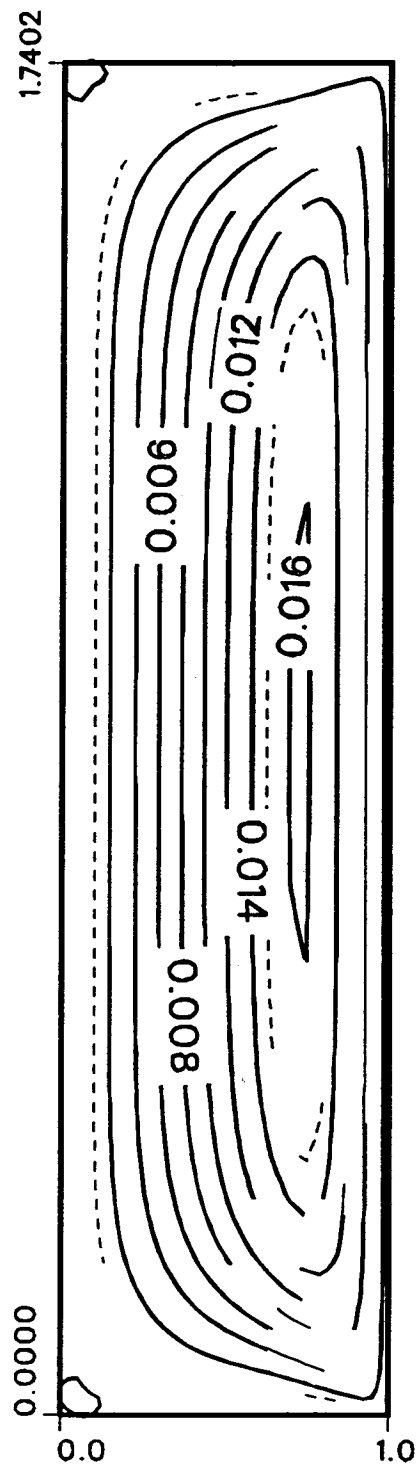


Figure 5-42: Stream function contours (flight angle 5.98° , rotational speed 66.5 rpm, discharge pressure 30 MPa, discharge rate 8.7 kg/hr, slip factor 0, paste concentration 146% g solid/g liquid, flight height 4.9mm).

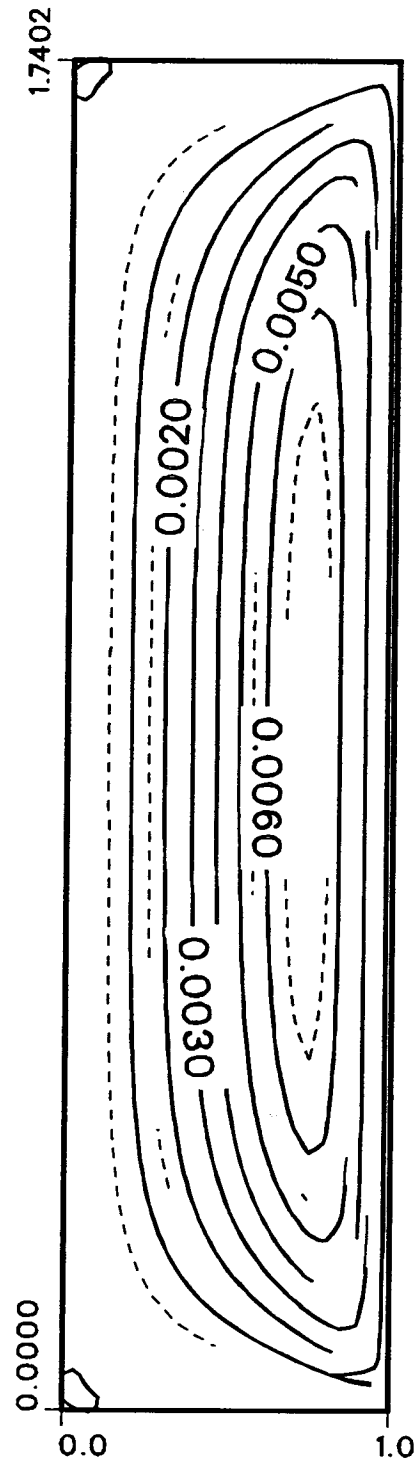


Figure 5-43: Stream function contours (flight angle 5.98° , rotational speed 66.5 rpm, discharge pressure 10 MPa, discharge rate 11.8 kg/hr, slip factor 0.3, paste concentration 146% g solid/g liquid, flight height 4.9mm).

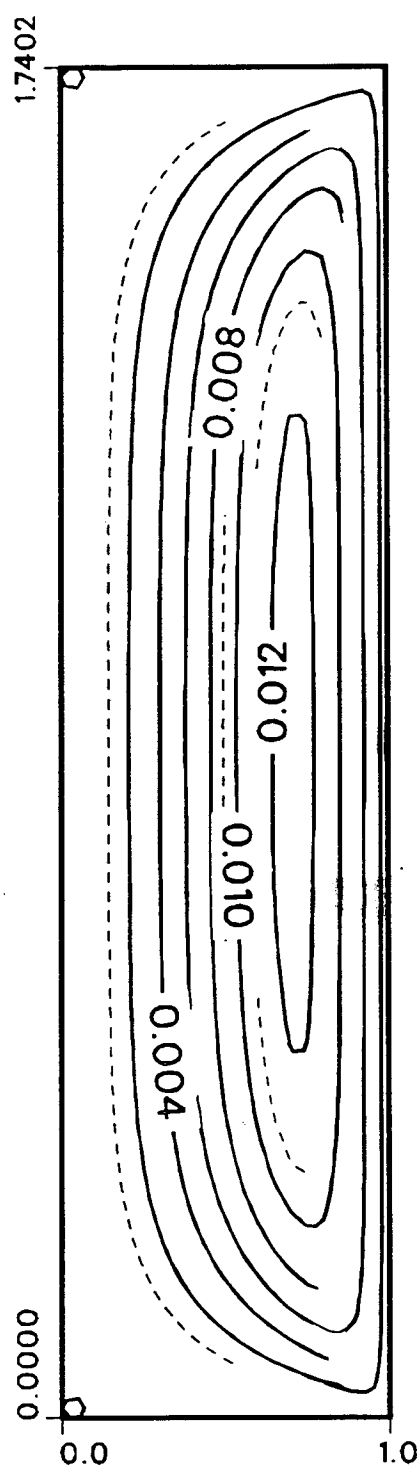


Figure 5-44: Stream function contour (flight angle 5.98° , rotational speed 66.5 rpm discharge pressure 30 MPa, discharge rate 2.3 kg/hr, slip factor 0.3, paste concentration 146% g solid/g liquid, flight height 4.9mm).

Figures 5-43 and 5-44 were obtained at the same discharge pressures but with $\kappa = 0.3$. By comparing these plots, the conclusion can be reached that slip at the boundaries also has a strong influence on the cross channel flow. When the slip exists, it reduces the cross channel circulation rate as is shown by the smaller maximum stream function values. The explanation is that in the absence of slip, more momentum is transferred to the paste in the y direction, which results in higher cross channel velocities. At the same rotational speed of the barrel, when slip occurs, less momentum is transferred to the paste and, therefore, a lower cross channel flow results.

Cross channel flow may be beneficial to biomaterial extrusion since, in most cases, the materials need to be well mixed. From the contour plots, it can be seen that there are two local countercirculating loops at the stationary corners. The paste is trapped in the corner vortices with little mass transfer to the main stream. This means that mixing is poor near these corners. To prevent this, the channel should be preferably designed with round corners having radii similar to the main stream contours shown in the figures.

5.3.9 Accuracy of Numerical Simulations

The simulation was generally conducted by dividing the channel section into 21×117 ($m \times n$) nodes; it was verified by dividing it into 41×233 nodes. Tables 5-4 and 5-5 show the typical calculated node values of the dimensionless down channel velocity, w , at different mesh sizes. The result shows that simulations obtained using different grid sizes yield similar values. This suggests that the model predictions are approximately converged.

Table 5-4: Simulated dimensionless down channel velocities adjacent to the flight for different mesh sizes (flight angle 5.98° , discharge pressure 20 MPa, discharge rate 5.93 kg/hr, slip factor 0.3, paste concentration 146% g solid/g liquid, flight height 4.9mm).

i	j=10 (21x117)	i	j=19 (41x233)
1	0.00000E+00	1	0.00000E+00
2	-1.18968E-02	3	-1.19369E-02
3	-2.08722E-02	5	-2.09099E-02
4	-2.59332E-02	7	-2.60339E-02
5	-2.81288E-02	9	-2.83486E-02
6	-2.83683E-02	11	-2.84862E-02
7	-2.74506E-02	13	-2.75518E-02
8	-2.54091E-02	15	-2.54549E-02
9	-2.17175E-02	17	-2.18197E-02
10	-1.55825E-02	19	-1.56119E-02
11	-5.92166E-03	21	-5.93829E-03
12	8.61387E-03	23	8.61716E-03
13	2.96413E-02	25	2.97252E-02
14	5.90575E-02	27	5.91254E-02
15	9.90458E-02	29	9.93631E-02
16	1.52038E-01	31	1.52192E-01
17	2.20612E-01	33	2.20693E-01
18	3.07316E-01	35	3.07575E-01
19	4.14434E-01	37	4.14772E-01
20	5.43728E-01	39	5.43752E-01
21	6.96191E-01	41	6.96191E-01

Table 5-5: Simulated dimensionless down channel velocities at $y = W/2$ for different mesh sizes (flight angle 5.98° , discharge pressure 20 MPa, discharge rate 5.93 kg/hr, slip factor 0.3, paste concentration 146% g solid/g liquid, flight height 4.9mm).

i	j=59 (21x117)	i	j=117 (41x233)
1	0.00000E+00	1	0.00000E+00
2	-1.32204E-02	3	-1.32694E-02
3	-2.31920E-02	5	-2.32000E-02
4	-2.86783E-02	7	-2.88010E-02
5	-3.07684E-02	9	-3.08343E-02
6	-3.05671E-02	11	-3.07105E-02
7	-2.95521E-02	13	-2.96657E-02
8	-2.76517E-02	15	-2.77363E-02
9	-2.37718E-02	17	-2.38161E-02
10	-1.67503E-02	19	-1.68116E-02
11	-5.01986E-03	21	-5.00900E-03
12	1.30196E-02	23	1.30909E-02
13	3.89653E-02	25	3.90602E-02
14	7.43173E-02	27	7.44246E-02
15	1.20486E-01	29	1.21499E-01
16	1.78802E-01	31	1.79830E-01
17	2.50545E-01	33	2.50855E-01
18	3.36952E-01	35	3.37338E-01
19	4.39236E-01	37	4.39378E-01
20	5.58590E-01	39	5.58595E-01
21	6.96191E-01	41	6.96191E-01

5.4 The Effect of Extrusion on Oil Extraction

The pastes (about 11 g) extruded at different discharge pressures were extracted with supercritical carbon dioxide at 35 MPa, 50°C and a flow rate of 1.8 g/min for approximately 11 hours using the equipment described in section 4.2.4.1 to examine how extrusion conditions affect extraction. Figure 5-45, which shows the results of these extraction experiments, indicates that the discharge pressure has some effects on the extraction efficiency. The higher the discharge pressure, the more oil was extracted with the same amount of supercritical carbon dioxide. A possible explanation is that the oil, which is in the form of small droplets (0.5-1 μm) enveloped by a thin layer of protein (Hofsten, 1970; Stanley *et. al.*, 1976), is difficult for supercritical carbon dioxide to penetrate. High pressure may cause more protein shells to be broken thus exposing more oil to the supercritical carbon dioxide. Therefore, the mass transfer area is much increased and, finally, results in the extraction of more oil with the same amount of supercritical fluid.

The extraction process can be divided into three stages. In the first stage, the linear stage, the oil and supercritical CO₂ have maximal contact, *i. e.*, all solid particles in the paste are covered with a layer of oil and the mass transfer area (contact area) between the CO₂ and oil is not changed by the extraction process. In this stage, the output CO₂ stream is saturated with oil, thus the amount of the extracted oil is proportional to the passed CO₂. In the second stage, corresponding to the curved portion of the extraction plot, sufficient oil has been extracted that the solid surfaces of the particles are starting to be exposed to CO₂. The mass transfer area is therefore decreasing and the output

CO₂ stream may no longer be saturated. In the third stage, where most of the oil in the paste has been extracted, the curves approach asymptotically the total oil content of the paste. For the present circumstances, this is about 39% (g oil/g paste).

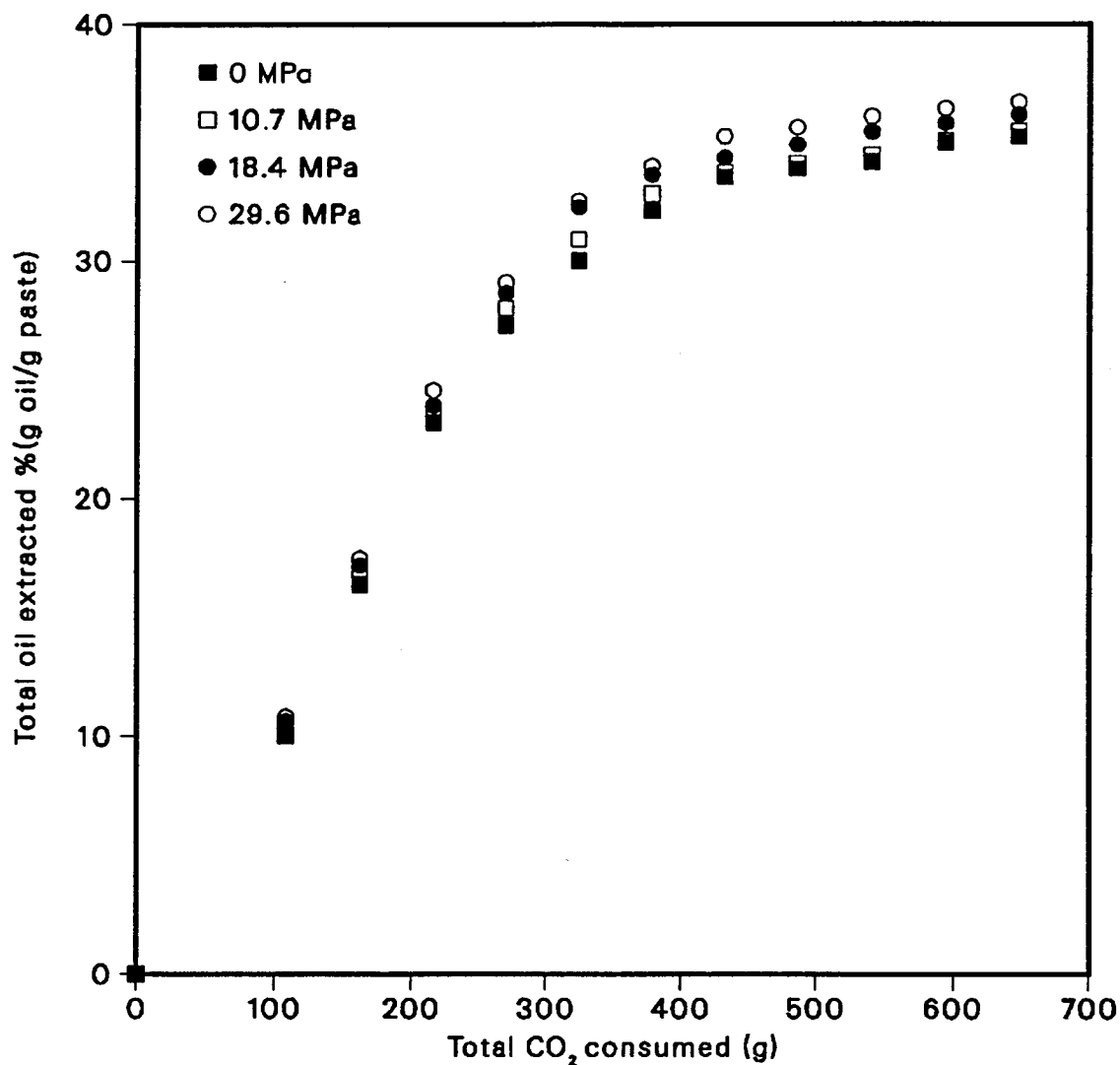


Figure 5-45: Effect of discharge pressure on supercritical fluid extraction of Canola oil. The pastes were either not extruded (0 Pa) or extruded at discharge pressures of 10.7 MPa, 18.4 MPa, 29.6 MPa.

CHAPTER SIX

CONCLUSIONS

This study has demonstrated that properly designed single screw extruders are effective in continuously delivering biomaterials, such as Canola pastes, for supercritical fluid extraction. Although the discharge pressure did not reach the desired value of 35 MPa, it fell well within the operating range of supercritical carbon dioxide extractors, *i. e.* $P \geq 30$ MPa. This study furthermore verified that the improved three-velocity mathematical model could well describe the behavior of Canola paste flowing in screw channels. The extruded Canola pastes were extracted with supercritical carbon dioxide and the extraction results showed that the discharge pressure of a screw extruder affected the oil yield.

The major findings of this study may be summarized as follows:

- 1) The apparent viscosities of Canola pastes have been thoroughly investigated at atmospheric pressure. An empirical equation, Equation (5-8) which relates the viscosity to temperature, concentration and shear rate has been determined. The equation applies over the temperature range $288\text{K} \leq T \leq 323\text{K}$; the concentration range $35.3\% \leq C \leq 95.7\%$ (g solid/g liquid) and the shear rate range $0.15 \leq \dot{\gamma} \leq 228 \text{ s}^{-1}$. It yielded satisfactory predictions when incorporated into the extrusion model.

- 2) The screw flight angle has a strong effect on the discharge rate and discharge pressure. A small flight angle can elevate the discharge pressure and enhance the discharge rate. Among the tested flight angles, namely 5.98° , 7.97° and 9.94° , the screw extruder with the smallest flight angle achieved the highest discharge pressure, 30 MPa, at the tested rotational speeds.
- 3) The rotational velocity of the screw has a strong effect on the discharge rate and discharge pressure. The greater the screw velocity, the higher the discharge pressure and discharge rate. The relationship between the rotational speed and discharge pressure and discharge rate is not linear for non-Newtonian materials like Canola pastes.
- 4) The standard no-slip assumption was found to be unsuitable for the extrusion of Canola pastes. A slip factor of $\kappa = 0.3$ was introduced and has been found to yield satisfactory predictions from the extrusion model.
- 5) An improved three-velocity model was developed in this study, and the existence of flight and slip effects were considered.
- 6) Although the yield stress of the concentrated Canola paste contributed to the plug flow region in the screw channel, the effect caused by the small flow behavior index ($n = 0.5$) predominates. Thus ignoring the yield stress in the model did not appear to introduce significant errors.
- 7) Good agreement has been achieved between experimental measurements and the predictions of the improved three-velocity model provided the slip factor, κ , was selected properly.

- 8) The effect of the discharge pressure of an extruder on the extractibility of oil from Canola pastes was explored. It was found that a high discharge pressure enhances the extractibility of Canola oil.

CHAPTER SEVEN

RECOMMENDATIONS

The following recommendations are made for future research:

- 1) As commercial extruders have to take raw seeds as the feed, it is necessary to study the complete extrusion process which includes feed, transition and metering sections when they are used as feeders for supercritical fluid extractors.
- 2) As extruders used for feeding supercritical fluid extractors always operate at high pressure, it is appropriate to investigate the apparent viscosity of Canola paste at full solid concentrations, high shear rates and high temperatures at an elevated pressure.
- 3) As it is necessary to reduce the slip effect to improve the performance of the screw extruder, roughening the flight and screw root surfaces should be carried out.
- 4) As a large yield stress contributes to the plug flow region in the extruder channel, consideration should be given to developing a model which takes this effect into account.
- 5) As commercial extruders always have gaps between the screw flights and barrel, it is necessary to develop a model that accounts for these gaps.

- 6) As an alternate approach, single screw extruders with restrictions or twin screw extruders may be able to generate higher discharge pressures and operate more efficiently. It is worthwhile exploring those devices as feeders for supercritical fluid extractors.

NOMENCLATURE

A	shear stress factor relates the torque reading and the shear stress of the rotational viscometer, $Pa/scale\ grad.$
a	Arrhenius equation constant, $Pa \cdot s.$
a_c	constant coefficient.
B	constant in Eliis fluid model.
b_c	constant coefficient.
C	Canola paste concentration, $g\ solid/g\ liquid.$
c	constant in Eliis fluid model.
D	screw diameter, $m.$
ΔE	activation energy, $J/k \cdot mol.$
E	consumed power of the extruder, $kw.$
e	flight thickness, $m.$
H	height of screw channel, $m.$
F_d	dimensionless drag flow correction factor.
F_{dc}	dimensionless drag flow curvature correction factor.
F_{de}	dimensionless drag flow end effect correction factor.
F_{dt}	dimensionless total drag flow correction factor.
F_p	dimensionless pressure flow correction factor.
F_p^*	shape correction factor.
F_{pc}	dimensionless pressure flow curvature correction factor.
F_{pe}	dimensionless pressure flow end effect correction factor.
F_{pt}	dimensionless total pressure flow correction factor.

G	Haake viscometer measuring drive unit and sensor system instrument factor, $mPa \cdot s / scale \text{ grad} \cdot min$.
G_1, G_2	flow rate calculation factors in Booy's model.
g	gravity acceleration, m/s^2 .
i	number of flights on a screw.
L	length of unrolled screw channel, m .
l	length of the capillary viscometer, m .
l_e	screw pitch length, m .
M	shear rate factor, min/s .
m	consistency coefficient, $Pa \cdot s^n$.
N_p	required power of the extruder, kw .
n	flow behavior index.
N	rotational speed, rpm .
N_p	required power of the electric moter, hp .
p	discharge pressure, Pa .
Δp	pressure drop across the capillary tube and the extruders, MPa .
Q	extruder discharge rate, kg/hr .
Q_{exp}	measured discharge rate from the capillary viscometer, mL/min .
Q_{pre}	predicted discharge rate for the capillary viscometer, mL/min .
R_c	universal gas constant, $J/mol \cdot K$.
R_o	radius of rotational viscometer sensor cup, m .
R_i	radius of rotational viscometer sensor rotor, m .
r	radius of the capillary tube, m .
S	torque reading from the rotational viscometer, $scale \text{ grad}$.
T	temperature, K .
T_e	required input torque of the extruder, $N \cdot m$.

x, y, z	components in Cartesian coordinates. x is along the height of channel; y is along the width of the channel and z is the down channel direction following the right-hand-rule.
V_x, V_y, V_z	dimensional velocities in x, y, z directions, m/s .
u, v, w	dimensionless velocities in x, y, z directions.
u_{max}	maximum velocity in the capillary tube, mm/s .
u_s	slip velocity in the capillary tube, mm/s .
V	screw top tip linear velocity, $m \cdot s^{-1}$.
V_y	y component of screw top tip linear velocity, $m \cdot s^{-1}$.
V_z	z component of screw top tip linear velocity, $m \cdot s^{-1}$.
W	width of screw channel, m .

Superscripts

k	k th iteration.
-----	-------------------

Subscripts

i	i th node along x border.
j	j th node along y border.

Greek Letters

α	constant coefficient.
β	constant coefficient.
χ	dimension less flow rate modification factor.
Δ	rate of deformation tensor.

δ	constant coefficient, distance of gap between screw flight and barrel, m .
ε	constant coefficient.
θ	flight angle, $^{\circ}$.
ρ	Canola paste density, kg/m^3 .
σ	constant coefficient.
γ	shear rate, s^{-1} .
η	apparent viscosity, $Pa \cdot s$.
η_{δ}	apparent viscosity at the gap between the screw flight tip and barrel, $pa \cdot s$.
κ	slip factor.
μ	viscosity of Newtonian fluid, $Pa \cdot s$.
μ_0	constant in Eliis fluid model.
τ	shear stress, Pa .
τ_0	yield stress, Pa .
τ_w	shear stress at walls, Pa .
Ω	vorticity.
ξ	combined variable of $\eta\Omega$.
ψ	stream function.

Other Symbols

∇^2	Laplacian operator.
∇^4	biharmonic operator.

REFERENCES

- Atkinson, B., Card, C. C. H. and Irons, B. M., "Application of the Finite Element Method to Creeping Flow Problems", *Trans. Inst. Chem. Engr.*, **48**, T276, 1970.
- Beach, D. H. C., "Rapeseed Crushing and Extraction", *High and Low Erucic Acid Rapeseed Oils*, J. G. Kramer, D. S. Frank, Eds., Academic Press, Toronto, 1983.
- Booy, M. L., "Influence of Channel Curvature on Flow, Pressure Distribution, and Power Requirements of Screw Pumps and Melt Extruders", *Soc. Plastics Engrs. Trans.*, **3**, 176, 1963.
- Booy, M. L., "Influence of Oblique Channel Ends on Screw-Pump Performance", *Polymer Enging. and Sci.*, January, 5, 1967.
- Boussinesq, M. J., "Memoire sur l'influence des frottements dans les mouvements reguliers des fluides", *Journal de Mathematique Pures et Appliquees*, series 2, **13**, 377, 1868.
- Brady, B. O.; Gambrell, R. P.; Dooley, K. M.; Knopf, F. C., "Supercritical Fluid Extraction of Hazardous Waste from Contaminated Soils", Conference Title: *American Chemical Society, Division of Environmental, Chemistry, 190th National Meeting*, **25**, No. 2, 246, 1985.

Brady, B. O.; Gambrell, R. P.; Dooley, K. M.; Knopf, F. C., "Supercritical Extraction of PCB Contaminated Soils", Conference Title: *Proceedings - International Conference on New Frontiers for Hazardous Waste Management*, United States Environmental Protection Agency, Office of Research and Development, (Report) EPA 600/9-85/025. Publ. by EPA, Cincinnati, OH, 479, 1985.

Brady, Basil O., Kao, Chien-Ping C.; Dooley, Kerry M.; Knopf, F. Carl;
"Supercritical Extraction of Toxic Organics from Soils", *Ind. Eng. Chem. Res.* **26**, No. 2, 261, Feb. 1987.

Bredeson, D.K., "Mechanical Oil Extraction", *Am. Oil Chem. Soc. J.*, **60**, 2, 211, 1983.

Brunner, G. and Peter, S., "On the Solubility of Glycerides and Fatty Acids in Compressed Gases in the Presence of an Entrainer", *Sep. Sci. and Tech.*, **17**, No. 1, 199, 1982.

Caswell, B. and Tanner, R. I., "Wirecoating Die Design Using Finite Element Methods", *Polym. Eng. Sci.*, **18**, 416, 1978.

Chen, J. W.; Muchmore, C. B.; Lin, T. C.; Tempelmeyer, K. E., "Supercritical Extraction and Desulfurization of Coal with Alcohols", *Fuel Process Technol.* **11** No. 3, 289, Dec. 1985

- Choi, K. J.; Nakhost, Z.; Krukonis, V. J.; Karel, M., "Supercritical Fluid Extraction and Characterization of Lipids From Algae *Scenedesmus, Obliquus*", *Food Biotechnology*, **1**, No. 2, 263, 1987.
- Choo, K. P., Hami, M.L. and Pittman, J. F. T., "Deep channel Operating Characteristics of a Single Screw Extruder. Finite Element Predictions and Experimental Results for Isothermal non-Newtonian Flow", *Polym. Enging. Soc.*, **21**, 100, 1981.
- Ciolfitto, Nick, *Private Communication*, RAM Hydraulics & Air Ltd., 1026A Auckland St., New Westminster, B. C., V3M 1K8, May, 1989.
- Clandinin, D. R., "Canola Meal for Livestock and Poultry", Pub. No. 59, D. R. Clandinin Ed. Canola Council of Canada, 1981.
- Darnell, W. H. and Mol, E. A. J., "Solids conveying in Extruder", *Soc. Plastics Eng. J.*, **12**, 20, 1956.
- DAS-8 Data Acquisition and Control Interface Board Manual, MetroByte Corporation, October, 1988.
- Davies, G. O. and Whitehead, J. C., "Design Challenges in Coal Liquefaction", Design 82, the Inst. of Chem. Engr., 251, 1982.
- Decker, H., Die Spritzmaschine, Hanover, Germany, Paul Troester Maschinefabrik, 1941.

DeHaven, E. S., *Ind. Eng. Chem.*, **51**, 813, 1959. Also, *Chem. Eng. Conference*, Montreal, Canada, April 23, 1958.

Denn, M. M., *Process Fluid Mechanics*, Englewood Cliffs, N. J., 1980.

Edmondson, I. R. & Fenner, R. T., "Melting of Thermoplastics in Single Screw Extruders", *Polymer*, **16**, 49, 1975.

Eggers, R., "High Pressure Extraction of Oil Seed", *Am. Oil Chem. Soc. J.*, **62**, No. 8, 1222, 1985.

Ely, J. F., "A Review of Supercritical Fluid Extraction", NBS Tech. Report, 1983.

EXP-16 Manual, MetroByte Corporation, March, 1985.

Ezell, G. H., "Viscosity of Concentrated Orange and Grapefruit Juice", *Food Technol.*, **13**, 9, 1959.

Fattori, M. J., "Supercritical Fluid Extraction of Canola Seed", doctoral dissertation, the University of British Columbia, November 1985.

Friedrich, J. P.; List, G. R.; Heakin, A. J., "Petroleum-free Extraction of Oil from Soybeans with Supercritical Carbon Dioxide", *J. Agric. Food Chem.*, **28**, No. 6, 1153, 1982.

- Friedrich, J. P.; List, G. R., "Characterization of Soybean Oil Extracted by Supercritical Carbon Dioxide and Hexane", *J. Agric. Food Chem.*, **39**, 192, 1982.
- FOA (Food and Agriculture Organization of the United Nations) Yearbook, Statistics Division of the Economic and Social Policy Department, *Production*, **44**, 140, 1990.
- Funazukuri, Toshitaka; Ogasawara, Sadao; Wakao, Noriaki; Smith, J. M., "Subcritical and Supercritical Extraction of Oil from Used Automotive Tire Samples", *J. of Chem. Eng. of Japan*, **18**, No.5, 455, Oct. 1985.
- Ghonasgi, D.; Ye, M.; Dooley, K. M.; Knopf, F. C., "High-Pressure Solvent Extraction and Catalytic Oxidation of Hazardous Wastes from Aqueous Streams", *J. of Hazardous Materials*, **24**, No. 2, 291, Sep., 1990.
- Gill, T. A. and Tung, M. A., "Rheological, Chemical and Microstructural Studies of Rapeseed Protein Dispersions", *J. Inst. Can. Sci. Technol. Aliment*, **9**, No., 2, 75, 1976.
- Glyder, B. S., and Holmes-Walker, W. A., "Screw Extrusion of Thermoplastics", *Intern. Plastics Eng.*, **2**, 338, 1962
- Gotsis, Z. Jr. A. D. and Kalyon, D. M., "Single Screw Extrusion Processing of Highly Filled Suspensions Including Wall Slip", *48th Annual Technical Conference, Soc. of Plastics Engng., INC. Technical Papers, ANTEC 90*, Vol. **XXXVI**, 160, 1990.

- Gray, M., "Supplying Plastic Compounds of India Rubber and Gutta Percha to Molding or Shaping Dies", British Patent 5056, 1879.
- Griffith, R. M., "Fully Developed Flow in Screw Extruders", *Ind. Eng. Chem. Fundam.*, **32**, No. 7, 67, 1978.
- Haan, A. B. DE; De Graauw, J., "Separation of Alkanes and Aromatics with Supercritical C₂H₆, CO₂, CClF₃, and CHF₃", *Separation Science and Technology*, **27**, No. 1, 43, Jan., 1992.
- Hand, D. B., Moyer, C., Ransford, J. R., Hening, J. C. and Whittenberger, R. T., "Effect of Processing Conditions on the Viscosity of Tomato Juice", *food Technol.* **9**, 228, 1955.
- Harper, J. C. and El Sahrigi, A. F., "Viscometric Behavior of Tomato Concentrates", *J. Food Sci.*, **30**, 470, 1965.
- Harper, J. M., *Extrusion of Foods*, v1, CRC Press Inc., Boca Raton, Florida, 1981.
- Hippo, Edwin J.; Crelling, John C., "Desulfurization of Single Coal Materials", *Fuel Processing Technology*, **27**, No. 3, 287, 1991.
- Hofsten, A. V., "Cellular Structure of Rapeseed", *Proc. Int. conference on the Science, Technology and Marketing of Rapeseed and Rapeseed Products*, Quebec, Can. Sept. 20-23, 70-85, 1970.

- Hovey, V. M., "History of Extrusion Equipment for Rubber and Plastics", *Wire and Wire Prod.*, **36**, 192, 1961.
- Irvin, T. R.; Roop, R. K.; Akgerman, A., "Supercritical Extraction of Toxic Contaminants from Water", Conference Title: the AIChE Spring National Meeting, 1987 Mar. 29, *AIChE symposium pap.* 35f, 15, 1987.
- Jacobi, H. R., *Screw Extrusion of Plastics*, London, Illiffe Books Ltd., 1963.
- Janssen, L. P. B. M., *Twin Screw Extrusion*, ESP Comp., Netherlands, 1978.
- Kaiser, H., "Screw Extrusion of Melted Plastics", Doctoral Dissertation, Virginia Polytechnic Inst., Va., 1967.
- Kaufman, M., "The Birth of the Plastics Extruder", *Polym. Plast.*, (June), 243, 1969.
- Kiparissides, C. and Vlachopoulos, J., "Finite Element Analysis of Calendering", *Polym. Eng. Sci.*, **16**, No. 10, 712, 1976.
- Lawal, A. and Kalyon, D. M., "Incorporation of Wall Slip in Non-Isothermal Modeling of Single Screw Extrusion Processing", Proceedings of the 1st Int. Conf. on Transport Phenomena in Processing, Ed. by Selcuk I. Guceri, Honolulu, Hawaii, Mar. 22-26, 1992.

- Kroesser , F. W., and Middleman, S., "The Calculation of Screw Characteristics for the Extrusion of Non-Newtonian Melts", *Polymer Eng. Sci.*, **5**, 231, (Oct.) 1965.
- Lefebvre, J., "Viscosity of Concentrated Protein Solutions", *Progress and Trends in Rheology*, ed. by Hanswalter Giesekus, etc., Proceedings of the First Conference of European Rheologists, Graz (Austria), April 14-16, p266, 1982.
- Liu, R., "Extraction with Supercritical Fluids", *Xian Dai Hua Gong (Modern Chemical Engineering, Chinese)*, **33**, 49, 1986.
- McKelvey, J. M., *Polymer Processing*, Wiley, New York, 1962.
- Maddock, B. H., "Pressure Development in Extruder Screw", *Soc. Plastics Engrs.*, J. 20, 1277, 1964.
- Maillefer, C., "An Analytical Study of the Single Screw Extruder, Part I", *Brit. Plastics*, 394, Oct. 1954.
- Maillefer, C., "An Analytical Study of the Single Screw Extruder, Part II", *Brit. Plastics*, 437, Nov. 1954.
- Maillefer, C., "A Two Channel Extruder Screw", *Modern Plast.*, **40**, 132, 1963.
- Martin, B., "Numerical Studies of Steady-state Extrusion Process", doctoral dissertation, University of Cambridge, 1969.

- Meskat, W., "Theorie der Stoffbewegung in Schneckenmaschinen", *Kunststoffe—Plastics*, **45**, 87, 1955.
- Metzner, A. B., *Advanced in Chemical Engineering*, edited by Drew, T. B., and Hoopes, J. W., Vol. 1, pp. 109, 111 Academic Press, New Yourk (1956).
- Middleman, S., "The Flow of Power-law Fluids in Rectangular Ducts", *Trans. Soc. Rheol.*, **9**, No. 1, 83, 1965.
- Mori, Y., and Matsumoto, T. K., "Analytical Study of Plastics Extrusion", *Rheol. Acta*, **1**, No. 2-3, 240, 1958.
- Muchmore, Charles B.; Kent, Albert C.; Lin, Ta-Chang, "Potential Products Resulting from Desulfurization of High Sulfur Content Coal with Supercritical Alcohols", Proceedings of the First International Conference, Columbus, OH, USA: Processing and Utilization of High Sulfur Coals, *Coal Science and Technology*, **9**, 751, Oct. 13-17, 1985.
- Narkis, M., and Ram, A., : "Extrusion Discharge Rate Equations Non-Newtonian Fluids", *Polymer Eng. Sci.*, **7**, No. 3, 161, 1967.
- Paguot, *IUPAC*, 1986.
- Pawlowski, J., unpublished report, Dormagen, Germany, farbenfabriken Bayer, 1949.

- Payne, A. R., "Effect of Dispersion on the Dynamic Properties of Filler-loaded Rubbers", *J. of Appl. Polym. Sci.*, **9**, 2273, 1965.
- Pearce, D. L. and Jordan, P. J., "Supercritical Fluid Extraction Prospects for Applications in New Zealand", Proceedings - IPENZ Annual Conference, pp 183-193, v2 *Power of Engineering*, Conference Location: New Plymouth, NZ, Feb. 15-19, 1988.
- Pearson, J. R. A., *Mechanics of Polymer Processing*, Elsevier Appl. Sci. Publ., Ltd., Crown House, Linton Rd., Barking, Essex, England, 1985.
- Pend, Yucheng; Cheng, Jianhua and Wu, Yuanjian, "the Mathematical Model of Solid Conveying Zone in Single Extruder", *43rd Annual Technical Conference, Soc. of Plastics Enger., INC., Technical Papers*, ANTEC 85, Vol. XXXI, 73, 1985
- Peter, S., "Chemical Engineering Applications of Supercritical Solvents", *Ber. bunsenges. Phys. Chem.*, **88**, 875, 1984.
- Prasad, R., Gottesman, M. and Scarella, R. A., "Decaffeination of Aqueous Extrats", U. S. patent, 4246291, 1981.
- Qian, Y., "Extraction with Supercritical Gases" *Xiandai Huagong/Modern Chemical Industry*, **4**, 24, Aug. 20, 1984.
- Roache, Patrick J., *Computational Fluid Dynamics*, Hermosa Publishers, Albuquerque, N.M., 1972.

- Robinson, W. B., Kimball, L. B., Ransford, J. R., Moyer, J. C. and Hand, D. B., "Factors Influencing the Degree of Settling in Tomato Juice", *Food Technol.*, **10**, 109, 1956.
- Roop, Robert K.; Hess, Richard K.; Akgerman, Aydin, "Supercritical Extraction of Organics from Water and Soil", *Journal of Hazardous Materials* **22**, No. 2, 259, Nov., 1989.
- Rowell, H. S. and Finlayson, D., "Screw Viscosity Pumps", *Engineering*, **114**, 606, 1922.
- Rowell, H. S. and Finlayson, D., "Screw Viscosity Pumps", *Engineering*, **126**, 249, 385, 1928.
- Schenkel, G., *Plastics Extrusion Technology and Theory*, Iliffe Books, Ltd., London, 1966.
- Shapiro, J., Halmos, A. L. & Pearson, J. R. A., "Melting in Single Screw Extruders. Part I: The mathematical Model. Part II: Solution for a Newtonian Fluid", *Polymer*, **17**, 905, 1976.
- Simonds, H. R., Weith, A. J. and Schack, W., *Extrusion of Plastics, Rubber and Metals*, Reinhold Publishing Corp., New York, 1952.

- Skelland, A. H. P., *Non-Newtonian Flow and Heat Transfer*, John Wiley & Sons, Inc., NY, 1967.
- Smit, C. J. B. and Nortje, B. K., "Observations on the Consistency of Tomato Paste", *Food Technol.*, **12**, 356, 1958.
- Speers, R. A. and Tung, M. A., "Concentration and Temperature Dependence of Flow Behavior of Xanthan Gum Dispersions", *J. of Food Sci.*, **51**, No. 1, 96, 1986.
- Stahl, E., Quirin, K. W., Glatz, A., Gerard, D. and Rau, G., "New Developments in the Field of High Pressure Extraction of Natural Products with Dense Gases", *Ber. Bunseng. Phys. Chem.*, **88**, 900, 1984.
- Stanley, D. W., Gill, T. A., de Man, J. M. and Tung, M. A., "Microstructure of Rapeseed", *Can. Inst. Food Sci. Technol. J.*, 9(2), 54, 1976.
- Streeter, V. L., ed., *Handbook of Fluid Dynamics*, Metzner, V. L., Section 7, p. 28, New York, McGraw-Hill, 1961.
- Tadmor, Z., "Fundamentals of Plasticating Extrusion, I Theoretical model for Melting", *Polym. Enging. Sci.*, **6**, No. 3, 185, 1966.
- Tadmor, Z. and Gogos, C. G., *Principles of Polymer Processing*, John Wiley & Sons, NY, 1979.

- Tadmor Z. and Klein, I., *Engineering Principles of Plasticating Extrusion*, Van Nostrand Reinhold Company, New York, NY, 1970.
- Thomas, D. G., "Transport Characteristics of Suspension: VIII. A Note of the Viscosity of Newtonian Suspensions of Uniform Spherical Particles", *J. of Colloid Science*, **20**, 267, 1965.
- Tung, M. A., "Rheology of Protein Dispersions", *J. of Texture Studies*, **9**, No. 3, 31, 1978.
- Tung, M. A., "Rheological Principles with Applications to Fats and Oils Products", lecture notes, Dept. of Food Sci., UBC, 1988.
- Van Alsten, J. V. and Eckert, C. A., "Mixed Supercritical Solvent for Selective Solubility Enhancement", *Am. chem. Soc., Div. of Fuel Chemistry*, preprints of papers, **30**, No. 3, 13, 1987.
- Weeks, D. J. and Allen, W. J., "Screw Extrusion of Plastics", *J. of Mechanical Enging. Sci.*, **4**, 380, 1962.
- Wheeler, J. A., and Whissler, E. H., *Am. Inst. Chem. Engrs., J.*, **11**, 207, 1965.
- White, F. M., *Viscous Fluid Flow*, McGraw-Hill, 1974.
- White, J. L., "Elastomer Rheology and Processing", *Rubber Chem. Technol.*, **42**, 257, 1969.

- Whittenberger, R. T. and Nutting, G. C., "Effect of Tomato Cell Structures on Consistency of Tomato Juice", *Food Technol.*, **11**, 19, 1957.
- Whittenberger, R. T. and Nutting, G. C., "High Viscosity of Cell Wall Suspension Prepared from Tomato Juice", *Food Technol.*, **12**, 420, 1958.
- Yashida (Tokyo), "Studies on the Extrusion of Molten Plastics (1st report) -- Viscosity Measurement of Polyethylene", *Chem. Eng.*, **21**, 26, 1957.
- Yashida (Tokyo), "Studies on the Extrusion of Molten Plastics (2st report) -- Graphical Representation of Screw Characteristics of an Extruder for Molding Pseudoplastics Materials Like Polyethylene", *Chem. Eng.*, **21**, 32, 1957.
- Yeo, Sang-Do, Akgerman, Aydin, "Supercritical Extraction of Organic Mixtures from Aqueous Solutions", *AIChE J.*, **36**, No. 11, 1743, Nov., 1990.
- Yilmazer, U. and Kalyon, D., "Slip Effects in Capillary and Parallel Disk Transitional Flow of Highly Filled Suspensions", *J. Rheol.*, **33**, No.8, 1197, 1989.
- Yueruem, Yuda, Tugluhan, Ayse, "Supercritical extraction and desulphurization of Beypazari lignite by ethyl alcohol/NaOH treatment. 1. Effect of ethyl alcohol/coal ratio and NaOH", *Sci. & Tech. Int.*, **8**, No. 2, 87, Feb. 1990.

Yueruem, Yuda, Tugluhan, Ayse, "Supercritical Extraction and Desulphurization of Beypazari Lignite by Ethyl Alcohol/NaOH Treatment 2, Kinetics", *Fuel/Sci. & Tech. Int*, **8**, No. 3, 221, Apr. 1990.

Zhu, F., Fang, S. and Wang, N., "Non-plug Flow Solid Conveying Theory", *47th Annual Technical Conference, Soc. of Plastics Enger. INC., Technical Papers*, ANTEC 89, Vol. **XXXV**, 87, 1989.

PAGINATION ERROR.

ERREUR DE PAGINATION.

TEXT COMPLETE.

LE TEXTE EST COMPLET.

NATIONAL LIBRARY OF CANADA.

BIBLIOTHEQUE NATIONALE DU CANADA.

CANADIAN THESES SERVICE.

SERVICE DES THESES CANADIENNES.

APPENDIX A

A.1 Detailed Derivation of Equations

A.1.1 Flow Equation

Differentiating equation 3-23 with respect to y gives:

$$\begin{aligned}
 \frac{\partial^2 p}{\partial x \partial y} &= 2 \frac{\partial^2 \eta}{\partial x \partial y} \frac{\partial u}{\partial x} + 2 \frac{\partial \eta}{\partial x} \frac{\partial^2 u}{\partial x \partial y} + 2 \frac{\partial \eta}{\partial y} \frac{\partial^2 u}{\partial x^2} \\
 &\quad + 2 \eta \frac{\partial^3 u}{\partial x^2 \partial y} + \frac{\partial^2 \eta}{\partial y^2} \frac{\partial u}{\partial y} + 2 \frac{\partial \eta}{\partial y} \frac{\partial^2 u}{\partial y^2} + \eta \frac{\partial^3 u}{\partial y^3} \\
 &\quad + \frac{\partial^2 \eta}{\partial y^2} \frac{\partial v}{\partial x} + 2 \frac{\partial \eta}{\partial y} \frac{\partial u}{\partial x \partial y} + \eta \frac{\partial \eta}{\partial y} \frac{\partial^2 v}{\partial x \partial y^2}
 \end{aligned} \tag{A1-1}$$

Differentiating Equation (3-24) with respect to x gives:

$$\begin{aligned}
 \frac{\partial^2 p}{\partial y \partial x} &= 2 \frac{\partial^2 \eta}{\partial x \partial y} \frac{\partial v}{\partial y} + 2 \frac{\partial \eta}{\partial y} \frac{\partial^2 v}{\partial x \partial y} + 2 \frac{\partial \eta}{\partial x} \frac{\partial^2 v}{\partial y^2} \\
 &\quad + 2 \eta \frac{\partial^2 v}{\partial x \partial y^2} + \frac{\partial^2 \eta}{\partial x^2} \frac{\partial u}{\partial y} + 2 \frac{\partial \eta}{\partial x} \frac{\partial^2 u}{\partial x \partial y} \\
 &\quad + \eta \frac{\partial^3 u}{\partial x^2 \partial y} + \frac{\partial^2 \eta}{\partial x^2} \frac{\partial v}{\partial y} + 2 \frac{\partial \eta}{\partial x} \frac{\partial^2 v}{\partial x^2} + \eta \frac{\partial^3 v}{\partial x^3}
 \end{aligned} \tag{A1-2}$$

Replacing the velocities u and v in equations (A1-1) and (A1-2) with derivatives of stream function, $u = \partial \psi / \partial y$ and $v = -\partial \psi / \partial x$ yields:

$$\begin{aligned}
 \frac{\partial^2 p}{\partial x \partial y} = & 2 \frac{\partial^2 \eta}{\partial x \partial y} \frac{\partial^2 \psi}{\partial x \partial y} + 2 \frac{\partial \eta}{\partial x} \frac{\partial^3 \psi}{\partial x \partial y^2} + 2 \frac{\partial \eta}{\partial y} \frac{\partial^3 \psi}{\partial x^2 \partial y} \\
 & + 2 \eta \frac{\partial^4 \eta}{\partial x^2 \partial y^2} + \frac{\partial^2 \eta}{\partial y^2} \frac{\partial^2 \psi}{\partial y^2} + \frac{\partial \eta}{\partial y} \frac{\partial^3 \psi}{\partial y^3} \\
 & - \frac{\partial^2 \eta}{\partial y^2} \frac{\partial^2 \psi}{\partial x^2} - \frac{\partial \eta}{\partial y} \frac{\partial^3 \psi}{\partial x^2 \partial y} + \frac{\partial \eta}{\partial y} \frac{\partial^3 \psi}{\partial y^3} \\
 & + \eta \frac{\partial^4 \eta}{\partial y^4} - \frac{\partial \eta}{\partial y} \frac{\partial^3 \psi}{\partial x^2 \partial y} - \eta \frac{\partial^4 \psi}{\partial x^2 \partial y^2}
 \end{aligned} \tag{A1-3}$$

$$\begin{aligned}
 \frac{\partial^2 p}{\partial y \partial x} = & \frac{\partial^2 \eta}{\partial x^2} \frac{\partial^2 \psi}{\partial y^2} + \frac{\partial \eta}{\partial x} \frac{\partial^3 \psi}{\partial x \partial y^2} - \frac{\partial^2 \eta}{\partial x^2} \frac{\partial^2 \psi}{\partial x^2} \\
 & - \frac{\partial \eta}{\partial x} \frac{\partial^3 \psi}{\partial x^3} + \frac{\partial \eta}{\partial x} \frac{\partial^3 \psi}{\partial x \partial y^2} + \eta \frac{\partial^4 \psi}{\partial x^2 \partial y^2} \\
 & - \frac{\partial \eta}{\partial x} \frac{\partial^3 \psi}{\partial x^3} - \eta \frac{\partial^4 \eta}{\partial x^4} - 2 \frac{\partial^2 \eta}{\partial x \partial y} \frac{\partial^2 \psi}{\partial x \partial y} \\
 & - 2 \frac{\partial \eta}{\partial y} \frac{\partial^3 \psi}{\partial x^2 \partial y} - 2 \frac{\partial \eta}{\partial x} \frac{\partial^3 \psi}{\partial x \partial y^2} - 2 \eta \frac{\partial^4 \psi}{\partial x^2 \partial y^2}
 \end{aligned} \tag{A1-4}$$

Subtracting A1-4 from A1-3 results in:

$$\begin{aligned}
& 2 \frac{\partial^2 \eta}{\partial x \partial y} \frac{\partial^2 \psi}{\partial x \partial y} + 2 \frac{\partial \eta}{\partial x} \frac{\partial^3 \psi}{\partial x \partial y^2} + \eta \frac{\partial^4 \psi}{\partial x^2 \partial y^2} + \\
& \frac{\partial^2 \eta}{\partial y^2} \frac{\partial^2 \psi}{\partial y^2} + 2 \frac{\partial \eta}{\partial y} \frac{\partial^3 \psi}{\partial y^3} - \frac{\partial^2 \eta}{\partial y^2} \frac{\partial^2 \psi}{\partial x^2} + \eta \frac{\partial^4 \eta}{\partial y^4} \\
& = -2 \frac{\partial^2 \eta}{\partial x \partial y} \frac{\partial^2 \psi}{\partial x \partial y} - 2 \frac{\partial \eta}{\partial x} \frac{\partial^3 \psi}{\partial x^3} - \eta \frac{\partial^4 \psi}{\partial x^2 \partial y^2} + \\
& \frac{\partial^2 \eta}{\partial x^2} \frac{\partial^2 \psi}{\partial y^2} - 2 \frac{\partial \eta}{\partial y} \frac{\partial^3 \psi}{\partial x^2 \partial y} - \frac{\partial^2 \eta}{\partial x^2} \frac{\partial^2 \psi}{\partial x^2} - \eta \frac{\partial^4 \psi}{\partial x^2}
\end{aligned} \tag{A1-5}$$

or

$$\begin{aligned}
& \eta \left(\frac{\partial^4 \psi}{\partial x^2} + \frac{\partial^4 \psi}{\partial x^2 \partial y^2} + \frac{\partial^4 \psi}{\partial y^4} \right) \\
& = -4 \frac{\partial^2 \eta}{\partial x \partial y} \frac{\partial^2 \psi}{\partial x \partial y} - 2 \frac{\partial \eta}{\partial x} \left(\frac{\partial^3 \psi}{\partial x^3} + \frac{\partial^3 \psi}{\partial x \partial y^2} \right) + \\
& \frac{\partial^2 \eta}{\partial x^2} \frac{\partial^2 \psi}{\partial y^2} - 2 \frac{\partial \eta}{\partial y} \left(\frac{\partial^3 \psi}{\partial x^2 \partial y} + \frac{\partial^3 \psi}{\partial y^3} \right) - \\
& \frac{\partial^2 \eta}{\partial x^2} \frac{\partial^2 \psi}{\partial x^2} - \frac{\partial^2 \eta}{\partial y^2} \frac{\partial^2 \psi}{\partial y^2} + \frac{\partial^2 \eta}{\partial y^2} \frac{\partial^2 \psi}{\partial x^2}
\end{aligned} \tag{A1-6}$$

Introducing the definition of vorticity given as follows:

$$\Omega = - \left(\frac{\partial^2 \psi}{\partial x^2} + \frac{\partial^2 \psi}{\partial y^2} \right) \tag{A1-7}$$

and

$$\nabla^2 \Omega = - \left(\frac{\partial^4 \psi}{\partial x^2} + \frac{\partial^4 \psi}{\partial x^2 \partial y^2} + \frac{\partial^4 \psi}{\partial y^4} \right) \tag{A1-8}$$

Equation (A1-6) therefore becomes:

$$\begin{aligned}
 -\eta \nabla^2 \Omega = & -4 \frac{\partial^2 \eta}{\partial x \partial y} \frac{\partial^2 \psi}{\partial x \partial y} + 2 \frac{\partial \eta}{\partial x} \frac{\partial \Omega}{\partial x} + \\
 & \frac{\partial^2 \eta}{\partial x^2} \frac{\partial^2 \psi}{\partial y^2} + 2 \frac{\partial \eta}{\partial y} \frac{\partial \Omega}{\partial y} - \\
 & \frac{\partial^2 \eta}{\partial x^2} \frac{\partial^2 \psi}{\partial x^2} - \frac{\partial^2 \eta}{\partial y^2} \frac{\partial^2 \psi}{\partial y^2} + \frac{\partial^2 \eta}{\partial y^2} \frac{\partial^2 \psi}{\partial x^2}
 \end{aligned} \tag{A1-9}$$

Furthermore adding

$$\frac{\partial^2 \eta}{\partial x^2} \Omega + \frac{\partial^2 \eta}{\partial y^2} \Omega \tag{A1-10}$$

to both sides of Equation (A1-9) and noticing

$$\nabla^2(\eta \Omega) = \eta \nabla^2 \Omega + 2 \frac{\partial \eta}{\partial x} \frac{\partial \Omega}{\partial x} + 2 \frac{\partial \eta}{\partial y} \frac{\partial \Omega}{\partial y} + \frac{\partial^2 \eta}{\partial x^2} \Omega + \frac{\partial^2 \eta}{\partial y^2} \Omega \tag{A1-11}$$

gives:

$$\nabla^2(\eta \Omega) = 4 \frac{\partial^2 \eta}{\partial x \partial y} \frac{\partial^2 \psi}{\partial x \partial y} - 2 \frac{\partial^2 \eta}{\partial x^2} \frac{\partial^2 \psi}{\partial x^2} - 2 \frac{\partial^2 \eta}{\partial y^2} \frac{\partial^2 \psi}{\partial x^2} \tag{3-38}$$

A.1.2 Shear Rate Equation for a Power Law Fluid in a Rotational Viscometer

As shown in Figure A2-1, a fluid element is taken from the gap between the cup and rotor of a rotational viscometer:

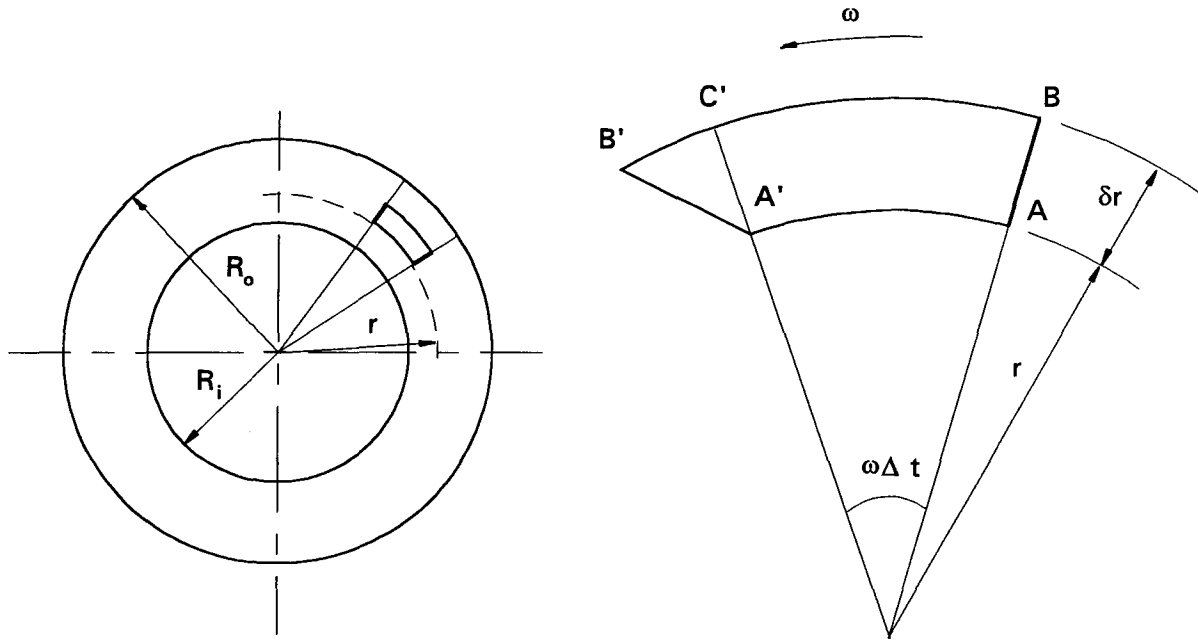


Figure A.1.2-1: Notation of a fluid element from a rotational viscometer

Since there is a velocity difference between the outside (BB') and the inside (AA') of the element, the line AB moves to $A'B'$ after time Δt . By the definition of shear strain:

$$\begin{aligned}
 \gamma &= \frac{B'C}{CA'} \\
 &= \frac{B'B - BC}{CA'} \\
 &= \frac{(r + \delta r)(\omega + \delta\omega)\Delta t - (r + \delta r)\omega\Delta t}{\delta r} \\
 &= - \frac{(r + \delta r)\delta\omega\Delta t}{\delta r}
 \end{aligned} \tag{A2-1}$$

where ω denotes the rotational speed of the fluid. As $\delta r \rightarrow 0$, the shear rate is given by:

$$\begin{aligned}\dot{\gamma} &= \frac{\gamma}{\Delta t} \\ &= -r \frac{d\omega}{dr}\end{aligned}\quad (\text{A2-2})$$

The definition of a power law with a yield stress is given by:

$$\tau = \tau_0 + m \left| \dot{\gamma} \right|^n \quad (\text{A2-3})$$

or in terms of torque, M , i. e.

$$\frac{M}{2\pi l} = \frac{M_0}{2\pi l} + m \left| \dot{\gamma} \right|^n \quad (\text{A2-4})$$

where M_0 is a yield torque. At this value, the rotor of the viscometer starts to move.

If the shear rate in Equation (A2-4) is taken always positive, the equation can be rearranged as:

$$\begin{aligned}\dot{\gamma} &= \frac{1}{m} \left(\frac{M - M_0}{2\pi l} \right)^{1/n} \\ &= -r \frac{d\omega}{dr}\end{aligned}\quad (\text{A2-5})$$

Integrating Equation (A2-5) from $\omega = \Omega$ at $r = R_i$ to $\omega = 0$ at $r = R_o$ gives:

$$\frac{1}{m} \left(\frac{M - M_o}{2\pi l} \right)^{1/n} \left[\frac{-2}{n} (R_o^{2/n} - R_i^{2/n}) \right] = \Omega \quad (\text{A2-6})$$

Replacing Ω with $2\pi N/60$ yields:

$$\frac{1}{m} \left(\frac{M - M_o}{2\pi l R_i^2} \right)^{1/n} \left[\frac{n}{2} \frac{R_o^{2/n} - R_i^{2/n}}{R_o^{2/n}} \right] = \frac{2\pi N}{60} \quad (\text{A2-7})$$

Replacing $\frac{1}{m} \left(\frac{M - M_o}{2\pi l R_i^2} \right)^{1/n}$ with $\dot{\gamma}$ in Equation (A2-7) gives:

$$\dot{\gamma} = \frac{\pi}{15n} \frac{R_o^{2/n}}{R_o^{2/n} - R_i^{2/n}} N \quad (\text{A2-8})$$

The average shear rate within the gap $R_o - R_i$ is approximated by:

$$\dot{\gamma} = \frac{\pi}{30n} N \left(\frac{R_o^{2/n}}{R_o^{2/n} - R_i^{2/n}} + \frac{R_i^{2/n}}{R_o^{2/n} - R_i^{2/n}} \right) \quad (\text{A2-9})$$

A.1.3 Flow Rate of a Power Law Fluid with Yield Stress in a Circular Tube

A force balance cross a cylinder taken from the tube can be expressed as:

$$\pi r^2 \Delta p = 2\pi r \tau L \quad (\text{A3-1})$$

or

$$\tau = \frac{r\Delta p}{2L} \quad (\text{A3-2})$$

where L and r are the length and radius of the cylinder; τ is the shear stress along the side of the cylinder at the radius r and Δp denotes the pressure drop cross the cylinder.

Differentiating τ with respect to r yields:

$$\frac{d\tau}{dr} = \frac{\Delta p}{2L} \quad (\text{A3-3})$$

On the other hand, differentiating the velocity u with respect to the shear stress τ gives:

$$\begin{aligned} \frac{du}{d\tau} &= \frac{du}{dr} \frac{dr}{d\tau} \\ &= -\dot{\gamma} \frac{dr}{d\tau} \\ &= -\dot{\gamma} \frac{2L}{\Delta p} \\ &= \frac{2L}{\Delta p} f(\tau) \end{aligned} \quad (\text{A3-4})$$

where $\dot{\gamma}$ is the shear rate at radius r in the tube.

Integrating Equation (A3-4) from u at r to u_s (the velocity caused by slip) at R , the radius of the tube gives:

$$u = u_s + \frac{2L}{\Delta p} \int_{\tau}^{\tau_w} f(\tau) d\tau \quad (\text{A3-5})$$

The flow rate in the tube can be found by integrating Equation (A3-5) in the range $0 \leq u \leq u_s$ at $0 \leq r \leq R$ as follows:

$$Q = \int_0^R 2\pi r u_s dr + \int_0^R 2\pi r \left(\frac{2L}{\Delta p} \int_{\tau}^{\tau_w} f(\tau) d\tau \right) dr \quad (\text{A3-6})$$

Equation (A3-6) indicates that the total flow rate from the tube is composed of two parts: the first part is the flow rate caused by the slip velocity and it is a plug flow. The second part is equivalent to the flow rate without slip happened. The latter can be found by integrating by parts:

$$\begin{aligned} Q_{ns} &= \int_0^R 2\pi r \left[\frac{2L}{\Delta p} \int_{\tau}^{\tau_w} f(\tau) d\tau \right] dr \\ &= \int_0^{\tau_w} 2\pi \frac{2L\tau}{\Delta p} \left[\frac{2L}{\Delta p} \int_{\tau}^{\tau_w} f(\tau) d\tau \right] \frac{2L}{\Delta p} d\tau \\ &= \frac{16\pi L}{\Delta p^3} \int_0^{\tau_w} \tau \left[\int_{\tau}^{\tau_w} f(\tau) d\tau \right] d\tau \\ &= \frac{8\pi L}{\Delta p^3} \left\{ \left[\tau^2 \int_{\tau}^{\tau_w} f(\tau) d\tau \right]_0^{\tau_w} - \int_0^{\tau_w} \tau^2 d \int_{\tau}^{\tau_w} f(\tau) d\tau \right\} \\ &= \frac{8\pi L}{\Delta p^3} \int_0^{\tau_w} \tau^2 f(\tau) d\tau \end{aligned} \quad (\text{A3-7})$$

For power law fluids with a yield stress, the shear rate can be expressed as:

$$\begin{aligned}
 \dot{\gamma} &= \left(\frac{\tau - \tau_0}{m} \right)^{1/n} \\
 &= \left(\frac{\tau - \tau_0}{m} \right)^N \\
 &= f(\tau)
 \end{aligned} \tag{A3-8}$$

Substituting Equation (A3-8) into (A3-7) and integrating the equation by parts yields the flow rate equation without slip:

$$\begin{aligned}
 Q_{ns} &= \frac{8\pi L^3}{\Delta p^3} \int_0^{\tau_w} \tau^2 \left(\frac{\tau - \tau_0}{m} \right)^N d\tau \\
 &= \frac{8\pi L^3 (\tau_w - \tau_0)^{N+1}}{\Delta p^3 m^N (N+1)} \left[\tau_w^2 - \frac{2(\tau_w - \tau_0)}{N+2} \left(\tau_w - \frac{\tau_w - \tau_0}{N+3} \right) \right]
 \end{aligned} \tag{A3-9}$$

A.2 Effects of Yield Stress and Flow Behavior Index on Plug Flow in a Circular Tube

Canola pastes exhibit viscoplasticity, *i. e.* they possess a yield stress below which they experience little or no deformation and hence behave in a plug like manner. It will be shown that pseudoplastic fluids with a low yield stress and small flow behavior index n can be modelled, in an approximate manner, by disregarding the yield stress, τ_0 . The dimensionless, fully-developed velocity profile of such fluids in a circular tube is given by the following equation (Denn, 1980):

$$\frac{u}{u_{ave}} = \frac{1 - \left[\left(\frac{r}{R} \tau_w - \tau_0 \right) / (\tau_w - \tau_0) \right]^{1+1/n}}{1 - \frac{2n}{2n+1} \left(1 - \frac{\tau_0}{\tau_w} \right) \left[1 - \frac{n}{3n+1} \left(1 - \frac{\tau_0}{\tau_w} \right) \right]} \quad (\text{A.2.1})$$

where $\tau_w = R\Delta p/2L$; L is the length and R is the radius of the tube; u_{ave} is the average velocity in the tube.

The dimensions of R and L were chosen to be the same as those of the capillary viscometer described in Chapter 4. Since the extruder was typically operated between 10 and 30 MPa, the Δp was set to 20 MPa.

Figure A.2-1 shows the steady state dimensionless velocity (u/u_{ave}) as a function of dimensionless radius (r/R), flow behavior index (n) and yield stress (τ_0). Curve (1) applies to $n = 1$ and $\tau_0 = 0$ (i. e., a Newtonian fluid) and the velocity profile has the familiar parabolic shape. Curve (2) was calculated for $n = 0.5$ and $\tau_0 = 0$. The velocity profile is almost flat near the center of the tube and therefore approximates plug flow in this region. When τ_0 is increased to 2000 Pa, 2850 Pa and 4000 Pa while keeping n at 0.5, the region where the velocity profile is flat increases somewhat as shown by Curves (3), (4) and (5). Decreasing the flow behavior index to $n = 0.1$ greatly increases the core region (see Curves (6) and (7) which were obtained for $n = 0.1$, $\tau_0 = 0$ Pa and $\tau_0 = 2850$ Pa, respectively) and the effect of τ_0 (up to 4000 Pa) is virtually insignificant. These findings demonstrate that, for Canola pastes ($n=0.5$, $\tau_0 = 2850$ Pa), the velocity distribution in a circular tube can be fairly well represented by neglecting the yield stress in the calculation.

Table A.2-1 gives the quantitative results for Curve (2) ($n = 0.5$, $\tau_0 = 0$ Pa) and Curve (4) ($n = 0.5$, $\tau_0 = 2850$ Pa). It is seen that the maximum error, i. e. the difference between the velocity ratios, is less than 7%. This indicates that ignoring the yield stress of Canola paste should not cause significant errors in the extruder simulation.

Table A.2-1: Comparison of curves (2) and (4) for dimensionless velocities at $\Delta p = 20$ MPa, $L = 1.5$ m and $R = 1/16''$.

Positions from the center of tube (dimensionless)	u/u_{ave} curve (2) (a)	u/u_{ave} curve (4) (b)	Error (%)
0	1.66734	1.56334	6.7
0.1	1.66596	1.56334	6.6
0.2	1.65567	1.56305	5.9
0.3	1.62662	1.55280	4.8
0.4	1.56847	1.53516	2.2
0.5	1.47062	1.48065	0.7
0.6	1.32220	1.38889	3.5
0.7	1.11219	1.15282	4.8
0.8	0.82939	0.88031	5.8
0.9	0.46247	0.43363	6.7
1	0	0	

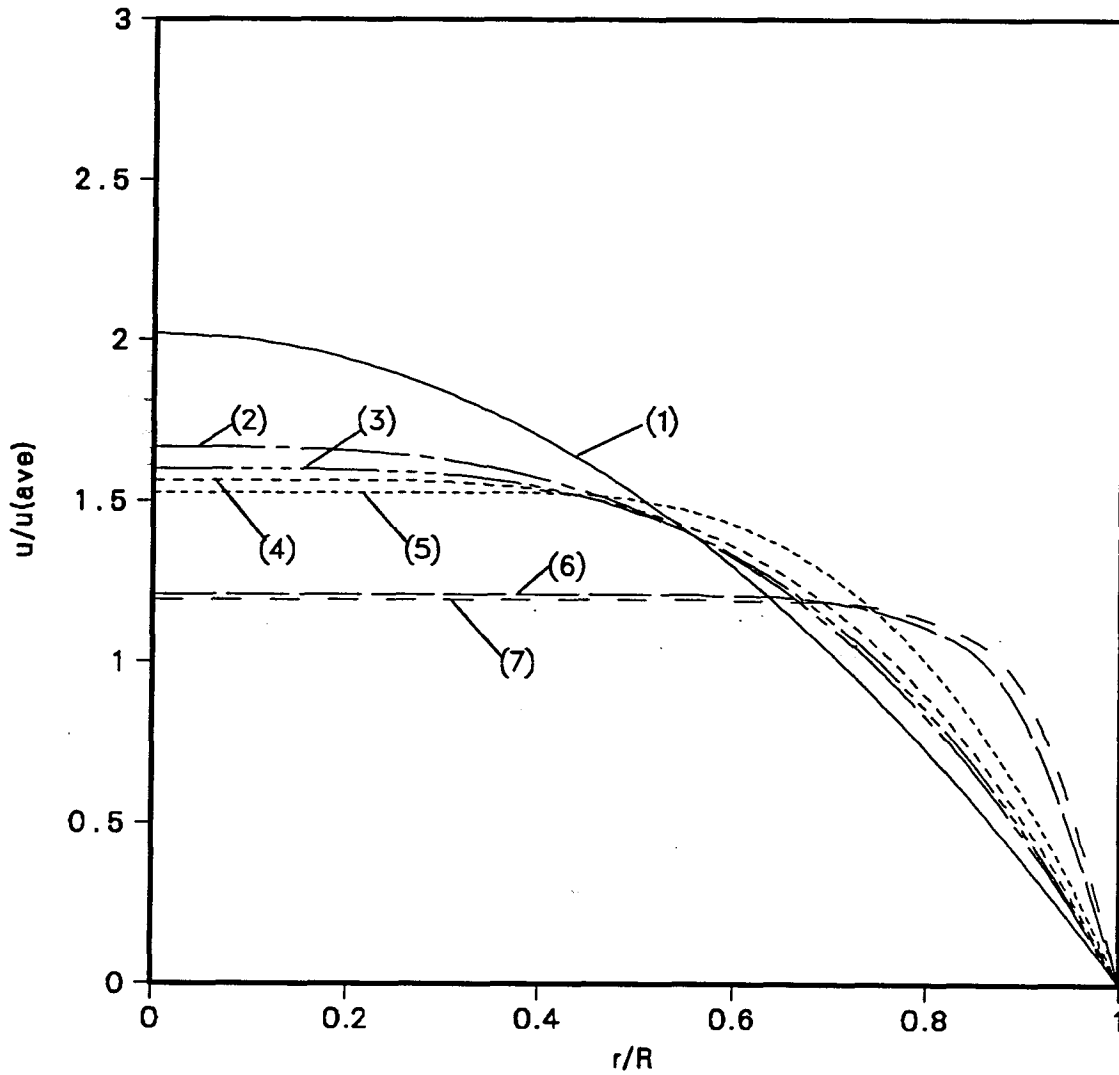


Figure A.2-1: Dimensionless velocity distribution in a circular tube. (1) $n = 1$, $\tau_0 = 0$; (2) $n = 0.5$, $\tau_0 = 0$; (3) $n = 0.5$, $\tau_0 = 2000$ Pa; (4) $n = 0.5$, $\tau_0 = 2850$ Pa; (5) $n = 0.5$, $\tau_0 = 4000$ Pa; (6) $n = 0.1$, $\tau_0 = 0$; (7) $n = 0.1$, $\tau_0 = 2850$ Pa.

A.3 List of Drawings of the Extruder

Table A.3-1: Extruder part list for Figure 4-15.

Part No.	Part Names	Materials	Drawing No.
1	Bolts (M 3/8 x 5")	Steel	
2	Left bearing holder	stainless steel	3
3	Radial bearing (1" diameter)		
4	Key (1/8 x 1/8 x 1)	tool steel	
5	Screw shaft	tool steel	2
6	Restrictor locker nut	steel	4
7	Cone restrictor	steel	5
8	Thermocouple		
9	Pressure transducer		
10	Outlet section barrel	Stainless steel	7
11	Inlet funnel	steel	
12	Inlet section barrel	Stainless steel	6
13	Thrust bearing holder	Stainless steel	8
14	Thrust bearing (1 1/8" diameter)		
15	key (1/8 x 1/8 x 1)	tool steel	
16	Supporter	aluminum alloy	
17	Base	steel	

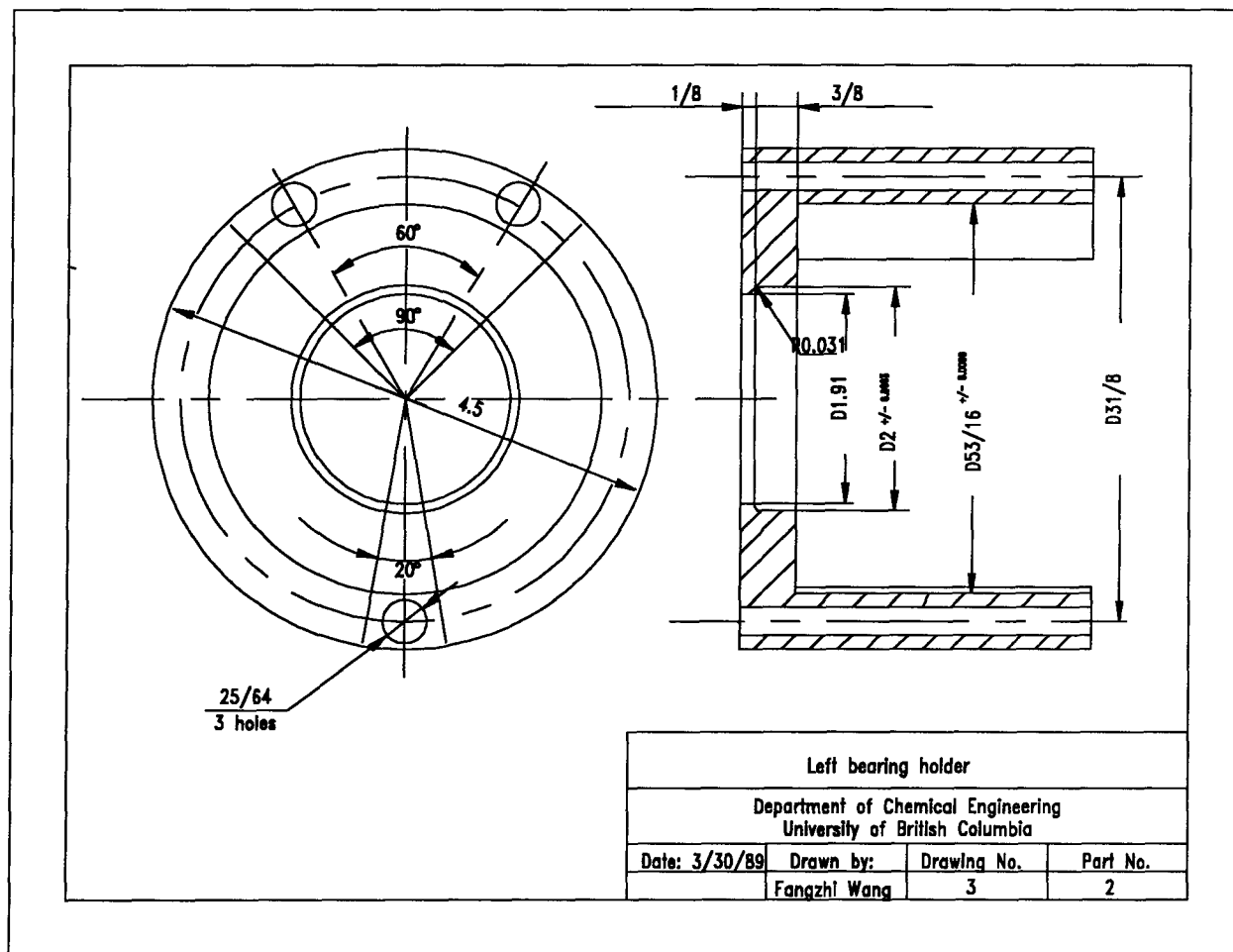


Figure A.3-1: Drawing 3 left bearing holder.

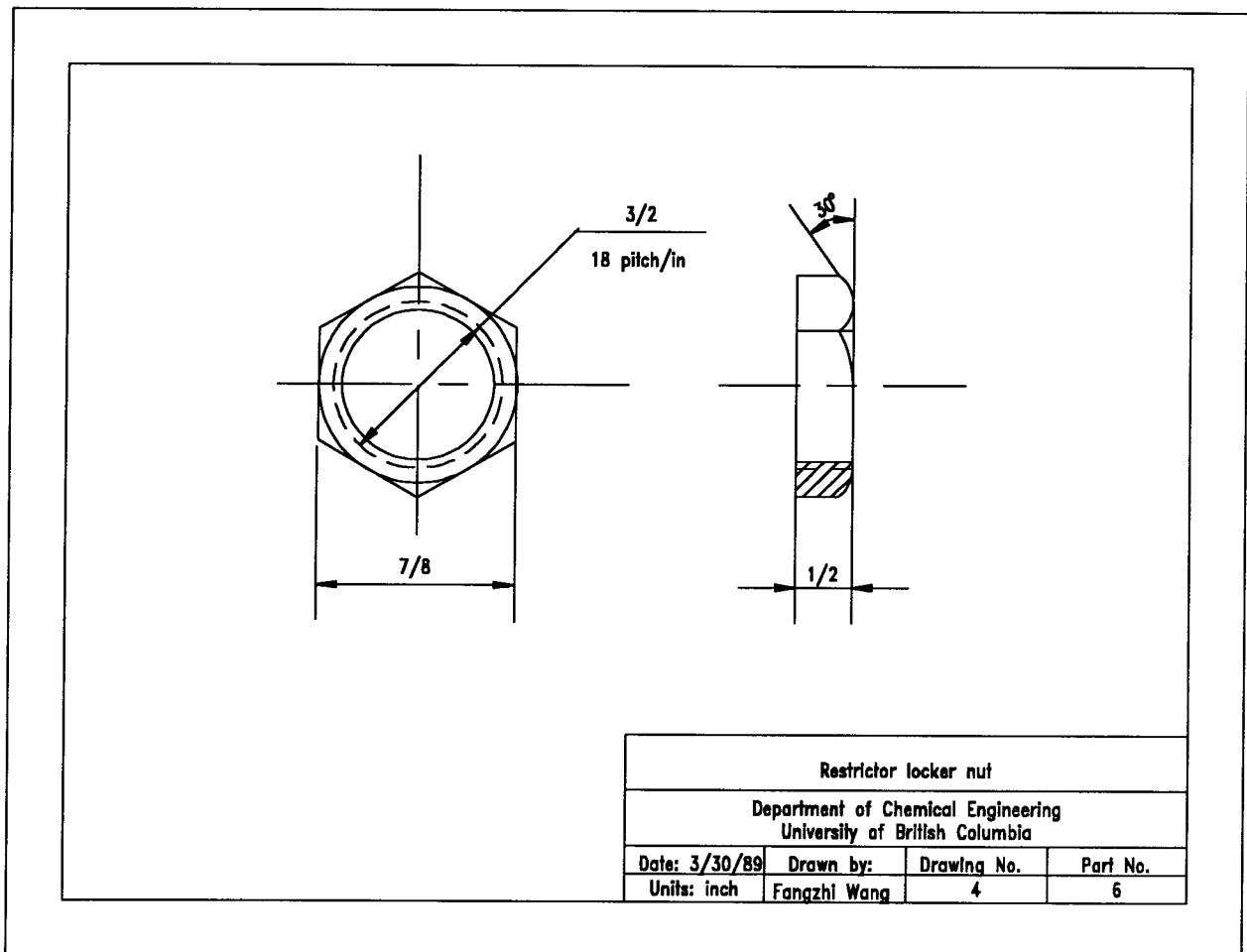


Figure A.3-2: Drawing 4 restrictor locker nut.

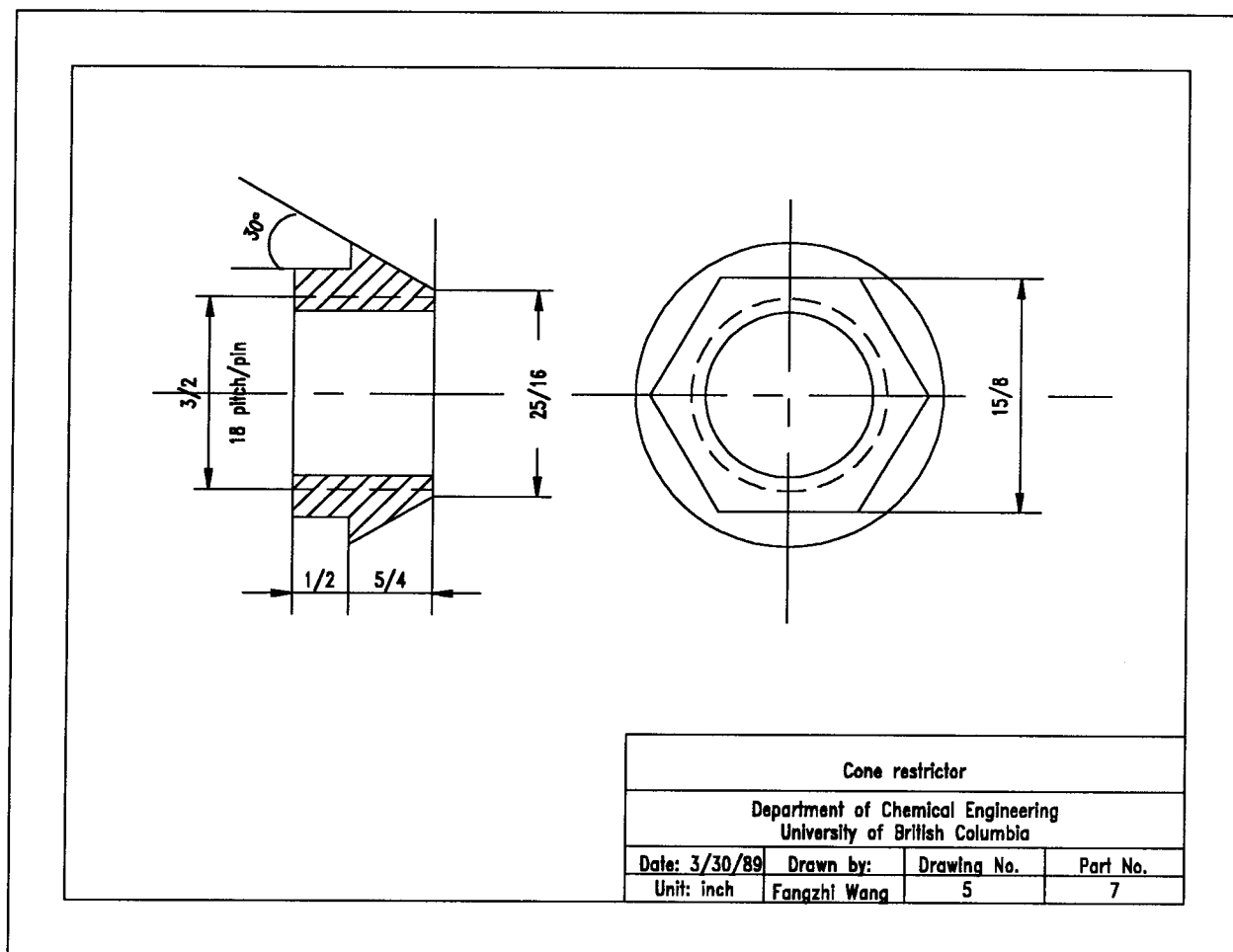


Figure A.3-3: Drawing 5 cone restrictor.

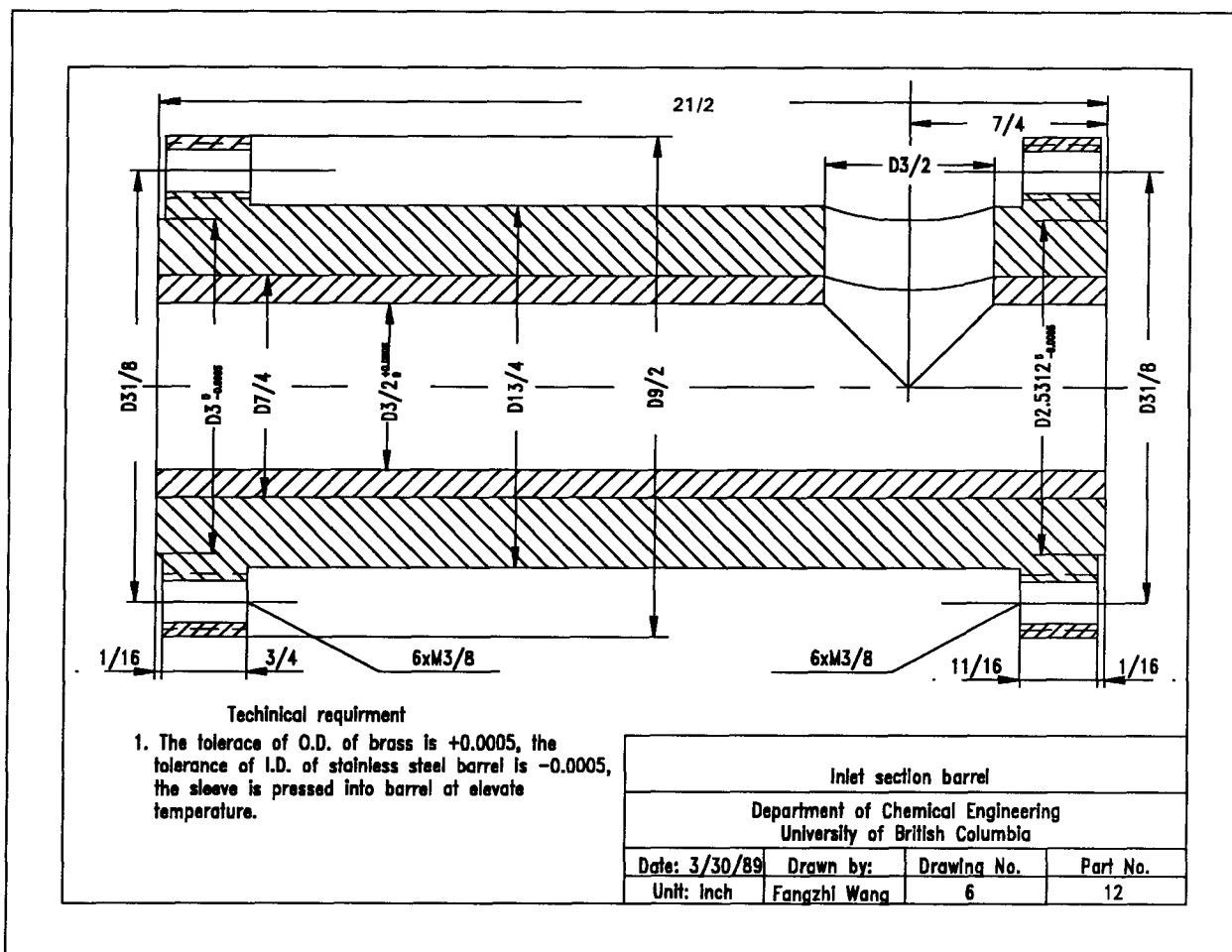


Figure A.3-4: Drawing 6 inlet section barrel.

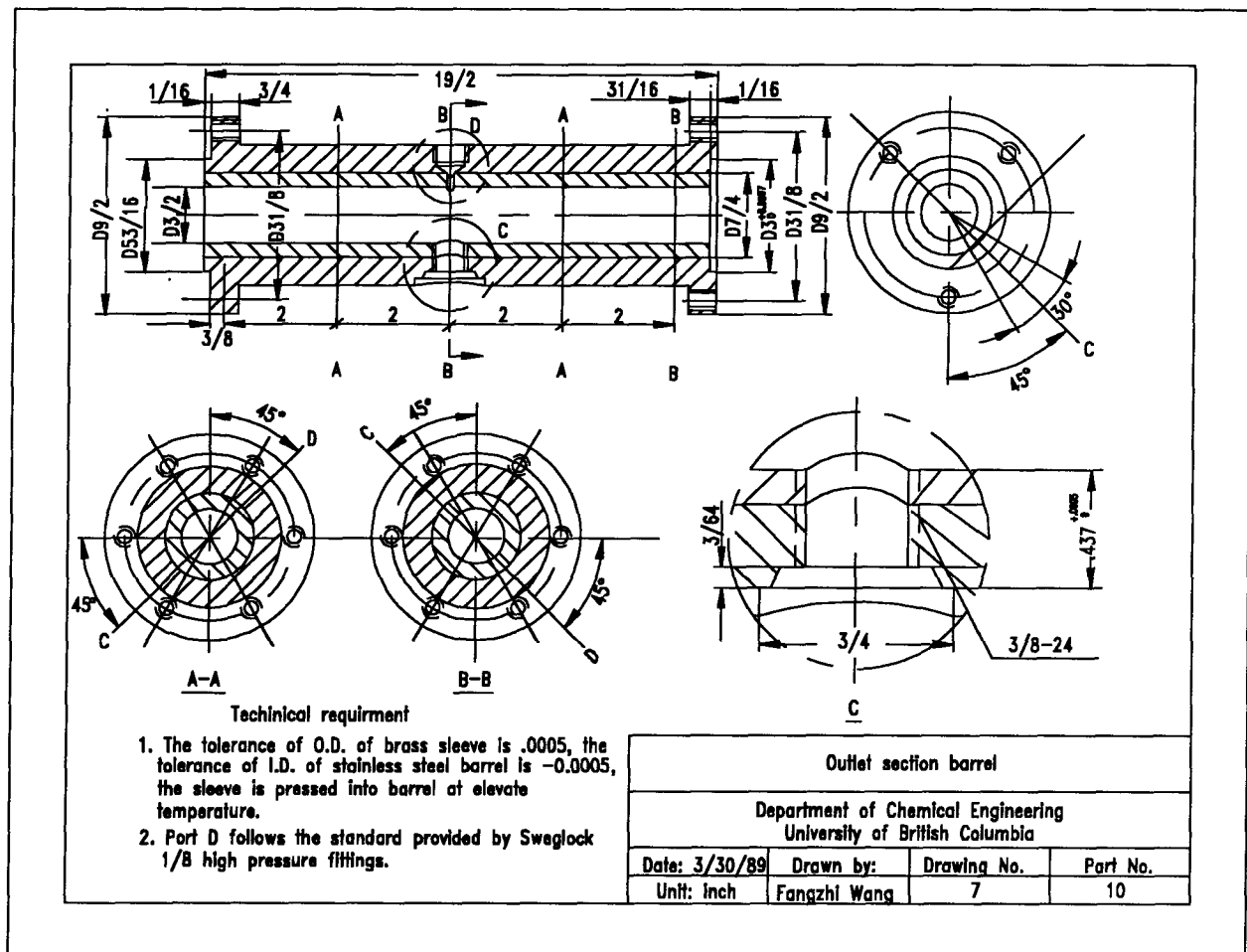


Figure A.3-5: Drawing 7 outlet section barrel.

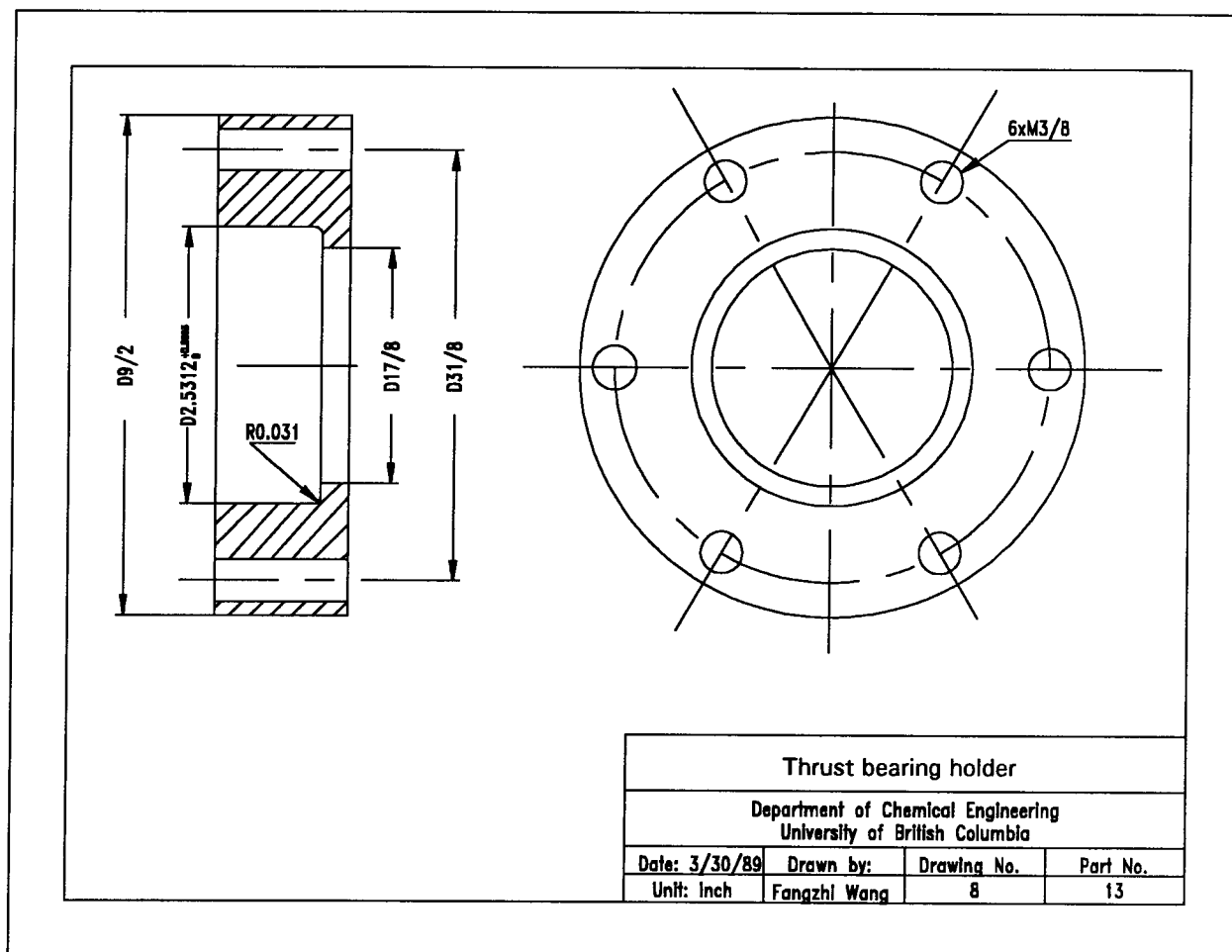
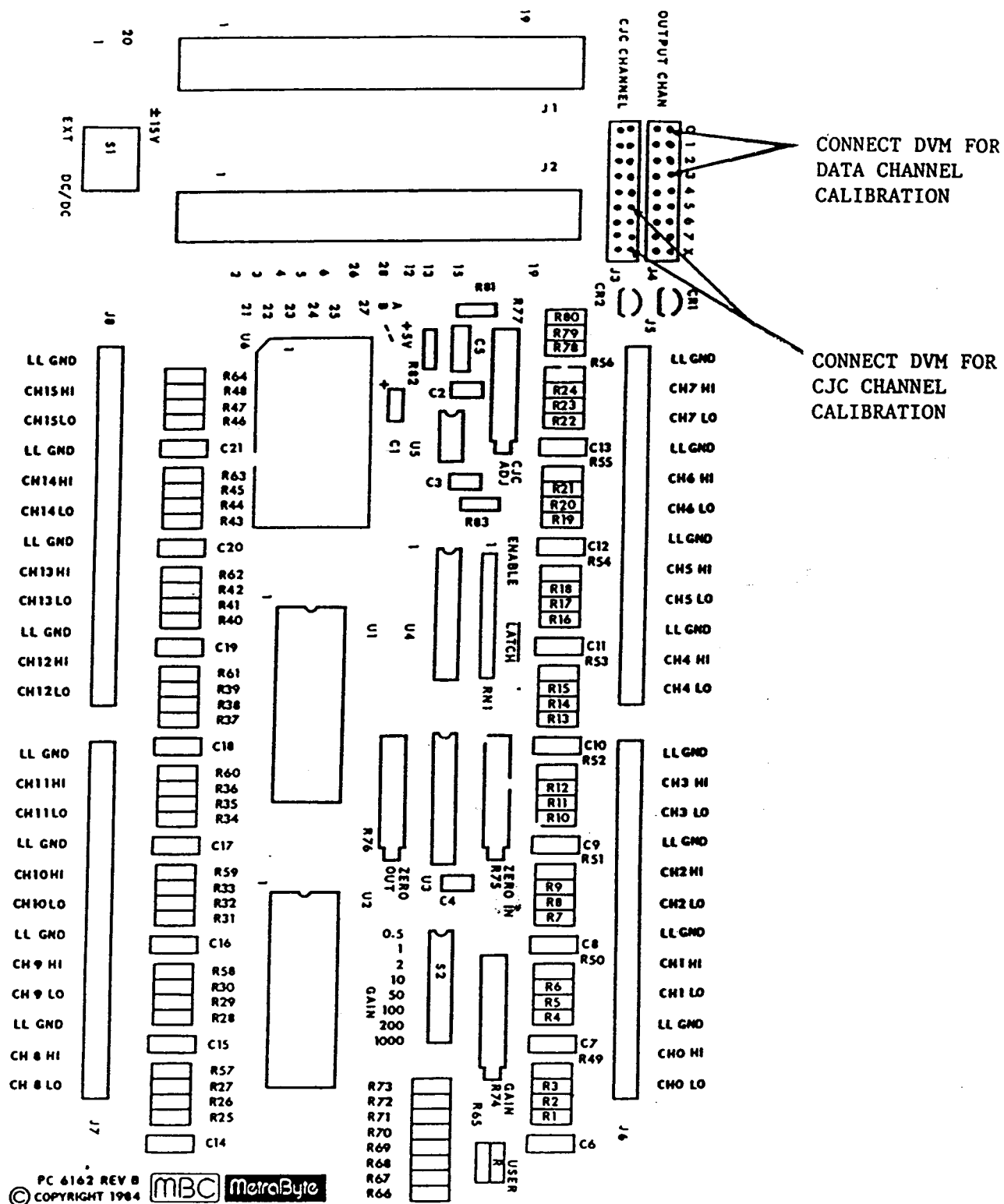


Figure A.3-6: Drawing 8 thrust bearing holder.



A.4 Circuit Diagrams of EXP-16

A.5 Listing of Experimental Results

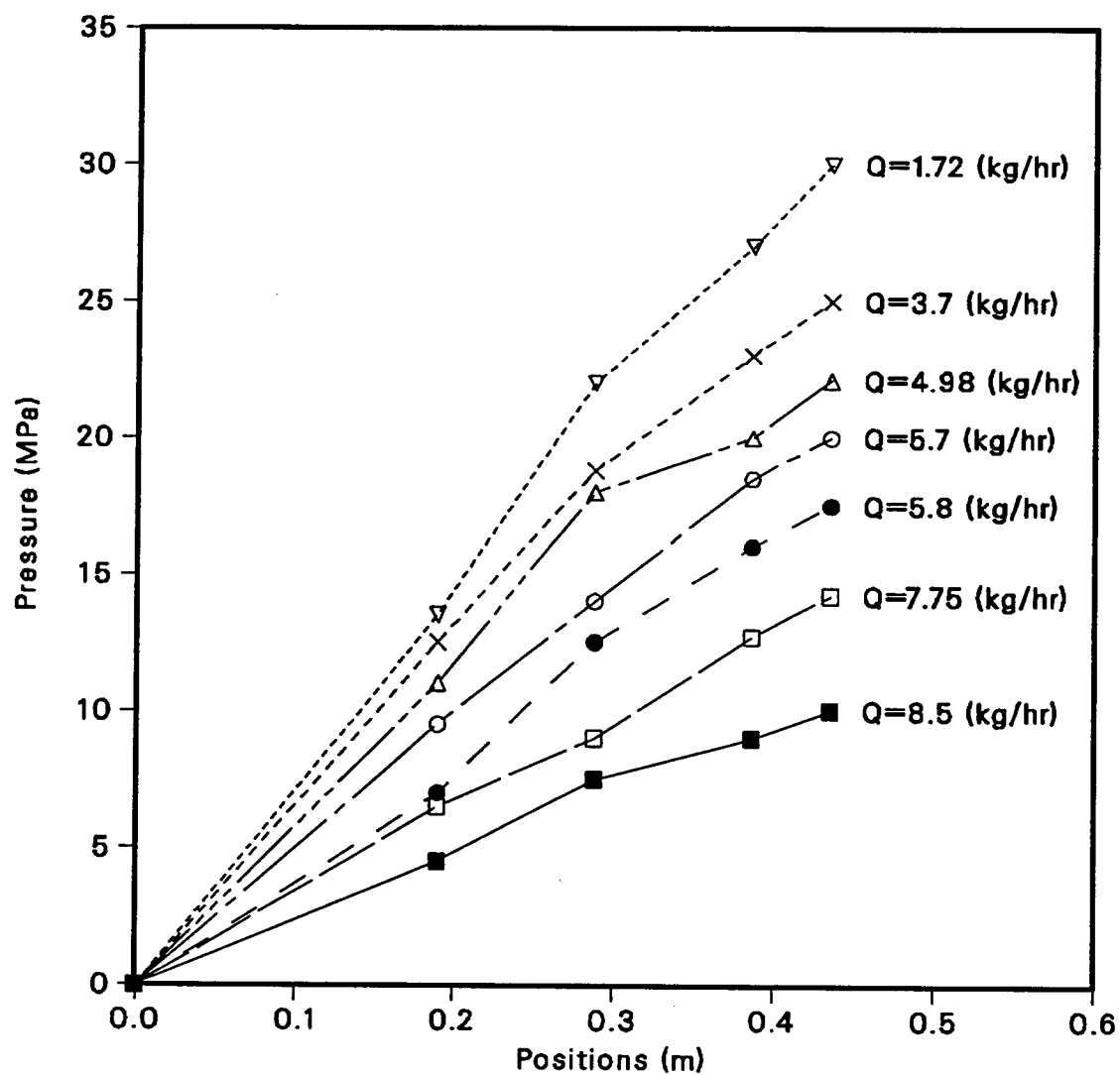


Figure A.5-1: Recorded pressure distribution along the extruder. Flight angle 5.98° , rotational speed 66.5 rpm, paste concentration 146% (g solid/g liquid).

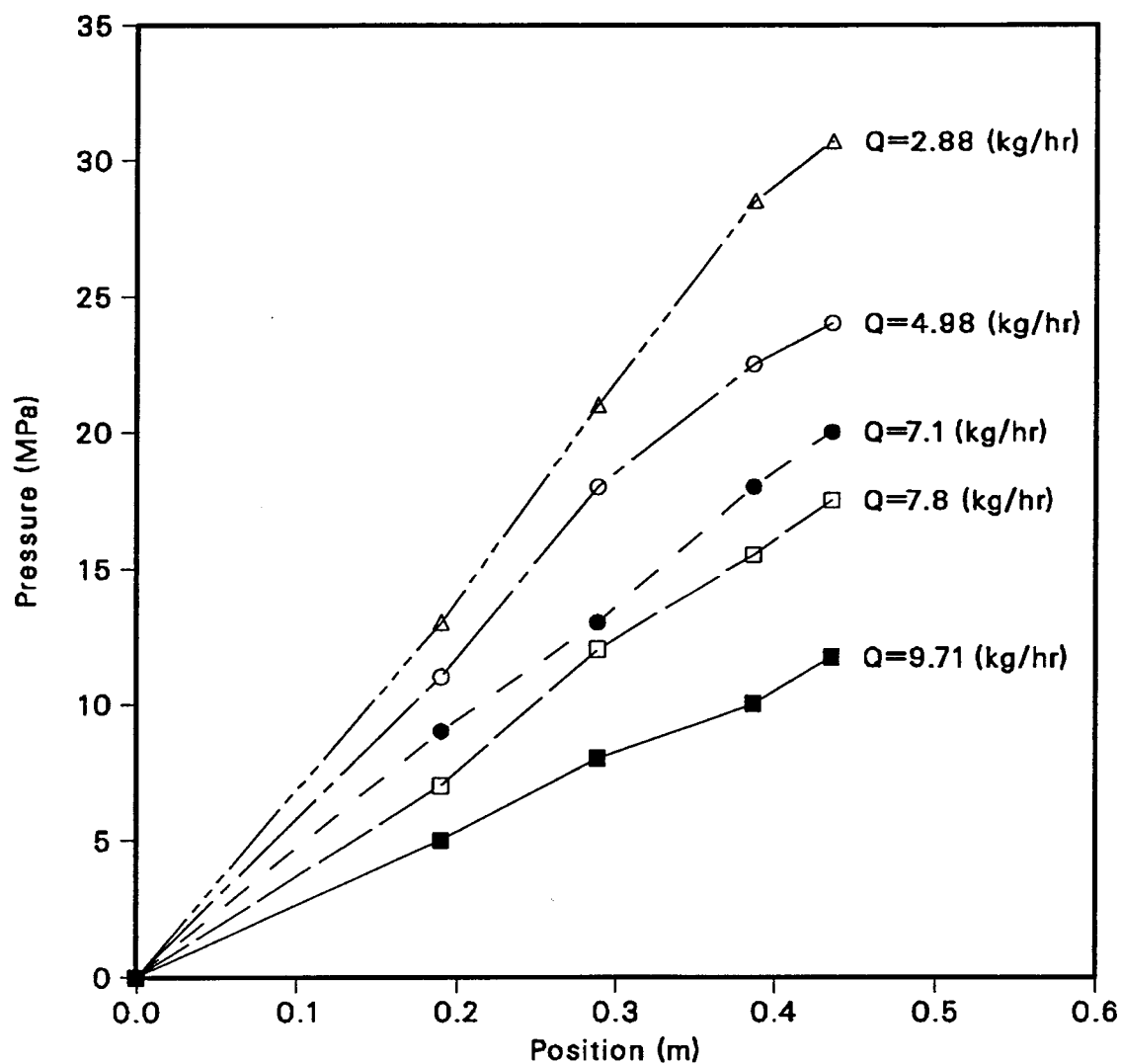


Figure A.5-2: Recorded pressure distribution along the extruder. Flight angle 5.98°, rotational speed 88.5 rpm, paste concentration 146% (g solid/g liquid).

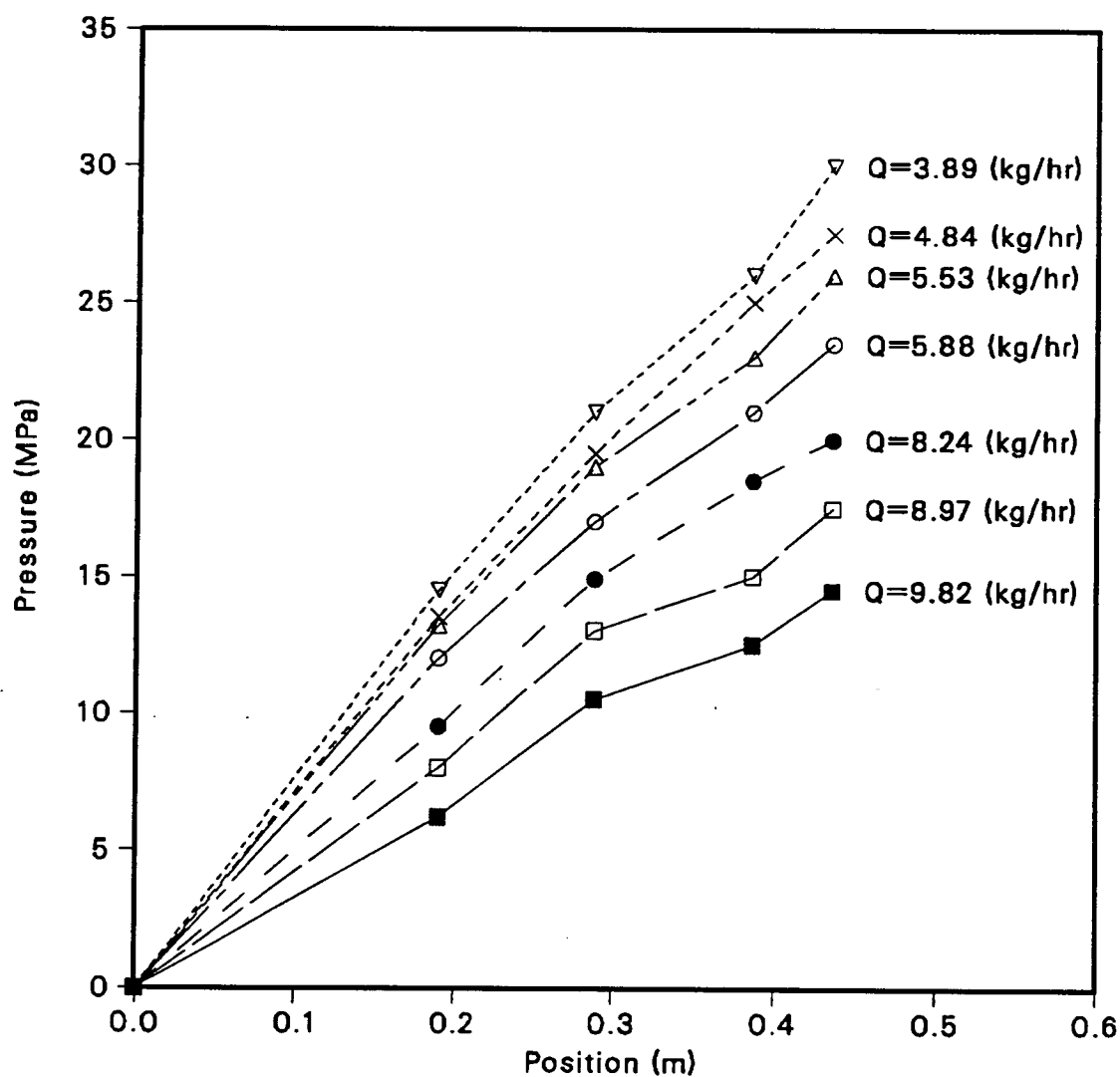


Figure A.5-3: Recorded pressure distribution along the extruder. Flight angle 5.98°, rotational speed 100.5 rpm, paste concentration 146% (g solid/g liquid).

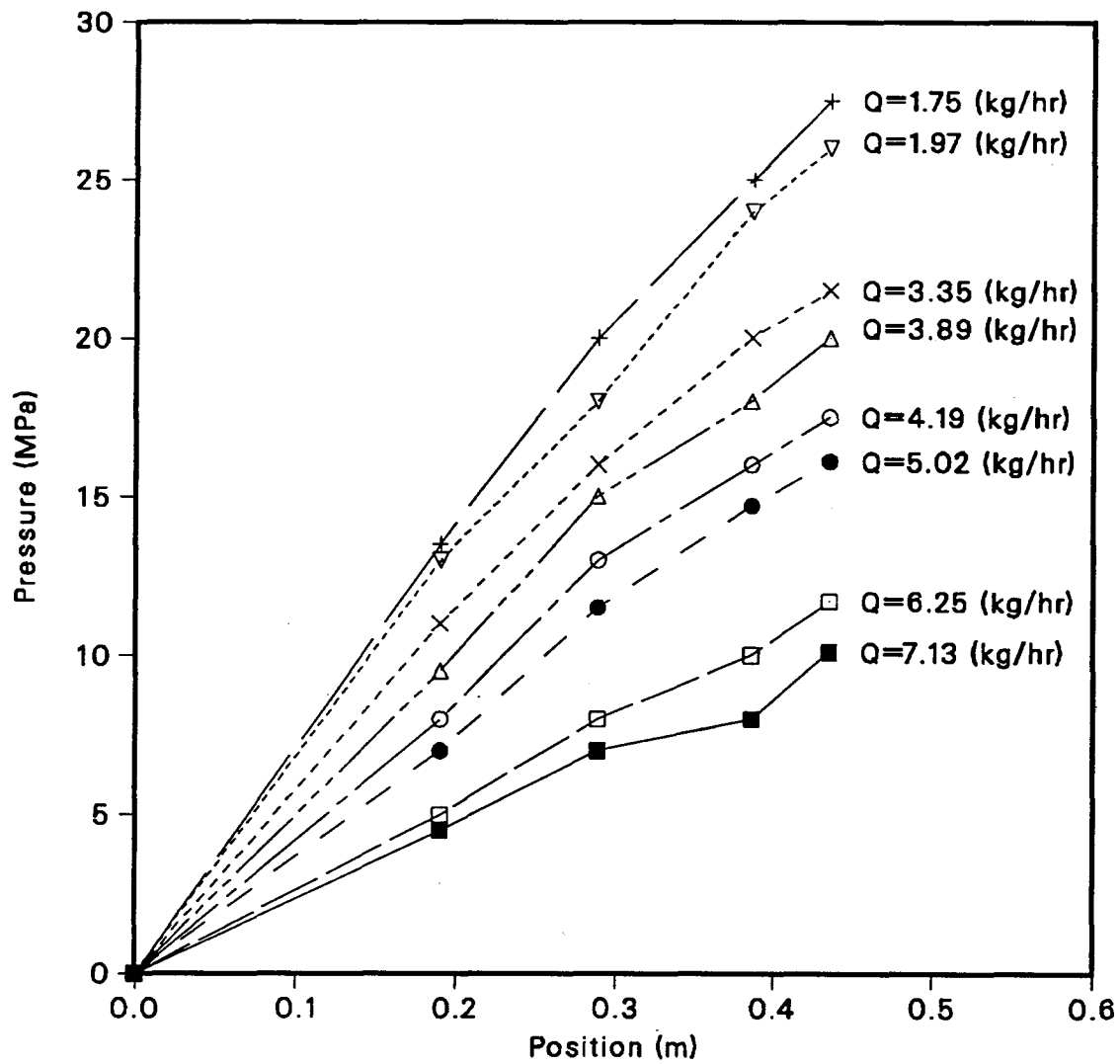


Figure A.5-4: Recorded pressure distribution along the extruder. Flight angle 7.97° , rotational speed 66.5 rpm, paste concentration 146% (g solid/g liquid).

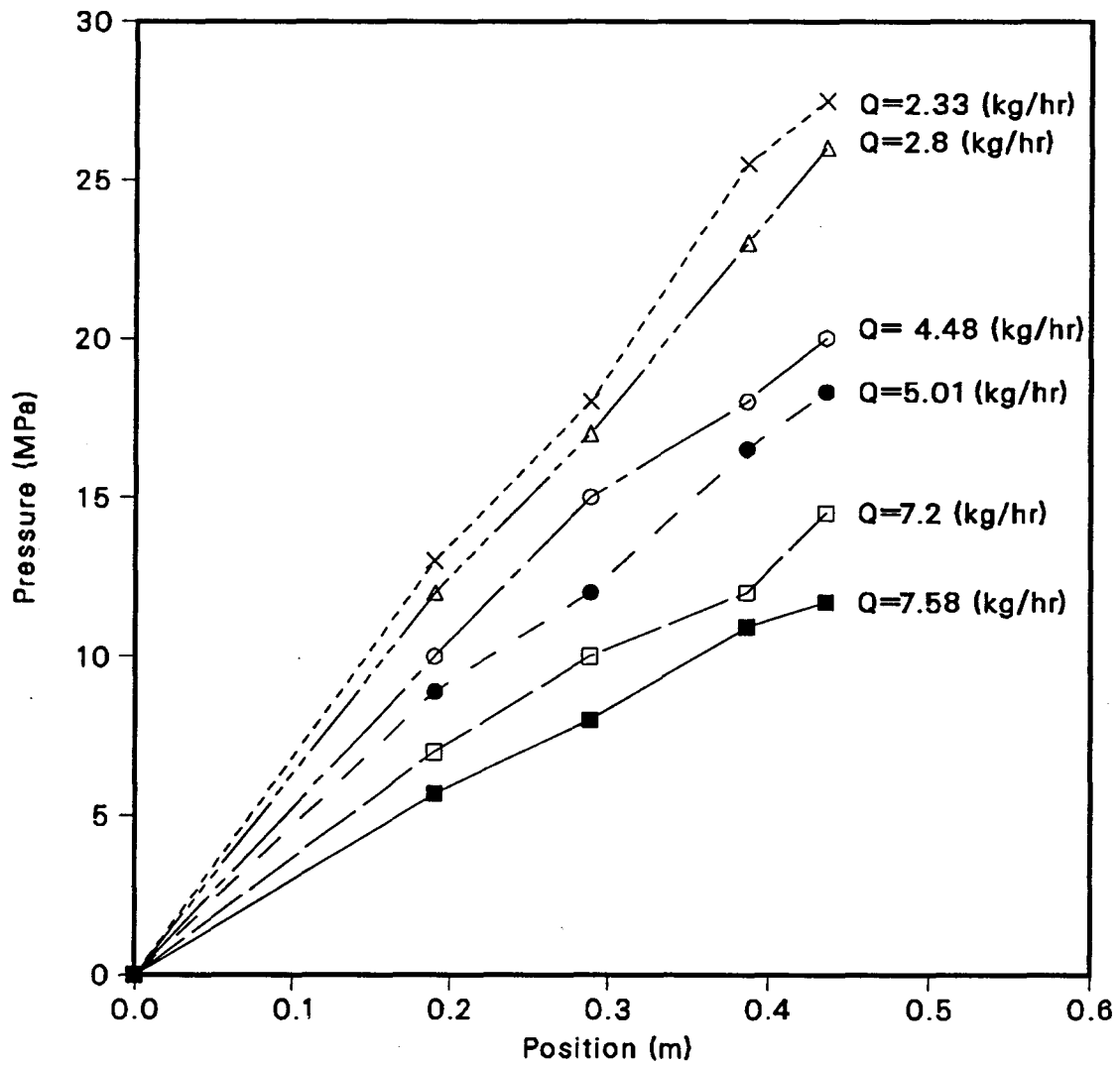


Figure A.5-5: Recorded pressure distribution along the extruder. Flight angle 7.97° , rotational speed 88.5 rpm, paste concentration 146% (g solid/g liquid).

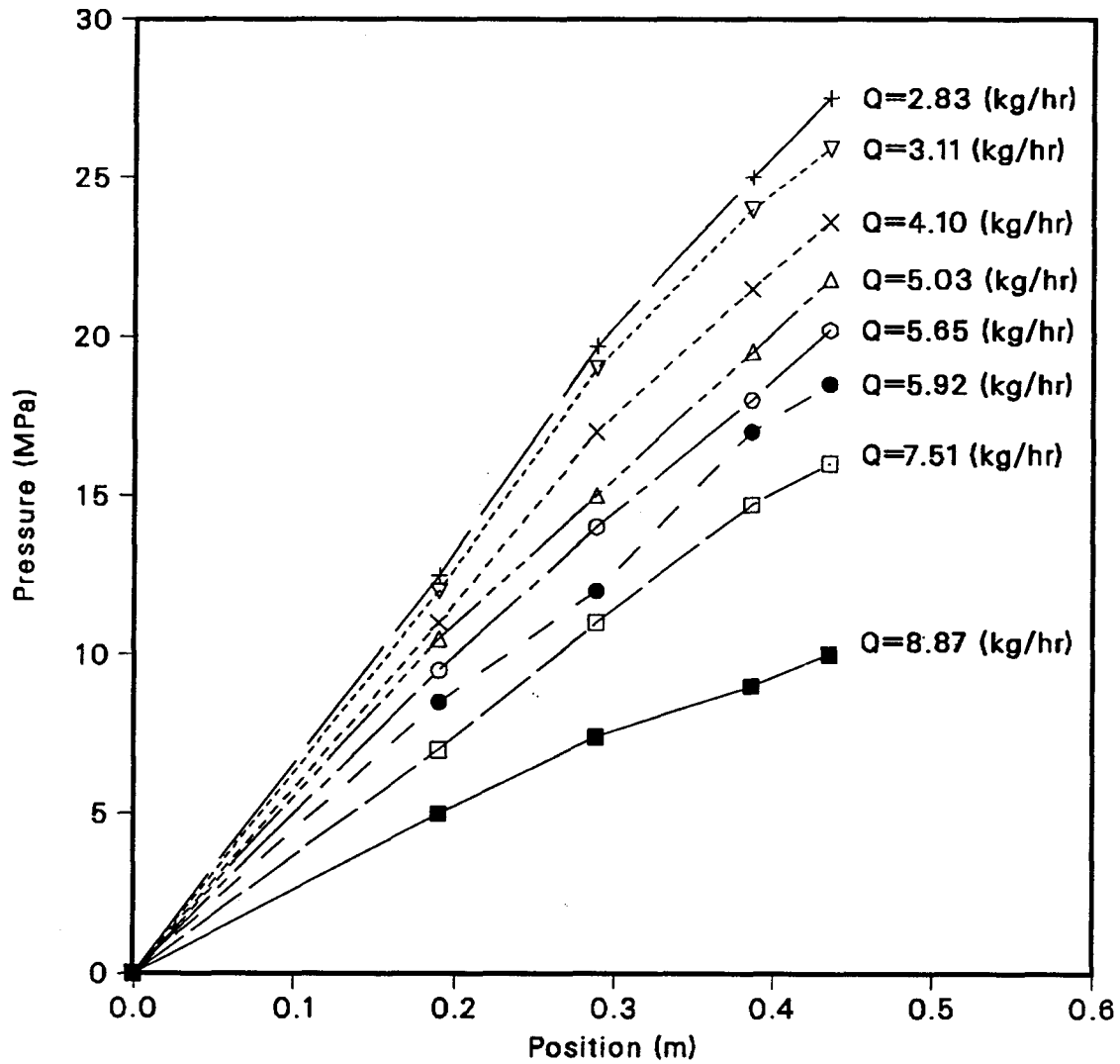


Figure A.5-6: Recorded pressure distribution along the extruder. Flight angle 7.97° , rotational speed 100.5 rpm, paste concentration 146% (g solid/g liquid).

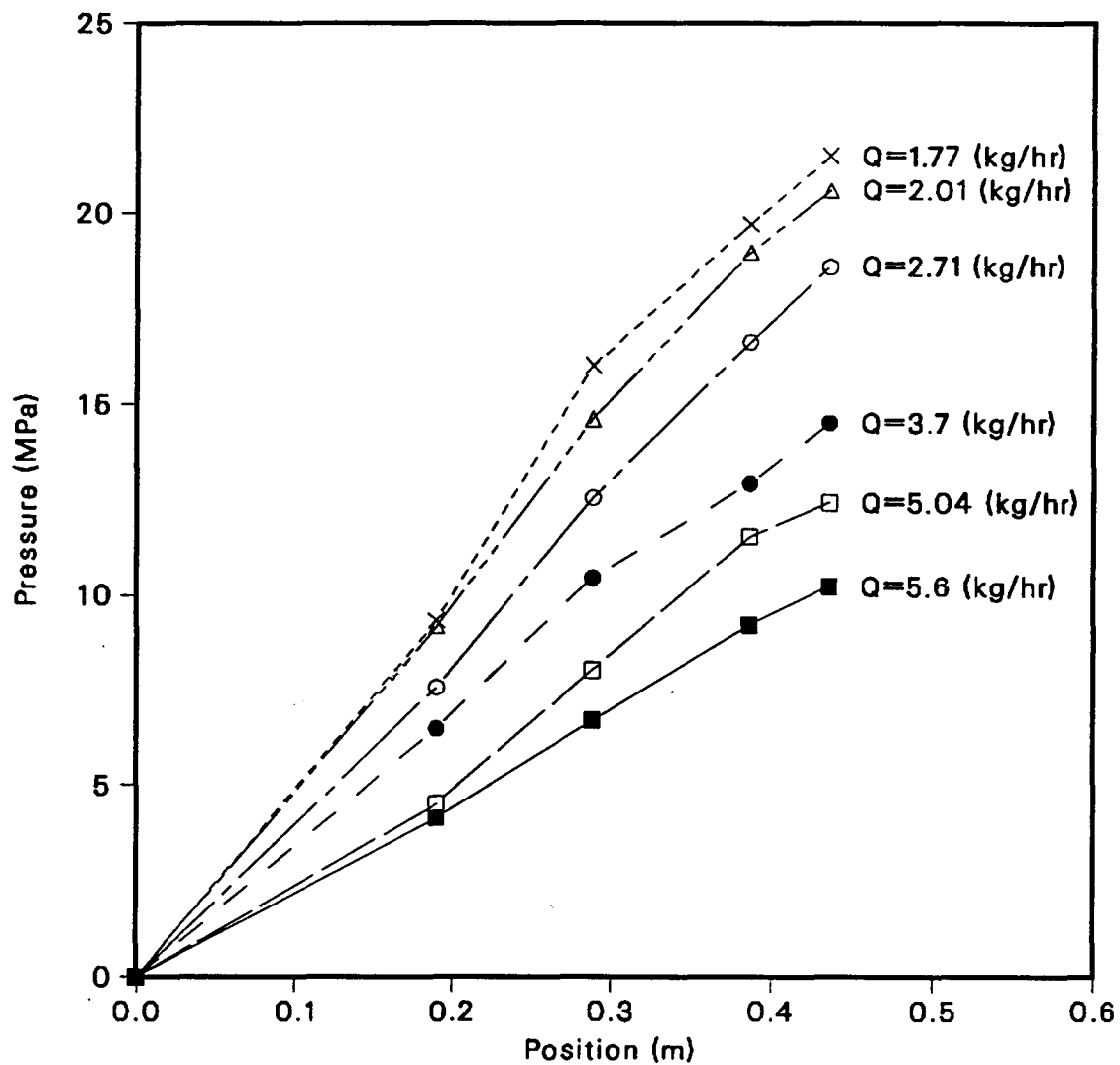


Figure A.5-7: Recorded pressure distribution along the extruder. Flight angle 9.94° , rotational speed 66.5 rpm, paste concentration 146% (g solid/g liquid).

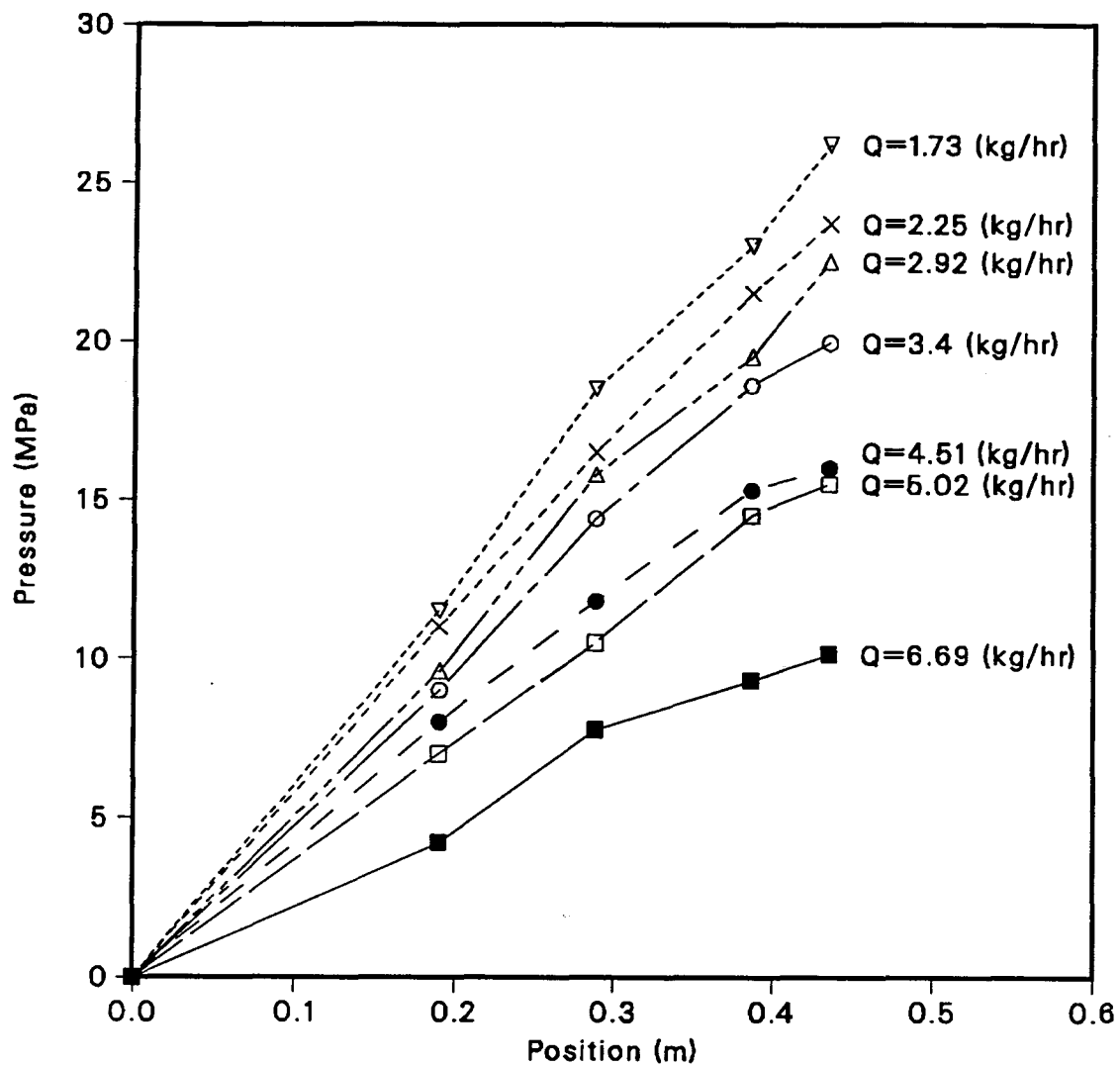


Figure A.5-8: Recorded pressure distribution along the extruder. Flight angle 9.94° , rotational speed 88.5 rpm, paste concentration 146% (g solid/g liquid).

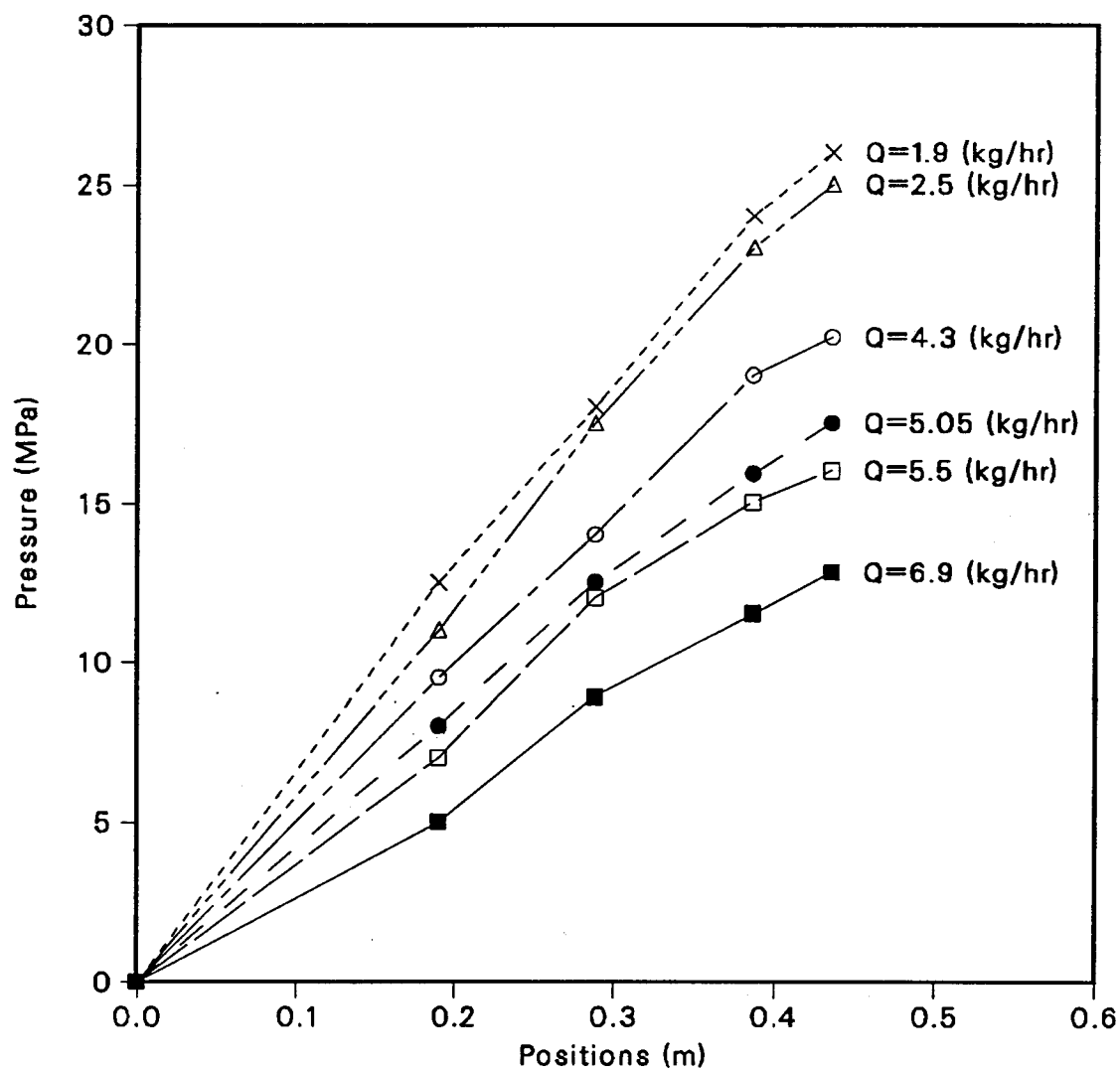


Figure A.5-9: Recorded pressure distribution along the extruder. Flight angle 9.94° , rotational speed 100.5 rpm, paste concentration 146% (g solid/g liquid).

A.6 Listing of Source Code of Computer Programs

A.6.1 FORTRAN Program for Extrusion Simulation

```

*****
*
*      *****               q2pla6r6.f               *****
*
*  A computer program for the calculation of a single screw
*  extruder by dividing the screw length into NP sections.
*  The flow rate is assumed to be the same in each section.
*
*  Variable definition:
*
*      ALENGT  length of a screw extruder, inch, real;
*      AMINDX  index used in apparent viscosity expression, real;
*      ALFA    angle of the screw flight, real. Three angles are
*              tested, 5.98, 7.97 and 9.94 degrees;
*      BDA, BDB, BDC, BDD  one dimensional arrays assigned
*              for boundary conditions; real;
*      CH      increment of flight, m, real;
*      CHWD    channel width, m, real;
*      CHHTA   channel height at the inlet, inch, real;
*      CHHTB   channel height at the outlet, inch, real;
*      COEFM   constant in apparent viscosity expression, real;
*      CONCEN  paste's concentration, real,
*              146% (g solid/q liquid);
*      CONV    to Imperial unit conversion factor, real;
*      DDETX   second derivative of apparent viscosity with
*              respect to x, two dimensional array,
*      DDETXY  dimensionless second derivative of apparent
*              viscosity with respect to x and y, two
*              dimensional array, real;
*      DDEYY   dimensionless second derivative of apparent
*              viscosity with respect to y, two
*              dimensional array, real;
*      DDFIXX  dimensionless second derivative of steam
*              function with respect to x ,two
*              dimensional array, real;
*      DDFIXY  dimensionless second derivative of steam
*              function respect to x and y, two
*              dimensional array, real;
*      DDFIYY  dimensionless second derivative of steam
*              function with respect to y , two
*              dimensional array, real;
*      DETX    dimensionless first derivative of steam
*              function with respect to x, two
*              dimensional array, real;
*      DETY    dimensionless first derivative of steam
*              function with respect to y, two
*              dimensional array, real;
*      DH      increment of flight height, m, real;
*      DPZDIM  dimensional dp/dz, Pa/m, one dimensional
*              array, real;
*      DPZUDM  dimensionless dp/dz, real;
*      DT      increment of temperature, C, real;

```

```

*      DWX      dimensionless first derivative of down      *
*               channel velocity with respect to x, two    *
*               dimensional array, real;                    *
*      DWY      dimensionless first derivative of down channel *
*               velocity with respect to x, two            *
*               dimensional array, real;                    *
*      ETA      dimensionless apparent viscosity, two      *
*               dimensional array, real;                    *
*      FLOIND    flow behavior index, n, in apparent viscosity *
*               expression, real;                          *
*      M        node number on x, integer;                 *
*      MAXITR    maximum iteration required by subroutine   *
*               D03EDF, integer;                           *
*      N        node number on y, integer;                 *
*      PI       ratio of the circumference of a circle to it *
*               diameter                                    *
*      POSINS    positions in the screw axis, in, real;    *
*      POSINZ    positions in z direction, m, real;        *
*      PRESSU    pressure values at each end of sections,  *
*               one dimensional array, real;               *
*      RHO       density of the Canola paste at a          *
*               concentration of 146%                      *
*      RELX, RELX2, RELX3, RELX4    relaxation factors; real; *
*      RHSFUN    right-hand-side function of PDE's         *
*      RWDIF     two dimensional working array, real;      *
*      SCREWN    rotational speed of a screw, rpm, real;   *
*      SCREWD    screw diameter, inch, real;               *
*      SCRWSP    screw's linear speed, m/s, real;          *
*      SLIP      slip factor, real;                        *
*      ESUM      experimental flow rate, kg/hr, real;      *
*      TEMPIN    temperature of the paste at the inlet, C, real; *
*      TEMPOT    temperature of the paste at the outlet, C, real; *
*      VELTYU    dimensionless velocity in x direction, two *
*               dimensional array, real;                    *
*      VELTYV    dimensionless velocity in y direction, two *
*               dimensional array, real;                    *
*      VELTYW    dimensionless velocity in x direction, two *
*               dimensional array, real;                    *
*      XA, XB, YA, YB    initial and end values of independent *
*               variables, real;                            *
*      U, UB, US, WK    one dimensional working arrays, real; *
*      WDIF      two dimensional working array, real;      *
*      WKARY1, WSAVE    two dimensional working arrays, real; *
*
*****
*
PROGRAM Q2P1A6
IMPLICIT REAL*8(A-H,O-Z)
PARAMETER (M=21,MM1=M-1,MM2=M-2,N=117,NM1=N-1,NM2=N-2,
1  MN=M*N,MNP=(M+1)*N,XA=0.DO,XB=1.DO,YA=0.DO,
2  CONV=0.0254D0,SCREWD=1.5D0*CONV,DX=XB/MM1,DXSQ=DX*DX,
3  AMINDX=4.85D0,CHHTA=.2D0*CONV,CHHTB=.15D0*CONV,
4  ALENGT=(19.2D0-7.D0/4.D0)*CONV,MAXITR=3000,NP=17,NP1=18,
5  LDA=(4.D0*M*N/3.D0)+.5D0,ACC=1.E-4,IR=0,
6  IFPSAV=(MM1+2)*(N+1)+7*MM1+3*NM1+76,ESUM=2.85D0,
7  ALFA=5.98D0,CONCEN=1.46D0,EPS=1.D-2,RHO=1270.D0,
8  RELX=0.27D0,RELX2=0.2D0,
9  SCREWN=88.5D0,SLIP=.3D0,TEMPIN=20.D0,TEMPOT=50.D0)
*
DIMENSION A(LDA,7),EVDIF(M,N),WDIF(M,N),BDA(N),BDB(N),
1  BDC(M),BDD(M),CH(NP),DDETX(M,N),DDETX(M,N),
2  DDETY(M,N),DDFIX(M,N),DDFIX(M,N),DDFIY(M,N),
3  DETX(M,N),DETY(M,N),DPZ(NP),DPZDIM(NP),DWX(M,N),
4  DWY(M,N),ETA(M,N),ETAVOR(M,N),FLOWM(NP),

```

```

5  FPSAVE(IFPSAV), POSIS(NP), POSIZ(NP), PRESSU(NP1),
6  RHS(LDA), RHSFUN(M,N), STRMFN(M,N), SUMFO(N), TEMP(NP),
7  U(LDA), UB(MN), US(LDA), VELTYU(M,N), VELTYV(M,N),
8  VELTYW(M,N), VORTIC(M,N), REVDIF(M,N), RWDIF(M,N),
9  WK(MNP), WKARY1(M,N), WSAVE(M,N)
COMMON SCRWSP, FLOIND, FLOWMS, CHHT
*
*   file f2 records the times of iterations
*
OPEN(UNIT=2, FILE='a6/q2p/r8m21s/p300/f2', STATUS='NEW')
OPEN(UNIT=3, FILE='a6/q2p/r8m21s/p300/dwx', STATUS='NEW')
OPEN(UNIT=4, FILE='a6/q2p/r8m21s/p300/dwy', STATUS='NEW')
OPEN(UNIT=5, FILE='a6/q2p/r8m21s/p300/et', STATUS='NEW')
OPEN(UNIT=7, FILE='a6/q2p/r8m21s/p300/ev', STATUS='NEW')
OPEN(UNIT=8, FILE='a6/q2p/r8m21s/p300/rhf', STATUS='NEW')
OPEN(UNIT=9, FILE='a6/q2p/r8m21s/p300/st', STATUS='NEW')
OPEN(UNIT=11, FILE='a6/q2p/r8m21s/p300/vo', STATUS='NEW')
OPEN(UNIT=12, FILE='a6/q2p/r8m21s/p300/wd', STATUS='NEW')
OPEN(UNIT=13, FILE='a6/q2p/r8m21s/p300/ud', STATUS='NEW')
OPEN(UNIT=14, FILE='a6/q2p/r8m21s/p300/vd', STATUS='NEW')
OPEN(UNIT=15, FILE='a6/q2p/r8m21s/p300/wud', STATUS='NEW')
OPEN(UNIT=16, FILE='a6/q2p/r8m21s/p300/uud', STATUS='NEW')
OPEN(UNIT=17, FILE='a6/q2p/r8m21s/p300/gen', STATUS='NEW')
OPEN(UNIT=18, FILE='a6/q2p/r8m21s/p300/vud', STATUS='NEW')
*
*   Geometric parameters, tolerance, temperature,
*   relaxation numbers are in alphabetic orders
*
DATA AP/300.D5/AE/3.5D-3/COEFM/0.271D0/DPZ/NP*0.D0/
1  DPZDIM/NP*0.D0/DPZUDM/0.D0/FLWM/NP*0.D0/DPZUD2/0.D0/
2  POSIS/NP*0.D0/POSIZ/NP*0.D0/DPZUD1/0.D0/PRESSU/NP1*0.D0/
3  SUM/0.D0/SUM1/0.D0/SUM2/0.D0/TEMP/NP*0.D0/
4  IC/0/ICC/0/IFLAGS/0/IFAIL/0/IG/0/IOUT/0/IJ/0/ITDPZU/0/
5  BDA/N*0.D0/BDB/N*0.D0/BDC/M*0.D0/BDD/M*0.D0/
*
*   The initial partial derivatives of down channel velocity, DWX and
*   DWY has to preset to non-zero value or the first approximated
*   apparent viscosity cannot be obtained as its negative index value
*   from the pseudoplastic behavior of power law.
*
6  DETX/MN*0.D0/DETY/MN*0.D0/DWX/MN*0.1D0/DWY/MN*0.1D0/
7  ETA/MN*1.D0/RELX3/0.2D0/RELX4/0.1D0/
8  RHSFUN/MN*0.D0/STRMFN/MN*0.D0/
9  VELTYW/MN*0.1D0/VORTIC/MN*0.D0/
1 DDFIXX(1,1)/0.D0/DDFIXX(M,1)/0.D0/
2 DDFIXX(1,N)/0.D0/DDFIXX(M,N)/0.D0/
3 DDFIYY(1,1)/0.D0/DDFIYY(M,1)/0.D0/
4 DDFIYY(1,N)/0.D0/DDFIYY(M,N)/0.D0/
5 ETAVOR(1,1)/0.D0/ETAVOR(M,1)/0.D0/
6 ETAVOR(1,N)/0.D0/ETAVOR(M,N)/0.D0/
*
*   Calculate the channel height and temperature
*   at end of first section
*
DH=(CHHTA-CHHTB)/(NP-1)
DT=(TEMPOT-TEMPIN)/(NP-1)
DALENG=ALENGT/(NP-1)
CH(1)=CHHTA-DH
PI=4.D0*DATAN(1.D0)
ALPHA=ALFA*PI/1.8D2
CONSTS=DSIN(ALPHA)*(1.D0-SLIP)
CONSTC=DCOS(ALPHA)*(1.D0-SLIP)
SINANG=DSIN(ALPHA)
COSANG=DCOS(ALPHA)

```

```

      CHWD=PI*SCREWD*SINANG-AE
      SCRWSP=SCREWN*SCREWD*PI/60.DO
      YB=CHWD/CH(1)
      DY=YB/NM1
      DYSQ=DY*DY
      ALZ=ALENGT/(DTAN(ALPHA))/SINANG
      TEMP(1)=TEMPIN+DT/2.DO
      FLOIND=-.444D0*CONCEN**.197D0
*
*   If restart number is one, read the data in /tmp/s1
*   or /tmp/s2, then skip over the initial computation
*   with Newtonian fluid assumption.
*
      IF(IR.EQ.1) THEN
        OPEN(UNIT=99,FILE='/tmp/s1',STATUS='OLD')
        READ(99,*)(WK(I),I=1,MNP),(FPSAVE(I),I=1,IFPSAV),
1       (BDA(I),BDB(I),I=1,N),(BDC(I),BDD(I),I=1,M)
        DO 20 J=1,N
          READ(99,*)(STRMFN(I,J),ETAVOR(I,J),VORTIC(I,J),
1       VELTYW(I,J),DDFIXX(I,J),DDFIYY(I,J),DDFIXY(I,J),
2       DDETXX(I,J),DDETTY(I,J),DDETXY(I,J),RHSFUN(I,J),
3       ETA(I,J),DWX(I,J),DWY(I,J),DETX(I,J),DETY(I,J),
4       WKARY1(I,J),WSAVE(I,J),I=1,M)
20      CONTINUE
        READ(99,*)(PRESSU(I),POSI(I),POSIZ(I),TEMP(I),FLOWM(I),
1       DPZ(I),DPZDIM(I),I=1,NP),ALZ,FLOWMS,CONSTS,CONSTC,
2       DPZUDM,SUM1,SUM2
        CLOSE(UNIT=15)
        ICC=0
        GOTO 118
      ENDIF
      DO 52 J=2,NM1
        VELTYU(1,J)=0.DO
        VELTYU(M,J)=0.DO
        VELTYV(1,J)=0.DO
        VELTYV(M,J)=CONSTS
        VELTYW(1,J)=0.DO
        VELTYW(M,J)=CONSTC
52      CONTINUE
      DO 54 I=1,M
        VELTYU(I,1)=0.DO
        VELTYU(I,N)=0.DO
        VELTYV(I,1)=0.DO
        VELTYV(I,N)=0.DO
        VELTYW(I,1)=0.DO
        VELTYW(I,N)=0.DO
54      CONTINUE
57      FLOWM(1)=COEFM*CONCEN**AMINDX*
1      DEXP(0.195D5/8.314/(273.15D0+TEMP(1)))
      FLOWMS=FLOWM(1)
      DPZDIM(1)=AP/ALZ
      DPZUDM=DPZDIM(1)*CH(1)**(FLOIND+2.DO)/
1      FLOWM(1)/SCRWSP**(FLOIND+1.DO)
      DPZ(1)=DPZUDM
*
*   Assume the right hand side is zero, solve the Poisson
*   equation to get initial stream function value
*   IC is for bigger loop, whereas ICC is for smaller loop
*   inside IC loop
*
      IC=0
      ICC=0
*
*   To the 1st calling, DELTA PSI=0 and PSI=0 @ all 4 boundaries

```



```

* i.e. Equation (3-60)
*
60  CALL H2GCID(XA,XB,MM1,1,YA,YB,NM1,1,0.D0,M,IER,FPSAVE)
    CALL H2GCSD(BDA,BDB,BDC,BDD,M,RHSFUN,PETR,FPSAVE,WK)
    IF(IER.GT.0) THEN
        WRITE(2,62) IER
62  FORMAT(2X,'IER=',I2,' RETURNED FORM ROUTINE H2GCID ON '
1    ', 'COMPUTATION OF STREAM FUNCTION AT LINE 60')
        GOTO 9000
    ENDIF
    DO 65 J=2,NM1
        DO 65 I=2,MM1
            RHSFUN(I,J)=STRMFN(I,J)+RELX*(RHSFUN(I,J)-STRMFN(I,J))
65  CONTINUE
*
* Move the stream function to STRMFN for later comparison
*
    CALL ARRMV(RHSFUN,STRMFN,M,N)
*
* Calculate the boundary values of vorticity
* AT Y=0
*
    DO 70 I=2, MM1
        BDC(I)=-2.D0*STRMFN(I,2)/DYSQ
*
* AT Y=W/H
*
        BDD(I)=-2.D0*STRMFN(I,NM1)/DYSQ
70  CONTINUE
*
* at X=0 and X=1
*
    DO 75 J=2,NM1
        BDA(J)=-2.D0*STRMFN(2,J)/DXSQ
*
* AT X=XB=1, the moving
*
        BDB(J)=2.D0*(DX*CONSTS-STRMFN(MM1,J))/DXSQ
75  CONTINUE
*
* At four corners
*
        BDA(1)=0.D0
        BDA(N)=0.D0
        BDB(1)=0.D0
        BDB(N)=0.D0
        BDC(1)=0.D0
        BDC(M)=0.D0
        BDD(1)=0.D0
        BDD(M)=0.D0
        DO 80 J=1,N
            DO 80 I=1,M
                RHSFUN(I,J)=0.D0
80  CONTINUE
*
* Solve Equation (3-61)
*
    CALL H2GCID(XA,XB,MM1,1,YA,YB,NM1,1,0.D0,M,IER,FPSAVE)
    CALL H2GCSD(BDA,BDB,BDC,BDD,M,RHSFUN,PETR,FPSAVE,WK)
    IF(IER.GT.0) THEN
        WRITE(2,82) IER
82  FORMAT(2X,'IER=',I2,' RETURNED FROM H2GCID ROUTINE ',
1    'ON COMPUTATION OF VORTICITY AT LINE 80')
        ENDIF

```

```

*
* if IC=0, means the right-hand-side function of Equation
* (3-40) is 0. Then the obtained vorticity is assigned to it
*
      IF(IC.EQ.0) GOTO 100
*
* IC is not zero. Check two successive obtained vorticity
* values to see whether they are close enough.
* If they are, then the flag IG=1, or relax it, save the newly
* obtained vorticity and iterate one more time.
*
      DO 85 I=2,MM1
        DO 83 J=2,NM1
          IF(DABS(VORTIC(I,J)-RHSFUN(I,J)).GT.EPS) GOTO 90
83      CONTINUE
85      CONTINUE
        IG=1
90      DO 98 J=2,NM1
        DO 95 I=2,MM1
          RHSFUN(I,J)=VORTIC(I,J)+RELX*
1      (RHSFUN(I,J)-VORTIC(I,J))
95      CONTINUE
98      CONTINUE
*
* Save RHSFUN, the vorticity value to VORTIC
* for next comparison, then solve Equation (3-39)
*
100     CALL ARRMV(RHSFUN,VORTIC,M,N)
      DO 105 I=1,M
        BDC(I)=0.D0
        BDD(I)=0.D0
105     CONTINUE
      DO 110 J=1,N
        BDA(J)=0.D0
        BDB(J)=0.D0
110     CONTINUE
*
* Assign right-hand-function values of Equation (3-39)
*
      DO 115 J=1,N
        DO 114 I=1,M
          RHSFUN(I,J)=-VORTIC(I,J)
114     CONTINUE
115     CONTINUE
      IC=IC+1
*
* IG=1 means that solving of the coupled Equations (3-60) and
* (3-61) has converged. So far, the stream function and
* vorticity have been obtained with assumption Newtonian fluid.
*
      IF(IG.EQ.1) GOTO 118
      GOTO 60
118     DO 2000 KP=1,NP-1
        CHHT=CH(KP)
119     ICC=ICC+1
120     IC=0
*
* If KP=1, it calculates Equation (3-60) one more time.
*
160     CALL H2GCID(XA,XB,MM1,1,YA,YB,NM1,1,0.D0,M,IER,FPSAVE)
        CALL H2GCSD(BDA,BDB,BDC,BDD,M,RHSFUN,PETR,FPSAVE,WK)
        IF(IER.GT.0) THEN
          WRITE(2,162) IER
162     FORMAT(2X,'IER=',I2,' RETURNED FROM H2GCID ON COMPUTATION',

```

```

1      ' OF STREAM FUNCTION AT LINE 160')
      GOTO 9000
      ENDIF
*
* Try to use stream function values as accurate as possible
*
      DO 165 J=2,NM1
        DO 165 I=2,MM1
          RHSFUN(I,J)=STRMFN(I,J)+RELX2*
            (RHSFUN(I,J)-STRMFN(I,J))
165    CONTINUE
*
* Save stream function for later comparison
*
      CALL ARRMOV(RHSFUN,STRMFN,M,N)
*
* Calculate the derivatives of apparent viscosity and vorticity,
* the right-hand-side function and boundary conditions of
* Equation (3-38). At Y=0
*
      DO 200 I=2, MM1
        DDFIYY(I,1)=2.DO*(STRMFN(I,2))/DYSQ
        DDFIXX(I,1)=0.DO
        ETA(I,1)=(DDFIYY(I,1)**2+DWY(I,1)**2)**
1      (FLOIND*.5D0)
        VORTIC(I,1)=-DDFIYY(I,1)
        BDC(I)=VORTIC(I,1)*ETA(I,1)
*
* AT Y=W/H
*
        DDFIYY(I,N)=2.DO*(STRMFN(I,NM1))/DYSQ
        DDFIXX(I,N)=0.DO
        ETA(I,N)=(DDFIYY(I,N)**2+DWY(I,N)**2)
1      *(FLOIND*.5D0)
        VORTIC(I,N)=-DDFIYY(I,N)
        BDD(I)=VORTIC(I,N)*ETA(I,N)
200    CONTINUE
*
* at X=0
*
      DO 220 J=2,NM1
        DDFIXX(1,J)=2.DO*(STRMFN(2,J))/DXSQ
        DDFIYY(1,J)=0.DO
        ETA(1,J)=(DDFIXX(1,J)**2+DWX(1,J)**2)
1      *(FLOIND*.5D0)
        VORTIC(1,J)=-DDFIXX(1,J)
        BDA(J)=ETA(1,J)*VORTIC(1,J)
*
* AT X=1
*
        DDFIXX(M,J)=-2.DO*(DX*CONSTS-STRMFN(MM1,J))/DXSQ
        DDFIYY(M,J)=0.DO
        ETA(M,J)=(DDFIXX(M,J)**2+DWX(M,J)**2)*(FLOIND*.5D0)
        VORTIC(M,J)=-DDFIXX(M,J)
        BDB(J)=ETA(M,J)*VORTIC(M,J)
220    CONTINUE
*
* At four corners
*
        BDA(1)=0.DO
        BDA(N)=0.DO
        BDB(1)=0.DO
        BDB(N)=0.DO
        BDC(1)=0.DO

```

```

      BDC(M)=0.D0
      BDD(1)=0.D0
      BDD(M)=0.D0
*
*   Calculate apparent viscosity and derivative of steam function
*   at all interior nodes,
*
      DO 242 I=2,MM1
        DO 240 J=2,NM1
          DDFIXX(I,J)=(STRMFN(I-1,J)-2.D0*STRMFN(I,J)
1            +STRMFN(I+1,J))/DXSQ
          DDFIYY(I,J)=(STRMFN(I,J-1)-2.D0*STRMFN(I,J)
1            +STRMFN(I,J+1))/DYSQ
          DDFIXY(I,J)=(STRMFN(I+1,J+1)-STRMFN(I-1,J+1)
2            +STRMFN(I-1,J-1)-STRMFN(I+1,J-1))/4.D0/DX/DY
          ETA(I,J)=(4.D0*DDFIXY(I,J)**2+(DDFIYY(I,J)-
1            DDFIXX(I,J)**2+DWX(I,J)**2
2            +DWY(I,J)**2)*(FLOIND*.5D0)
          VORTIC(I,J)=-DDFIXX(I,J)-DDFIYY(I,J)
240      CONTINUE
242      CONTINUE
*
*   For four corners: at x=0 and y=0
*
      ETA(1,1)=(ETA(2,1)+ETA(1,2))/2.D0
*
*   At Y=1 and X=0
*
      ETA(1,N)=(ETA(1,NM1)+ETA(2,N))/2.D0
*
*   At X=1 and Y=0
*
      ETA(M,1)=(ETA(M,2)+ETA(MM1,1))/2.D0
*
*   At X=1 and Y=1
*
      ETA(M,N)=(ETA(M,NM1)+ETA(MM1,N))/2.D0
*
*   Calculate the derivatives of ETA, apparent viscosity
*   at all interior nodes
*
      DO 260 I=2,MM1
        DO 260 J=2,NM1
          DDETYX(I,J)=(ETA(I,J-1)-2.D0*ETA(I,J)+
1            ETA(I,J+1))/DYSQ
          DDETXX(I,J)=(ETA(I-1,J)-2.D0*ETA(I,J)+
1            ETA(I+1,J))/DXSQ
          DDETXY(I,J)=(ETA(I+1,J+1)-ETA(I-1,J+1)
1            -ETA(I+1,J-1)+ETA(I-1,J-1))/4.D0/DX/DY
260      CONTINUE
*
*   Calculate the right-hand-side function of Equation (3-38)
*
      DO 280 I=2,MM1
        DO 270 J=2,NM1
          RHSFUN(I,J)=-2.D0*DDETXX(I,J)*DDFIYY(I,J)
1            +4.D0*DDETXY(I,J)*DDFIXY(I,J)-2.D0*
2            DDETYX(I,J)*DDFIXX(I,J)
270      CONTINUE
280      CONTINUE
*
*   Solve Equation (3-41) to obtain ETA-VORTICITY
*
      CALL H2GCID(XA,XB,MM1,1,YA,YB,NM1,1,0.D0,M,IER,FPSAVE)

```

```

        CALL H2GCSD(BDA,BDB,BDC,BDD,M,RHSFUN,PETR,FPSAVE,WK)
        IF(IER.GT.0) THEN
        WRITE(2,290) IER
290      FORMAT(2X,'IER=',I2,' RETURNED FROM ROUTINE H2GCID '
1        , 'ON COMPUTATION OF ETAVOR')
        GOTO 9000
        ENDIF
*
*   It does not need compare for the 1st computation.
*
        IF(IC.EQ.0) GOTO 320
*
*   When IC is not a zero, find relative differences of
*   ETA-VORTICITY at each interior node. If the differences
*   fall within the preset tolerance then go to next step
*   to calculate down channel velocity from Equation (3-25).
*
        DO 300 J=2,NM1
            DO 295 I=2,MM1
                EVDIF(I,J)=(ETAVOR(I,J)-RHSFUN(I,J))
                REVDIF(I,J)=DABS(EVDIF(I,J))/ETAVOR(I,J)
295          CONTINUE
300        CONTINUE
            DO 310 J=2,NM1
                DO 305 I=2,MM1
                    IF(REVDIF(I,J).GT.EPS) GOTO 320
305          CONTINUE
310        CONTINUE
            CALL ARRMV(RHSFUN,ETAVOR,M,N)
            CALL STMRT(RHSFUN,ETA,M,N)
            CALL STBDZO(BDA,BDB,BDC,BDD,M,N)
            GOTO 430
320        IF(IC.GT.600) THEN
                RELX3=.1D0
                RELX4=.05D0
            ELSE
                RELX3=.2D0
                RELX4=0.1D0
            ENDIF
            DO 330 J=2,NM1
                DO 325 I=2,MM1
                    RHSFUN(I,J)=ETAVOR(I,J)+RELX3*(RHSFUN(I,J)-ETAVOR(I,J))
325          CONTINUE
330        CONTINUE
*
*   Save RHSFUN to ETAVOR for next comparison
*
        CALL ARRMV(RHSFUN,ETAVOR,M,N)
*
*   Dividing ETAVOR by ETA at all interior nodes and at the moving
*   boundary nodes as well to get right-hand-side function of
*   Equation (3-37)
*
        CALL STMRT(RHSFUN,ETA,M,N)
*
*   Set the boundary condition for stream
*   function Poisson equation
*
        CALL STBDZO(BDA,BDB,BDC,BDD,M,N)
        IC=IC+1
        IF(IC.GT.600) THEN
            WRITE(2,429) IC,ICC
429        FORMAT('LINE 429','IC=',I8,'ICC=',I8)
        ENDIF

```

```

*
*   Go to 160 to solve Equation (3-39)
*
      GOTO 160
430    DO 440 J=2,NM1
        DO 435 I=2,MM1
            DETX(I,J)=(ETA(I+1,J)-ETA(I-1,J))/2.DO/DX
            DETY(I,J)=(ETA(I,J+1)-ETA(I,J-1))/2.DO/DY
435    CONTINUE
440    CONTINUE
*
*   Calculate down channel velocity component W
*
450    DO 480 J=1,NM1-1
        DO 470 I=1,MM1-1
            K=(J-1)*(MM1-1)+I
            A(K,1)=(-DETY(I,J)*DY+2.DO*ETA(I,J))*DXSQ
            A(K,2)=0.DO
            A(K,3)=(-DETX(I,J)*DX+2.DO*ETA(I,J))*DYSQ
            A(K,4)=-4.DO*ETA(I,J)*(DXSQ+DYSQ)
            A(K,5)=(DETX(I,J)*DX+2.DO*ETA(I,J))*DYSQ
            A(K,6)=0.DO
            A(K,7)=(DETY(I,J)*DY+2.DO*ETA(I,J))*DXSQ
            RHS(K)=DPZUDM*DXSQ*DYSQ*2.DO
            UB(K)=VELTYW(I+1,J+1)
470    CONTINUE
480    CONTINUE
        DO 500 I=2,MM1-2
*
*   The boundary conditions, at Y=0, w=0
*
            A(I,1)=0.DO
            A(I,2)=0.DO
*
*   At Y=W/H, w=0
*
            IX=I+(N-3)*(M-2)
            A(IX,6)=0.DO
            A(IX,7)=0.DO
500    CONTINUE
        DO 520 J=2,N-3
*
*   at X=0, w=0
*
            IY=(J-1)*(MM2)+1
            A(IY,3)=0.DO
            A(IY,6)=0.DO
*
*   X=1, w=COS(ALPHA)
*
            IY=J*(MM2)
            RHS(IY)=RHS(IY)-A(IY,5)*CONSTC-A(IY,2)*CONSTC
            A(IY,2)=0.DO
            A(IY,5)=0.DO
520    CONTINUE
*
*   For four corners. At bottom left
*
            A(1,1)=0.DO
            A(1,2)=0.DO
            A(1,3)=0.DO
            A(1,6)=0.DO
*
*   At top left corner

```

```

*
      K=1+(N-3)*(MM2)
      A(K,3)=0.D0
      A(K,6)=0.D0
      A(K,7)=0.D0
*
*   At bottom right corner
*
      RHS(MM2)=RHS(MM2)-A(MM2,5)*CONSTC
      A(MM2,1)=0.D0
      A(MM2,2)=0.D0
      A(MM2,5)=0.D0
*
*   At top right corner
*
      K=(MM2)*(NM2)
      RHS(K)=RHS(K)-A(K,2)*CONSTC-A(K,5)*CONSTC
      A(K,2)=0.D0
      A(K,5)=0.D0
      A(K,6)=0.D0
      A(K,7)=0.D0
*
*   Solve the equation to get the dimensionless down channel
*   velocity, w
*
      CALL D03EDF(MM2,NM2,LDA,A,RHS,UB,MAXITR,ACC,US,U,IOUT,
1        NUMIT,IFAIL)
      IF(IFAIL.GE.1) THEN
        WRITE(2,530) IFAIL,ICC
530      FORMAT(1X,'IFAIL=',I4,' CALL OF D03EDF ','ICC=',I4)
        GOTO 9000
      ENDIF
*
*   Save the newly obtained dimensionless w velocities
*
560      DO 580 J=1,NM2
          DO 570 I=1,MM2
              WSAVE(I+1,J+1)=VELTYW(I+1,J+1)
              VELTYW(I+1,J+1)=U(I+(J-1)*(MM2))
570          CONTINUE
580      CONTINUE
*
*   AT BOUNDARY VELOCITY W HAS KNOWN
*
      DO 600 I=1,M
          VELTYW(I,1)=0.D0
          VELTYW(I,N)=0.D0
600      CONTINUE
      DO 620 J=2,NM1
          VELTYW(1,J)=0.D0
          VELTYW(M,J)=CONSTC
620      CONTINUE
      DO 640 J=2,NM1
          DO 640 I=2,MM1
              DWX(I,J)=(VELTYW(I+1,J)-VELTYW(I-1,J))/2.D0/DX
640          CONTINUE
          DO 650 I=2,MM1
              DO 650 J=2,NM1
                  DWY(I,J)=(VELTYW(I,J+1)-VELTYW(I,J-1))/2.D0/DY
650          CONTINUE
          DO 660 I=2,MM1
              DWY(I,1)=(3.D0*VELTYW(I,1)-4.D0*VELTYW(I,2)+
1              VELTYW(I,3))/2.D0/DY
              DWY(I,N)=(3.D0*VELTYW(I,N)-4.D0*VELTYW(I,NM1)+

```

```

1      VELTYW(I,NM2))/2.DO/DY
      DWX(I,N)=0.DO
      DWX(I,1)=0.DO
660    CONTINUE
      DO 680 J=2,NM1
1      DWX(1,J)=(3.DO*VELTYW(1,J)-4.DO*VELTYW(2,J)+
1      VELTYW(3,J))/2.DO/DX
      DWX(M,J)=(3.DO*VELTYW(M,J)-4.DO*VELTYW(MM1,J)+
1      VELTYW(MM2,J))/2.DO/DX
      DWY(M,J)=0.DO
      DWY(1,J)=0.DO
680    CONTINUE
      DWX(1,1)=0.DO
      DWY(1,1)=0.DO
      DWX(1,N)=0.DO
      DWY(1,N)=0.DO
      DWX(M,N)=0.DO
      DWY(M,N)=0.DO
      DWX(M,1)=0.DO
      DWY(M,1)=0.DO
      ICC=ICC+1
      WRITE(2,691)IC,ICC,KP
691    FORMAT('LINE 691','IC=',I8,'ICC=',I8,'KP=',I3)
      IF(ICC.GT.3000) THEN
1      WRITE(2,700)ICC
700    FORMAT(1X,'ICC=',I4,' TOO MANY INTERATION. LOOKS ',
1      'UNREASONABLE.')
      GOTO 9000
      ENDIF
*
* Find the relative difference of down channel velocity
*
      DO 710 J=2,NM1
      DO 705 I=2,MM1
      WDIF(I,J)=VELTYW(I,J)-WSAVE(I,J)
      RWDIF(I,J)=DABS(WDIF(I,J)/WSAVE(I,J))
705    CONTINUE
710    CONTINUE
      IMAX=0
      JMAX=0
      AMAX=0.DO
*
* Find the maximum value in the array RWDIF.
*
      DO 715 J=2,NM1
      DO 714 I=2,MM1
      IF(AMAX.LT.RWDIF(I,J))THEN
      AMAX=RWDIF(I,J)
      IMAX=I
      JMAX=J
      ENDIF
714    CONTINUE
715    CONTINUE
      WRITE(2,716)IC,ICC,IMAX,JMAX,AMAX,SUM
716    FORMAT('C',I3,' CC',I4,' MX(',I2,',',I3,')=',E11.4,
1      'SUM',E11.4)
*
* If the maximum in the array RWDIF is larger than the tolarence
* then do the computation once more.
*
      IF(AMAX.GT.EPS) GOTO 830
*
* If AMAX falls within the torlerance, use the velocity to
* calculate the discharge rate with two dimensional trapezoidal

```



```

* integration method.
*
      SUMFO(1)=0.D0
      SUMFO(N)=0.D0
      DO 770 J=2,NM1
        SUMFO(J)=0.D0
        DO 750 I=1,M-4,4
          SUMFO(J)=SUMFO(J)+(2.D0*DX/45.D0)*(7.D0*(VELTYW(I,J)+
1          VELTYW(I+4,J))+32.D0*(VELTYW(I+1,J)+
2          VELTYW(I+3,J))+12.D0*VELTYW(I+2,J))
750      CONTINUE
770      CONTINUE
      SUMFT=0.D0
      DO 790 I=1,N-4,4
        SUMFT=SUMFT+(2.D0*DY/45.D0)*(7.D0*(SUMFO(I)+SUMFO(I+4))+
1        32.D0*(SUMFO(I+1)+SUMFO(I+3))+12.D0*SUMFO(I+2))
790      CONTINUE
      SUM=SUMFT*RHO*SCRWSP*CH(KP)*CH(KP)*3600.D0
      RSUM=(DABS(SUM-ESUM))/ESUM
      WRITE(2,222)RSUM,SUM
222      FORMAT('rsum=',E12.7,'sum=',E12.7)
      IF(AMAX.GT.EPS.AND.RSUM.GT..1D0) GOTO 830
      WRITE(2,791)SUM,CHHT,SUMFT,RSUM,SUM
791      FORMAT(' line 791 ','sum=',E11.4,'chht=',E11.4,
1      'sumft=',E11.4/)
      IF(IFLAGS.EQ.1) GOTO 795
*
* Save the first calculation
*
      IFLAGS=1
      SUM1=SUM
      DPZUD1=DPZUDM
      DPZUDM=1.5D0*DPZUDM
      ICC=0
      GOTO 450
795      SUM2=SUM
      DPZUD2=DPZUDM
*
* To get pressure gradient by interpolation
*
      DPZUDM=DPZUD1+(ESUM-SUM1)/(SUM2-SUM1)*(DPZUD2-DPZUD1)
      SUM1=SUM2
      DPZUD1=DPZUD2
      WRITE(2,828)DPZUDM,DPZUD1,DPZUD2
      IF(DABS((SUM-ESUM)/ESUM).LE..1D0) GOTO 900
828      FORMAT(' 828 dpzudm,dpzud1,dpzud2 ',3(E12.4,2X))
      ITDPZU=ITDPZU+1
830      DO 840 J=2,NM1
        DO 835 I=2,MM1
          VELTYW(I,J)=WSAVE(I,J)+RELX4*(VELTYW(I,J)-WSAVE(I,J))
835      CONTINUE
840      CONTINUE
      CALL ARRMV(VELTYW,WSAVE,M,N)
*
* restart the calucation with new dwx and dwy
*
      GOTO 120
900      DO 940 I=2,MM1
        DO 920 J=2,NM1
          VELTYU(I,J)=- (STRMFN(I,J+1)-STRMFN(I,J-1))/DY/2.D0
920      CONTINUE
940      CONTINUE
      DO 960 J=2,NM1
        DO 950 I=2,MM1

```

```

      VELTYV(I,J)=(STRMFN(I+1,J)-STRMFN(I-1,J))/DX/2.DO
950    CONTINUE
960    CONTINUE
      CALL ARRWRI(DWX,DWY,ETA,ETAVOR,RHSFUN,STRMFN,VELTYW,
1      VELTYU,VELTYV,VORTIC,M,N,IC,ICC,KP)
      DPZ(KP)=DPZUDM
      DPZDIM(KP)=DPZUDM*SCRWSP**(FLOIND+1.DO)*FLOWM(KP)/
1      CH(KP)**(FLOIND+2.DO)
      PRESSU(KP+1)=PRESSU(KP)+(DALENG/SINANG)*DPZDIM(KP)
      POSIS(KP)=DALENG/CONV*DFLOAT(KP)
      CH(KP+1)=CH(KP)-DH
      YB=CHWD/CH(KP+1)
      DY=YB/NM1
      DYSQ=DY*DY
      POSIZ(KP)=POSI(KP)*CONV/SINANG
      TEMP(KP+1)=TEMP(KP)+DT
      FLOWM(KP+1)=COEFM*CONCEN**AMINDX*
1      DEXP(.164D5/8.314/(273.15D0+TEMP(KP+1)))
      FLOWMS=FLOWM(KP+1)
      WRITE(17,1500)
1500   FORMAT(/'POSI(IN)',1X,'POSIZ(m)',1X,'PRESSURE',1X,
1      'TEMP',3X,'FLOWM',4X,'DPZ',6X,'DPZDIM',3X,'CHHT')
      WRITE(17,1510)(POSI(I),POSIZ(I),PRESSU(I+1),
1      TEMP(I),FLOWM(I),DPZ(I),DPZDIM(I),CH(I),I=1,NP)
1510   FORMAT(1X,F5.2,4X,F4.2,2X,E11.4,F6.2,1X,F7.1,
1      F8.4,E11.4,E11.4)
      WRITE(17,1520)ESUM,ALFA,SCREWN,SCRWSP,KP,M,N,FLOIND,
1      CHHT**(FLOIND+2.DO),SCRWSP**(FLOIND+1.DO)
1520   FORMAT(' ESUM=',F6.2,' ALFA=',F5.2,' SCREWN=',F5.1,
1      ' SCRWSP=',F6.1,' KP=',I3,' M=',I3,' N=',I3/
2      ' n=',F8.4,' H**(n+1)=' ,E10.3,
3      ' V**(n+1)=' ,E10.3)
      ITDPZU=0
      ICC=0
*
* Sometimes, the computer is interrupted. The calculation
* is lost. The large amount of CUP is wasted. Save the
* obtained values to be used as a set of initial values for
* recalculation.
*
      OPEN(UNIT=99,FILE='/tmp/sl',STATUS='NEW')
      WRITE(15,*)(WK(I),I=1,MNP),(FPSAVE(I),I=1,IFPSAV),
1      (BDA(I),BDB(I),I=1,N),(BDC(I),BDD(I),I=1,M)
      DO 1600 J=1,N
        WRITE(99,*)(STRMFN(I,J),ETAVOR(I,J),VORTIC(I,J),
1        VELTYW(I,J),DDFIXX(I,J),DDFIYY(I,J),DDFIXY(I,J),
2        DDETXX(I,J),DDETTY(I,J),DDETXY(I,J),RHSFUN(I,J),
3        ETA(I,J),DWX(I,J),DWY(I,J),DETX(I,J),DETY(I,J),
4        WKARY1(I,J),WSAVE(I,J),I=1,M)
1600   CONTINUE
      WRITE(99,*)(PRESSU(I),POSI(I),POSIZ(I),TEMP(I),FLOWM(I),
1      DPZ(I),DPZDIM(I),I=1,NP),ALZ,FLOWMS,CONSTS,CONSTC,
2      DPZUDM,SUM1,SUM2
      CLOSE(UNIT=99)
2000   CONTINUE
9000   CLOSE(UNIT=2)
      END
*
* This subroutine is for reckoning righthand side
* function of the stream function equation
*
      SUBROUTINE STMRT(RHSFUN,ETA,M,N)
      IMPLICIT REAL*8(A-H,O-Z)
      DIMENSION RHSFUN(M,N),ETA(M,N)

```

```

      DO 20 J=2,N-1
        DO 20 I=2,M-1
          RHSFUN(I,J)=-RHSFUN(I,J)/ETA(I,J)
10      CONTINUE
20      CONTINUE
      RETURN
      END

*
* This subroutine is for moving the same dimensional
* array1 to array2
*
      SUBROUTINE ARRMov(ARRAY1,ARRAY2,M,N)
      IMPLICIT REAL*8(A-H,O-Z)
      DIMENSION ARRAY1(M,N),ARRAY2(M,N)
      DO 20 J=1,N
        DO 10 I=1,M
          ARRAY2(I,J)=0.D0
          ARRAY2(I,J)=ARRAY1(I,J)
10      CONTINUE
20      CONTINUE
      RETURN
      END

*
* This subroutine is for print the obtained results
*
      SUBROUTINE ARRWRI(DWX,DWY,ETA,ETAVOR,RHSFUN,STRMFN,VELTYW,
1  VELTYU,VELTYV,VORTIC,M,N,IC,ICC,KP)
      IMPLICIT REAL*8(A-H,O-Z)
      COMMON SCRWSP,FLOIND,FLOWM,CHHT
      DIMENSION DWX(M,N),DWY(M,N),ETA(M,N),ETAVOR(M,N),STRMFN(M,N),
1  RHSFUN(M,N),VELTYW(M,N),VORTIC(M,N),VELTYU(M,N),VELTYV(M,N)
      C=FLOWM*SCRWSP**FLOIND/CHHT**FLOIND
      DO 1000 J=1,N
        WRITE(3,30)KP,J,(DWX(I,J),I=1,M)
30      FORMAT('Z=',I2,' J=',I3/5(1X,E13.6))
        WRITE(4,30)KP,J,(DWY(I,J),I=1,M)
        WRITE(5,30)KP,J,(ETA(I,J)*C,I=1,M)
        WRITE(7,30)KP,J,(ETAVOR(I,J),I=1,M)
        WRITE(8,30)KP,J,(RHSFUN(I,J),I=1,M)
        WRITE(9,30)KP,J,(STRMFN(I,J),I=1,M)
        WRITE(11,30)KP,J,(VORTIC(I,J),I=1,M)
        WRITE(12,30)KP,J,(VELTYW(I,J)*SCRWSP,I=1,M)
        WRITE(13,30)KP,J,(VELTYU(I,J)*SCRWSP,I=1,M)
        WRITE(14,30)KP,J,(VELTYV(I,J)*SCRWSP,I=1,M)
        WRITE(15,30)KP,J,(VELTYW(I,J),I=1,M)
        WRITE(16,30)KP,J,(VELTYU(I,J),I=1,M)
        WRITE(18,30)KP,J,(VELTYV(I,J),I=1,M)
1000    CONTINUE
      RETURN
      END

*
* This routine is for setting the boundary value into zero
*
      SUBROUTINE STBDZO(BDA,BDB,BDC,BDD,M,N)
      IMPLICIT REAL*8(A-H,O-Z)
      DIMENSION BDA(N),BDB(N),BDC(M),BDD(M)
      DO 10 I=1,M
        BDC(I)=0.D0
        BDD(I)=0.D0
10      CONTINUE
      DO 20 I=1,N
        BDA(I)=0.D0
        BDB(I)=0.D0
20      CONTINUE

```

```

RETURN
END

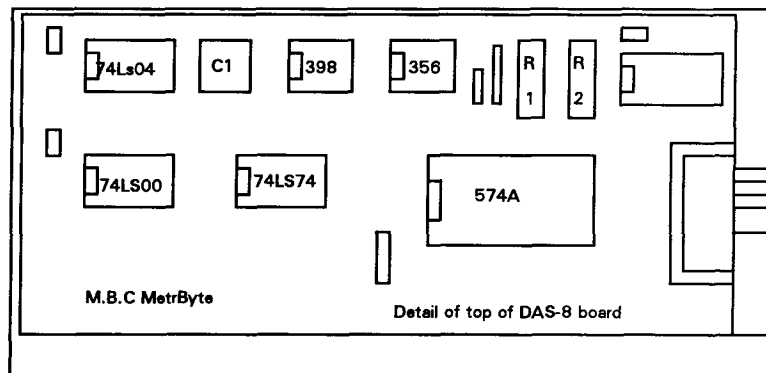
```

A.6.2 BASIC Program for Calibration of Data Acquisition Interface

```

100 *****
110 *
120 '*                      CALIBRATION AID PROGRAM
130 '* MetraByte Corporation                      Rev. 1.10  4-25-84
140 *****
142 '
145 'Initialization
150 CLEAR, 49152!
160 SCREEN 0,0,0:KEY OFF:CLS:WIDTH 80
180 DEF SEG = 0
190 SG = 256 * PEEK(&H511) + PEEK(&H510)
200 SG = SG + 49152!/16
210 DEF SEG = SG
220 BLOAD "DAS8.BIN", 0
230 OPEN "DAS8.ADR" FOR INPUT AS #1
240 INPUT #1, BASADR%
250 CLOSE #1
260 DAS8 = 0
270 FLAG% = 0
280 MD% = 0
290 CALL DAS8 (MD%, BASADR%, FLAG%)
298 '
299 'Draw board outline
300 IF FLAG% <> 0 THEN PRINT "INSTALLATION ERROR"
330 LOCATE 12,10:PRINT
340 LOCATE 13,10:PRINT
350 LOCATE 14,10:PRINT
360 LOCATE 15,10:PRINT
370 LOCATE 16,10:PRINT
380 LOCATE 17,10:PRINT
390 LOCATE 18,10:PRINT
400 LOCATE 19,10:PRINT
410 LOCATE 20,10:PRINT
420 LOCATE 21,10:PRINT
435 LOCATE 24,1:COLOR 15,0:PRINT "Press <ESC> to exit to BASIC - Any
other key to continue calibration":COLOR 7,0

```



```
438 LOCATE 25,1:PRINT"CALDAS8: DAS-8 CALIBRATION PROGRAM
MetraByte Corporation";
440 '
442 'Adjust -F.S.
443 FS%=0
444 LOCATE 10,1:PRINT SPC(79):LOCATE 10,1:COLOR 15,0:PRINT"Apply
input of -4.9988v and adjust for -2047/8:   ";;COLOR 31,0:PRINT
CHR$(25):COLOR 7,0
446 '
450 'Display A/D output on screen
460 MD%=1:LT%(0)=0:LT%(1)=7 'Mux limits
470 CALL DAS8 (MD%,LT%(0),FLAG%) 'Set limits
480 MD%=4:DT%=0 'Do 1 A/D conversion
490 FOR I = 0 TO 7
500 CALL DAS8 (MD%, DT%, FLAG%)
510 LOCATE 1+I,13:PRINT USING "Channel # output = #####"      Errors
= ##";I;DT%;FLAG%
520 NEXT I
530 A$ = INKEY$
540 IF A$ = "" GOTO 450
550 IF A$=CHR$(27) THEN CLS:LOCATE 1,1:END
560 IF FS%=0 GOTO 610
570 IF FS%=1 GOTO 442
600 '
610 'Adjust +F.S.
612 FS%=1
620 LOCATE 10,1:PRINT SPC(79):COLOR 15,0:LOCATE 10,1:PRINT"Apply
input of +4.9963v and adjust for +2046/7:   ";;COLOR 31,0:PRINT
CHR$(25):COLOR 7,0
630 GOTO 450
```

□

A.7 List of Material Suppliers

Canbra Food Ltd., Lethridge,
Albert, Canada

Canola seeds
Canola raw oil

Canon Instrument Company, P.O.
Box 16, State College, PA 16804-
0016, USA

Viscosity standard
N30000

Data Instruments Inc., Leexington,
MA

high precise pressure
transducer

Eaton Corporation
Fluid Power Operations
Hydraulics Division
15151 Highway 5
Eden Prairie, MN 55344
Tel.: (612) 937-9800

Hydraulic motors
2000 series
Mdl. 103-1032

Estrin Industrial Equipment
1696 West 5th Ave.
Vancouver, B.C.
Tel. (604) 731-5371

Electric Motor
20 hp, 256T

Haake Mess-Technik GmbH u. Co.
USA: Haake Inc.
244 Saddle River Road
Saddle Brook
N. J. 07662
Tel.: (201) 843-7070

Rotational viscometer
Rotovisco RV12

Laboratory Technologies
Corporation
400 Research Drive
Wilmington, MA 01887
Tel.: (508) 657-5400

Notebook data
logging software

MetraByte Corporation
440 Myles Standish Boulevard
Taunton, MA. 02780, USA
Tel.: (508) 880-3000
Omega Engineering Inc.
An Omega Technologies Company
One Omega Drive, Box 4047
Stamford, CT 06907-0047
Fax: (203) 259-7700

RAM Hydraulics & Air Ltd.
1026 Auckland St.
New Westminster, B.C.
Tel.: (604) 525-1604

Data logging
interface
DAS-8 and Exp-16

Thermocouples
JHIN-18-RSC-12
pressure transducers
PX-600

Hydraulic pumps
M11AA2A,
Variable flow control
valve FCR-51
Control valve
SPV4-HP